



UNIVERSIDADE FEDERAL DE MINAS GERAIS
INSTITUTO DE GEOCIÊNCIAS
PROGRAMA DE PÓS-GRADUAÇÃO EM GEOLOGIA



TESE DE DOUTORADO

Gênese e controle dos depósitos hematíticos-magnetíticos encaixados no Complexo Guanhães

AUTORA Flávia Cristina Silveira Braga

ORIENTAÇÃO: Prof. Carlos Alberto Rosière

COORIENTAÇÃO: João Orestes Schneider Santos

Nº 44

BELO HORIZONTE
DATA (17/06/19)



**UNIVERSIDADE FEDERAL DE MINAS GERAIS
INSTITUTO DE GEOCIÊNCIAS
PROGRAMA DE PÓS-GRADUAÇÃO EM GEOLOGIA**

Área de Concentração: Geologia Econômica e Aplicada

Gênese e controle dos depósitos hematíticos-magnetíticos encaixados no Complexo
Guanhães

por

Flávia Cristina Silveira Braga

Tese apresentada ao Programa de Pós-Graduação
em Geologia do Instituto de Geociências da
Universidade Federal de Minas Gerais como
requisito parcial à obtenção do título de Doutor
em Geologia Econômica e Aplicada.

Orientação: Prof. Carlos Alberto Rosière
Coorientação: João Orestes Schneider Santos

Belo Horizonte, 17 de junho de 2019

B813g Braga, Flávia Cristina Silveira.
2019 Gênese e controle dos depósitos hematíticos-magnetíticos encaixados no Complexo Guanhães [manuscrito] / Flávia Cristina Silveira Braga. – 2019.
228 [51] f., enc.: il. (principalmente color.)

Orientador: Carlos Alberto Rosière.
Coorientador: João Orestes Schneider Santos.
Tese (doutorado) – Universidade Federal de Minas Gerais, Instituto de Geociências, 2019.
Área de concentração: Geologia Econômica e Aplicada.
Bibliografia: f. 157-176.
Inclui anexos.

1. Geologia econômica – Minas Gerais – Teses. 2. Minérios de ferro – Minas Gerais – Teses. 3. Metalogenia – Teses. 4. Geoquímica – Teses. I. Rosière, Carlos Alberto. II. Santos, João Orestes Schneider. III. Universidade Federal de Minas Gerais. Instituto de Geociências. IV. Título.

CDU: 553 (815.1)

Ficha catalográfica elaborada por Graciane A. de Paula – CRB6 3404



UNIVERSIDADE FEDERAL DE MINAS GERAIS

PROGRAMA DE PÓS-GRADUAÇÃO EM GEOLOGIA



FOLHA DE APROVAÇÃO

Gênese e controle dos depósitos hematíticos-magnetíticos encaixados no Complexo Guanhães

FLÁVIA CRISTINA SILVEIRA BRAGA

Tese submetida à Banca Examinadora designada pelo Colegiado do Programa de Pós-Graduação em GEOLOGIA, como requisito para obtenção do grau de Doutor em GEOLOGIA, área de concentração GEOLOGIA ECONÔMICA E APLICADA.

Aprovada em 17 de junho de 2019, pela banca constituída pelos membros:

Prof. Carlos Alberto Rosière - Orientador
UFMG

Prof. Maria Emilia Schuteski Della Giustina
UnB

Prof. Hermínio Arias Nalini Júnior
UFOP

Prof. Tiago Amâncio Novo
UFMG

Prof. Rosaline Cristina Figueiredo e Silva
UFMG

Belo Horizonte, 17 de junho de 2019.

*Feliz aquele que transfere o que sabe e aprende o que ensina.
O saber se aprende com mestres e livros.
A Sabedoria, com o corriqueiro, com a vida e com os humildes.
O que importa na vida não é o ponto de partida, mas a caminhada.
Caminhando e semeando, sempre se terá o que colher.*

Cora Coralina

AGRADECIMENTOS

Durante a longa caminhada até a conclusão desta tese foram muitos os que direta ou indiretamente apoiaram e torceram pela concretização deste sonho. Expresso a todos a minha imensa gratidão.

A Deus por todas as oportunidades que tive e que me permitiram finalizar esta etapa.

Ao orientador Carlos Alberto Rosière pelo constante apoio, dedicação, e pelas discussões que proporcionaram grande desenvolvimento profissional e pessoal. Para mim é uma imensa honra e orgulho tê-lo como orientador desde o mestrado. Ao coorientador João Orestes pelo incentivo, apoio e principalmente pela enorme ajuda durante meu período na Austrália. Ao orientador do período de doutorado sanduíche, Steffen Hagemann pelo grande incentivo, discussões e sugestões.

A Coordenação de Aperfeiçoamento de Pessoal de Nível Superior - Brasil (CAPES) pelo apoio financeiro, em especial pelo bolsa do Programa de Doutorado Sanduíche no Exterior (Pr. nº 88881.134959/2016-01). A Fundação de Amparo à Pesquisa de Minas Gerais pelo apoio financeiro (FAPEMIG/VALE CRA - RDP-00067-10-2011 e CRA-APQ 01178-15).

A empresa BEMISA pela disponibilidade de informações, apoio durante as etapas de campo e acesso aos testemunhos de sondagem. Aos então funcionários da BEMISA Paulo Rogério da Costa, Bruno Teles de Souza, Wagnei Geraldo Eustáquio Vital e Ericson da Silva Nascimento pelo apoio durante os trabalhos de campo.

Ao geólogo e amigo Rui Monteiro pela indispensável ajuda na primeira etapa de campo. Aos amigos de pós-graduação Jorge Roncato, Sérgio Martins, Sylvio Gomes e Luciano Bruno Oliveira pelas discussões e apoio durante os momentos difíceis. Aos demais colegas da pós-graduação pelas discussões e apoio. Agradeço as colegas do período na Austrália Juliane Uchôa e Jéssica Bogossian pelos momentos de descontração e pela vivência.

Aos Professores Tiago Novo, Hermínio Nalini, Rosaline Fiqueiredo, Lydia Lobato, Geraldo Norberto Sgarbi e Alexandre Chaves pelas discussões e sugestões. Aos professores Peter C. Hackspacher (UNESP) e Cristiano Lana (UFOP) pela permissão do uso de laboratórios. Ao Centro de Pesquisa Professor Manoel Teixeira da Costa (CPMTC) e funcionários.

Aos pesquisadores da University of Western Australia Malcolm Roberts e Heejin Jeon, da Curtin University, Neal J. McNaughton e Noreen Evans e da University of Tasmania, Leonid Danyushevsky, Paul Olin, and Ivan Belousov pelo apoio durante minhas análises, pelas discussões e sugestões.

Aos meus familiares e amigos pela torcida, mesmo que por ventura o trabalho tenha nos afastado temporariamente. A minha mãe pelo carinho, incentivo, paciência e imensurável dedicação. Ao meu pai pela torcida, entusiasmo e orgulho. As minhas tias (Rozângela, Rosiléia e Remilda) pela paciência, acolhida, carinho. Ao meu irmão pelo incentivo. Ao Pedro pelo

companheirismo, incentivo para continuar na área acadêmica, atenção, paciência e grande ajuda durante as etapas de campo.

Enfim, a todos que de alguma forma participaram desta importante etapa da minha vida.

Resumo

Os depósitos de ferro de alto teor (>60% wt. Fe) de Horto-Baratinha (HBD) e Cuité (CTE) estão localizados na margem leste do Cráton do São Francisco, oeste da Faixa Araçuaí. Os corpos de minério estão hospedados em formação ferrífera (itabirito) associada com mica xistos e anfibólio xistos paraderivados, de fácies anfibolito e com idade máxima de deposição estateriana, cercados por granitoides estaterianos da Suíte Borrachudos e gnaisses neoarqueanos do Complexo Guanhães. Toda a sequência é cortada por corpos pegmatíticos com idade de cristalização entre 560 e 490 Ma. A sequência metassedimentar é cronocorrelata com os Grupos Serra da Serpentina e Serra de São José (unidade basal do Supergrupo Espinhaço). A formação ferrífera foi deformada durante a Orogênese Brasiliiana, e sua estrutura está transposta por uma xistosidade plano-axial, definida por hematita lamelar e quartzo. Os metassedimentos de HBD sofreram ao menos três estágios de deformação gerando um padrão de redobramento tipo domos e bacias em escala de depósito. A sequência de CTE sofreu deformação em um ambiente transpressivo gerando zonas de cisalhamento e falhas de empurraõ com vergência para SE. Três fácies de minério de alto teor, hospedadas em itabirito, foram identificadas: minério hematítico granular com idióblastos de magnetita, que é a fácie dominante; lentes secundárias de minério hematítico lamelar-granular e minério magnetítico. Os dados de ETR+Y em rocha total indicam que a formação ferrífera é do tipo plataformal (Lago Superior) com baixa contaminação detritica. As texturas e composições microquímicas dos óxidos de ferro identificados no itabirito, minério e no pegmatito indicam três fases de mineralização. (1) Recristalização metamórfica, lixiviação parcial de Si nas zonas de cisalhamento e formação da hematita lamelar durante os estágios sin- a tardi-deformacionais (580 - 560 Ma) da Orogênese Brasiliiana. (2) Fusão parcial do granito Borrachudos durante os estágios tardi- a pós-deformacionais / colapso gravitacional do orógeno (560 - ~530 Ma). Durante esta fase, fluidos de alta temperatura oriundos das intrusões pegmatíticas interagiram com as rochas hospedeiras, resultando na formação de kenomagnetita e lixiviação de sílica. (3) Durante a fase final do colapso gravitacional (~530 - 490 Ma) a sequência foi soerguida e ocorreu a mistura dos fluidos magmáticos com fluidos meteóricos, o que gerou a progressiva oxidação da kenomagnetita em martita e hematita granular. A composição química similar entre os óxidos de ferro do minério e do pegmatito indicam sua origem intimamente relacionada. Titânio e Mn foram elementos móveis durante a fase de metassomatismo de contato, gerando Mn-magnetita e Ti-hematita. Zircões dos metassedimentos, do granito e do gnaisse sofreram um processo de recristalização em condição sub-sólida devido à interação com os fluidos hidrotermais, o que afetou a composição química e isotópica desses cristais.

Palavras-chave: hidrotermalismo Brasiliano, minério de ferro, Bloco Guanhães, metalogênese, geoquímica.

Abstract

Horto-Baratinha (HBD) and Cuité (CTE) high-grade iron ore deposits (>60% wt. Fe) are located at the eastern margin of the São Francisco Craton, western part of the Araçuaí Orogenic Belt. The high-grade bodies are hosted in metamorphosed iron formation (itabirite) associated with paraderived mica schists and amphibole schist of amphibole facies and Statherian maximum deposition age, enclosed by Statherian granitoids of the Borrachudos Suite and Neoarchean gneiss of the Guanhães Complex. Pegmatic bodies with crystallization age of 560 to 490 Ma crosscut all units. The metasedimentary sequence is correlated with the Orosirian-Statherian Serra da Serpentina and Serra de São José Groups (basal unit of the Espinhaço Supergroup). The iron formation was deformed during the Brasiliano Orogeny, and the banded structure is transposed by an axial planar schistosity, defined by lamellar hematite and quartz, enveloping high-grade ore lenses. The country rocks in HBD have undergone at least three stages of deformation making up a dome and basin deposit-scale refolding shape. The CTE sequence undergone a transpressive deformation generating shear zones and SE-verging thrust faults. Three high-grade iron ore facies were identified, granular hematitic ore with magnetite idiomorphs, which is the predominant facies in both deposits, and secondary lamellar-granular hematitic ore and magnetitic ore lenses. The whole-rock REE+Y data of the itabirite are very similar to platformal (Lake Superior) iron formations with an overall low abundance of detrital components. The texture and the microchemical composition of the iron oxides identified in itabirite, iron ore, and pegmatite indicate three mineralization phases. (1) The metamorphic recrystallization and transposition of the sedimentary structures, Si-leaching along shear zones and crystallization of lamellar hematite during the syn-collisional and late-collisional stages (580 - 560 Ma) of the Brasiliano Orogeny. (2) Partial melting of the Borrachudos granite during the late-collisional and post-collisional/gravitational collapse of the orogeny (560 - ~530 Ma). During this phase, high-temperature fluids from pegmatite interacted with country rocks, resulting in the formation of kenomagnetite and Si-leaching. (3) During the final stage of gravitational collapse (~530 - 490 Ma), when the sequence was uplifted, the mixing between meteoric and magmatic fluids promoted the oxidation of kenomagnetite to martite and granular hematite. The general similar composition between the iron oxides from ore and pegmatite indicates their closely related origin. Titanium and Mn were mobile during the metasomatic high fluid/rock interactions, generating Mn-rich magnetite and Ti-rich hematite. Zircons from metasedimentary rocks, granite, and gneiss suffered recrystallization at sub-solidus conditions, due to the interaction with hydrothermal fluids affecting their chemical and isotopic composition.

Keywords: Brasiliano hydrothermalism, iron ore, Guanhães Block, metallogenesis, geochemistry.

LISTA DE SIGLAS E ABREVIATURAS

bdl	<i>below detection limit</i>
BIF	<i>Banded iron formation</i>
BSE	<i>Back-scattered electrons</i>
CMCA	<i>Centre for Microscopy, Characterisation and Analysis</i>
CODES	<i>Centre for Ore Deposit and Earth Sciences</i>
CTE	Cuité
EDS	<i>Energy Dispersive Spectrometry</i>
EMP	<i>Electron microprobe</i>
ETR	Elementos terras raras
Ga	Giga anos
GO	<i>Granular hematitic ore</i>
HBD	Horto-Baratinha
HREE	<i>Heavy Rare Earth Element</i>
ICP-ES	<i>Inductively Coupled Plasma Emission Spectrometric</i>
ICP-MS	<i>Inductively Coupled Plasma Mass Spectroscopy</i>
IF	<i>Iron formation</i>
LA-ICP-MS	<i>Laser Ablation- Inductively Coupled Plasma- Mass Spectrometry</i>
LGO	<i>Lamellar-granular hematitic ore</i>
LOPAG	Laboratório de Preparação de Amostras para Geoquímica e Geocronologia
LREE	<i>Light Rare Erath Element</i>
LST	<i>Lithium heteropolytungstate</i>
Ma	Milhões de anos
Mesoarc	<i>Mesoarchean</i>
MEV	Microscópio eletrônico de Varredura
MO	<i>Magnetic ore</i>
Neoarc	<i>Neoarchean</i>
Oro	<i>Orosirian</i>
PAAS	<i>Post-Archean Australian shale</i>
Paleoarc	<i>Paleoarchean</i>
QF	Quadrilátero Ferrífero
RBF	<i>Radial Basis Function</i>
REE	<i>Rare earth elements</i>
REE+Y	<i>Rare earth elements plus yttrium</i>

REM	<i>Revista Escola de Minas - International Engineering Jornal</i>
Rhy	<i>Rhyacian</i>
RSD	<i>Relative standard deviation</i>
SD	<i>Standard deviation</i>
SdEM	Serra do Espinhaço Meridional
SEM	<i>Scanning Electron Microscope</i>
SHRIMP	<i>Sensitive High Resolution Ion Microprobe</i>
Sid	<i>Siderian</i>
SIMS	<i>Secondary ion mass spectrometry</i>
SMOW	<i>Standard Mean Ocean Water</i>
SN	<i>Shale normalization</i>
Sta	<i>Statherian</i>
TTG	Tonalito-trondhjemito-granodiorito
UFOP	Universidade Federal de Ouro Preto
UNESP	Universidade Estadual Paulista
UWA	<i>University of Western Australia</i>
WDS	<i>Wavelength Dispersive Spectroscopy</i>

Abreviações de nomes de minerais

Act	Actinolita
Amp	Anfibólio
Arg	Argilominerais
Apy	Arsenopirita
Ap	Apatita
Bt	Biotita
Cbt	Carbonato
Cl	Clorita
Cld	Cloritoide
Crd	Cordierita
Cpy	Calcopirita
Czo	Clinozoisita
Ept	Epidoto
Fds	Feldspato
Grt	Granada

Gte	Goetita
Hem	Hematite
HemL	Hematita lamelar
HemG	Hematita granular
Hrn	Hornblenda
Ilm	Ilmenita
Kf	Feldspato potássico
Ky	Cianita
Kmag	(keno)magnetita
Mar	Martita
Mnz	Monazita
Mrc	Microclina
Ms	Muscovita
Pgl	Plagioclásio
Po	Pirrotita
Prl	Pirofilita
Py	Pirita
Qtz	Quartzo
Ser	Sericita
Sll	Sillimanita
Tlc	Talco
Ttn	Titanita
Trm	Tremolita
Tur	Turmalina
Zr	Zircão

SUMÁRIO

1. INTRODUÇÃO	1
1.1. Localização	2
1.2. Objetivos	3
1.2.1. Objetivo geral	3
1.2.2. Objetivos específicos	3
1.3. Metodologia	3
1.3.1. Modelamento geológico implícito	5
1.3.2. Geotermometria	8
1.3.3. Geocronologia por isótopos U-Pb	8
1.3.4. Análise química de rocha total	10
1.3.5. LA-ICP-MS nos óxidos de ferro	10
1.3.6. WDS em zircão	12
1.3.7. Isótopos de oxigênio em zircões	12
1.3.8. Isótopos Lu-Hf	14
1.4. Estruturação da tese	15
2. CONTEXTO GEOLÓGICO REGIONAL	17
2.1. Estratigrafia	17
2.1.1. Complexo Mantiqueira	17
2.1.2. Greenstone belt - Supergrupo Rio das Velhas	17
2.1.3. Complexo Guanhães	18
2.1.5. Supergrupo Espinhaço	20
2.1.6. Suíte Borrachudos	21
2.2. Arcabouço geotectônico	23
3. ARTIGO I - THE HORTO-BARATINHA ITABIRITE-HOSTED IRON ORE: A BASAL FRAGMENT OF THE ESPINHAÇO BASIN IN THE EASTERN SÃO FRANCISCO CRATON	26
3.1. Abstract	26
3.2. Introduction	27
3.3. Regional geology	28
3.3.1. Gneissic terranes (Guanhães Block and Mantiqueira Complex)	28
3.3.2. Iron formations in the Southern Espinhaço fold and thrust belt	29
3.3.3. The Rio das Velhas Greenstone belt	29

3.3.4. Magmatic units	29
3.4. Methodology	31
3.4.1. Fieldwork and petrographic studies	31
3.4.2. Geothermometry	31
3.4.3. Calculation of structural parameters	31
3.4.4. Geochronology	32
3.5. Lithostratigraphic characterization of Horto-Baratinha deposit	32
3.5.1. Metamorphic Complex	32
3.5.2. The Borrachudos Suite	33
3.5.3. Metasedimentary sequence	34
3.6. Pegmatite	36
3.7. High-grade iron ore bodies	36
3.8. Structural analysis	37
3.8.1. Structural elements	37
3.8.2. Structural domains	39
3.8.3. Microstructural aspects	40
3.9. Metamorphism	43
3.10. The paragenetic sequence of the iron oxides generations	45
3.11. Geochronology U-Pb SHRIMP	46
3.12. Discussions	49
3.13. Conclusions	55
3.14. Acknowledgments	55

4. ARTIGO II - DEPICTING THE 3D GEOMETRY OF ORE BODIES USING IMPLICIT LITHOLOGICAL MODELING: AN EXAMPLE FROM THE HORTO-BARATINHA IRON DEPOSIT, GUANHÃES BLOCK, MG 57

4.1. Abstract	57
4.2. Introduction	57
4.3. Geological setting	58
4.3.1. Stratigraphy	58
4.3.2. Structures	60
4.4. 3D lithological modeling	61
4.5. 3D implicit lithological modeling of the Horto-Baratinha iron ore deposit	62
4.6. Results and discussions	64
4.7. Conclusion	66

4.8. Acknowledgments 67

**5. ARTIGO III - CUITÉ IRON ORE DEPOSIT – A TECTONIC SLICE OF LOWER
ESPINHAÇO IN GUANHÃES TECTONIC BLOCK 68**

5.1. Abstract 68

5.2. Resumo 69

5.3. Introduction 69

5.4. Geochronological methodology 70

5.5. Geological Setting 71

5.6. Regional Tectonic Setting 72

5.7. The Cuité deposit 73

5.7.1. Lithostratigraphy 73

5.7.2. High-grade iron ore bodies 75

5.7.3. Structural Features 78

5.7.4. The paragenetic sequence of iron oxides generations 80

5.7.5. U-Pb geochronology 81

5.8. Results and discussions 82

5.8.1. Age and correlation with other iron formation-bearing sequences 82

5.8.2. Structural setting and evolution 83

5.8.3. Tectonic fabric and mechanisms of enrichment 84

5.9. Conclusion 86

5.10. Acknowledgments 86

**6. ARTIGO IV - CONSTRAINTS ON THE FORMATION OF ITABIRITE-HOSTED
IRON ORE DEPOSITS AT THE GUANHÃES BLOCK (BRAZIL) BY CONTACT
METASOMATISM WITH PEGMATITE INTRUSIONS 87**

6.1. Abstract 87

6.2. Introduction 88

6.3. Regional geology 88

6.4. Methodology 90

6.4.1. Geochronology U-Pb SHRIMP – sample selection and methods 90

6.4.2. Whole-rock geochemistry 91

6.4.3. In situ LA-ICP-MS analysis of iron oxides 92

6.5. The HBD and CTE geological setting 93

6.5.1. Age of the pegmatites 96

6.5.2. Iron formation 97

6.5.3. Hypogene iron ore	97
6.5.4. Paragenetic sequence of the iron oxides	99
6.6. Whole-rock geochemistry	100
6.6.1. Major oxide elements	100
6.6.2. Trace and rare earth elements	101
6.7. Iron oxide LA-ICP-MS chemistry	106
6.7.1. Mineral chemistry of iron oxides from iron formation	106
6.7.2. Mineral chemistry of iron oxides from hypogene iron ore	107
6.7.3. Mineral chemistry of iron oxides from pegmatite	110
6.7.4. The main chemical changes related to hydrothermal alteration	111
6.7.5. Kenomagnetite chemistry and discrimination diagrams	113
6.7.6. Comparisons with other iron ore deposits	114
6.8. Discussion	115
6.8.1. Origin of the Pegmatite	115
6.8.2. Chemical and textural changes during iron mineralization	116
6.8.3. Mineralization process in HBD and CTE	120
6.9. Conclusions	121

**7. ARTIGO V - EDIACARAN-CAMBRIAN FAR-FIELD HYDROTHERMAL EVENT
IN THE SOUTHEAST BRAZIL: EVIDENCE FROM ZIRCON U-PB SHRIMP, TRACE
ELEMENTS, LU-HF AND OXYGEN ISOTOPES 124**

7.1. Abstract	124
7.2. Introduction	125
7.3. Geological Setting	126
7.2.1. Hydrothermalism associated with Brasilian Orogeny	129
7.4. Methodology	130
7.5. Results	132
7.5.1. Textural characterization	132
7.5.2. Zircon U-Pb ages	135
7.5.3. Chemical composition	139
7.5.4. Lu-Hf signature	142
7.5.5. Oxygen isotope signatures	144
7.6. Discussion	146
7.6.1. Age of the hydrothermal event	146
7.6.2. Th/U ratio	147

7.6.3. Trace elements and isotopic changes associated with hydrothermalism	148
7.6.4. Tectonic setting, hydrothermalism and zircon changes implications	149
7.7. Conclusions	150
7.8. Acknowledgements	153
8. CONCLUSÕES	154
9. REFERÊNCIAS BIBLIOGRÁFICAS	157
ANEXOS (APPENDICES)	177

1. INTRODUÇÃO

A origem dos depósitos de ferro representa um intrigante problema científico de interesse econômico. A composição, textura e mineralogia dos minérios são a chave para entendimento de sua gênese e controle. A gênese de corpos de minério de ferro é amplamente discutida na literatura (e.g. Taylor et al., 2001; Rosière et al., 2008; Thorne et al., 2009; Evans et al., 2013; Figueiredo e Silva et al., 2013; Hensler et al., 2014; Hagemann et al., 2016) sendo a definição dos processos envolvidos importante na caracterização da jazida, de forma a auxiliar a prospecção de novos depósitos, bem como otimizar as reservas já conhecidas. A presente tese de doutorado apresenta o estudo de depósitos hematíticos-magnetíticos da parte sul do Bloco Guanhães, região com predomínio de unidades basais do Cráton do São Francisco (Complexo Guanhães, Complexo Mantiqueira, Supergrupo Rio das Velhas), localizada na borda E-SE da Serra do Espinhaço Meridional e NE do Quadrilátero Ferrífero (QF), a fim de desenvolver o modelo de sua gênese, estruturação, e estabelecer as relações genéticas e temporais entre minérios hematíticos-magnetíticos granular e minérios especularíticos.

O Complexo Guanhães ocorre com ampla distribuição geográfica na região centro-leste do Estado de Minas Gerais, com cerca de 250 km de extensão na direção N-S. Trata-se de uma sequência composta por gnaisses e migmatitos TTG (tonalito-trondjemito-granodiorito), corpos graníticos, rochas metavulcanossedimentares e sequências metassedimentares portadoras de formações ferríferas, de médio grau metamórfico, entre xisto verde alto a anfibolito (Noce et al., 2007b). A idade provável das unidades metassedimentares era considerada como sendo arqueana (Noce et al., 2007b), o que é questionado por dados recentes. Silveira Braga et al. (2015) obtiveram idade mínima em zircão detritico, pelo método U-Pb SHRIMP, de 1.668 ± 23 Ma nos metasedimentos do depósito de Morro Escuro, e Barrote et al. (2017) obtiveram idade mínima de 2.181 ± 23 Ma (U-Pb SHRIMP e LA-ICP-MS) em metassedimentos do depósito de Jambreiro, localizado próximo a cidade de Guanhães.

O Complexo Mantiqueira apresenta associação de corpos máficos e granitoides de composição tonalítica a granítica, datados entre 2.220 e 2.050 Ma (Noce et al., 2007b). O Supergrupo Rio das Velhas representa um pacote do tipo *greenstone belt*, com registros eruptivos félscicos datados de 2.792 ± 11 Ma a 2.751 ± 9 Ma (Noce et al., 2005) na região do QF. Na porção leste da Serra do Espinhaço Meridional, localizada a oeste do Bloco Guanhães, há sequências de rochas metassedimentares associadas aos Grupos Serra da Serpentina e Serra de São José, depositadas entre os períodos Orosiriano e Estateriano (Rolim et al., 2016).

As sequências metassedimentares do Bloco Guanhães hospedam depósitos de minério de ferro hematíticos-magnetíticos os quais apresentam uma íntima associação com intrusões de pegmatito e veios de quartzo. A presente tese de doutoramento propõe definir o empilhamento estratigráfico dos

depósitos e os eventos ígneos e hidrotermais associados à transformação da BIF (*Banded iron formation*) em minério de alto teor com base em estudos isotópicos e microquímicos.

1.1. Localização

O principal foco do estudo são os depósitos de ferro de Horto-Baratinha e Cuité, localizadas nos municípios de Santa Maria de Itabira e Antônio Dias respectivamente, região do vale do rio Doce, leste do estado de Minas Gerais (Figura 1.1). O depósito de Horto-Baratinha foi uma antiga mina de minério de ferro que operou até a década de 80, e é atualmente explorada pela BEMISA (Brasil Exploração Mineral SA). A extração de minério em Cuité está desativada desde 2014.

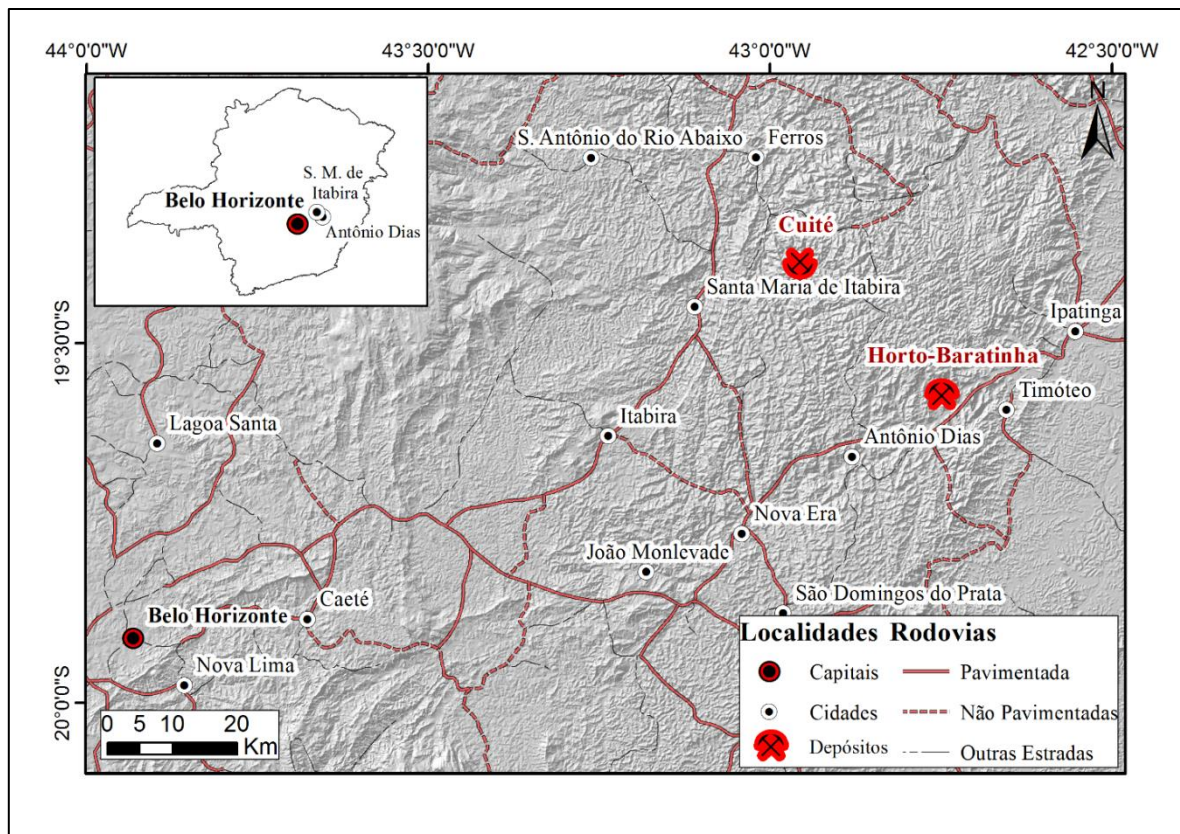


Figura 1.1: Localização dos depósitos de Horto-Baratinha e Cuité.

O acesso ao depósito de Cuité é feito a partir de Belo Horizonte pela BR-381, por cerca de 70 km até o trevo de Itabira. A partir deste trevo segue-se pela MG-134, MG-129 e BR-120 aproximadamente 60 km até próximo à sede do município de Santa Maria de Itabira. A partir da BR-120 segue-se por via não pavimentada, sentido sudeste, por 17 km até o distrito de Hematita. De Hematita prossegue-se por mais 20 km em via não pavimentada, sentido nordeste até o depósito de Cuité.

O acesso ao depósito de Horto-Baratinha, a partir de Belo Horizonte, é feito pela BR-381, por 208 km até o trevo de acesso para o município de Timóteo. Após o trevo, passar pela ponte sobre o

Rio Piracicaba, na BR-381, e acessar a primeira entrada para via não pavimentada a esquerda. Prosseguir pela via não pavimentada por 8 km, sentido sudeste, até o depósito de Horto-Baratinha.

1.2. Objetivos

1.2.1. Objetivo geral

Esclarecer a gênese do minério de ferro, particularmente os corpos hematíticos-magnetíticos presentes na porção sul do Bloco Guanhães, região com predomínio de unidades basais do cráton do São Francisco, e gerar um modelo metalogenético consolidado que sirva de suporte para prospecção e definição de reservas.

1.2.2. Objetivos específicos

A fim de alcançar o objetivo geral, são listados abaixo os objetivos específicos fundamentais:

- 1) Determinar as características estruturais, petrográficas e mineralógicas do minério de ferro magnetítico, hematítico, protominério e das encaixantes.
- 2) Determinar a idade da sequência metassedimentar portadora de BIF e das rochas ígneas associadas à mineralização, correlacionando tais idades com os depósitos presentes no contexto geológico regional, bem como com importantes depósitos de ferro de características semelhantes presentes no Brasil e no mundo.
- 3) Analisar as transformações mineralógicas e químicas sofridas pelos diferentes tipos de minério e determinar as características da alteração hidrotermal durante a transformação da BIF em minério de alto teor.
- 4) Caracterizar o processo hidrotermal vinculado à orogênese Brasiliiana, em especial seu registro em zircões ígneos e detriticos.

1.3. Metodologia

A metodologia aplicada para atingir cada objetivo específico do trabalho é descrita de forma sucinta a seguir. Os itens mais relevantes da metodologia são descritos em detalhe nos subitens presentes neste tópico bem como nos capítulos 3 a 7.

1) Determinar as características estruturais, petrográficas e mineralógicas do minério de ferro magnetítico, hematítico, protominério e das encaixantes.

1.1) Levantamento de dados de campo e coleta de amostras nos depósitos de Cuité e Horto Baratinha, bem como na região ao redor dos depósitos. Foram descritos 223 pontos em campo e coletadas 99 amostras.

1.2) Interpretação da descrição de 72 testemunhos de sondagem de Horto-Baratinha (5.672 metros de sondagem) cedidos pela BEMISA, checagem dos testemunhos e coleta de 38 amostras de rocha e 20 amostras de alíquota de brita dos testemunhos de sondagem.

1.3) Estudo petrográfico com o uso de microscópio ótico de luz transmitida e refletida de 60 lâminas (delgada e delgada/polida) dos principais litotipos da sequência, para determinação de suas características mineralógicas e texturais.

1.4) Análise estrutural do depósito Horto-Baratinha, através da subdivisão da área em blocos e cálculo dos seguintes parâmetros estruturais: autovalores (s_1, s_2, s_3), autovetores (v_1, v_2, v_3), parâmetro de forma K ($K = (\ln(s_1/s_2))/(\ln(s_2/s_3))$), que mostra o gradiente de irradiação das linhas a partir da origem, e parâmetro de força C ($C = \ln(s_1/s_3)$), que mostra a intensidade da orientação preferencial. Todos os cálculos e plotagens foram realizados no *software* OpenStereo 0.1.2 ©2009-2011 (Grohmann e Campanha, 2010).

1.5) Confecção de modelo geológico 3D do depósito de Horto-Baratinha pelo método de modelagem implícita através do *software* Leapfrog® (explicação detalhada sobre o método no **item 1.3.1**).

1.6) Estudo do metamorfismo através de análise qualitativa e semi-quantitativa. A análise qualitativa foi baseada na individualização das paragêneses minerais de cada unidade desenvolvidas sincinemáticas à foliação regional. A análise semi-quantitativa foi realizada através de cálculos geotermométricos baseados em análise microquímica de granada e biotita obtidas por WDS (*Wavelength Dispersive Spectroscopy*) no *Centre for Microscopy, Characterisation and Analysis* (CMCA) da *University of Western Australia* (UWA), em Perth, Austrália (explicação detalhada sobre o método no **item 1.3.2**).

2) Determinar a idade da sequência metassedimentar portadora de BIF e das rochas ígneas associadas à mineralização.

2.1) Análise de zircões detriticos provenientes dos metassedimentos para determinação da idade máxima de deposição. Cinco amostras de xistos paraderivados foram datadas, duas do depósito de Cuité e três do depósito de Horto-Baratinha. Foram também analisados zircões de duas amostras de pegmatitos que cortam toda a sequência, para correlação com a idade da mineralização, duas amostras de granito presentes nas redondezas dos depósitos, os quais são provável fonte dos corpos pegmatíticos, e portanto relacionados ao processo de mineralização, e ainda uma amostra de gnaisse do embasamento. O método de análise utilizado foi SHRIMP (*Sensitive High Resolution Ion Microprobe*), feito na *Curtin University*, em Perth, Austrália (explicação detalhada sobre o método no **item 1.3.3**).

3) Analisar as transformações mineralógicas e químicas sofridas pelos diferentes tipos de minério e determinar as características da alteração durante a transformação da BIF em minério de alto teor.

3.1) Caracterização geoquímica de rocha total de 2 amostras de itabirito e 15 amostras de minério de ferro. As análises foram realizadas pelo laboratório *Bureau Veritas Commodities*, Canadá, pelo método ICP (explicação detalhada sobre os métodos no **item 1.3.4**).

3.2) Caracterização microquímica das diferentes gerações de óxidos de ferro (hematita lamelar, hematita granular, martita e magnetita) presentes nos diversos litotipos. Foram analisados um total de 192 spots em 5 amostras de minério de ferro, 2 amostras de itabirito e 2 amostras de pegmatito. O método de análise foi LA-ICP-MS, e foi realizada na *University of Tasmania*, em Hobart, Austrália (explicação detalhada sobre o método no **item 1.3.5**).

4) Caracterizar o processo hidrotermal vinculado a orogênese Brasiliiana, em especial seu registro em zircão.

4.1) Microanálises de elementos maiores, menores e traços em zircões por WDS, realizado no laboratório do CMCA da UWA, Austrália (explicação detalhada sobre o método no **item 1.3.6**). Foram analisados zircões hidrotermais e não hidrotermais das seguintes regiões: Horto-Baratinha, Cuité, Morro Escuro e Morro do Pilar.

4.2) Análise de isótopos de oxigênio em zircões, utilizando o equipamento CAMECA IMS 1280 ion microprobe, do CMCA, UWA (explicação detalhada sobre o método no **item 1.3.7**).

4.3) Análise Lu-Hf em zircões utilizando equipamento LA-ICP-MS Agilent 7700 (CompexPro 102, Coherent) da *Curtin University*, Perth, Austrália (explicação detalhada sobre o método no **item 1.3.8**).

1.3.1. Modelamento geológico implícito

A construção do modelo litológico *wireframe* a partir de dados de sondagem é uma tarefa demorada e complexa realizada rotineiramente pelos geólogos de mina (Cowan et al., 2003). O método tradicional de definição explícita 3D dos contatos geológicos depende muito de um processo demorado de digitalização manual. Baseado em métodos de interpolação de dados, a modelagem implícita primeiro define uma função contínua tridimensional que descreve a distribuição da rocha. Esta função volumétrica é cortada por uma superfície geológica, e permite a extração do objeto 3D de forma automatizada e eliminando a necessidade de digitalização manual da superfície (Cowan et al., 2003).

O modelamento tradicional de sólidos utiliza uma miscelânea de triângulos para definir a superfície. Tal método é denominado como modelo “explícito” de um sólido pois a superfície é definida manualmente pelos seus elementos e arranjos. O método explícito requer a digitalização das linhas de contorno de um corpo complexo tridimensional através da visualização de dados de

sondagem em sucessivas seções. As linhas desenhadas em 2D são em seguida agrupadas utilizando linhas de amarração para definir a conectividade tridimensional entre as polilinhas. As polilinhas de amarração são então trianguladas para produzir modelo de triangulação 3D do sólido. Durante este processo de modelamento, o geólogo deve primeiramente garantir que a posição dos limites litológicos verificadas nos furos de sondagem foram respeitadas, e em segundo lugar, incorporar qualquer tendência de direção local que o depósito possa ter durante o processo de digitalização (Cowan et al., 2003). O desenho manual das polilinhas 2D é a parte mais demorada do trabalho e requer um modelador experiente para construir geometrias complexas com as ferramentas de digitalização. O modelo produzido dessa maneira é único para cada interpretação individual do geólogo, e não é exatamente replicado por outros. Isto ocorre pois as tendências direcionais e a suavização que o geólogo introduz durante o processo de modelamento é único e individual, portanto, interpretações são escritas no modelo sólido durante sua construção manual (Cowan et al., 2003). Tal método não permite a atualização rápida do modelo ou uma construção semi-automática com novos dados disponíveis (Cowan et al., 2003; Knight et al., 2007; Boyle e Latscha, 2013). Devido a isso, o modelamento geológico é conduzido em campanhas.

Um modelo “implícito” de um sólido, segundo Cowan et al. (2003), é dado pela função definida ao longo do espaço. Esta função do volume é modelada a partir dados de sondagem espacialmente interpolados e a superfície do sólido é extraída como uma triangulação desta função. Conforme descrito pelos autores supracitados, a superfície a ser modelada não é construída diretamente, como feito no método explícito, mas ao contrário são finitas aproximações das superfícies com detalhes infinitos. Estas superfícies estão implícitas de existir em uma função de volume contínua, portanto são referidas como “superfícies implícitas”.

A Figura 1.2 ilustra a diferença de metodologia utilizada nos métodos implícito e explícito. A tradicional modelagem explícita consiste em ligar manualmente os pontos de contato produzindo um contato de forma angulosa (Figura 1.2B). É de inteiro escolha do modelador incluir pontos extras entre os pontos de contato observados para suavizar a superfície. Também deve ser notado que a posição de pontos adicionais de contato é arbitrária. Para construir um modelo implícito de contato, a função volume com uma isosuperfície que inclui os pontos de contato e pontos conectando-os deve ser criada. A função é criada no espaço ao especificar um valor de pontos selecionados e interpolar o restante ao longo do espaço. Para garantir que todos os pontos de contato estão incluídos na isosuperfície, os mesmos valores são atribuídos para estes pontos. Convencionalmente o valor zero é atribuído. Isto não é suficiente para construir a isosuperfície requerida, porque uma interpolação desses pontos permitirá o aparecimento do valor zero em qualquer lugar. Para produzir um *locus* para os pontos com valor zero, que estejam confinados ao contorno que inclui os pontos de contato, regiões deverão ser especificadas onde a função torna-se positiva e negativa. Conforme ilustrado na Figura

1.2, uma das litologias foi escolhida para ter valor positivo e a outra valor negativo. A superfície de contato foi então traçada como uma interpolação de dados dispersos. Uma vez que os dados foram interpolados no espaço, a isosuperfície zero pode ser extraída a partir de uma função como a superfície de contato entre os dois litotipos em qualquer resolução (Cowan et al., 2003).

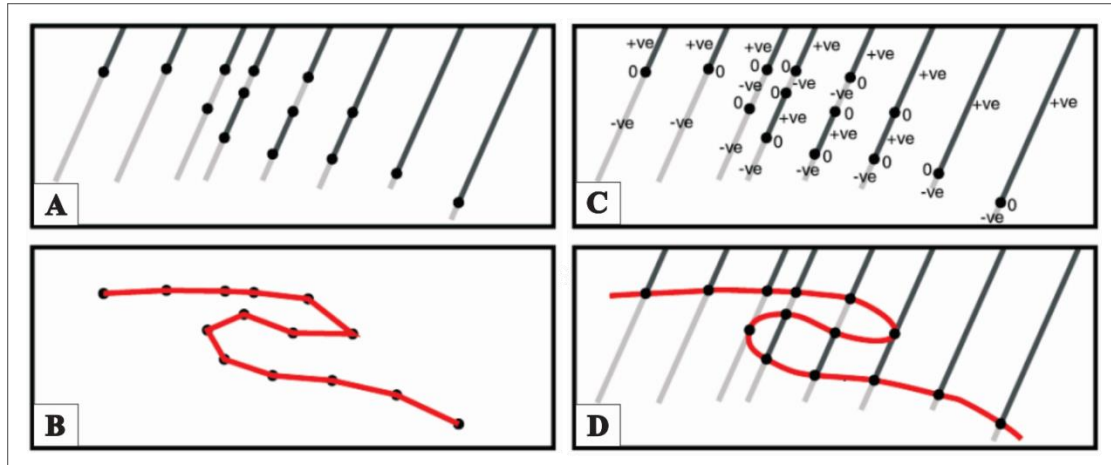


Figura 1.2: Comparação entre modelagem explícita e implícita. (A) Trama hipotética de furos de sondagem em 2D a partir de banco de dados de sondagem tridimensional. As cores preta e cinza representam duas litologias e a superfície de contato é interpretada como sendo uma dobra reclinada. (B) Uma polilinha angular desenhada manualmente representa a junção manual dos pontos de contatos (pontos pretos). (C) Os dados da sondagem podem ser codificados de acordo com sua posição relativa da superfície de contato. Para os pontos localizados na superfície de contato é atribuído valor zero, e os pontos fora da superfície são atribuídos valores positivos e negativos. (D) A interpolação espacial dos valores dos dados, e subsequente avaliação do isocontorno dos valores iguais a zero (isosuperfície em 3D), produz a superfície de contato entre os dois litotipos. A função 3D é contínua e, portanto, a superfície de contato pode ser analisada em qualquer resolução desejada. Fonte: (Cowan et al., 2003).

Ao comparar o método tradicional de modelagem por contorno empregado pelos pacotes de *softwares* padrões da indústria mineral com a modelagem implícita em um depósito de ouro, Knight et al. (2007) concluíram que o método implícito fornece uma alternativa viável ao método tradicional. Os autores compararam modelagem implícita realizada pelo *software* Leapfrog®, com a modelagem tradicional utilizando o *software* MineSight®. Os resultados do estudo indicaram que a técnica de modelagem implícita é acurada, flexível e eficiente.

A modelagem implícita utiliza Função de Base Radial (RBF) para interpolar teor e litologia em 3D. A interpolação RBF representa a função como uma soma das chamadas funções básicas, com pesos lineares da mesma maneira que a Krigagem, que é um método de regressão usado em geoestatística para interpolar dados. A diferença entre a Krigagem e a interpolação RBF é que na primeira usa-se a função covariância obtida a partir dos dados (variograma), já a segunda utiliza uma função básica que é escolhida a partir de um conjunto padrão (Cowan et al., 2003). A interpolação RBF, por ser um método de interpolação global, requer que todos os pontos de dados sejam usados para calcular os coeficientes (ou seja, os pesos atribuídos a cada valor). Por isso, uma das limitações

do RBF é o fato de que grandes conjuntos de dados resultam em problemas de armazenamento de dados (Cowan et al., 2003). Ao comprar RBF e Krigagem, Fazio (2013) demonstra que os dois métodos possuem uma estrutura semelhante e, como consequência, características da Krigagem tais como variância da interpolação, também podem ser implementadas em Redes RBF, desde que sejam respeitadas as restrições exigidas por cada método. O autor explica que apesar da equivalência matemática, as Redes RBF são bem mais rápidas que a Krigagem pois interpola de uma forma em que os pesos não precisam ser recalculados para cada ponto interpolado. Stewart et al. (2014) mostram, ao comparar RBF e Krigagem, que na situação de controle de teor onde o espaçamento dos dados é menor que o limite do variograma, os resultados de estimativa utilizando RBF são virtualmente indistinguíveis dos obtidos por Krigagem Ordinária.

1.3.2. Geotermometria

Os cálculos geotermométricos foram realizados com base nas associações granada–biotita, sin-cinemáticas à foliação principal. Tais cálculos foram realizados utilizando as microanálises dos silicatos citados, através do *software* TWQ 2.02 (Berman, 1991). Esses cálculos possibilitam a determinação da temperatura com erro de ± 50 °C. A rotina utilizada foi a de Holland e Powell (1990).

As microanálises foram realizadas no CMCA-UWA, em aparelho de microssonda eletrônica modelo JEOL8530F EPMA, utilizando 15 kV de voltagem de aceleração, 20 nA de corrente, *spot* de 5 μm . Foram obtidas de três a dez análises pontuais em cada cristal utilizando a mesma rotina para cada mineral. As análises foram realizadas segundo a seguinte sequência: (i) aquisição de imagens de elétrons secundários e retroespelhados (BSE) com resolução de alguns nanômetros, visando à observação de possíveis zonamentos químicos e, (ii) obtenção de microanálises. O método de análise foi o WDS, e foram analisados os seguintes elementos: SiO₂, Al₂O₃, FeO, MgO, MnO, CaO, Na₂O, K₂O e TiO₂, Cr₂O₃. As fórmulas estruturais foram calculadas com base em 24 oxigênios para biotita e 12 para granada.

1.3.3. Geocronologia por isótopos U-Pb

O método U-Pb é comumente utilizado para determinar a idade de cristalização, metamorfismo ou idade máxima de deposição. O método envolve dois processos de decaimento separados, com meia vida distintas: $^{238}\text{U} \rightarrow ^{206}\text{Pb}$ com meia vida de 4,47 Ga e $^{235}\text{U} \rightarrow ^{207}\text{Pb}$ com 704 Ma. O sistema U-Pb raramente permanece fechado em rochas silicáticas, devido a mobilidade do chumbo e especialmente a do urânio, sob condições de baixo metamorfismo e intemperismo. No entanto, devido ao duplo processo de decaimento, é possível a obtenção da idade mesmo de sistemas perturbados (Dickin, 2005). O zircão é um dos minerais mais utilizados para esse tipo de análise, visto que é um mineral que incorpora urânio em sua formação e não incorpora chumbo, além de ter alta temperatura de fechamento (Dickin, 2005).

1.3.3.1. Preparação das amostras

As amostras coletadas foram processadas pelos métodos convencionais, com britagem, moagem e peneiramento no laboratório LOPAG (Laboratório de Preparação de Amostras para Geoquímica e Geocronologia) da UFOP (Universidade Federal de Ouro Preto) e no Instituto de Geociências da Universidade Estadual Paulista (UNESP), em Rio Claro. A concentração de pesados da fração de 60 a 250 mesh foi feita por bateia. A fração 60-250 mesh foi tratada com líquido denso (LST ou Bromofórmio), para remoção refinada dos minerais mais leves, e com separador magnético Frantz LB1, para eliminação de minerais magnéticos tais como zircões intensamente metamitizados. Os zircões foram catados manualmente e montados em pastilha de *epoxy*, a qual foi polida e metalizada com carbono para confecção de imagens de elétrons retro-espalhados (BSE) no MEV modelo TESCAN VEGA3 no CMCA-UWA. As imagens BSE serviram de base para escolha dos *spots* a serem analisados por SHRIMP, e foram críticas para apreciação apurada de características internas dos cristais de modo a evitar análise em áreas com grande quantidade de Pb comum (inclusões, fraturas, áreas metamíticas), as quais são facilmente identificadas e delimitadas nas imagens BSE.

A metamitização natural de zircões resulta da acumulação de defeitos radiogênicos na estrutura cristalina causada por decaimento radioativo de pequenas quantidades de U e Th substituindo Zr (Woodhead et al., 1991). A metamitização é caracteristicamente marcada por mudanças físicas do cristal, incluindo significativo decréscimo da densidade, índice de refração e birrefringência (Holland e Gottfried, 1955). Pidgeon et al. (1966) comprovaram a partir de experimentos que simulavam a ação de fluidos hidrotermais em zircões, que a perda de Pb episódica é um processo importante e é considerado como uma possível explicação para muitas relações isotópicas discordantes de U-Pb em zircões naturais.

1.3.3.2. Geocronologia por SHRIMP

A montagem em *epoxy* foi coberta por película de ouro para as análises no SHRIMP. A maioria dos *spots* analisados no SHRIMP foi feita entre 20-30 µm, no entanto as análises de regiões de zircões hidrotermalizados foi feita com *spot* de 10 µm. Cinco escaneamentos foram utilizados para cada *spot* de zircão detritico, e seis escaneamentos nas análises de zircões ígneos e hidrotermais.

Os seguintes dados foram analisados em zircão: $^{196}\text{Zr}2\text{O}$, ^{204}Pb , *background*, ^{206}Pb , ^{207}Pb , ^{208}Pb , ^{238}U , ^{248}ThO , ^{254}UO . Os padrões D23 e NBS611 foram usados para identificar a posição do pico de massa do ^{204}Pb , enquanto a calibração do conteúdo de Pb/U foi realizada usando os padrões de zircão M257 de 561,3 Ma (Nasdala et al., 2008) e BR266 de 559 Ma e 903 ppm de U (Stern, 2001). As idades $^{207}\text{Pb}/^{206}\text{Pb}$ foram utilizadas para todos os grãos detriticos e as idades $^{206}\text{Pb}/^{238}\text{U}$ foram

utilizadas para zircão com idade Ediacarana ou inferior. Todos os dados em zircão detritico com correção comum de Pb maior que 1% foram rejeitadas durante o primeiro escaneamento.

As incertezas de idades individuais foram cotadas a 1σ , enquanto que a idade dos *plots* foram calculadas no nível 2σ (aproximadamente 95% confiança). Dados do SHRIMP foram reduzidos utilizando programa SQUID (Ludwig, 2001) e *plots* foram preparados usando ISOPLOT/Ex (Ludwig, 2003).

1.3.4. Análise química de rocha total

As análises químicas de rocha total foram realizadas pelo Laboratório Bureau Veritas (Canadá). Os métodos utilizados para as análises quantitativas foram: (i) ICP-ES (*Inductively Coupled Plasma Emission Spectrometric*), com fusão da amostra por metaborato de lítio e digestão com HNO_3 , para os óxidos maiores e elementos menores; (ii) ICP-MS (*Inductively Coupled Plasma Mass Spectroscopy*), com fusão da amostra por metaborato/tetraborato de lítio e digestão com água régia (apenas metais-base), para elementos traços e terras raras; (iii) carbono e enxofre foram analisados pelo método LECO devido ao baixo limite de detecção. Os dados de elementos terras raras foram normalizados ao PAAS - *Post Archean Australian Shale* (McLennan e Taylor, 1991).

1.3.5. LA-ICP-MS nos óxidos de ferro

1.3.5.1. Preparação das amostras e métodos analíticos

Um total de 9 amostras (5 amostras de minério de ferro, 2 amostras de itabirito, 2 amostras de pegmatito) contendo diferentes gerações de óxidos de ferro dos depósitos de Horto-Baratinha e Cuité foram selecionadas para microanálises com o intuito de gerar dados que auxiliassem na interpretação das mudanças químicas ocorridas no processo de enriquecimento do itabirito. As análises de elementos traços e terras raras (ETR) foram realizadas por LA-ICP-MS, pois este método fornece menores limites de detecção que o WDS.

A amostras selecionadas foram serradas e preparadas em *epoxy* formando pastilhas arredondadas de 1 polegada de diâmetro e 12 mm de espessura. Em seguida a pastilha foi polida. Foram confeccionadas imagens de BSE de todas as pastilhas no MEV modelo TESCAN VEGA3 no CMCA-UWA, para análise textural detalhada dos minerais, verificação de possíveis zoneamentos químicos e seleção acurada dos *spots* a serem analisados. A análise LA-ICP-MS foi realizada utilizando equipamento Agilent 7500cs ICP-MS acoplado com Resonetics ResolutionArF 193 nmExcimer laser, no *Centre for Ore Deposit and Earth Sciences* (CODES) da *University of Tasmania*, Hobart, Austrália. As amostras foram ablacionadas em célula geométrica constante M50 (Laurin Technic, Austrália) em atmosfera de He (fluxo 0,6 L/min) e o aerossol misturado com gás Ar (fluxo 0,6 L/min), para transporte para o LA-ICP-MS. O tamanho do *spot* do laser foi 30 μm para as

análises dos óxidos de ferro e do padrão BCR-2G, e 60 µm para análise do padrão GSD-1G (Jochum et al., 2005). A frequência utilizada foi 10 Hz e a energia de 3.5 J/cm². Os seguintes isótopos foram medidos: ⁷Li, ²³Na, ²⁴Mg, ²⁷Al, ²⁹Si, ³¹P, ³⁴S, ⁴³Ca, ⁴⁵Sc, ⁴⁷Ti, ⁴⁹Ti, ⁵¹V, ⁵³Cr, ⁵⁵Mn, ⁵⁷Fe, ⁵⁹Co, ⁶⁰Ni, ⁶³Cu, ⁶⁵Cu, ⁶⁶Zn, ⁶⁹Ga, ⁷¹Ga, ⁷⁵As, ⁸⁸Sr, ⁸⁹Y, ⁹⁰Zr, ⁹³Nb, ⁹⁵Mo, ⁹⁸Mo, ¹⁰⁷Ag, ¹¹⁸Sn, ¹²¹Sb, ¹³³Cs, ¹³⁷Ba, ¹³⁹La, ¹⁴⁰Ce, ¹⁴⁶Nd, ¹⁴⁷Sm, ¹⁵³Eu, ¹⁵⁷Gd, ¹⁶³Dy, ¹⁶⁶Er, ¹⁷²Yb, ¹⁷⁵Lu, ¹⁷⁸Hf, ¹⁸¹Ta, ¹⁸²W, ¹⁹⁷Au, ²⁰⁶Pb, ²⁰⁷Pb, ²⁰⁸Pb, ²⁰⁹Bi, ²³²Th, ²³⁸U. Os dados referentes aos *counts* gerados por segundo (cps) foram reduzidos utilizando-se o programa SILLS (Guillong et al., 2008).

1.3.5.2. Redução dos dados

Dois diferentes isótopos de mesmo elemento (⁶³Cu, ⁶⁵Cu; ⁶⁹Ga, ⁷¹Ga; ⁹⁵Mo, ⁹⁸Mo) foram medidos com objetivo de monitorar potenciais interferências, tais como ⁷Li/⁵⁶Fe em ⁶³Cu do padrão, ou ²⁴Mg/⁴⁰Ar e ⁴⁹Ti/¹⁶O em ⁶⁵Cu de óxidos de ferro que tenham alta concentração de Mg e/ou Ti. De maneira similar ⁹⁵Mo e ⁹⁸Mo foram analisados para monitorar interferência do ⁹⁵Mo com ⁵⁵Mn/⁴⁰Ar, bem como ⁶⁹Ga e ⁷¹Ga foram medidos para monitorar interferências com ⁵³Cr/¹⁶O e ⁵⁵Mn/¹⁶O respectivamente.

As análises LA-ICP-MS perfuram o mineral em profundidade menor que 10µm. Fases de ganga inclusas nos óxidos ou presentes abaixo da superfície deles e que não foram detectadas pelas imagens de BSE e por luz refletida, podem também serem perfuradas. Isto pode resultar em uma contaminação no sinal puro do óxido de ferro. Caracteristicamente as fases de ganga apresentam uma significativa redução do espectro de Fe e simultâneo aumento de outros picos do espectro, tais como Si, Ca, Al, Mg, ETR, conforme ilustrado na Figura 1.3. Durante a redução manual dos dados, estes sinais misturados foram excluídos e, portanto, não foram utilizados para cálculo da abundância dos elementos.

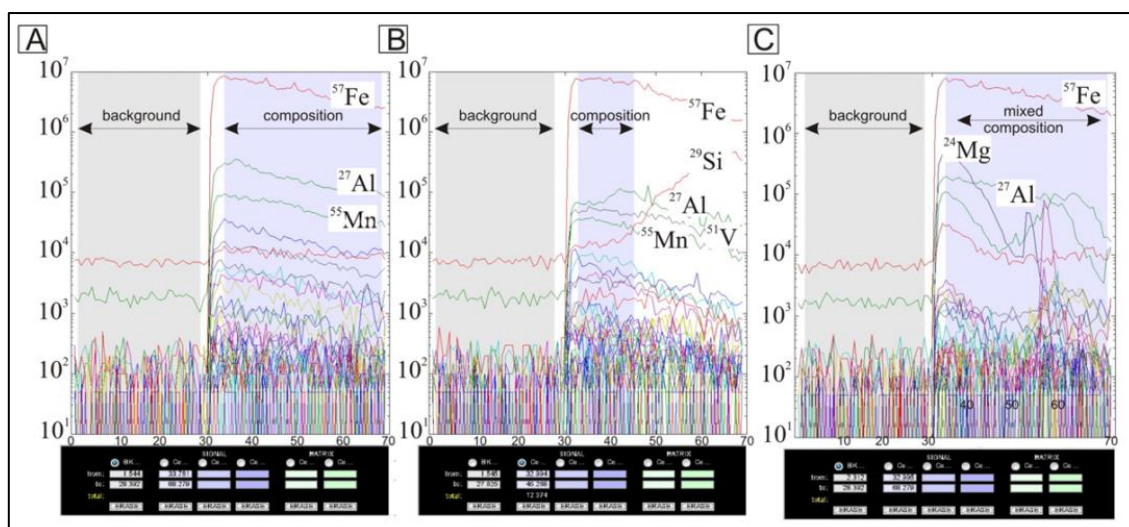


Figura 1.3: Comparação entre diferentes espectros de LA-ICP-MS, onde o eixo X representa o tempo de ablação em segundos e o eixo Y o número de *counts*. O primeiro espectro representa a medida do *background*, o segundo representa a concentração analisada nos óxidos de ferro. O campo indicado com *composition* representa a região do espectro

escolhida para cálculo da abundância dos elementos. (A) Espectro normal, com alto pico de ^{57}Fe . (B) Espectro que apresenta contaminação após 45s de análise, onde observa-se aumento do pico de ^{29}Si , provavelmente devido a ablação de quartzo. (C) Entre 30 e 40s alta concentração de ^{27}Al , ^{24}Mg e ^{29}Si no espectro o que indica uma ablação de silicato neste intervalo. Intervalos do espectro que indicam contaminação foram excluídos no processo de redução de dados. Fonte: (Hensler et al., 2015).

1.3.6. WDS em zircão

O processo de preparação dos cristais de zircão para análise WDS é o mesmo adotado para amostras analisadas por SHRIMP, conforme descrito no **item 1.3.3.1** deste capítulo. Os *spots* para análise foram escolhidos com base em imagens de BSE. As pastilhas em epoxy foram metalizadas com carbono para realização das análises. Deu-se preferência por analisar os mesmos *spots* datados pelo método SHRIMP. A análise WDS foi realizada na microssonda eletrônica modelo JEOL8530F EPMA, utilizando 25 kV de voltagem de aceleração e 80 nA de corrente. O tamanho do *spot* foi de 5 μm .

Os elementos analisados foram: Si, Mg, Na, Zr, Ca, Th, U, Pb, Y, Ti, Fe, Ce, Gd, Nd, Yb, Hf, Lu, Er, Dy, P, Ta, Nb. Foram analisados 178 *spots*.

1.3.7. Isótopos de oxigênio em zircões

Existem três isótopos estáveis de oxigênio ^{16}O (99,763%), ^{17}O (0,0375%) e ^{18}O (0,1995%) (Rollinson, 1993). O fracionamento isotópico é exibido em partes por mil, pela razão entre $^{18}\text{O}/^{16}\text{O}$, representada pelo símbolo $\delta^{18}\text{O}$, e dada pela seguinte fórmula:

$$\delta^{18}\text{O} = [((^{18}\text{O}/^{16}\text{O})_{\text{amostra}} - (^{18}\text{O}/^{16}\text{O})_{\text{SMOW}}) / (^{18}\text{O}/^{16}\text{O})_{\text{SMOW}}] \times 1000.$$

O padrão adotado comumente é o *Standard Mean Ocean Water* (SMOW). Os valores de $\delta^{18}\text{O}$ calculados a partir da fórmula acima mostram se a amostra analisada está enriquecida (valores positivos) ou empobrecida (valores negativos) em oxigênio pesado, em relação ao padrão (Rollinson, 1993). Medidas de isótopos de oxigênio em rochas e minerais ajudam no entendimento da história magmática, termal e de fluidos da crosta (Mojzsis et al., 2001). Esta análise foi utilizada com o intuito de identificar possíveis alterações nos valores de $\delta^{18}\text{O}$ dos zircões induzidas por fluidos hidrotermais, uma vez que zircões alterados por fluidos são em geral isotopicamente mais pesados que domínios não alterados (Davies et al., 2015).

As taxas de troca de oxigênio em zircões são muito lentas, o que permite preservação da composição isotópica de oxigênio do protólito mesmo em altas taxas de metamorfismo e até em anatexia (Mojzsis et al., 2001; Valley, 2003). Segundo Valley (2003) zircões magmáticos podem preservar os valores ígneos de $\delta^{18}\text{O}$ mesmo com subsequente metamorfismo de alto grau, alteração hidrotermal, assimilação magmática e anatexia. No entanto, o autor considera que a presença de microfraturas bem como altas taxas de fluidos podem acelerar as trocas, e mudar significativamente

a composição isotópica dos zircões. As imperfeições nos cristais de zircão causadas pela radiação também aumentam a difusão e troca de oxigênio pela criação de vias rápidas de troca com o meio externo ao cristal (Valley, 2003). Em casos extremos de defeitos devido à radiação, metamitização e microfraturamento, feições comuns observadas nos zircões da área de estudo, há uma maior facilidade para a troca de oxigênio através desses novos caminhos de difusão presentes no cristal, e precipitação de novas fases nas fraturas (Valley, 2003).

Valley (2003) enumerou os mecanismos capazes de alterar a composição isotópica de oxigênio original dos zircões: difusão de volume (borda para o centro), recristalização, sobrecrescimento, precipitação de materiais ao longo das microfraturas, presença de vias rápidas de troca (inclusões, defeitos do cristal, traços de fissão). Claesson *et al.* (2016) citam os seguintes estágios envolvidos no processo de metamitização de zircões a partir de decaimento α : fase I a qual é dominada pela acumulação de defeitos pontuais; fase II na qual os defeitos da fase anterior aparecem interconectados, e com presença de região amorfas; fase III na qual domina a morfologia amorfa.

Zircões que experimentaram trocas com fluidos podem ser indiretamente identificados porque esta troca causa distúrbios em diversas de suas propriedades químicas. Davies *et al.* (2015) citam as seguintes mudanças que podem ser observadas: alterações na composição de $\delta^{18}\text{O}$; perturbação do sistema U-Pb, reconhecido pela discordância nas idades $^{206}\text{Pb}/^{238}\text{U}$ e $^{207}\text{Pb}/^{235}\text{U}$; alteração no zoneamento observado nas imagens de CL e de BSE; elevado conteúdo de elementos traços. O acumulado de domínios amorfos ao longo do tempo nos zircões pode também provocar redução da sua densidade (Holland and Gottfried, 1955).

A geoquímica de isótopos de oxigênio de magmas derivados da crosta refletem o longo período de mistura de derivados mantélicos e crustais. Sedimentos reciclados e outros materiais supra-crustais comumente tem $\delta^{18}\text{O}$ mais alto que o mantélico devido à baixa temperatura do processo, mas valores mais baixos de $\delta^{18}\text{O}$ são também possíveis (Valley, 2003). Análises de $\delta^{18}\text{O}$ em zircões que foram datados proporcionam informações sobre crescimento e maturação da crosta (Valley, 2003).

1.3.7.1. Procedimentos de análise

Os *spots* para análise foram escolhidos com base em imagens de BSE, e deu-se preferência por analisar os mesmos *spots* datados pelo método SHRIMP. As pastilhas em *epoxy* foram metalizadas com ouro para realização das análises, realizados no equipamento CAMECA IMS 1280 *ion microprobe in multicollection mode*, do CMCA-UWA. Foram analisados 76 *spots*, e o padrão utilizado foi TEMORA 2 (Kita *et al.*, 2009). Um laser estático de ~3 nA Cs+ com uma energia de impacto de 20 keV e um diâmetro de 10-15 μm é focado sobre a superfície da amostra. Parâmetros do instrumento incluem: aumento de x130 entre amostra e campo de abertura, contraste de abertura de 400 μm , campo de abertura 4000 μm , 110 μm *entrance slit*, 500 μm *exit slits*, e 40 eV *band bass*.

para a energia de *slit* com um deslocamento de 5 eV para a banda de maior energia. Íons secundários O⁻ são acelerados a 10 keV e analisados com poder de resolução de massa de aproximadamente 2.200 (10% altura do pico máximo) usando um detector dual *Faraday cup*. As análises consistem de quatro ciclos de 20 segundos, com uma precisão média de ~0.1‰ (1 SE). Para as análises usa-se um laser de Cs⁺ focado de ~1.5 nA.

1.3.8. Isótopos Lu-Hf

Dados isotópicos Lu-Hf fornecem informações petrogenéticas importantes sobre a rocha hospedeira, evolução da crosta e manto (Xie et al., 2008). Combinado com informações de BSE, isótopos de oxigênio, elementos traços e temperatura de cristalização, análises recentes de zircão tem sido satisfatoriamente aplicadas em estudos como traçador metamórfico, caracterização de mistura de magmas, crescimento crustal e proveniência sedimentar entre outros (Xie et al., 2008). Conforme reportado por Claiborne *et al.* (2006) o fracionamento crescente do magma leva a um aumento da concentração de Hf nos cristais de zircão.

Durante a geração de magma ocorre o fracionamento de Lu para Hf, sendo o ¹⁷⁶Lu um radionuclídeo que sofre decaimento β⁻ para o isótopo estável ¹⁷⁶Hf, com tempo de meia-vida de aproximadamente 35 bilhões de anos (Kinny and Maas, 2003). Portanto, o sistema Lu-Hf pode ser usado para traçar a história da diferenciação química da crosta e do manto. A composição isotópica do Hf de material não fracionado (Lu/Hf = condrito) difere do manto depletado (Lu/Hf > condrito) e crosta enriquecida (Lu/Hf < condrito), (Kinny and Maas, 2003). O desvio da composição isotópica de Hf a partir do condrito em um tempo t são indicadas em mil e dado pela seguinte fórmula:

$$\epsilon_{\text{Hf}} = [(\text{Hf}^{176}/\text{Hf}^{177})_t / (\text{Hf}^{176}/\text{Hf}^{177})_{\text{chondrites}} - 1] \times 10^4$$

O valores positivos de εHf ocorrem em amostras com valores de ¹⁷⁶Hf/¹⁷⁷Hf maiores que o condrito no tempo t, enquanto que valores menores de ¹⁷⁶Hf/¹⁷⁷Hf que o condrito resultam em εHf negativo.

1.3.8.1. Procedimentos de análise

Os *spots* para análise foram escolhidos com base em imagens de BSE, e deu-se preferência por analisar os mesmos *spots* datados pelo método SHRIMP. O equipamento utilizado foi LA-ICP-MS Resonetics resolution M-50A excimer laser, acoplado a Nu Plasma II multi-collector da *Curtin University*. Foram feitas análises com dois tamanhos de *spots*, 50 µm (159 análises) e 33 µm (44 análises). Foram utilizados os seguintes parâmetros de instrumento: 30 s ablação, 10Hz, 2.2 J/cm², 2 pulsos de limpeza, 55 s coleta do *background*. O Mud Tank (Woodhead e Herdt, 2005) foi usado como padrão primário para todas as razões de Hf corrigidas. O R33 (Fisher et al., 2014) foi usado

como padrão primário para correção das razões Lu/Hf. Os seguintes isótopos foram medidos: ^{180}Hf , ^{179}Hf , ^{178}Hf , ^{177}Hf , ^{176}Hf , ^{175}Lu , ^{174}Hf , ^{173}Yb , ^{172}Yb , and ^{171}Yb .

1.4. Estruturação da tese

A tese está estruturada em 5 artigos científicos, os quais estão presentes nos capítulos 3 a 7 deste volume. A seguir é apresentado um resumo dos temas abordados em cada um desses capítulos.

O tema central do artigo I (**capítulo 3**) é a idade da sequência metassedimentar presente no depósito de Horto-Baratinha bem como seu significado geotectônico. Para tanto foram realizadas descrições detalhadas da estratigrafia do depósito e de suas macro e microestruturas, análise estrutural, geotermometria (**item 1.3.2**) e ainda utilizados parte dos dados obtidos pela geocronologia U-Pb (**item 1.3.3**). O objetivo principal desse artigo é descrever em detalhe o arcabouço estrutural do depósito e apresentar a correlação estratigráfica da sequência metassedimentar. Este artigo foi publicado na revista Journal of South America Earth Science (doi: 10.1016/j.jsames.2018.11.013).

O artigo II (**capítulo 4**) trata da metodologia de modelamento litológico implícito (**item 1.3.1**) aplicado ao depósito de Horto-Baratinha. O objetivo principal do trabalho é demonstrar a aplicação da modelagem litológica implícita incorporando dados de sondagem com dados de mapeamento de superfície. Além disso, o trabalho mostra a estreita relação espacial dos corpos de minério de ferro de alto teor com as intrusões pegmatíticas. Este artigo foi publicado na revista REM (*International Engineering Jornal* – doi: 10.1590/0370-44672018720167).

O artigo III (**capítulo 5**) trata da caracterização do depósito de Cuité. Os objetivos do trabalho são apresentar a correlação estratigráfica da sequência metassedimentar presente no depósito utilizando dados da geocronologia U-Pb (**item 1.3.3**), descrever feições texturais dos corpos de minério, e as principais feições estruturais do depósito.

O tema central do artigo IV (**capítulo 6**) é a caracterização dos mecanismos de mineralização em ferro e sua correlação com as intrusões pegmatíticas. Para tanto foram utilizadas as análises química de rocha total do itabirito e minério de Horto-Baratinha e Cuité (**item 1.3.4**), as microanálises das diferentes gerações de óxidos de ferro presentes nos depósitos (**item 1.3.5**) e os dados de geocronologia U-Pb de duas amostras de pegmatitos do depósito Horto-Baratinha (**item 1.3.3**). Foram ainda realizadas comparações com outros depósitos nacionais e internacionais. Neste trabalho são apresentadas as transformações químicas ocorridas no processo de enriquecimento do protominério para minério, sua evolução e associação com eventos geotectônicos.

O artigo V (**capítulo 7**) aborda o registro em zircões do evento hidrotermal Brasiliense na borda leste do cráton do São Francisco. Para tanto são utilizadas as seguintes análises realizadas em zircões: geocronologia U-Pb (**item 1.3.3**); microquímica em zircões dos depósitos de Horto-Baratinha, Cuité, Morro Escuro e Morro do Pilar (**item 1.3.6**); isótopos de oxigênio (**item 1.3.7**);

isótopos Lu-Hf (**item 1.3.8**). Neste trabalho são descritas as transformações químicas e isotópicas provocadas pelo evento hidrotermal Brasiliano e sua relação com os pegmatitos da província pegmatítica oriental brasileira.

2. CONTEXTO GEOLÓGICO REGIONAL

A região estudada localiza-se na porção oeste da faixa orogênica Araçuaí, próximo a borda leste do Cráton São Francisco (Figura 2.1), segundo delimitação do cráton de Alkmim et al. (2006). A área está inserida em unidades arqueanas, representantes do embasamento do Cráton do São Francisco, e em granitoides da Suíte Borrachudos, unidades estas retrabalhados pela orogênese Brasiliiana no Neoproterozoico (Noce et al., 2007a; Silva, 2000). Segundo mapas regionais (Pedrosa-Soares et al., 1994; Oliveira e Leite, 2000; Silva, 2000; Pinto e Silva, 2014) a unidade metassedimentar, portadora de formação ferrífera presente na área de estudo é considerada uma sequência *greenstone belt* de idade arqueana pertencente ao Supergrupo Rio das Velhas. Formações ferríferas do contexto geológico regional são correlacionadas principalmente ao Complexo Guanhães, à base no Supergrupo Espinhaço, aos Supergrupos Minas e Rio das Velhas (Figura 2.1).

2.1. Estratigrafia

2.1.1. Complexo Mantiqueira

O Complexo Mantiqueira representa uma das unidades do embasamento cratônico retrabalhada pela orogênese Brasiliiana. O litotipo predominante é um biotita-anfibólio ortognaisse bandado de composição tonalítica a granítica, com frequentes lentes e boudins de anfibolito (Noce et al., 2007b). O bandamento e a foliação exibidos pelos gnaisses têm orientação N-S e ângulo de mergulho baixo, que foram possivelmente formados durante a orogênese Brasiliiana (Noce et al., 2007b), embora a idade de cristalização U-Pb SHRIMP dos zircões seja de 2.137 ± 19 a 2.041 ± 7 Ma (Noce et al., 2007a).

2.1.2. Greenstone belt - Supergrupo Rio das Velhas

Segundo Silva (2000) o Supergrupo Rio das Velhas aflora na folha Coronel Fabriciano (folha SE.23-Z-D-V) como estreitas faixas inseridas nos ortognaisse do Complexo Mantiqueira e intrudidas por granitos da Suíte Borrachudos. Segundo o autor tais faixas estão metamorfisadas na fácies anfibolito, localmente granulito, e são constituídas por rochas metaultramáticas e metamáficas, xistos maficos, metacherts, formações ferríferas, rochas calcissilicáticas, mármore, xistos e gnaisses metapelíticos e quartzitos.

Devido à mistura dos litotipos e a dimensão reduzida dos corpos, Silva (2000) justifica que não foi possível mapeá-los separadamente, mesmo agrupando-os em unidades, devido à escala de trabalho (1.100.000). Por isso, o autor optou por cartografá-los sob a denominação de Supergrupo Rio das Velhas Indiviso.

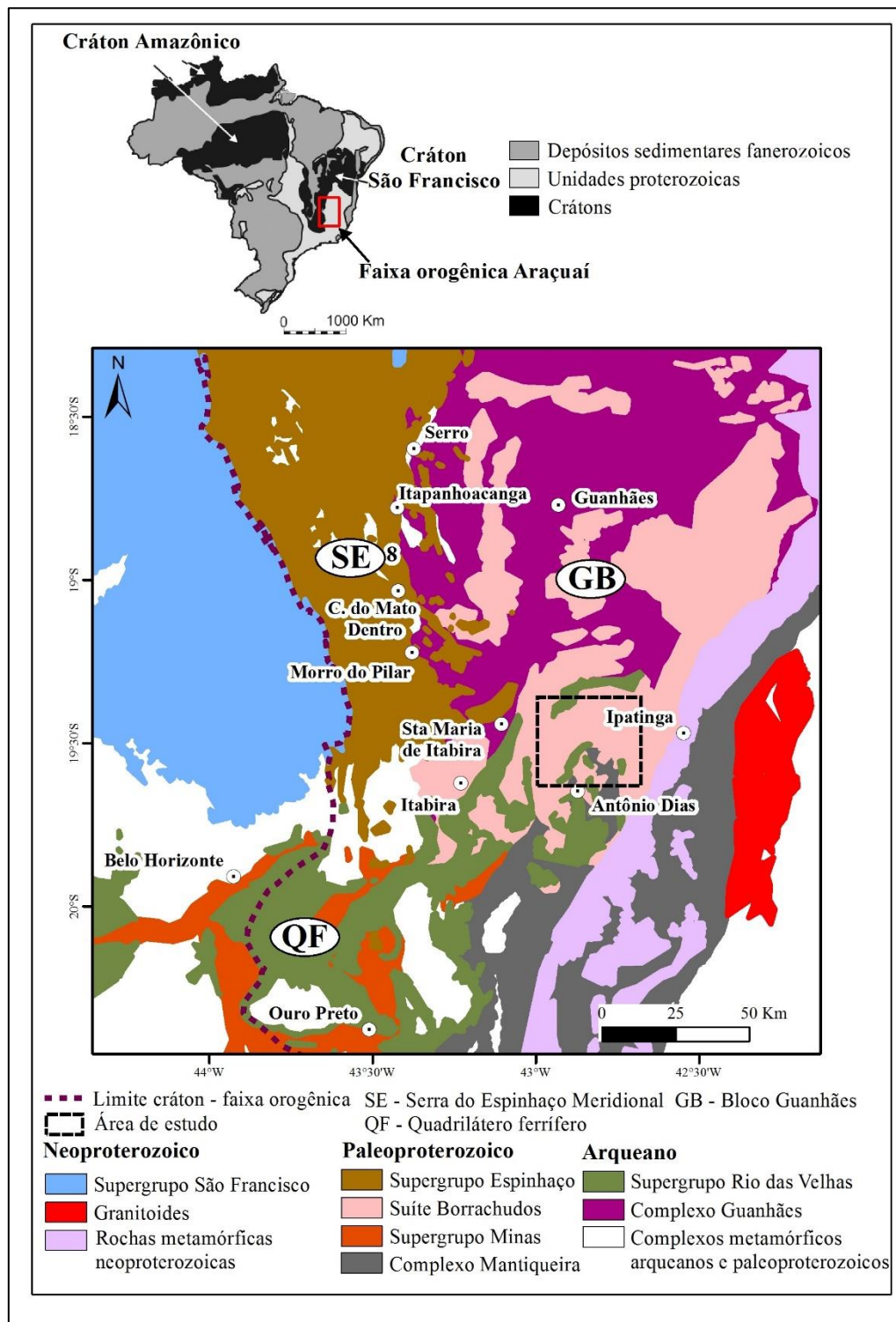


Figura 2.1: Mapa geológico regional o qual exibe a localização da área de estudo e distribuição das principais unidades geológicas portadoras de formação ferrífera bandada. Distribuição das unidades modificado de Pinto e Silva (2014). Limite do Cráton do São Francisco baseado em Alkmim et al. (2006).

2.1.3. Complexo Guanhães

Também denominado de Grupo Guanhães, o Complexo Guanhães ocorre com ampla distribuição geográfica na região centro-leste do Estado de Minas Gerais. Trata-se de uma sequência

composta por gnaisses e migmatitos TTG, corpos graníticos, rochas metavulcanossedimentares e sequências metassedimentares portadoras de BIF, de alto grau metamórfico, entre xisto verde alto a anfibolito (Noce et al., 2007b). As rochas metavulcanossedimentares ocorrem como faixas estreitas e descontínuas intercaladas entre rochas gnáissicas (Dussin et al., 2000).

De acordo com Grossi-Sad (1997) e Grossi-Sad et al. (1990a), as faixas de formação ferrífera do Complexo Guanhães apresentam espessura de até cerca de 60 m e uma continuidade ao longo do *strike* por várias centenas de metros. Do ponto de vista mineralógico são compostas por bandas ricas em hematita/magnetita e bandas de quartzo. Os teores de ferro variam entre 20 e 45%, mas podem atingir 70% nas áreas ricas em magnetita. Os corpos magnetíticos aparecem intercalados com corpos hematíticos, estes de granulação grossa, sem clara relação estrutural, e cortados por zonas especularíticas.

Silva et al. (2002) dataram os gnaisses aflorantes nos arredores da cidade de Guanhães, através do método SHRIMP, em 2.867 ± 10 Ma, 2.711 ± 11 Ma, 2.710 ± 6 Ma, 527 ± 45 Ma, 519 ± 5 Ma, 497 ± 68 Ma, sendo os três primeiros valores correspondentes à idade de cristalização, e os três últimos à idade de metamorfismo associada a orogênese Brasiliana, provavelmente a fase de colapso extensional deste orógeno, que teria ocorrido no intervalo 525-480 Ma (Pedrosa Soares et al., 2011, 2001). Silva et al. (2002) sugerem que o Complexo Guanhães possa corresponder a uma extensão do embasamento arqueano do domínio cratônico do QF no domínio da Faixa Araçuaí, e não a um terreno alóctone, de caráter paraderivado como postulado por Grossi-Sad et al. (1990b).

Barrote (2016) identificou nos arredores de Guanhães uma unidade basal composta por granito-gnaisses foliados, localmente charnokito, e uma sequência supracrustal constituída por quartzito na base e no topo, intercalado por BIF. Segundo o autor, o quartzito da base e do topo da sequência são muito semelhantes, apresentam granulação de média a grossa e textura sacaroidal. O autor descreve a presença de granada-anfibólito-xisto como camadas intercaladas ao pacote de quartzitos na região próxima ao contato com as BIFs. As BIFs, que por estarem metamorfizadas são denominadas como itabiritos, foram classificadas em dois tipos, de acordo com sua estruturação: bandada e a sem bandamento. A mineralogia principal é composta por quartzo, hematita (especular, granular e lobular) e magnetita. Também ocorre sericitita, anfibólito (série tremolita-actinolita e hornblenda), epidoto e biotita. Como minerais secundários o autor descreve clorita e carbonato. Segundo Barrote (2016), os itabiritos apresentam distribuição de ETR+Y similares a outras BIFs pré-cambrianas, particularmente às BIFs da Sequência do Morro Escuro (Silveira Braga et al., 2015), sem anomalia verdadeira de Ce e com razão Y/Ho próximo aos valores típicos de água do mar. O autor supracitado cita ainda a presença das seguintes rochas intrusivas:

- ortoanfibolitos como produto do metamorfismo de corpos intrusivos de rocha básica, os quais ocorrem intercalados em todas as unidades identificadas, em contato brusco, concordante, com foliação paralela a de suas encaixantes;
- metagranitoides intrusivos e pegmatitos associados cortando toda a sequência de rochas supracrustais.

Dados geocronológicos de Barrote et al. (2017) indicam que a sequência metassedimentar apresenta idade máxima de deposição orosiriana sendo, portanto, correlacionada com os Grupos Serra da Serpentina e Serra de São José definidos por Rolim et al. (2016) – **item 2.1.5** a seguir.

2.1.5. Supergrupo Espinhaço

O Supergrupo Espinhaço é constituído por rochas paleo-mesoproterozoicas, cujas características estratigráficas foram definidas principalmente por Pflug (1968) e Schöll e Fogaça (1979), que descreveram oito formações na região da Serra do Espinhaço Meridional (SdEM): São João da Chapada, Sopa-Brumadinho, Galho do Miguel, Santa Rita, Córrego dos Borges, Córrego da Bandeira, Córrego Pereira e Rio Pardo Grande. A respeito do agrupamento dessas formações em unidades litoestratigráficas maiores, podem ser encontradas na literatura diversas propostas (Dossin et al., 1984; Knauer, 1990; Martins-Neto, 2000; Almeida-Abreu e Renger, 2002), sendo atualmente aceita a divisão em dois grupos: o Grupo Guinda e o Grupo Conselheiro Mata, que correspondem, respectivamente, às sequências de base e de topo do Supergrupo Espinhaço (Figura 2.2). Almeida-Abreu e Renger (2002) incluem na sua definição do Supergrupo Espinhaço, além dos citados grupos Guinda e Conselheiro Mata, as várias unidades supracrustais típicas da borda leste da Serra do Espinhaço Meridional, que são reunidas por esses autores sob a denominação de Grupo Serro.

Chemale et al. (2012), a partir de dados geocronológicos em zircões detritícios (U-Pb SHRIMP e LA-ICP-MS), dividem o Supergrupo Espinhaço em duas bacias: o Espinhaço Inferior, representado pelas Formações Bandeirinha e São João da Chapada, que correspondem a uma sequência de rifte intracontinental formada entre 1.680 Ma e 1.800 Ma; Espinhaço Superior, composto pelas Formações Sopa Brumadinho, Galho do Miguel, Santa Rita, Córrego dos Borges, Córrego Bandeira, Córrego Pereira e Rio Pardo, relacionadas a uma bacia do tipo rift-sag com idade máxima de deposição de 1.192 Ma (Figura 2.2).

Rolim et al. (2016) descrevem duas sequências portadores de formações ferríferas ao longo da borda leste da SdEM, depositadas entre os períodos Orosiriano e Estateriano, o Grupo Serra da Serpentina, que representa uma bacia tipo rift-sag com baixa atividade tectônica, e o Grupo Serra de São José, bacia rift tectonicamente ativa nos estágios iniciais da abertura do rift Espinhaço (Figura 2.2). O Grupo Serra da Serpentina tem idade máxima orosiriana (idade mínima de 1.990 ± 16 Ma obtida por Rolim et al. (2016) em zircão detritico pelo método U-Pb SHRIMP), e consiste de

metassedimentos clásticos finos na base, e sedimentos químicos no topo, incluindo BIF, correspondentes as formações Meloso e Serra do Sapo respectivamente, correlacionáveis, segundo os autores, a sequência pré-Espinhaço do Grupo Costa Sena. O Grupo Serra de São José está em contato erosional sobre o Grupo Serra da Serpentina e é dividido nas formações Lapão, Itapanhoacanga, Jacém e Canjica. A formação Itapanhoacanga apresenta idade máxima de deposição estateriana (idade mínima obtida de 1.666 ± 32 (Rolin et al., 2016) e 1.668 ± 23 Ma (Silveira Braga et al., 2015) em zircão detritico pelo método U-Pb SHRIMP), a qual coincide com a idade máxima de deposição da formação São João da Chapada (Chemale et al., 2012).

2.1.6. Suíte Borrachudos

O nome Suíte Borrachudos foi adotado por Grossi-Sad et al. (1990a) para caracterizar os corpos graníticos intrusivos no embasamento arqueano da região leste da SdEM, entre Itabira e Guanhães. Distinguem-se os corpos Itabira, Açucena, Petí, Morro do Urubu, São Félix e Senhora do Porto. Diversos autores (*e.g.* Dossin et al., 1993; Fernandes et al., 1994; Dussin e Dussin, 1995; Fernandes, 2001; Magalhães et al., 2018) caracterizam a Suíte Borrachudos como constituída por granitos de assinatura geoquímica alcalina anorogênica gerados a partir da abertura do rifte Espinhaço, no final do Paleoproterozoico.

Esta suíte é constituída de rochas bastante homogêneas, de granulação média a grossa, de cor cinza a rosa quando fresca, e cinza amarelada quando intemperizada, e tendo biotita como principal mineral máfico, seguida pelo anfibólio hastingsita (Fernandes, 2001; Fernandes et al., 1994). A mineralogia principal desta unidade é composta por microclina, albite, quartzo, biotita e hornblenda, e têm como minerais acessórios mais comuns allanita, zircão, magnetita e ilmenita (Fernandes et al., 1994).

Silva et al. (2002) dataram uma amostra proveniente do corpo Açucena, através do método SHRIMP, em 1.740 ± 8 Ma, e Dossin et al. (1993) obtiveram idade Pb-Pb igual a 1.729 ± 14 Ma. Estes granitos constituem rochas posteriores aos eventos do Riaciano e que portanto, foram submetidos exclusivamente à deformação Brasiliana (Dussin e Dussin, 1995).

Inseridos na Suíte Borrachudos são encontradas intrusões pegmatíticas, algumas das quais de interesse econômico devido à presença de berilos que são explorados como gemas (variedade águamarinha e esmeralda) e como minério de Be (Marciano, 1995; Preinfalk et al., 2002). A formação de esmeralda está relacionada a reação metassomática entre os pegmatitos anatéticos ricos em Be com rocha ultrabásicas ricas em Cr (Preinfalk et al., 2002). Dados isotópicos indicam que a idade de cristalização desses pegmatitos está relacionada ao final do evento Brasiliano (Marciano, 1995; Preinfalk et al., 2002). Preinfalk et al. (2002) obtiveram idade de 477 ± 14 Ma pelo método Rb-Sr,

Marciano (1995) alcançou idade de 519 ± 19 Ma por K-Ar em muscovita e Ferreira (2017) obteve idade de 474 ± 8 Ma utilizando microanálises de U-Th-Pb em monazita por microssonda eletrônica.

(A)

Serra do Espinhaço Central					
	Supergroupo	Grupo	Tipo de bacia	Litotipo	Formação
ESPINHAÇO	Guinada	Conselheiro Mata	Rift-Sag	metasiltito, metadolomito	Rio Pardo
				quartzito	Corr. Pereira
				metapelito, quartzito	Corr. Bandeira
				quartzito	Corr. dos Borges
				metapelito	Santa Rita
	Marinho raso			Rift	quartzito
metaconglomerado, quartzitos, metapelitos, metavulcânicas					Sopa-Brumadinho
Costa Sena⁵			Rift	quartzitos, metaconglomerado, metavulcânica	São João da Chapada 1683 ± 11 Ma ¹
				quartzito, metaconglomerado	Bandeirinha 1737 ± 11 Ma ²
RIO PARAÚNA				sericita-quartzo xisto, quartzito, filito, formação ferrífera	Barão de Guaicuí 2049 ± 16 Ma ³
				xisto verde, metavulcânica, quartzito, filito	Pedro Pereira

(B)

Serra da Serpentina					
	Formação	Litotipo	Tipo de bacia	Grupo	Supergroupo
RIO PARAÚNA	Canjica	BIFs	Rift	Serra da Serpentina	ESPINHAÇO
	Jacém	metapelito			
	Itapanhoacanga 1666 ± 32 Ma ⁴	quartzito, meta-conglomerado	Sag	Serra de São José	
	Lapão	metaconglomerado, quartzito			
	Serra da Sapo	BIFs, metadolomito			
Meloso 1990 ± 16 Ma ⁴	sericita quartzo xisto, quartzito, filito				

Figura 2.2: (A) Coluna estratigráfica da Supergrupo Espinhaço na porção central SdEM. (B) Coluna estratigráfica dos grupos Serra da Serpentina e Serra de São José. Colunas retiradas de Rolim et al. (2016). Dados geocronológicos: (1) (Chemale et al., 2012); (2) (Santos et al., 2013); (3) (Machado et al., 1989); (4) (Rolim et al., 2016).

2.2. Arcabouço geotectônico

Os principais eventos tectônicos registrados no contexto geológico regional foram as orogêneses Transamazônica (também denominada de orogênese Riaciana por Brito Neves et al. (2014) – 2.100 Ma) e Brasiliana (800-500 Ma), conforme sintetizado na Tabela 2.1. Entre estes ocorreram dois importantes conjunto de eventos extensionais, o rift Espinhaço (~1.700 Ma) e o rift Araçuaí (~900 Ma).

Evento tectônico	Período	Principais características deste evento no Bloco Guanhães e arredores
Orogênese Riaciana ou Transamazônica	2.300-2.050 Ma	Remobilização dos complexos granito-gnáissicos.
Tafrogênese Espinhaço	1.750-1700 Ma	Desenvolvimento episódico da bacia tipo <i>rift-sag</i> pré-Espinhaço, com baixa atividade tectônica, rica em águas ferruginosas, e deposição do Grupo Serra da Serpentina. ¹ Abertura de extensivo rifte de direção N-S associado com abundante magmatismo ácido. Intusão de metariolitos e granitos com envolvimento de fusão parcial de rochas arqueanas, siderianas e orosirianas, com alta contaminação crustal. ²
Deposição	1.680-1.800 Ma	Deposição do Espinhaço inferior (incluindo Grupo Serra de São José), em ambiente rifte intracontinental. ^{3,4}
	<1.192 Ma	Deposição do Espinhaço superior em bacia tipo <i>rift-sag</i> . ³
Tafrogênese Araçuaí	~900 Ma	Intrusões máficas da Suíte Pedro Lessa. Deposição em ambiente rifte, margem passiva e oceânico. ⁵
Orogênese Araçuaí	630-480 Ma	Deformação e atividade ígnea associados aos estágios colisionais e ao colapso gravitacional do orógeno. ⁶

Tabela 2.1: Síntese dos principais eventos tectônicos registrados no Bloco Guanhães. Fonte: ¹Renger et al. (1994), ²Magalhães et al. (2018), ³Chemale et al. (2012), ⁴Rolim et al. (2016), ⁵Machado et al. (1989), ⁶Pedrosa-Soares et al. (2011).

O evento Riaciano representou o período de remobilização dos complexos granito-gnáissicos do sudeste do Cráton do São Francisco (Renger et al., 1994), e segundo Brito Neves et al. (2014) ocorreu entre 2.300 e 2.050 Ma. Segundo os autores supracitados, há ainda registo de um evento Orosiriano (2.050 – 1.800 Ma) que contempla orogêneses independentes que representam os estágios finais iniciados no Riaciano.

Na fase do rifte Espinhaço ocorreu a sedimentação das formações basais do Supergrupo homônimo (Figura 2.3). Vulcanismo ocorreu num estágio precoce à bacia e esteve ativo durante sua sedimentação (Dussin e Dussin, 1995). Nas bordas da bacia em formação ocorreu intrusão de plútons graníticos, sendo a Suíte Borrachudos o conjunto de plútons que intrudiu o embasamento a sudeste da Faixa Araçuaí (Dussin et al., 2000).

Um segundo evento de extensão afetou a região da SdEM no início do Neoproterozóico (~900 Ma), quando foi depositado o Grupo Macaúbas (Figura 2.3) a norte da região de Diamantina (Dussin e Dussin, 1995; Pedrosa-Soares et al., 2001; Pedrosa-Soares et al., 2007).

A Orogênese Brasiliiana foi responsável pela individualização do Cráton do São Francisco e das Faixas Móveis adjacentes (Almeida, 1977). Este evento tectônico produziu no domínio da Faixa Araçuaí, deformação crescente de oeste para leste, atingindo condições rúpteis-dúcteis na porção oriental da Cordilheira Espinhaço e rúpteis a não deformadas em direção ao interior do cráton (Figura 2.3). A Orogênese Brasiliiana também gerou cavalgamentos de direção N-S com vergência para oeste, e na Faixa Araçuaí, e uma sucessão de zonas com dobras assimétricas com vergência para oeste, separadas por zonas de cisalhamento dúctil.

Alkmim *et al.* (2007) subdividiram o Orógeno Araçuaí em dez compartimentos, os quais desempenharam papéis distintos na evolução deste orógeno. Os compartimentos são os seguintes (Figura 2.4): i) Cinturão de Cavalgamentos da SdEM; ii) Zona de Cisalhamento da Chapada Acauã; iii) Zona de dobramentos de Salinas; iv) Corredor Transpressivo de Minas Novas; v) Saliência do Rio Pardo e sua zona de interação com o Aulacógeno do Paramirim; vi) Bloco de Guanhães; vii) Zona de Cisalhamento de Dom Silvério e estruturas associadas; viii) Zona de Cisalhamento de Itapebi e estruturas associadas; ix) Núcleo cristalino (*i.e.*, a zona interna de alto grau que representa o núcleo do orógeno); e x) Cinturão Oeste-Congolês.

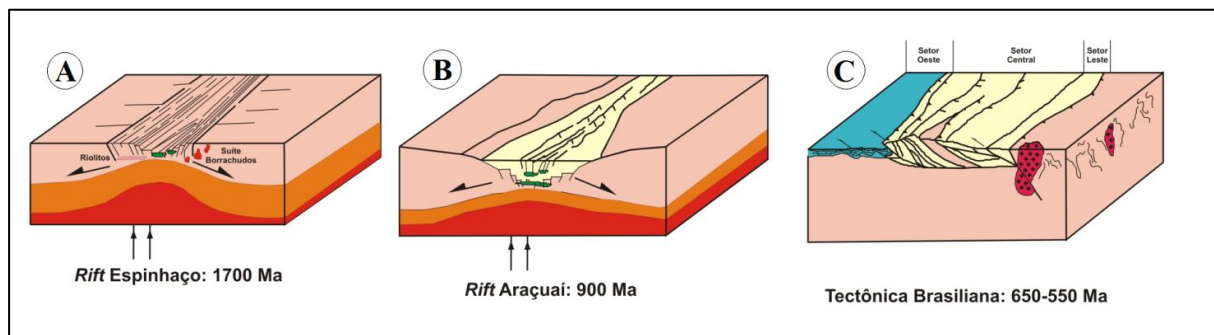


Figura 2.3: Representação esquemática da evolução geodinâmica do Espinhaço Meridional do Paleo-Mesoproterozoico até o final do Neoproterozoico (Modificado de Dussin and Dussin (1995)).

A região em foco situa-se no Bloco Guanhães, que corresponde a um alto estrutural que expõe o embasamento do orógeno. Este bloco foi subdividido por Alkmim et al. (2006) em três domínios: leste, central e oeste. Os domínios oeste e leste são caracterizados pela presença de falhas reversas e de empurrão de direção N-S, sendo que no primeiro estas falhas colocam lascas do embasamento sobre rochas do Espinhaço, e no segundo colocam rochas do Grupo Macaúbas sobre o embasamento. O domínio central é balizado pela zona de cisalhamento Pedra Branca a sul, Sabinópolis a oeste e Virgolândia a leste, de direção preferencial N-S. Esta porção do Bloco de Guanhães possui grau metamórfico anfibolito alto, superior aos outros domínios, e expõe um nível crustal mais profundo do que as porções adjacentes. Seu soerguimento deu-se entre 509-480 Ma, idade provável do colapso gravitacional do orógeno (Peres et al., 2004).

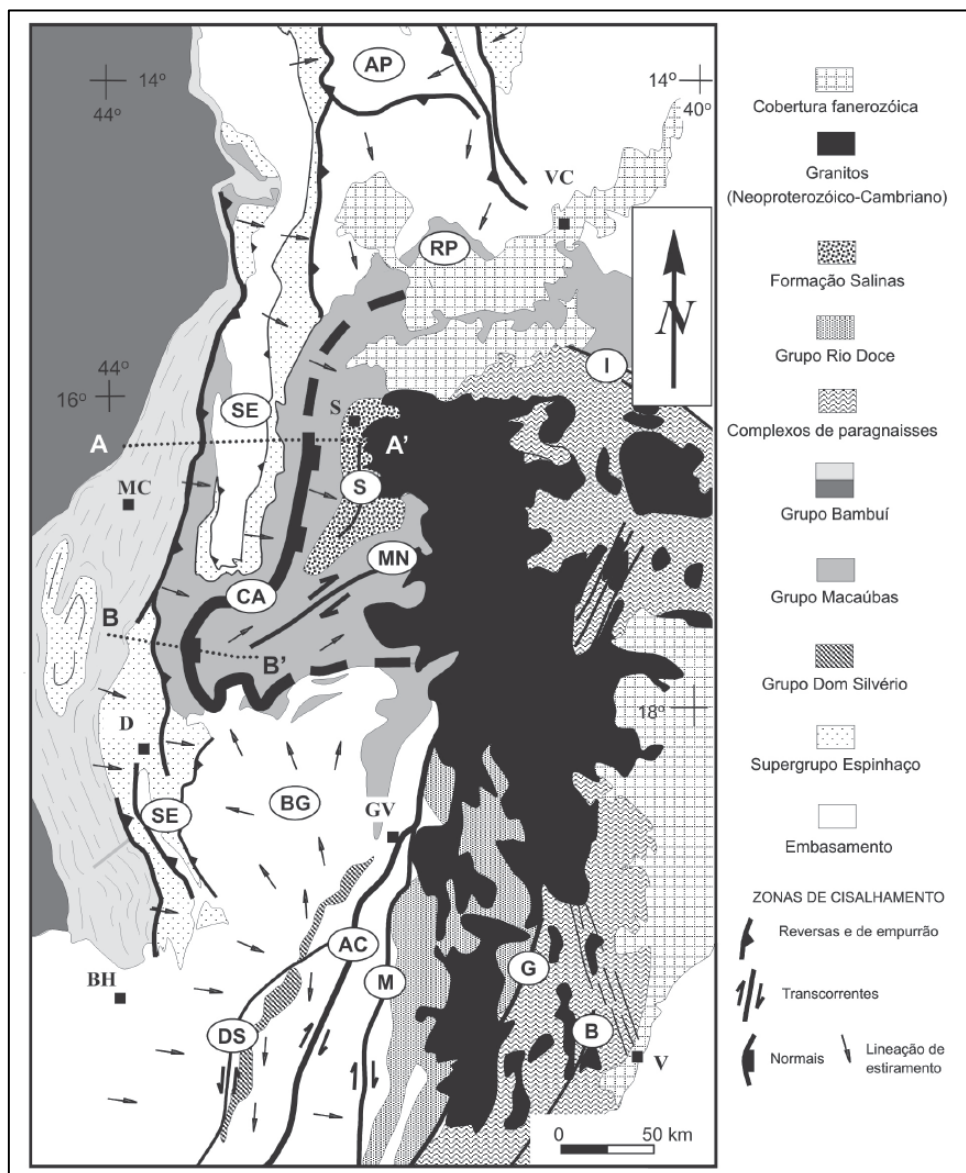


Figura 2.4: Mapa tectônico esquemático do Orógeno Araçuaí, enfatizando os seus compartimentos e grandes zonas de cisalhamento. SE: Cinturão de cavalgamentos da Serra do Espinhaço Meridional; CA: Zona de Cisalhamento da Chapada Acauã; S: Zona de dobramentos de Salinas; MN: Corredor transpressivo de Minas Novas; RP: Saliência do Rio Pardo e zona de interação com o Aulacógeno do Paramirim; BG: Bloco de Guanhães; DS: Zona de Cisalhamento de Dom Silvério; I: Zona de Cisalhamento de Itapebi; AC: Zona de Cisalhamento de Abre Campo; M: Zona de Cisalhamento de Manhuaçu; G: Zona de Cisalhamento de Guacuá; B: Zona de Cisalhamento de Batatal. Figura retirada de Alkmim et al. (2007).

Santos et al. (2019) propõem que a área do Cráton do São Francisco é maior que a estipulada por trabalhos anteriores (*e.g.* Pedrosa Soares et al., 2001; Alkmim et al., 2006). Segundo os autores, as regiões limites do cráton foram fortemente afetadas pela Orogênese Brasiliana, onde o imbricamente tectônico entre áreas riacianas-arqueanas com fatias tectônicas neoproterozoicas são comuns. Estas regiões limítrofes são delimitadas como metacrátions segundo definição de Liégeois et al. (2013), e portanto, podem ser consideradas como pertencentes ao domínio cratônico.

3. ARTIGO I - THE HORTO-BARATINHA ITABIRITE-HOSTED IRON ORE: A BASAL FRAGMENT OF THE ESPINHAÇO BASIN IN THE EASTERN SÃO FRANCISCO CRATON

Flávia Cristina Silveira Braga^{ab}, Carlos Alberto Rosière^c, João Orestes Schneider Santos^{de}, Steffen G. Hagemann^d, Neal J. McNaughton^e, Pedro Valle Salles^{bf}

^a Graduate Program, Instituto de Geociências, Universidade Federal de Minas Gerais, Belo Horizonte, MG, Brazil

^b Faculdade de Engenharia, Universidade do Estado de Minas Gerais, João Monlevade, MG, Brazil

^c Instituto de Geociências, Universidade Federal de Minas Gerais, Belo Horizonte, MG, Brazil

^d Centre for Exploration Targeting, University of Western Australia, Perth, WA, Australia

^e Curtin University of Technology, Perth, WA, Australia

^f Centro Federal de Educação Tecnológica de Minas Gerais, Belo Horizonte, MG, Brazil

* Corresponding author. E-mail addresses: flaviacsbraga@gmail.com (F.C. Silveira Braga), crosiere@gmail.com (C.A. Rosière), orestes.santos@bigpond.com (J.O.S. Santos), steffen.hagemann@uwa.edu.au (S.G. Hagemann), n.mcnaughton@curtin.edu.au (N.J. McNaughton), pedrovallesalles025@gmail.com (P.V. Salles)

Published in: Journal of South America Earth Science, 90(2019): 12-33.

DOI: 10.1016/j.jsames.2018.11.013

3.1. Abstract

The Horto-Baratinha (HBD) iron ore deposit is located at the eastern border of São Francisco Craton, comprising BIF-hosted high-grade bodies (>60 wt.% Fe) associated with polydeformed quartz-mica-schists, amphibole-schist of Statherian maximum deposition age, enclosed by Statherian granitoids of the Borrachudos Suite and Neoarchean gneiss. All the sequence is crosscut by undeformed dikes and sills of pegmatitic bodies probably formed during Late Ediacaran-Cambrian. The metasedimentary sequence is stratigraphically correlatable with the Orosirian-Statherian Serra da Serpentina and Serra de São José Groups that comprise the basal units of the Espinhaço Supergroup and was intensively segmented into distinct tectonic blocks. The sedimentary/diagenetic bedding of the metamorphosed BIF (itabirite) is generally transposed by an axial planar schistosity. The lamellar hematite from itabirite is the oldest iron oxide generation, which was formed during the syn-deformational stage, parallel-oriented to the rock foliation. The (keno)magnetite grains from itabirite, iron ore and pegmatite bodies developed as idioblasts that grew over the foliation formed during late and post-deformational stages. Magnetite oxidizes subsequently to martite and granular hematite. Coarse lamellar hematite crystals randomly oriented in the border of the pegmatitic bodies also formed during the post-deformational stage due to hydrothermal reaction with itabirite. The country rocks have undergone at least three stages of deformation developed during the syn-collisional and late-collisional (Ediacaran to early-Cambrian) phases of the Brasiliano Orogeny: stage 1 with the development of a pervasive foliation (S_1), parallel to axial plane to tight folds and transposition of all sedimentary structures; stage 2 with folding of S_1 ; stage 3 with refolding of S_1 . Both fold systems interfere with each other making up a dome and basin refolding shape. During the late-collisional

(Ediacaran to early-Cambrian) and post-collisional/gravitational collapse (Cambrian) the sequence was intruded by anatetic pegmatic bodies, which are part of the Eastern Brazilian Pegmatite Province, one of the most significant pegmatitic regions worldwide. The fluid related with these intrusions could be related with the Si leaching, crystallization of magnetite and granular hematite, and consequent formation of high-grade iron bodies.

Keywords: itabirite, iron ore, Espinhaço Supergroup, refolding

3.2. Introduction

The Horto-Baratinha Deposit (HBD) comprises medium to coarse-grained granoblastic magnetite and hematite orebodies discontinuously developed in contact with metric to decametric pegmatitic bodies. Similar deposits (*e.g.* Piçarrão, Liberdade, Jambreiro, Candonga, Cuité) are exposed in the Guanhães Block along the eastern border of São Francisco Craton (Figure 3.1). These deposits are hosted by itabirite (metamorphosed banded iron formation - BIF), associated with psammo-pelitic layers, inserted into crystalline rocks, commonly in contact with or in the proximity of Paleoproterozoic granitoid of the Borrachudos Suite (Barrote et al., 2017; Gomes et al., 2018). Along the Espinhaço fold-thrust belt (Figure 3.1) the BIF-bearing massive iron bodies (*e.g.* Serra do Sapo, Serra da Serpentina, Morro do Pilar, Morro Escuro) are mainly composed by platy hematite and controlled by shear zones (Gomes et al., 2018; Rolim et al., 2016; Silveira Braga et al., 2015).

The BIF-bearing sequence from HBD is considered an inlier of the Neoarchean Rio das Velhas greenstone belt (Pinto and Silva, 2014; Silva, 2000) in the Archean and Paleoproterozoic crystalline rocks comprising the Mantiqueira and Guanhães Complexes. Alkmim et al (2007) interpreted the Guanhães Block as a tectonic unit of the western part of the Neoproterozoic Araçuaí Orogenic belt (Figure 3.1) that developed as a basement high and site of non-deposition during the sedimentation of the post-Rhyacian units. The block remained as a rigid *butress* that has been partially preserved of the thrusts and passively controlled the geometry of folds of the Araçuaí belt throughout the evolution of the Brasiliano collage, from Neoproterozoic to the Cambrian (Brito Neves et al., 2014; Noce et al., 2007b; Silva, 2000).

Recent geochronological results from similar deposits (Barrote et al., 2017; Silveira Braga et al., 2015) have opened space for the alternative interpretation that the BIF sequence represent tectonic enclaves of Orosirian-Statherian units such as the Serra da Serpentina and Serra de São José Groups (Rolim et al., 2016) and the gneisses of the Guanhães Block comprise metamorphic rocks of different origin and ages. The HBD high-quality magnetite/granular hematite coarse-grained ore is the main source of exploitation being unequivocally associated with voluminous pegmatite veins.

In this paper we aim a detailed description of the deposit to characterize the age of the sequence and iron ore mineralization, the variation of textural features associated with the structural

evolution, providing a new insight of the tectonic environment and consequences for the interpretation of the Guanhães Block as an active fragment of the lower crust comprised by juxtaposed tectonic slices amalgamated and uplifted during the Brasiliano Orogeny.

3.3. Regional geology

3.3.1. Gneissic terranes (*Guanhães Block and Mantiqueira Complex*)

The Guanhães Block (GB – Figure 3.1) is a major tectonic unit (Alkmim et al., 2007), delineated by shear zones. The Guanhães Block exposes deeper crustal level with a higher metamorphic grade than the adjacent blocks, such as Serra do Espinhaço fold-thrust belt Block (SE – Figure 3.1) located at northeast (Alkmim et al., 2006). The Guanhães Block is comprised mainly by TTG (tonalite-trondhjemite-granodiorite) gneiss, migmatite, and granitic bodies, commonly displaying mylonitic fabric, that together with discontinuous strings of BIF-bearing metasedimentary and metavolcanic rocks (Dussin et al., 2000; Noce et al., 2007a) make up the Guanhães Complex. The gneissic rocks of the Guanhães Complex delivered a wide variety of ages: $2,867 \pm 10$ Ma, $2,711 \pm 11$ Ma, $2,710 \pm 6$ Ma, 527 ± 45 Ma, 519 ± 5 Ma, 497 ± 68 Ma (Silva et al. (2002) – U-Pb SHRIMP). The first three ages indicate crystallization ages, and the others are metamorphic ages associated with the Brasiliano orogenesis (Schmitt et al., 2004). The Guanhães Complex is intruded by the anorogenic granitic bodies of the Borrachudos Suite (Dossin et al., 1993; Dussin and Dussin, 1995; Fernandes, 2001; Fernandes et al., 1994) emplaced along the eastern border of São Francisco craton during the Paleoproterozoic. This unit was dated by Silva et al. (2002) at $1,740 \pm 8$ Ma using U-Pb SHRIMP in zircon crystals, and by Dossin et al. (1993) at $1,729 \pm 14$ Ma by zircon Pb-evaporation method.

Located at the south of the Guanhães Block, upper-amphibolite to lower-granulite facies, mylonitic felsic to intermediate orthogneisses (biotite gneiss, biotite-hornblende gneiss, charnockite, and enderbite) comprise the Mantiqueira Complex (Figure 3.1). The Mantiqueira Complex is considered a Meso- and Neo- Archean terrane generated in a convergent margin setting (3,200–2,750 Ma) and reworked during the Rhyacian with magmatic additions between 2,200–2,044 Ma, due to the development of a Cordilleran arc along the margin of the São Francisco protocratonic landmass (Noce et al., 2007a, 2007b; Silva et al., 2002).

Several BIF-bearing sequences that host high-grade iron orebodies are widespread in Guanhães Block and considered a part of the Archean Complex, but very little information is available about these units. Barrote et al. (2017) described a fragmented supracrustal sequence inserted in the gneissic rocks, comprising quartzites with a maximum deposition age of $\sim 2,180$ Ma associated with the iron formation. They usually host high-grade deposits that have been intermittently exploited such as Piçarrão, Liberdade, Jambreiro, Condonga, Cuité that are concentrated along the western and southern border of Guanhães Block (Figure 3.1).

3.3.2. Iron formations in the Southern Espinhaço fold and thrust belt

The Southern Espinhaço Block (SE – Figure 3.1) is a 700 km long, NS-trending and west-verging system of faults and folds that fringe the eastern edge of the São Francisco Craton (Alkmim et al., 2006). The SE belt is comprised mainly by the clastic metasediments of the Statherian-Stenian, Espinhaço Supergroup deposited between 1,800 and 1,000 Ma (Chemale et al., 2012; Martins-Neto, 2000; Pflug, 1968; Schöll and Fogaça, 1979), the Neoproterozoic Macaúbas Group (Alkmim et al., 2007; Almeida-Abreu and Renger, 2002), the Orosirian-Statherian Serra da Serpentina and Serra de São José Groups BIF-bearing units (Rolim et al., 2016).

The SHRIMP detrital zircon data from clastic sediments delivered a maximum deposition age of $1,990 \pm 16$ Ma for the Serra da Serpentina Group that were correlated with the Barão de Guaicuí Group ($2,019 \pm 16$ Ma) of the Paraúnas Supergroup (Machado et al., 1989; Rolim et al., 2016). The Serra de São José Group and enclosed Canjica iron formation (Rolim et al., 2016) is separated from the Serra da Serpentina Group by an erosional unconformity. This unit was deposited at the beginning of the Statherian periods with a maximum depositional age of $1,666 \pm 32$ Ma (Rolim et al., 2016) during the early stages of development of the Espinhaço basin.

3.3.3. The Rio das Velhas Greenstone belt

Located at south and southeast of the Guanhães Block occur several tectonic slices of undefined metavolcanic sedimentary sequences that are correlated to the Neoarchean Rio das Velhas greenstone belt (Oliveira and Leite, 2000; Pinto and Silva, 2014; Silva, 2000). The Rio das Velhas Supergroup has its largest expression in the Quadrilátero Ferrífero Mineral Province where underlies the Paleoproterozoic units of the Minas Supergroup (QF – Figure 3.1), and hosts world-class gold deposits (Lobato et al., 2001). Noce et al. (2005) determined the age of graywacke samples related to the eruptive event at $2,792 \pm 11$, $2,773 \pm 7$ and $2,751 \pm 9$ Ma.

3.3.4. Magmatic units

The Brasiliano Orogeny at the eastern edge of the São Francisco Craton generated orogenic igneous rocks from c. 630 Ma to c. 480 Ma (Suites G1, G2, G3, G4, and G5 - (Pedrosa Soares et al., 2011). The Eastern Brazilian Pegmatite Province, one of the most important pegmatitic region worldwide, is correlated to the post-deformational stage of this igneous activity.

Pegmatitic bodies are found intruded in the Borrachudos Suite, Guanhães and Mantiqueira Complexes and the supracrustal rocks, some of them with economic interest due to the presence of beryls that are exploited as gems (aquamarine and emerald variety) and as Be ore (Marciano, 1995; Preinfalk et al., 2002). Isotopic data indicate that the crystallization age of these pegmatites is mainly related to the Brasiliano Orogeny, with age around 480 Ma (Marciano, 1995; Preinfalk et al., 2002).

The mineralization episode of pegmatites described in Santa Maria de Itabira (or Nova Era-Itabira-Ferros) district, which have significant deposits of emerald, alexandrite, and aquamarine (Figure 3.1), is late Neoproterozoic to Cambrian in age (hydrothermal system and anatetic pegmatite), but there is no evidence of intrusive granites directly associated with these deposits, according to Pedrosa-Soares et al. (2011) and references therein.

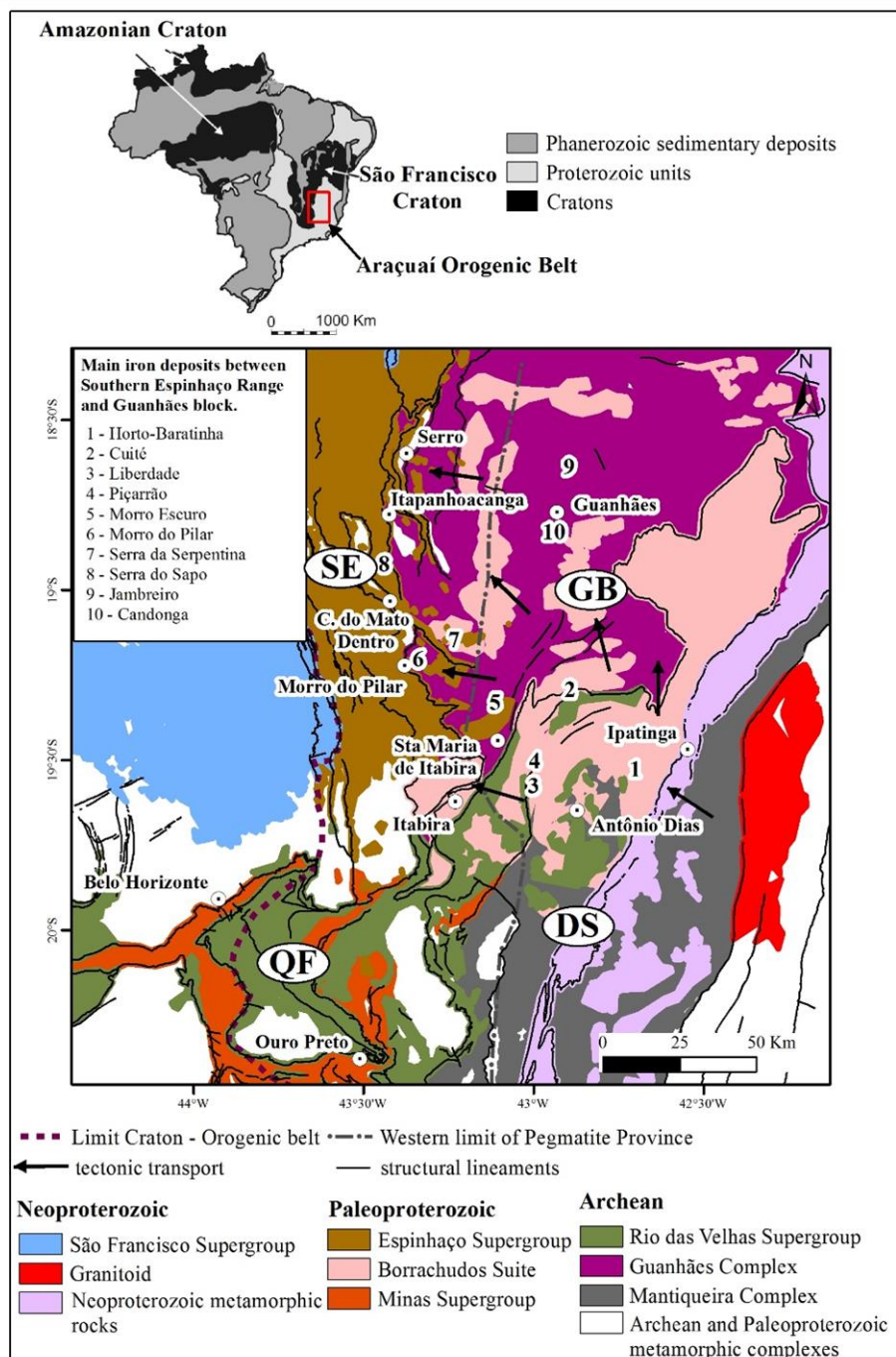


Figure 3.1: Regional map showing the location of the main iron deposits between Southern Espinhaço Range and Guanhães Block, at southeast border of São Francisco Craton, and the distribution of the main geological units. The distribution of the geological units is based on Pinto and Silva (2014). Abbreviations: SE - Serra do Espinhaço fold-thrust belt Block GB- Guanhães Block, DS – Dom Silvério shear zone, QF – Quadrilátero Ferrífero Mineral Province.

3.4. Methodology

3.4.1. Fieldwork and petrographic studies

The fieldwork activities in the studied area included surface geological mapping with detailed work conducted along the pits and around it, description of 223 waypoints, access to the lithological description of 72 diamond drill cores (total = 5,672 m), and collection of 60 samples for the preparation of thin and polished sections.

3.4.2. Geothermometry

The chemical composition of biotite and garnet were obtained using the SEM JEOL8530F EPMA electronic microprobe, at 15 kV accelerating voltage and 20 nA current, at the Centre for Microscopy, Characterization and Analysis (CMCA), University of Western Australia (UWA), Perth, Australia. The minerals were analyzed with WDS (Wavelength-Dispersive Spectrometers) for SiO₂, Al₂O₃, FeO, MgO, MnO, CaO, Na₂O, K₂O and TiO₂, Cr₂O₃. Back-scattered images (BSE) were obtained.

The software TWQ 2.02 (Berman, 1991) was used for geothermometric calculations of maximum temperature (T) with the purpose of establishing the metamorphic conditions using the (Holland and Powell, 1990) equations.

3.4.3. Calculation of structural parameters

The following parameters from the regional foliation (S_1) data of each domain were calculated: eigenvectors (v_1, v_2, v_3); eigenvalues (s_1, s_2, s_3); the shape parameter K ($K = (\ln(s_1/s_2)) / (\ln(s_2/s_3))$), which gives the gradient of straight lines radiating from the origin; and the strength parameter C ($C = \ln(s_1/s_3)$), which measures the strength of the preferred orientation. The two-axis ratio plot $\ln(s_2/s_3)$ versus $\ln(s_1/s_2)$ proposed by Woodcock (1977), which conforms to the convention established by Flinn (1962) for strain ellipsoids and is analogous to the proposed modification of Ramsay (1967), was used to establish the girdle and cluster tendencies of the S_1 data (Figure 3.10). As explained by Woodcock (1977) axially symmetric clusters plot where $s_2=s_3$ (along the line $\ln(s_2/s_3) = 0$); axially symmetric great-circle girdles plot where $s_1=s_2$ (along the line $\ln(s_1/s_2) = 0$); and the rest of the graph is occupied by distributions that have both cluster and girdle tendencies. These distributions can be quantified by the parameter K , where distributions with equal girdle and cluster tendencies plot on the line where $K = 1$ ($s_1/s_2 = s_2/s_3$), girdles plot below this line ($0 \leq K < 1$), and clusters plot above ($1 < K \leq \infty$), (Woodcock, 1977). The parameter C measures the strength of the preferred orientation and is represented in the plot as lines (Figure 3.10).

For clustering distributed data was calculated the S_1 mean and for girdle distribution were calculated the great-circle attitude and its axis. All the calculations and stereograms were done using the OpenStereo 0.1.2 ©2009-2011 software (Grohmann and Campanha, 2010).

3.4.4. Geochronology

Zircon grains from schist, granite and gneiss samples were analyzed U-Pb SHRIMP method (Sensitive High-Resolution Ion Microprobe) at Curtin University in Perth, Australia. The samples were processed with conventional crushing, grinding and screening methods at the LOPAG-DEGEO laboratory at Universidade Federal de Ouro Preto (UFOP), Brazil and at the Instituto de Geociências of Universidade Estadual Paulista (UNESP), at Rio Claro, Brazil. After the screening, the heavy fraction concentration of 60-250 mesh was realized by panning. After the concentration, the samples were sieved and washed to remove any very fine material (of clay and silt size). The 60-250 mesh fraction was treated with heavy liquid (LST, lithium heteropolytungstate) to remove light minerals and with Frantz LB1 magnetic separator to concentrate the less magnetic minerals such as non-metamict zircon. Zircon was handpicked and organized in an epoxy mount, which was polished and carbon-coated for SEM (Scanning Electron Microscope) study using BSE that were taken using a TESCAN VEGA3 at the CMCA-UWA. Imaging of the zircon with BSE is critical for identifying internal features, such as the core and rims, and to avoid areas with high common lead content (inclusions, fractures, and metamict areas). Analyzing the BSE images was possible to conclude that the SHRIMP method is the most indicated for the samples of the study area, because they are very fractured, metasomatized and metamict, due to this, the LA-ICP-MS spots ($\sim 40 \mu\text{m}$) could generate mixed and discordant ages.

Epoxy mounts were coated with gold for SHRIMP analyses. Most SHRIMP analytical spots were in the diameter range of 20-30 μm but the analyses of recrystallized zones used a spot size of only 10 μm . Six scans were used for each spot analysis of magmatic zircons and five for detrital zircons. The following masses were analyzed for zircon: $^{196}\text{Zr}_2\text{O}$, ^{204}Pb , background, ^{206}Pb , ^{207}Pb , ^{208}Pb , ^{238}U , ^{248}ThO , ^{254}UO . The calibration was conducted using the zircon standard M257 (561.3 Ma). All data on with common lead correction greater than 1% were rejected during the first scan. The uncertainties of individual ages are quoted at the 1σ level, whereas the ages plotted are calculated at 2σ levels (about 95% confidence). SHRIMP data were reduced using SQUID software (Ludwig, 2001) and plots were prepared using ISOPLOT/Ex (Ludwig, 2003).

3.5. Lithostratigraphic characterization of Horto-Baratinha deposit

3.5.1. Metamorphic Complex

Orthogneiss (TTG-type) that crops out in the surroundings of the HBD area is correlated with the Mantiqueira Complex (Silva, 2000) and interpreted as part of the basement of metasedimentary

sequence (Figure 3.2). These rocks exhibit a medium grain size (0.01 – 3 mm), with granoblastic to granolepidoblastic fabric. The main minerals are quartz, plagioclase, microcline, biotite and hornblende, all oriented parallel to the foliation, especially the last two. The accessories are allanite, zircon, titanite, apatite, monazite and opaque minerals. Quartz and feldspar present lobate shapes of grain boundaries. The main lithotype is the biotite gneiss.

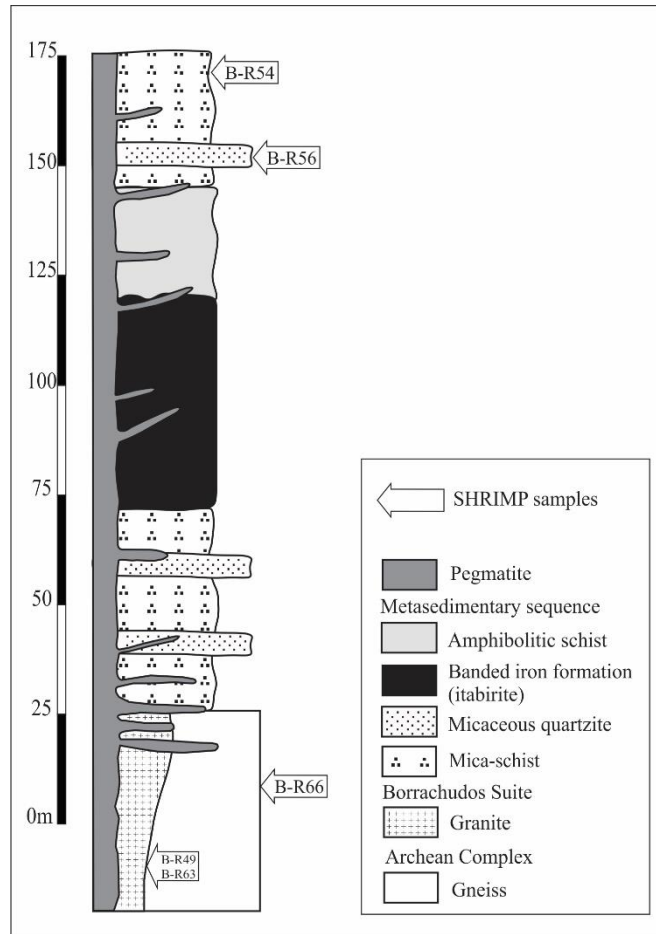


Figure 3.2: Simplified lithostratigraphic column of HBD.

3.5.2. *The Borrachudos Suite*

The granite from Borrachudos Suite (Açucena Pluton, Figures 3.2 and 3.3) is present around the metasedimentary unities, exhibit a fine to medium grain size (0.1 – 2 mm), with granoblastic to granolepidoblastic fabric. The main minerals are quartz, microcline, plagioclase, biotite, muscovite, hornblende and opaque minerals (magnetite and hematite). The accessories are apatite, titanite, and zircon.

The granite commonly exhibits myrmekitic texture (intergrowth of quartz in plagioclase and microcline) and a penetrative foliation defined mainly by biotite and usually parallel to the supracrustal transposition foliation (S_1).

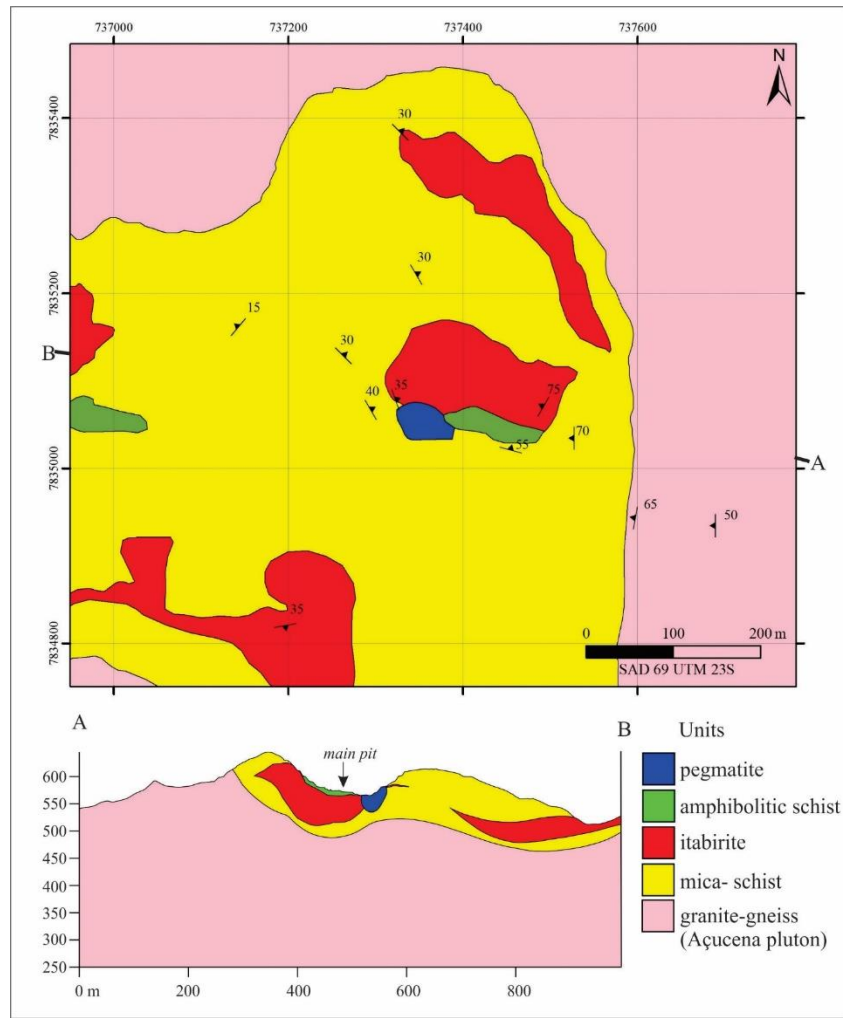


Figure 3.3: Geological map and section of HBD.

3.5.3. Metasedimentary sequence

3.5.3.1. Mica-schist

A wide mineralogical variety of aluminous micaceous schists with quartzite layers comprises the top and bottom of the sequence in HBD (Figure 3.2, 3.3 and 3.4): muscovite-quartz schist, quartz-biotite garnet schist, quartz-biotite-muscovite schist, biotite-sillimanite schist. The main minerals are quartz, muscovite, biotite, sillimanite, garnet, tourmaline, kyanite, zoisite, cordierite, opaque minerals (mainly magnetite and hematite). The accessory minerals are chlorite, zircon, monazite, apatite, carbonate, zoisite, and titanite. There is also feldspar as main mineral close to the contact with pegmatite. The biotite has pleochroism from yellow-brown to yellow-green. The yellow-brown biotite is Mg-rich.



Figure 3.4: An overview of the Horto-Baratinha main pit, with the location of the units identified: XIS (mica-schist unit), XIF (amphibolitic schist unit), ITA (itabirite and iron ore), PEG (pegmatite). The dotted lines represent the contacts.

3.5.3.2. Amphibolitic schist

Above the itabirite and under the top-micaceous schist there is a scattered occurrence of para-amphibolitic schist, which grades towards ferruginous near the contact with the underlying BIF (Figure 3.2, 3.3 and 3.4). The essential minerals are hornblende, tremolite-actinolite, quartz, pyrophyllite, talc, cordierite and opaque minerals (lamellar and granular hematite, magnetite). The accessory minerals are titanite, ilmenite, and apatite. The lamellar hematite occurs oriented parallel to the rock foliation, and as inclusion in amphibole, which sometimes has a porphyroblastic texture.

3.5.3.2. Itabirite

The itabirite occurs between upper and lower schists (Figure 3.2, 3.3, 3.4 and 3.5A) it is composed mainly by quartz, lamellar and granular hematite. Chlorite and tremolite-actinolite occur as accessories minerals. The rock has a millimetric bedding that is parallel to the foliation, defined by the alternation of millimetric bands quartz-rich and iron oxides-rich. Locally it is observed idioblastic (keno)magnetite over the foliation/bedding. The itabirite is mineralogically homogenous, as that observed by Silveira Braga et al. (2015) at Morro Escuro, Rolim et al. (2016) at Espinhaço Range and Barrote et al. (2017) at Guanhães (Figure 3.1). This homogenous aspect is quite different from that described at QF, where the itabirites present a wider variety of compositional facies (Rosière et al., 2008; Rosière and Chemale, 2000).

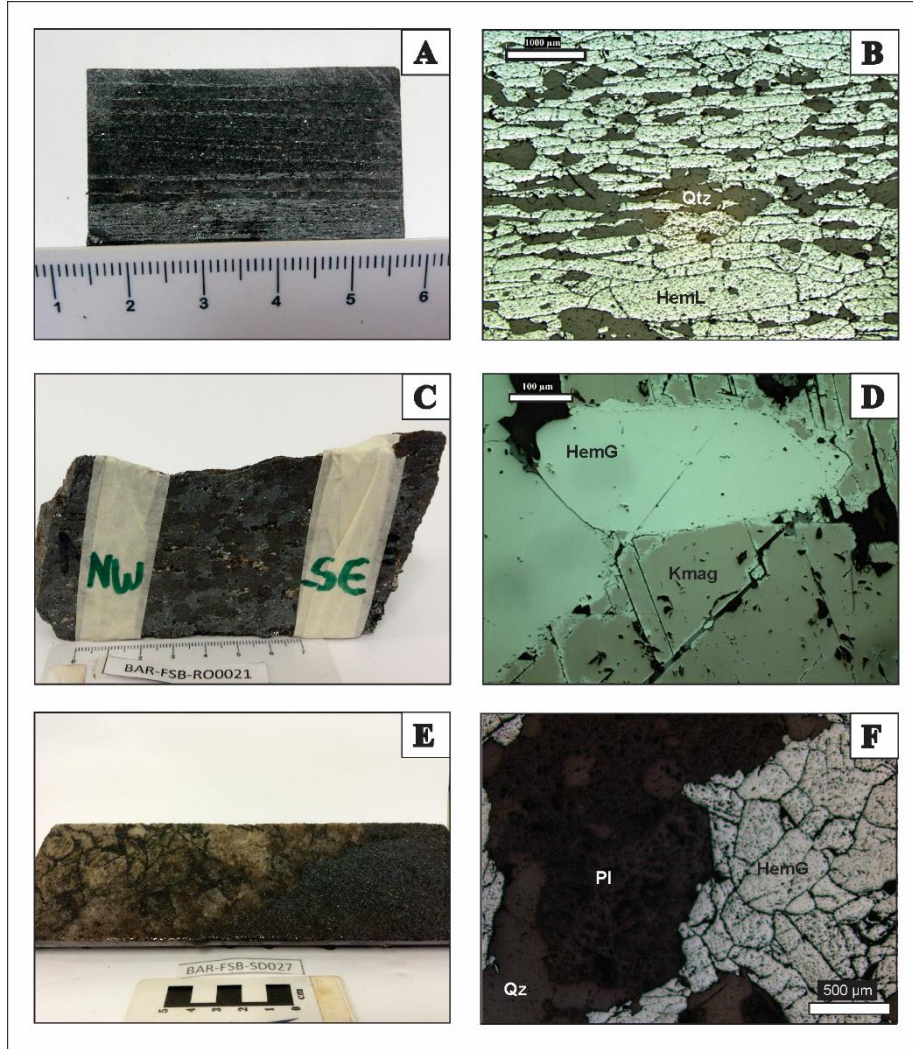


Figure 3.5: Photographs (A, C and E) and photomicrographs (B, D, and F – uncrossed polarized reflected light) showing different Fe-oxides from itabirite, iron ore and pegmatite. (A and B) Itabirite with lamellar hematite and quartz. (C and D) Iron ore sample with coarse-grained (keno)magnetite partially oxidized to granular hematite. (E and F) Pegmatite with granular hematite, quartz, and saussuritized plagioclase. Abbreviations: HemL – lamellar hematite, HemG – granular hematite, Kmag – (keno)magnetite, Qz – quartz, Pl – plagioclase.

3.6. Pegmatite

Metric to decametric pegmatite dikes and sills bodies (few centimeters to 30 m thick) crosscut the granites and metasediments (Figure 3.4). They are coarse-grained (>5mm), undeformed, and composed mainly by quartz, microcline, plagioclase, biotite, and muscovite. Decimetric to metric magnetitic iron ore enclaves are present inside the metric pegmatite bodies.

3.7. High-grade iron ore bodies

High-grade iron ore bodies (>60% wt. Fe) are hosted in the itabirite unit and is fine to coarse-grained (0.01 mm – 3.0 mm). These bodies are metric to decametric and composed mainly by granular hematite and magnetite, with lamellar hematite, ilmenite, quartz, carbonate (calcite and dolomite), chlorite, cummingtonite-grunerite, tremolite-actinolite, biotite, talc, apatite and muscovite as

accessories (Figure 3.5C-D). The granular hematite presents mosaic granoblastic fabric and twinning lamellae. The magnetite occurs as medium to coarse crystals, hypidiomorphic, with diffuse contacts due to the oxidation process to hematite along the border and octahedral cleavage planes (Figure 3.5C-D). The talc and amphibole commonly occurs in the ore as fibro-radial aggregates, however, some crystals are oriented.

3.8. Structural analysis

3.8.1. Structural elements

The ductile deformation in HBD is characterized by a main regional foliation (S_1), which is defined in the deformed granite by the orientation of phyllosilicates, quartz, and feldspar; in the itabirite and some portion of iron ore by lamellar hematite and quartz orientation and, in other supracrustal rocks by the orientation of phyllosilicates, sillimanite and quartz. Tight to isoclinal intrafolial folds are present in itabirite and schists, in which the S_1 planes are parallel to the axial plane (Figure 3.6). The compositional banding of the orthogneiss is parallel to the foliation (S_1) and it is the result of the original bedding transposition by polycyclic orogenic events (Transamazonian / Rhyacian Orogeny and Brasiliano Orogeny – Neoproterozoic). The tectonic reworking during the Brasiliano collage generated mylonitic fabric in the gneiss, especially near the contact with Borrachudos granite (Oliveira and Leite, 2000).

The open to tight folds of the mica-schist unit are centimeter- to meter-scale (Figure 3.7). They display varying axis orientation, distributed along the 035/10 best-fit girdle, with two main directions N-S and WNW-ESE (Figure 3.8A). The majority of them has low dip angle. Crenulation lineation (L_c) is rarely associated with a cleavage and it is statistically between the punctual and great circle distribution, with 355/20 average value (Figure 3.8B). Mineral lineation (L_m) defined by elongated phyllosilicates and tremolite-actinolite needles has N-S direction and low dip angles, similar to the fold axis orientation (Figure 3.8C). Where S_1 is centimetric to metric folded, it is possible to observe that the L_m is positioned parallel to the fold axis. The presence of spaced cleavage is rare. The L_m is distributed in the 283/36 best-fit girdle, indicating that L_m is folded. Axial planes (P_A) measurements are distributed in the 140/55 best-fit great circle, with 320/35 pole (Figure 3.8D). Therefore, there is an axial fold dispersion and variation of the axial surfaces and lineations, which indicates a refolding process.

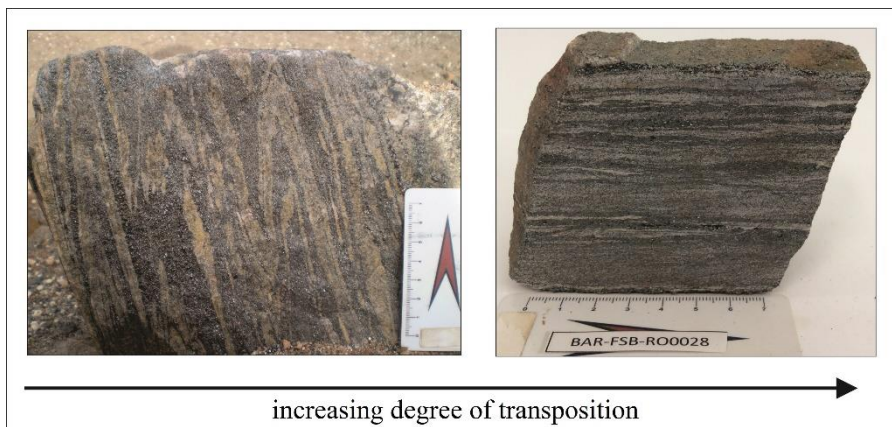


Figure 3.6: Variation in bands thickness of the itabirite from left to right indicating the transposition and obliteration of the itabirite layering to a homogeneous foliation that is parallel to the isoclinal intrafolial folds.

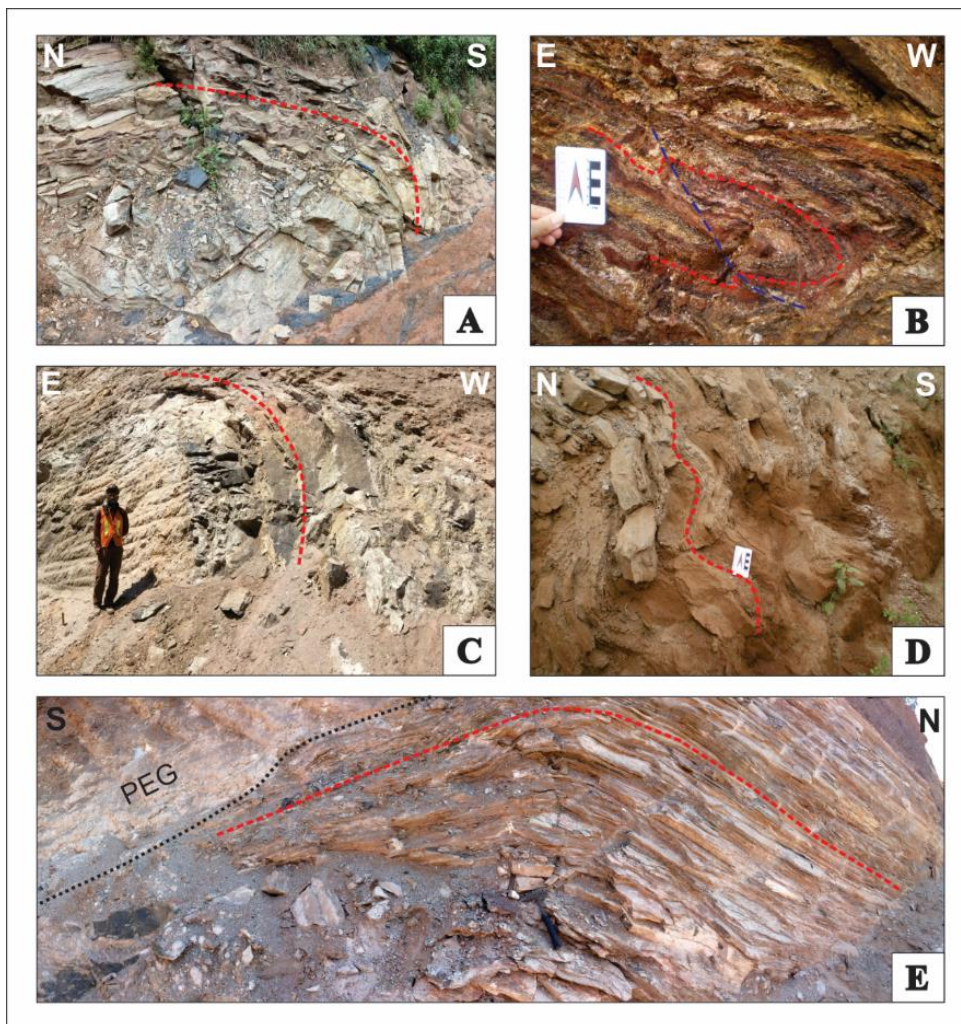


Figure 3.7: Out-crops of macro-folds in the mica-schist unit of HBD. (A) Folded quartzite, axis 335/20, axial plane 60/45 (UTM 737169 / 78352334 / 531). (B) Tight folded schist saprolite, axis 205/10, axial plane 280/20 (UTM 737051 / 7835045 / 572). (C) Close folded quartzite, axis 110/65, axial plane 25/30. (D) Open folded layers of quartzite and mica-schist (UTM 737348 / 7835188 / 541). (E) Open folded mica-schist with pegmatite intrusion, axis 90/15, axial plane 175/80 (UTM 737310 / 7835046 / 600).

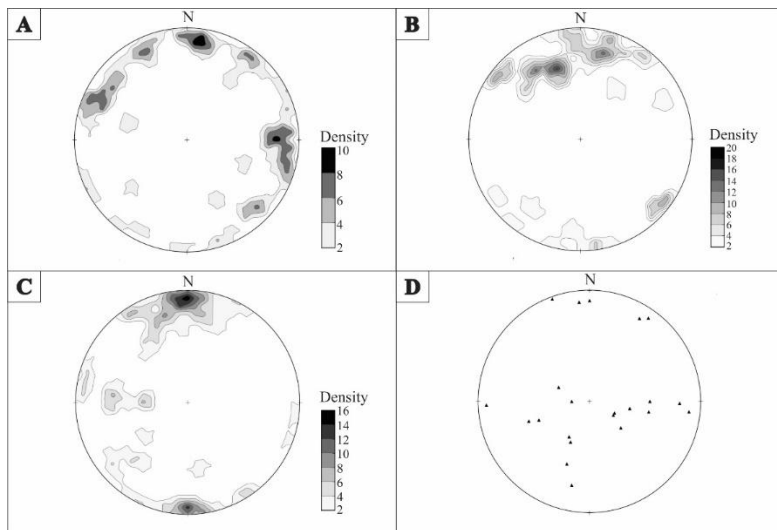


Figure 3.8: Stereograms of the following structures: (A) fold axis ($n=43$), (B) crenulation lineation ($n=30$), (C) mineral lineation ($n=44$), (D) Poles to axial plane ($n=22$). The stereograms were plotted in equal area, lower hemisphere. The contour stereograms (A, B, C) were plotted using counting method (small circle count - 1% area).

3.8.2. Structural domains

To better understand the S_1 dispersion data and delimit regions with cylindrical S_1 distribution, the study area was divided into domains and 366 S_1 measurements were used (Figure 3.9 and Table 3.1).

The structural measurements highest density is in HBD main pit, due to the quality and abundant rock exposure, so this region has smaller and greater amount of areas than the rest of studied area (Figure 3.9). The entire area of HBD was divided into squares of 80 m side. As some of these areas presented less than four S_1 measurements, some squares were grouped to avoid areas with insufficient data to determine the necessary structural parameters. The measurements lack of some regions is due to the deficiency of out-crops measurable. The grouping resulted in twenty-one areas identified by letters A to U (Figure 3.9B). Structural measurements around HBD were divided into two groups, one to the north (RegN) and the other to the south (RegS), (Figure 3.9A). Some of the S_1 groups were subdivided to regroup S_1 data with evident cluster or best-fit girdle distribution (areas F, K, and N).

Using S_1 data of each area were calculated the following parameters: eigenvectors; eigenvalues; the shape parameter K and the strength parameter C (Table 3.1, Figure 3.10). The eigenvectors-three shows two main directions, NNW-SSE (more prominent), WNW-ESE (Figure 3.11). These two directions are similar to the axial directions measured in out-crop scale folds; therefore, they represent the fold axis of the various deformation phases. It is understood that N-S fold axis direction was the main and, thus the superposed folding was controlled by the shape of this first folding phase.

Area	n	Expected distribution	Mean plane	Axis	K	C
A	11	Girdle	-	137/00	0.88	5.75
B	12	Girdle	-	358/07	0.41	3.62
C	7	Cluster	67/22	-	2.09	5.45
D	5	Girdle	-	54/45	0.59	6.01
E	9	Cluster	322/12	-	2.47	4.85
F1	17	Cluster or Girdle		-	1.08	3.52
F2	9	Cluster	78/23	-	3.88	5.15
G	10	Girdle	-	234/44	0.62	3.14
H	4	Girdle	-	353/27	0.42	7.97
I	19	Cluster	334/18	-	1.83	4.59
J	39	Cluster	69/26	-	2.36	3.23
K1	8	Girdle	-	262/53	0.3	5.18
K2	6	Cluster	249/32	-	1.65	4.77
L	11	Cluster	24/24	-	2.52	3.97
M	7	Cluster	46/30	-	1.2	4.75
N1	8	Girdle	-	65/57	0.74	5.62
N2	7	Girdle	-	84/16	0.71	5.86
N3	11	Girdle	-	351/11	0.49	4.81
O	16	Girdle	-	273/11	0.42	3.89
P	12	Girdle	-	354/13	0.38	3.92
Q	5	Girdle	-	024/12	0.5	4.96
R	10	Girdle	-	221/05	0.82	2.92
S	5	Cluster	002/21	-	1.19	4.13
T	4	Girdle	-	90/14	0.23	4.89
U	3	There are too few points in file	-	-	-	-
RegN	35	Cluster	48/13	-	1.89	3.09
RegS	36	Cluster	68/18	-	3.46	2.82

Table 3.1: Structural parameters of each area.

3.8.3. Microstructural aspects

The Borrachudos granite is strongly foliated and shows evidence of deformation, such as stretched feldspar crystals and recrystallized quartz. It is also observed undulatory extinction and subgrains of quartz, which represents a diffusive mass transfer microstructure of the intracrystalline plastic deformation. Monomineralic coronas, also known as moats, are found in some plagioclase crystals. This texture represents a reaction rim and may be formed by an igneous zoning process, or it could be a result of metamorphic reactions that redistributed the plagioclase in response to local volume changes during metamorphism.

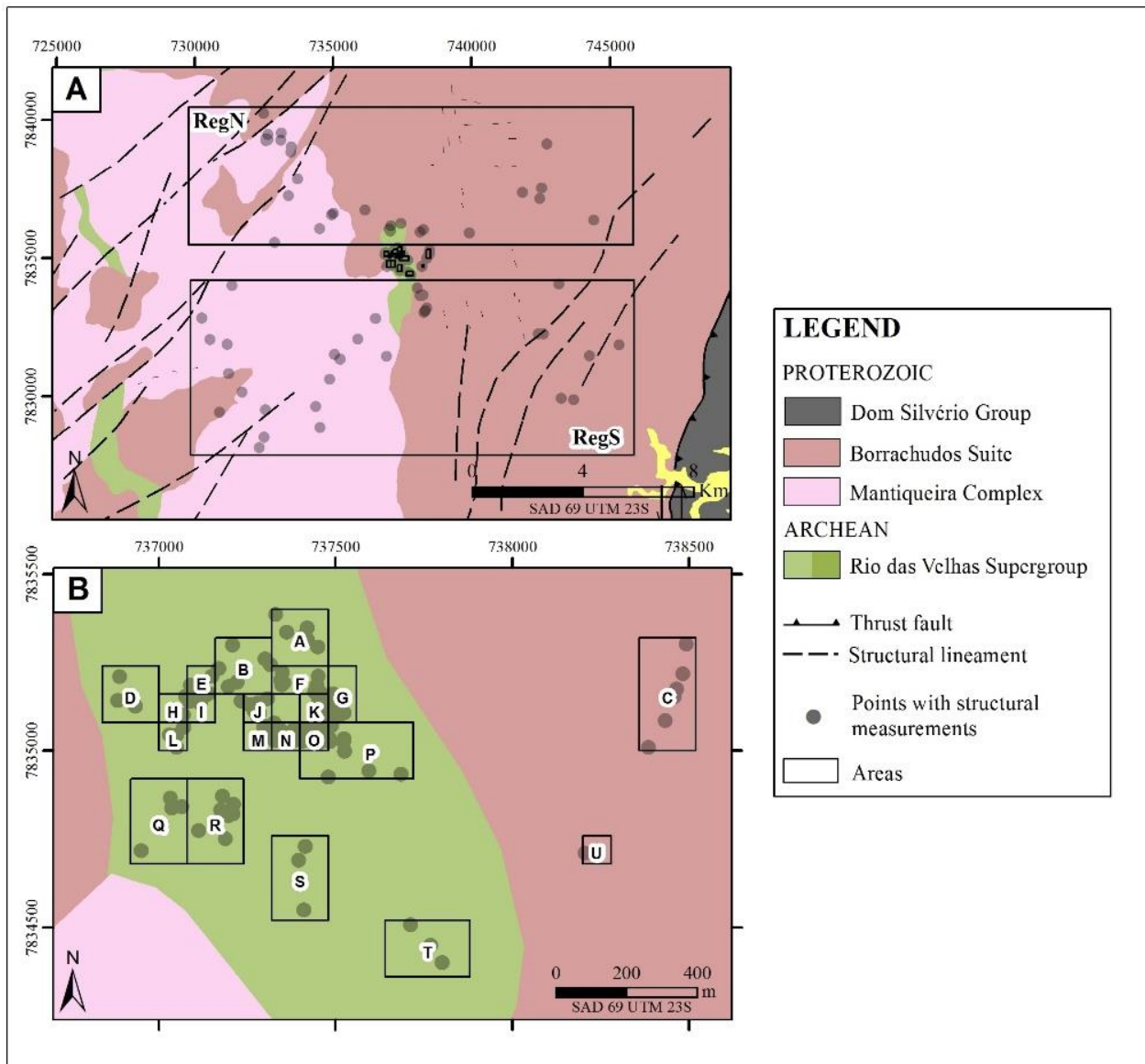


Figure 3.9: Maps with the location of the twenty-three areas used to the cylindricity analysis of S_1 data. (A) Regional overview of the studied area, where is possible to see the limit of two areas (RegN and RegS). (B) Detail of the in HDB mine area showing the twenty-one areas identified by letters, A to U. The distribution of the geological units is based on Pinto and Silva (2014).

The garnet and kyanite from the mica-schists present porphyroblastic texture. The garnet inclusions trails (Si) are continuous with the fabric external to the porphyroblast (Se), but Si and Se have different shape and orientation, which indicates a syntectonic porphyroblast growth (Figure 3.12A). The porphyroblast growth occurred during prograde condition, as indicated by the coarsening of Si towards the margin of the crystal, and the growth chemical zoning, characterized by a pyrope concentration in the rim, grossular, and spessartine concentration in the core, which indicates progressive nucleation. There are syn-tectonic sillimanite aggregates type δ , verging to the south (Figure 3.13C).

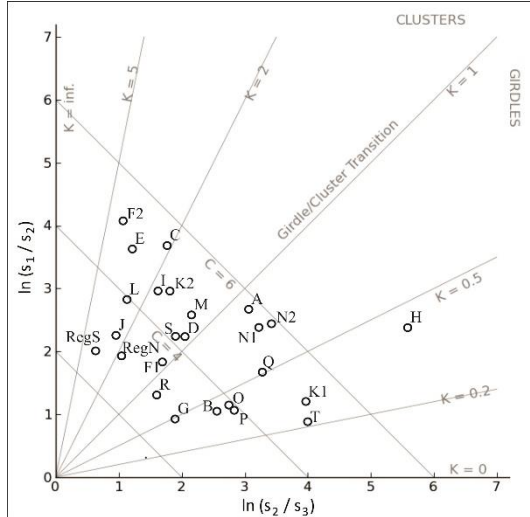


Figure 3.10: Two-axis logarithmic plot of the ratios of normalized eigenvalues (s_1 , s_2 e s_3).

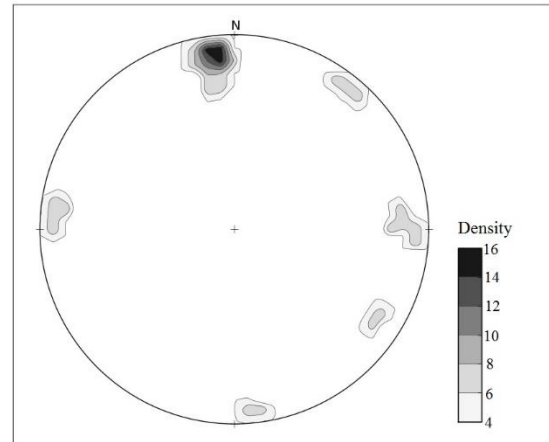


Figure 3.11: Contour stereogram of the eigenvector 3. The stereogram was plotted using the equal-area projection, lower hemisphere, with counting method (small circle count - 1% area).

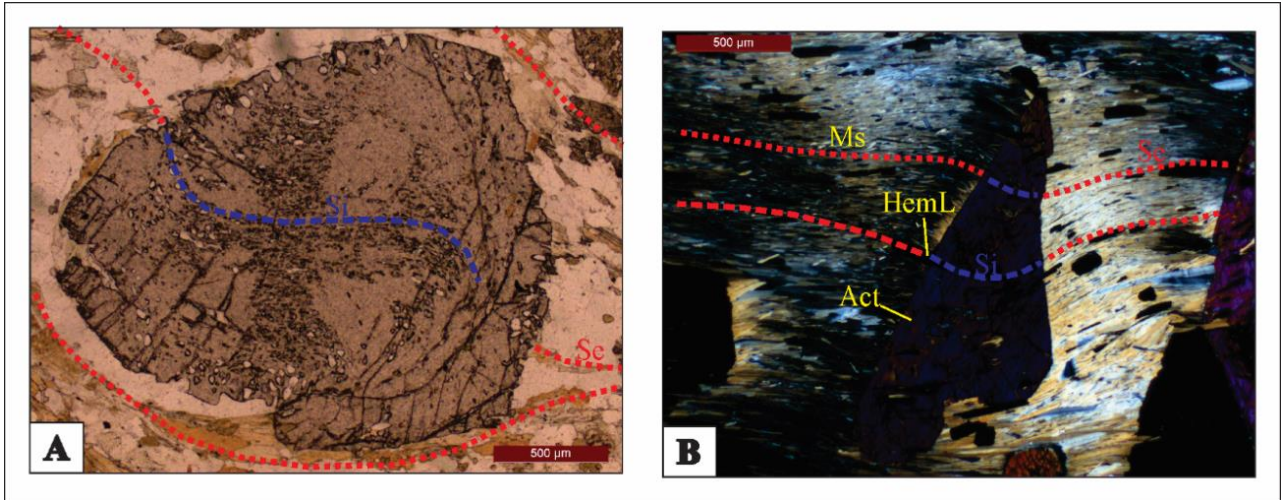


Figure 3.12: Photomicrographs of porphyroblastic minerals. (A) Garnet with inclusions trails (Si) continuous with the fabric external to the porphyroblast (Se), however, with different shape and orientation. (B) Actinolite with inclusions trails (Si), composed mainly by lamellar hematite, continuous with the fabric external to the porphyroblast (Se), and both have similar shapes and orientations.

Quartz in the mica-schist often presents undulatory extinction and subgrains, and rarely chessboard pattern, which consists of approximately square subgrains. Quartz ribbons are also common displaying flat grain boundaries approximately perpendicular to the mica flakes. Quartz mica rocks at higher metamorphic grades commonly have this distinctive microstructure (Blenkinsop, 2002). Another intracrystalline deformation evidence is the presence of kink bands in biotite (Figure 3.13B).

The foliation of mica-schists was folded in micro scale, open to tight. The fabric is lepidoblastic and granoblastic, with the development of a continuous schistosity, commonly wave to anastomosed and locally crenulated. The rare S-C structures developed in micro shear zones and

indicate a dextral movement to the south (Figure 3.13A). Sigmoidal quartz, granitic, and deformed sillimanite porphyroblasts in the mica-schist unit indicate a dextral S-verging movement.

The amphibolitic schist has actinolite crystals with internal trails (Si), composed mainly by lamellar hematite, which are continuous with the external porphyroblast fabric (Se). The Si is continuous with Se and both have similar shape and orientation, which indicates a post-tectonic growth (Figure 3.12B). However in some samples is possible to recognize that the tremolite-actinolite crystals are parallel to the foliation (S_1), indicating syn-tectonic formation. Lamellar hematite in amphibolitic schist occurs parallel to the foliation, magnetite has fine ilmenite inclusions and occurs as coarse crystals parallel and over the foliation. Granular hematite came from the magnetite oxidation and it is over S_1 , so it is considered a post-tectonic mineral.

Quartz present in the itabirite has commonly polygonal contacts and undulatory extinction and, locally it presents flat grain boundaries parallel to the lamellar hematite basal plane. As the lamellar hematite has a strong preferred orientation, the impeding effect on the quartz boundary growth could be created a grain shape fabric in quartz, which has grown parallel to the fabric shape (Blenkinsop, 2002). The granular hematite occurs predominantly parallel to the foliation. Tiny relics of (keno)magnetite and martite are recognizable in granular hematite. The sedimentary/diagenetic bedding of the itabirite is totally transposed by axial planar schistosity (S_1), with the development of structural layering defined by the alternation of millimetric bands of quartz and iron oxides (hematite and magnetite - Figure 3.6). Centimetric to millimetric intrafolial folds are ubiquitous.

3.9. Metamorphism

The mineral assemblages of the different HBD lithostratigraphic units consistently constrain the regional metamorphic grade to the amphibolite facies (Table 3.2). The association that defines the foliation of the pelitic schists, indicates conditions of the sillimanite and, more rarely, the kyanite zone (Yardley, 2004).

Geothermometric calculations were based on microanalysis of the core and rim of synkinematic garnet and biotite (from the matrix) selected from one sample from the mica-schist unit (Table 3.3 and 3.4). The garnet composition is predominantly almandine (molar fraction 62.54-72.32), however, there are broadly concentric zoning between the pyrope (16.62-34.20), grossular (1.81-11.42) and spessartine (0.64-7.91) components, with a pyrope concentration in the rim, grossular, and spessartine concentration in the core. The biotite composition is predominantly phlogopite (62.06-72.78) and secondary annite (20.29-26.48) and siderophyllite (7.23-13.03).

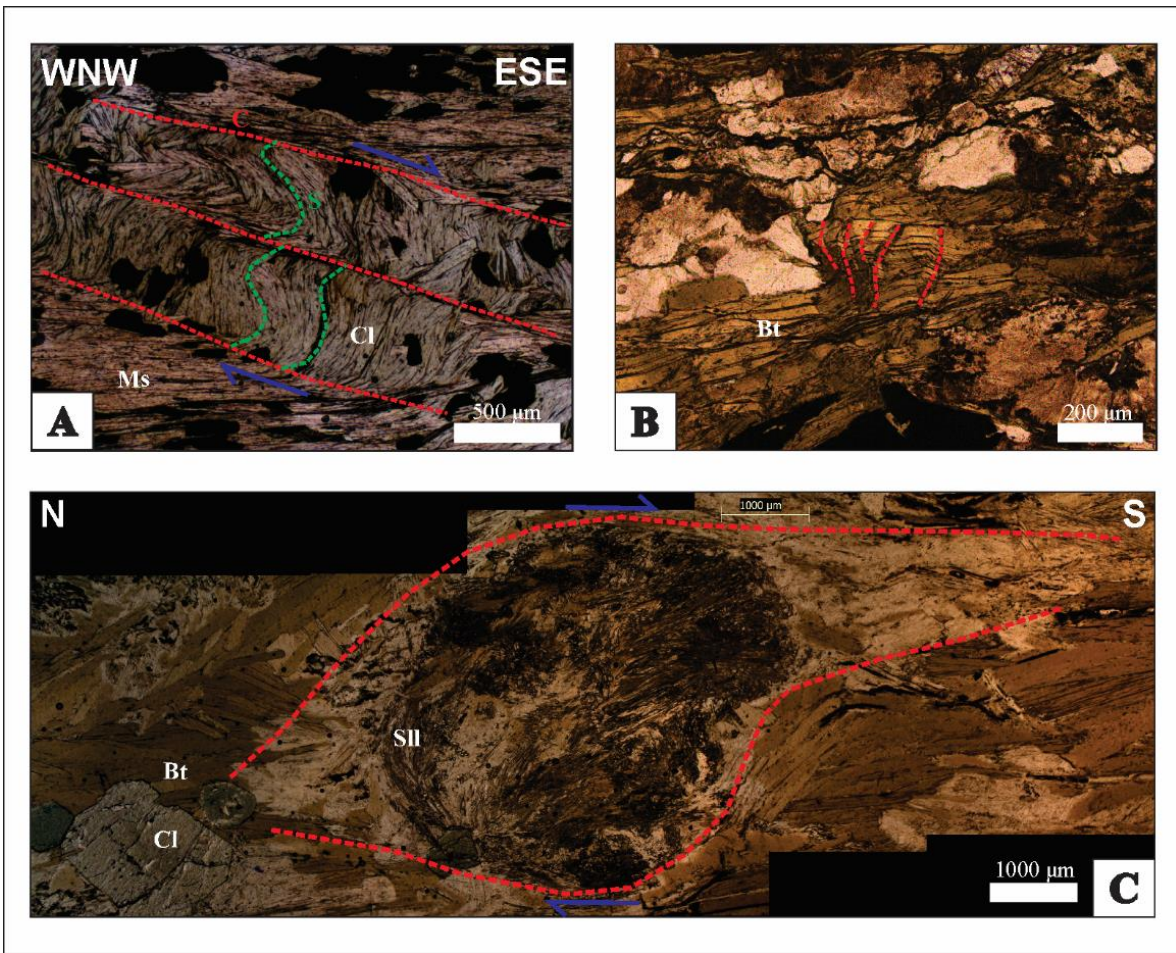


Figure 3.13: Microstructures in the mica-schist unit. Photomicrographs were taken under the uncrossed polarized transmitted light. (A) S-C structure indicating movement to the south. (B) Kink bands in biotite. (C) Sillimanite aggregates type δ , verging to the south. Abbreviations: Ms – muscovite, Cl – chlorite, Bt – biotite, SII – sillimanite.

One independent reaction was obtained from the quartz-biotite-garnet schist, exhibiting a minimum temperature of 550 °C (± 50 °C) and a maximum temperature of 690 °C (± 50 °C), considering pressure around 6 kbar. These values indicate that the garnet growth with prograde conditions and the metasedimentary rocks experienced intermediate to high amphibolite facies conditions (Figure 3.14).

Unit	Paragenesis	Facies
Archean Complex and Borrachudos Suite	Qz + Pl + Mc + Bt + Hbl	Amphibolite
Micaceous schist	Qz + Ms + Bt + SII + Grt + Tur + Ky + Ept + Crd + HemL	Amphibolite
Amphibolitic schist	Hbl + Tr-Act + Qz + HemL	Amphibolite
Itabirite	Qz + HemL + Chl + Tr-Act	Greenschist to Amphibolite

Table 3.2: Synkinematic mineral assemblages and metamorphic facies of each lithostratigraphic unit from the HBD. Abbreviations: Qz - quartz, Pl - plagioclase, Ms - muscovite, Bt - biotite, Mc - microcline, Ept - epidote, Grt - garnet, Ky - kyanite, Hbl - hornblende, SII - sillimanite, Tur - Tourmaline, Crd - Cordierite, Chl - chlorite, Tr - tremolite, Act - actinolite, HemL - lamellar hematite.

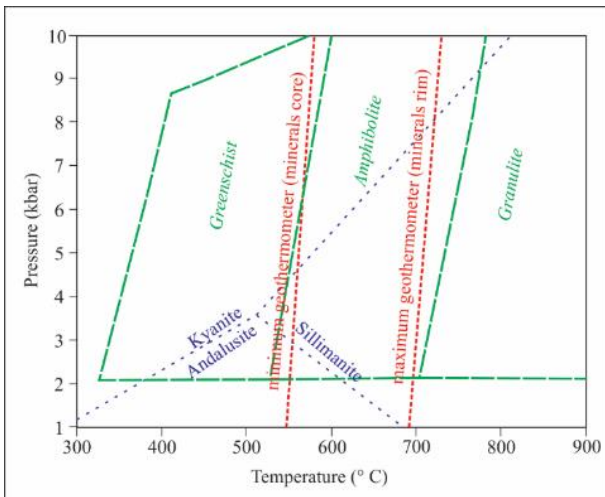


Figure 3.14: P-T Diagram prepared from the microanalysis of garnet and biotite from the quartz-biotite-garnet schist, using the TWQ 2.02 software. The two-geothermometry lines (red) correspond to the following metamorphic reaction: phlogopite + almandine = annite + pyrope.

Garnet		
wt%	rim	core
SiO₂	38.58	37.43
Al₂O₃	22.54	21.74
MgO	9.01	4.47
CaO	0.96	3.42
MnO	0.30	3.57
FeO	29.33	29.74
Total	100.72	100.36
Si	2.96	2.96
Al_{IV}	0.04	0.04
Al_{VI}	2.00	1.99
Fe⁺²	1.88	1.97
Mg	1.03	0.53
Mn	0.02	0.24
Ca	0.08	0.29
Py	34.2	17.4
Al	62.5	65.1
Sp	0.6	7.9
Gr	2.6	9.6

Table 3.3: Garnet chemical composition from the maximum (crystal rim) and minimum (crystal core) geothermometry lines obtained.

Biotite		
wt%	rim	core
SiO₂	37.60	37.15
TiO₂	1.43	1.48
Al₂O₃	18.09	17.59
FeO	11.52	11.76
MgO	16.48	16.22
MnO	bdl	bdl
Na₂O	0.01	0.02
K₂O	0.12	0.15
H₂O⁺	2.02	2.77
Total	96.92	96.83
Si	5.58	5.43
Al_{IV}	2.42	2.57
Al_{VI}	0.74	0.46
Ti	0.16	0.16
Fe⁺²	1.43	1.44
Mn	-	-
Mg	3.64	3.53
Na	0.03	0.04
K	1.83	1.81
H₂O	2.00	2.70
%H₂O	2.02	2.77

Table 3.4: Biotite chemical composition from the maximum (crystal rim) and minimum (crystal core) geothermometry lines obtained. Abbreviation: bdl – below detection limit.

3.10. The paragenetic sequence of the iron oxides generations

The lamellar hematite from itabirite, and also from schist units, is the oldest iron oxide generation, which was formed during the syn-deformational stage, parallel-oriented to the rock foliation (Figure 3.15). The (keno)magnetite from itabirite, iron ore, pegmatite, and schists are

positioned predominantly over the foliation and was formed during the tardi and post-deformational stages. The progressive martitization of (keno)magnetite to granular hematite occurred during the tardi and post-deformational stages (Figure 3.15). Coarse lamellar hematite crystals randomly oriented in the border of the pegmatitic bodies were formed during post-deformational stage probably due to contact reaction with the itabirite.

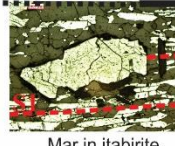
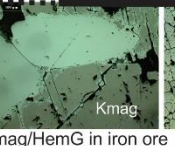
Iron oxides textures	Deformational stage		
	syn-deformacional	tardi-deformacional	post-deformacional
Lamellar hematite (HemL)	 Intra folial fold in itabirite	 HemL in itabirite	 Coarse HemL in pegmatite
(keno)Magnetite (Kmag)		 Kmag in itabirite	 Kmag in pegmatite
Martite (Mar)		 Mar in itabirite	 Kmag/Hem iron ore with Mar
Granular hematite (HemG)		 HemG in itabirite	 Kmag/HemG in iron ore

Figure 3.15: Paragenetic sequence of the different iron oxides generations and their chronological relation to the local tectonic setting. Photomicrographs were taken under uncrossed polarized reflected light.

3.11. Geochronology U-Pb SHRIMP

Detrital zircons from the upper mica-schist unit (Table 3.5) were analyzed to correlate the metasedimentary sequence from HBD with other BIF-bearing sequences from São Francisco Craton basement. The crystallization age of three igneous rock samples (Table 3.5) were determined by U-Pb zircon ages. The samples stratigraphic position is present in Figure 3.2.

Sample code	Rock	Number of spots analyzed
B-R54	Mica-quartz schist	21
B-R56	Micaceous quartzite	22
B-R49	Granite	8
B-R63	Granite	9
B-R66	Gneiss	10

Table 3.5: List of samples analyzed by SHRIMP.

The two mica-schist unit samples (B-R54 and B-R56) analyzed by SHRIMP have subrounded to rounded detrital zircons, indicating short transport distance from the source.

Sixteen crystals from sample B-R54 were analyzed (Figure 3.16). From the 15 detrital spots analyzed most of the population is Neoarchean (71% of the sample), but with significant Statherian source (14% of the sample –Figure 3.17A). The youngest age found was $1,671 \pm 20$ Ma, which points to a Late Paleoproterozoic (Statherian) maximum sedimentation age. There are also zircon grains Paleoarchean (7%) and Mesoarchean (7%). The crystals frequently have recrystallized zones, mainly in the rims, which are lighter in the BSE images and richer in Pb than the other areas (Figure 3.16A, B, C). Six spots were analyzed in these regions which presented very low Th/U ratio (0.0045-0.0196) and ages between 496.4 ± 5.7 Ma and 537.2 ± 6.0 Ma (Figure 3.18A).

Twenty zircon grains from sample B-R56 were analyzed (Figure 3.16 D, E, F). From the 16 detrital spots analyzed 50% are Neoarchean, 25% Mesoarchean, 19% Paleoarchean and 6% Statherian (one Statherian age of $1,729.4 \pm 12.8$ Ma - Figure 3.17D). Some zircon grains have also recrystallized rims (Figure 3.16E, F). Four spots of these regions were analyzed, resulting in ages from 517.8 ± 2.9 and 541.1 ± 17.1 Ma.

Two granite samples from Borrachudos Suite (Açucena Pluton) were analyzed by SHRIMP (B-R49 and B-R63 – see Figure 3.2). Seven zircon grains from sample B-R49 were analyzed (Figure 3.16G). They are prismatic and have very thin recrystallized rims, where one spot was analyzed. A regression through the analyzed spots define a Pb-loss Discordia with an upper intercept age of $1,745.6 \pm 9.4$ Ma (MSWD = 2.9), interpreted as the crystallization age. The lower intercept is Cambrian and defines the age of the recrystallization zone (491.7 ± 6.1 Ma – Figure 3.18B).

The zircons from the sample B-R63 are more metamict and fractured than those from sample B-R49 (Figure 3.16H). Seven crystals were analyzed, 6 spots done in zircon core and 3 in the recrystallized rim. A regression through these points define a Pb-loss Discordia with an upper intercept age of $1,740 \pm 10$ Ma (MSWD = 1.6), interpreted as crystallization age, and lower intercept at 495.3 ± 5.6 Ma (Figure 3.18C). The ages obtained in the crystals rims varies from 484 ± 3 Ma to 525 ± 5 Ma.

One gneiss sample (B-R66) from the crystalline basement, collected approximately 4.5 Km north-west of HBD was analyzed (Figure 3.16I). Eight zircon grains were analyzed. The sample B-R66, as the granite samples B-R63 and B-49, has prismatic zircons with very thin recrystallization rims in some crystals. Three of the ten spots analyzed are located in these rims and resulted in discordant ages that were discarded of interpretation (Appendix 1A). The other ages generated a Pb-loss Discordia with the upper intercept at $2,713.3 \pm 6.5$ Ma (MSWD = 5.4), interpreted as the crystallization age of the sample (Figure 3.18D), and lower intercept at 540 ± 20 Ma.

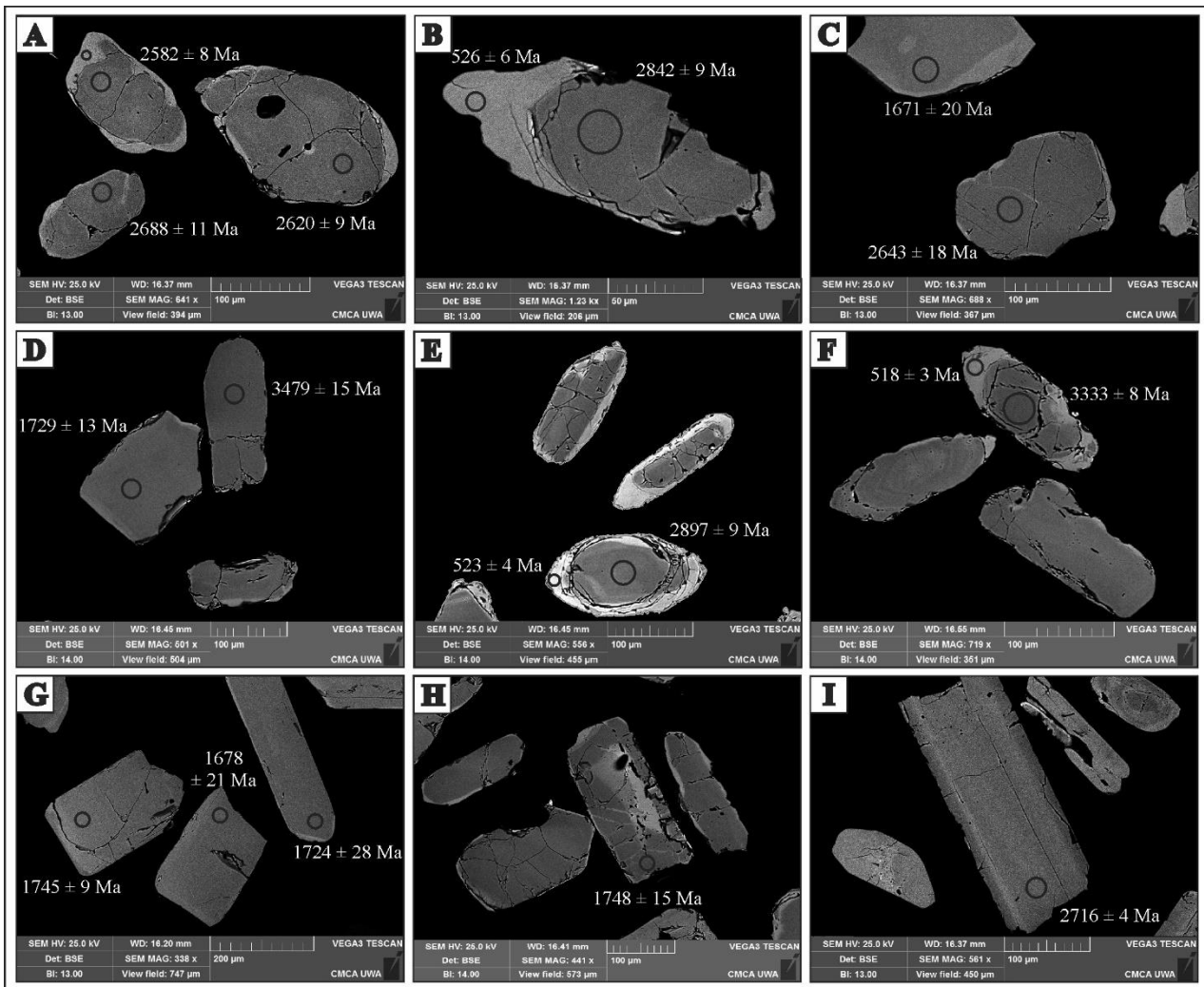


Figure 3.16: Back-scattered images (BSE) of zircons with location of the spots analyzed from the following samples: (A), (B) and (C) mica-quartz schist B-R54; (D), (E) and (F) micaceous quartzite B-R56; (G) granite B-R49; (H) granite B-R63; (I) gneiss B-R66.

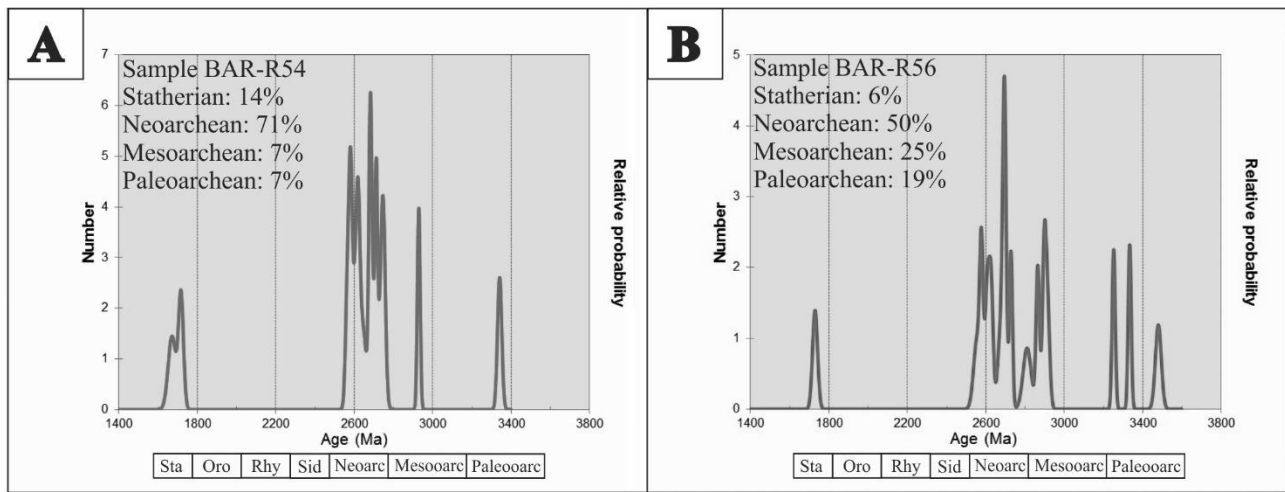


Figure 3.17: Density probability plot of SHRIMP ages of detrital zircon grains from the mica-schist unit. (A) Sample B-R54. (B) Sample B-R56. Abbreviations: Sta – Statherian, Oro – Orosirian, Rhy – Rhyacian, Sid – Siderian, Neoarc – Neoarchean, Mesoarc – Mesoarchean, Paleoarc – Paleoarchean.

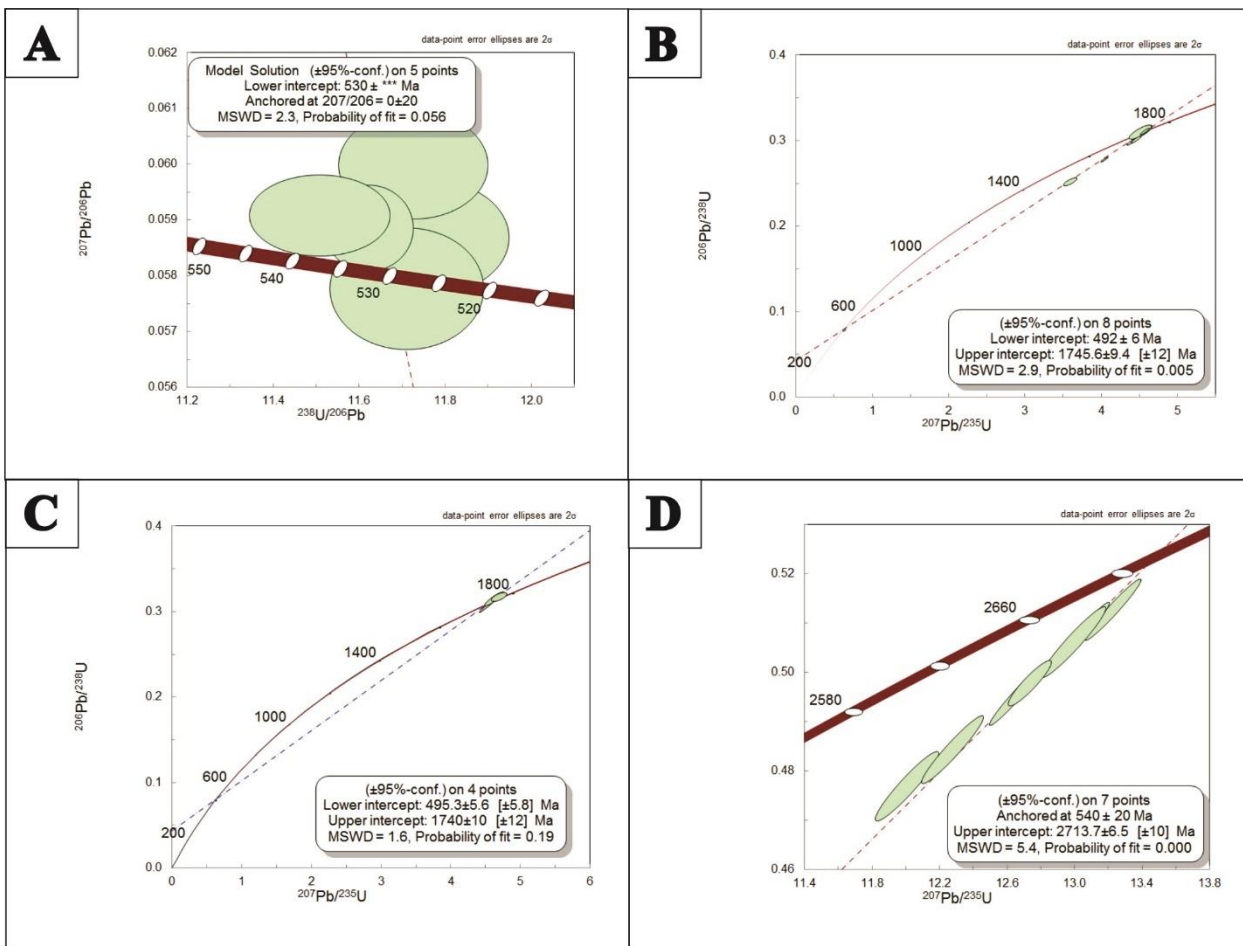


Figure 3.18: Concordia and Discordia diagrams of zircon ages from the following samples: (A) schist (recrystallized zone) – B-R54; (B) granite – B-R49; (C) granite – B-R63; (D) gneiss – B-R66.

3.12. Discussions

Metamorphism: The lithostratigraphic units that crop out the region of HBD comprise metagranitic-gneissic rocks, itabirite-bearing psammo-pelitic metasedimentary sequence, which underwent to amphibolite facies metamorphism, and pegmatitic dikes and sills. Geothermometric calculations based on the microchemical analysis in garnet and biotite core and rim generated one independent reaction exhibiting a minimum temperature of 550 °C (± 50 °C) and a maximum temperature of 690 °C (± 50 °C), considering pressure around 6 kbar. These values indicate prograde metamorphic conditions upper amphibolite facies. The chessboard patterns observed in quartz grains from the schist is a high-T solid-state deformation fabric (Kruhl, 1996) and helps to constrain the deformation in the β -quartz field. These calculations are consistent with earlier results from Müller et al. (1986). These authors calculated a metamorphic temperature for the Guanhães Complex varying from 462 to 613 °C based on ^{18}O data on quartz/garnet/biotite and interpreted it as a regional metamorphic temperature. ^{18}O data on the quartz/magnetite mineral pair in itabirite from the Piçarrão deposit (Figure 3.1) delivered values between 606 to 814 °C. The metamorphic grade calculated for HBD is nevertheless higher than in other analyzed domains such as the west located Morro Escuro area

(Figure 3.1), which ranged from 512 to 560 °C (± 50 °C) with a pressure of 5.9 ± 1 kbar determined at the base of the metasedimentary sequence (Silveira Braga et al., 2015) indicating an eastward positive temperature gradient. Geothermometric results are also consistent with the textural features and mineral paragenesis of the Guanhães Complex, contrasting with low to intermediate metamorphic mineralogy in the metasedimentary sequences of the Espinhaço Supergroup at the homonymous fold and thrust belt.

Structural evolution: The Horto-Baratinha BIF sequence was affected for at least three deformation phases, associated with the collisional stages (630-560 Ma) of the Brasiliano Orogeny. The first phase is associated with the early development of shear zones parallel to the lithologic contact between the units, probably associated with low-angle thrusts that point to an allochthonous position of the deposit, which was uplifted from deeper crustal levels as indicated by the geothermometric data. The intensive strain undergone by the metasedimentary units caused transposition and obliteration of all sedimentary structures and generation of the foliation plane (S_1) in the axial plane position of isoclinal intrafolial folds in the iron formation (Figure 3.6). The metasedimentary package has further undergone flexural folding in shallower levels with axes trending N-S and E-W (phases 2 and 3 respectively) comprising a dome and basin interference pattern (type 1 of Ramsay, 1967; Ghosh et al., 1993; Silveira Braga et al., 2018), (Figure 3.19). Barrote (2016) has also been described superposed deformation in the Jambreiro iron deposit (Figure 3.1) with coaxial axes trending NW-SE comprising a zig-zag interference pattern (type 3 of Ramsay, 1967) at mesoscale.

The iron formation and high-grade ore fabric: The high strain undergone by the iron formation from the HBD caused the crystallization and grain growth of oriented platy crystals of hematite (lamellar hematite) and the deformation of the other mineral components that define a continuous schistosity S_1 (Figure 3.15). The same situation occurs in other BIF-sequences from the eastern border of São Francisco Craton as well as in the high-strain domain of the QF (Rosière et al., 2001). Hypidioblastic to xenoblastic post-deformational magnetite crystals overgrow the foliated fabric. They are progressively oxidized to martite and inverted to new hypidiomorphic hematite that comprises a granoblastic fabric (Figure 3.15). Coarse random lamellar hematite crystals appear at the contact zone with pegmatite bodies.

A similar scenario is observed in other deposits from the Guanhães Block such as Piçarrão, Liberdade, Jambreiro and Candonga (Figure 3.1), although in many cases (keno)magnetite occur as relics in martite or subhedral hematite crystals are intergrown with the fine platy hematite that comprise the rock matrix (Barrote et al., 2017; Gomes et al., 2018). The temporal and spatial relationships between magnetite and hematite is not always clear in these deposits, but the presence

of some magnetite relicts in platy hematite indicates that part of this mineral has predated at least one generation the hematite (Barrote et al., 2017; Gomes et al., 2018).

Age and correlation with other deposits: SHRIMP data of detrital zircon grains from the upper mica schist delivered age of $1,671 \pm 20$ Ma for the youngest grain. This age is much younger than the presumed Rio das Velhas greenstone belt (Oliveira and Leite, 2000; Silva, 2000) and the surrounding gneisses of the Mantiqueira and Guanhães Complexes, as indicated by the crystallization age of $2,713.3 \pm 6.5$ Ma delivered by the orthogneiss located north of HBD, which is similar to results obtained from earlier geochronological work (Silva et al., 2002). The Mantiqueira and Guanhães Complexes seems to be related to the same period of intense magmatic activity, however, the second one contains tectonic slices of Paleoproterozoic metasedimentary sequences.

The metagranite present around the deposit has a Statherian crystallization age and is related to the anorogenic Borrachudos Suite, emplaced during the nucleation of the Espinhaço rift system (Dossin et al., 1993; Dussin and Dussin, 1995; Fernandes, 2001; Fernandes et al., 1994).

The present results indicate that the upper psammitic layer of the Horto-Baratinha Sequence is correlatable with basal units of the Espinhaço Supergroup that were deposited between 1,800 Ma and 1,680 Ma (Chemale et al., 2012), and with the Itapanhoacanga Formation of the Serra de São José Group at the Serpentina Range (Figure 3.1), as proposed by Rolim et al. (2016), (Figure 3.20). The itabirite layer is here tentatively correlated with the Serra do Sapo Formation of the Serra da Serpentina Group, and not with the Canjica Formation, the upper unit of the Serra de São José Group, because the Canjica BIF layer is much less thick and occur in a smaller area than Serra do Sapo BIF, as described by Rolim et al. (2016). Therefore, the lower psammitic layer is here correlated with Meloso Formation (Figure 3.20).

The main zircons source of the metasedimentary rocks is Statherian, Paleo-, Meso- and Neo-Archean. The same ages clusters were obtained from detrital zircons of metasedimentary rocks associated with iron formations from Guanhães (Barrote et al., 2017), Serro (Silveira 2016) and Santa Maria de Itabira (Silveira Braga et al., 2015). However, the distribution of detrital zircon grains in these regions also displays a significant cluster indicating a major Rhyacian and Orosirian source, which is attributed to the rocks from the magmatic-tectonic Minas accretionary event (Teixeira et al., 2015). The Paleoarchean ages correspond to the oldest crustal rocks that were dated in the gneissic complexes from the southern São Francisco Craton (Hartmann et al., 2006; Machado et al., 1996). The Neoarchean and Mesoarchean detrital zircons source are probably the TTG terrains of the Gouveia and Guanhães Complexes (Noce et al., 2007a, 2007b).

The association of early Statherian psammo-pelitic units, para-amphibolites (metacarbonates) and iron formations indicating a platform environment is similar to the scenario described in the

Serpentina Range by Rolim et al (2016) as well in other areas of the Guanhães Block and Espinhaço Ridge (Barrote et al., 2017; Silveira Braga et al., 2015) – Figure 3.20.

The Horto-Baratinha sequence has undergone hydrothermal alteration and iron mineralization with the development of voluminous granoblastic high-grade orebodies at the contact zone with the pegmatite veins. The age of the pegmatite indicates they formed in the course of the Brasiliano Orogeny, during the uplift and late to post-collisional gravitational collapse (560 – 490 Ma), (Marciano, 1995; Pedrosa Soares et al., 2011; Preinfalk et al., 2002) and delivered magmatic hydrothermal fluids. This Cambrian hydrothermal event is registered in the recrystallization zones along the zircons rims and fractures ubiquitously found in the Guanhães Complex (Barrote et al., 2017) and in the eastern border of the Espinhaço thrust belt (Rolim et al., 2016; Silveira Braga et al., 2015); as well as in the crystallization of monazite (495.6 ± 2.2 Ma) in the Conceição iron deposit at the eastern high-strain domain of the QF (Cabral et al., 2015).

Genetic interpretations: The presence of foliated lens-shaped high-grade iron ore bodies (>60 wt.% Fe) parallel to the regional schistosity and axial plane of mesoscopic folds as described in the deposits of Morro Escuro, Morro do Pilar, Serra da Serpentina and Serra do Sapo (Gomes et al., 2018; Oliveira et al., 2017; Rolim et al., 2016; Silveira Braga et al., 2015) points to a mechanism of residual enrichment associated with syntectonic pressure solution and leaching of quartz during the early shear stage of the tectonic evolution. This process developed with the involvement of low to moderate temperature metamorphic fluids (Oliveira et al., 2017) along shear zones in a similar manner as advocated by Rosière et al. (2013) for the schistose ores from the QF.

In the HBD as well as in Piçarrão and Liberdade deposits (Gomes et al., 2018), however, high-grade orebodies are comprised mainly by magnetite and granular hematite that occur at the contact zone with the Cambrian pegmatite dikes. Fluid inclusion studies in quartz and pegmatite veins from Piçarrão and Liberdade (Figure 3.1) suggest that the interactions of anatetic fluids with BIF led to the silica leaching and iron enrichment, resulting in high-grade iron ore bodies (Gomes et al., 2018). Gomes et al. (2018) describe that the loss of silica in the BIF coincided with local crystallization of quartz-rich veins in some parts of high-grade orebodies and, this process is contemporaneous with the transformation of magnetite to granular hematite.

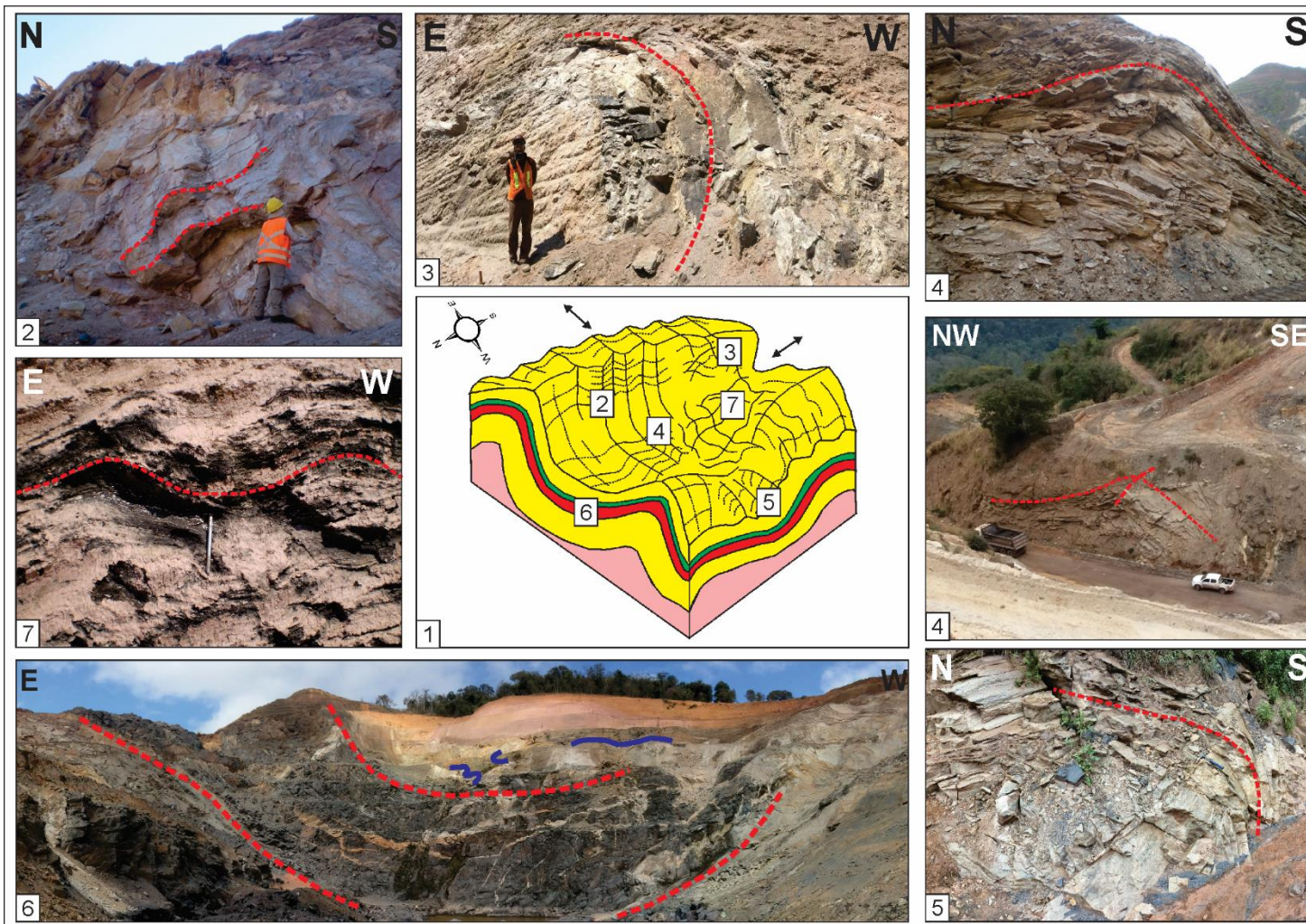


Figure 3.19: Experimental soft model obtained by Ghosh et al. (1993) in a superposed buckling experiment in the center (1). Around it, there are pictures of HBD, which are correlated with different parts of the model: (2) open folds of quartz-mica schist; (3) close folded quartzite with ESE-WNW axial direction; (4) dome structure in quartz-mica schist; (5) close folded quartzite with NNW-SSE axial direction; (6) overview of decametric basin; (7) open fold of mica schist with N-S axial direction.

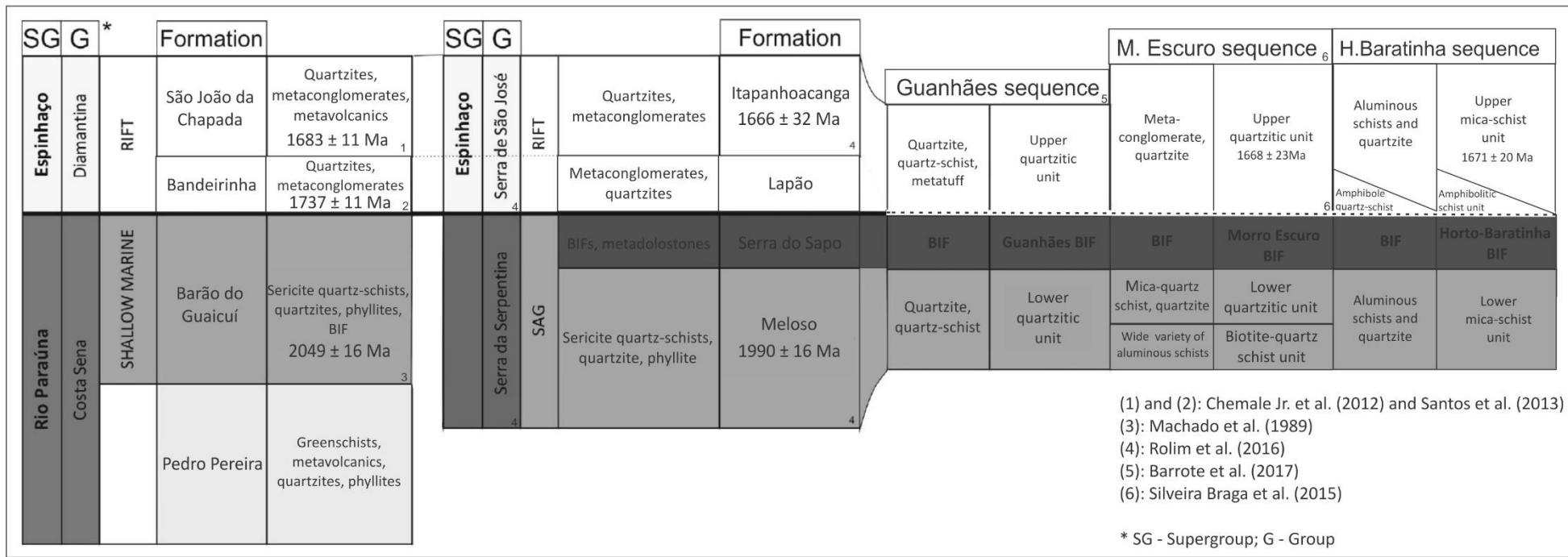


Figure 3.20: Stratigraphic chart of the Espinhaço Supergroup in the central portion of Southern Espinhaço (Chemale et al., 2012; Martins-Neto, 2000; Santos et al., 2013) correlated with the stratigraphic chart of the Serra da Serpentina and Serra de São José groups in the Serpentina Range (Rolin et al., 2016) and to the lithostratigraphic stacking of the Guanhães (Barrote et al., 2017), Morro Escuro (Silveira Braga et al., 2015) and Horto-Baratinha (this study) iron deposits. Modified from Barrote et al. (2017).

3.13. Conclusions

- 1) The lithostratigraphic units in the Horto-Baratinha deposit comprise metagranitic-gneissic rocks and an amphibolite facies BIF-bearing psammo-pelitic metasedimentary sequence.
- 2) SHRIMP data of detrital zircon grains of the upper mica-schist unit delivered a Statherian age for the youngest grains, much younger than the originally proposed age by Oliveira and Leite (2000) and Silva (2000). These results also indicate that the lower and upper meta-psammitic layer and associated iron formation are stratigraphically correlatable with the Serra da Serpentina (<1,990 Ma) and Serra de São José Groups (<1,666 Ma) (Rolim et al., 2016) defined at the Eastern Border of Espinhaço belt and were deposited after the lower limit of the Great Oxygenation Event.
- 3) The Horto-Baratinha sequence is also correlatable with the Morro Escuro (Silveira Braga et al., 2015) and other similar BIF-bearing supracrustal units (Barrote et al., 2017; Gomes et al., 2018; Rolim et al., 2016; Rosière et al., 2017) that occur as tectonic enclaves in the gneissic rocks of the Neoarchean Guanhães Crystalline Complex (Silva et al., 2002) and together comprise the Guanhães tectonic block. These enclaves are probably segments of contemporaneous or para-contemporaneous Fe-rich sequences deposited from Fe-fertilized waters probably during the opening of an intracratonic sag basin prior to the initiation of the Espinhaço rift at ca. 1.8 Ga (Rolim et al., 2016, Rosière et al., 2017).
- 4) The deformation of the units that comprise the Horto-Baratinha sequence developed progressively along at least three deformation phases associated with a basement-evolved thrust tectonic during the collisional stages of the Araçuaí Orogeny that uplifted and juxtaposed Neoarchean gneissic rocks and amphibolite facies metamorphic supracrustal units of Orosirian and Statherian ages that now comprise the Guanhães Block. During this evolution developed a pervasive schistosity associated with intrafolial isoclinal folds that caused the obliteration of primary structures. These structures were subsequently overprinted by a superposed fold system comprising a deposit-scale dome-and-basin shape.
- 5) During the post-collisional stage (560 – 490 Ma) pegmatitic dikes and sills intruded the sequence causing a hydrothermal alteration in the iron formations and country rocks as indicated by the recrystallization zones in the zircon grains and the formation of massive magnetite/granular hematite high-grade iron orebodies.

3.14. Acknowledgments

This study was financed by the Coordenação de Aperfeiçoamento de Pessoal de Nível Superior - Brasil (CAPES) - Finance Code 001 (scholarship / Programa de Doutorado Sanduíche no Exterior /

Pr. nº 88881.134959/2016-01) and Fundação de Amparo à Pesquisa de Minas Gerais (FAPEMIG/VALE CRA - RDP-00067-10-2011).

The authors would like to express their gratitude to BEMISA and its team for supplying drill hole data and support the field work in Horto-Baratinha mine. A special thanks to Rui Monteiro by the support during the field work and to Peter C. Hackspacher (UNESP) and Cristiano Lana (UFOP) by the permission to use the preparation sample lab. Thanks to Malcolm Roberts (CMCA-UWA) by the support during the geothermometry analysis. We also thank the anonymous reviewer for constructive criticism and R. Fuck for the editorial handling.

4. ARTIGO II - DEPICTING THE 3D GEOMETRY OF ORE BODIES USING IMPLICIT LITHOLOGICAL MODELING: AN EXAMPLE FROM THE HORTO-BARATINHA IRON DEPOSIT, GUANHÃES BLOCK, MG

Flávia Cristina Silveira Braga^{ab}, Carlos Alberto Rosière^c, João Orestes Schneider Santos^{de}, Steffen G. Hagemann^d, Neal J. McNaughton^e, Pedro Valle Salles^{bf}

^a Graduate Program, Instituto de Geociências, Universidade Federal de Minas Gerais, Belo Horizonte, MG, Brazil

^b Faculdade de Engenharia, Universidade do Estado de Minas Gerais, João Monlevade, MG, Brazil

^c Instituto de Geociências, Universidade Federal de Minas Gerais, Belo Horizonte, MG, Brazil

^d Centre for Exploration Targeting, University of Western Australia, Perth, WA, Australia

^e Curtin University of Technology, Perth, WA, Australia

^f Centro Federal de Educação Tecnológica de Minas Gerais, Belo Horizonte, MG, Brazil

* Corresponding author. E-mail addresses: flaviacsbraga@gmail.com (F.C. Silveira Braga), crosiere@gmail.com (C.A. Rosière), orestes.santos@bigpond.com (J.O.S. Santos), steffen.hagemann@uwa.edu.au (S.G. Hagemann), n.mcnaughton@curtin.edu.au (N.J. McNaughton), pedrovallesalles025@gmail.com (P.V. Salles)

Published in: REM, Int. Eng. J., 72(3): 435-443. DOI: 10.1590/0370-44672018720167

4.1. Abstract

The definition of geological domains is essential for mineral exploration and is traditionally done manually, section by section, in a laborious, time consuming and subjective process, to construct a 3D model. The technique referred to as implicit modeling is an option to model deposits in a fast and practical manner. This article presents the lithological model of the Horto-Baratinha iron deposit, located in the Antônio Dias municipality, central-eastern part of Minas Gerais state, constructed using the Leapfrog Geo® software. The deposit is situated at the Guanhães tectonic block that is a basement domain of the Neoproterozoic Araçuaí Orogenic belt. The deposit is comprised of itabirite-hosted high-grade iron bodies (>60 wt.% Fe) associated with polydeformed mica schists, amphibole schist with a Statherian maximum deposition age, enclosed by Statherian granitoids of the Borrachudos Suite and crosscut by undeformed pegmatite dikes crystallized during Late Ediacaran-Cambrian. The sequence was affected by progressive multiple deformation phases, associated with the collisional stage of the Brasiliano Orogeny (630-560 Ma), generating a dome and basin mesoscale refolding shape. The model points the proximity between high-grade bodies and pegmatite indicating the possibility that the intrusions contribute to the iron mineralization.

Keywords: implicit lithological modeling, iron ore, Guanhães Block

4.2. Introduction

The 3D geological modeling is considered a powerful tool to analyze and assess the structural framework of ore deposits. The construction of 3D models is usually done manually by linking digitalized 2D sections. In the last decade, various software started to work with the implicit modeling process, in which the geological attributes of a given rock mass is mathematically represented by a

three-dimensional function. Compared with the traditional method, the implicit modeling reduces user-based modeling bias by generating surfaces from lithological and structural data without manual digitization and linkage of sections or level plans (Cowan et al., 2003; Knight et al., 2007; Vollgger et al., 2015).

This paper discusses the use of the implicit lithological modeling for ore deposits delineation. As an example, we modeled the 3D geometry of the Horto-Baratinha iron ore deposit (HBD) located in the Guanhães tectonic block, near the southern end of the Espinhaço Range, Minas Gerais. Our goal is to demonstrate the application of implicit lithological modeling incorporating drill hole and surface mapping data. In addition, we compare our results with a model produced using exclusively drill hole data.

4.3. Geological setting

The HBD is located in the Antônio Dias municipality, central-east part of Minas Gerais (Figure 4.1). Geologically, it is part of the Guanhães basement Block, a major morphotectonic feature of the Neoproterozoic Araçuaí belt (Alkmim et al., 2006). The 250 km long and 140 km wide Guanhães Block is made up of Archean gneisses, a large volume of Statherian granites of the anorogenic Borrachudos Suite, and tectonically dismembered supracrustal assemblages, which include schists, quartzites and itabirites (Alkmim et al., 2007; Brito Neves et al., 2014; Noce et al., 2007b; Rosière et al., 2018; Silva et al., 2002; Silva, 2000). The Horto-Baratinha orebody is hosted by one of these tectonic slices of metasedimentary rocks, specifically by itabirites (metamorphosed iron formation - IF) interlayered with metamorphic psammo-pelitic units (Silveira Braga et al., 2019a).

According to regional geological maps, the IF-bearing sequence from HBD is considered an inlier of Rio das Velhas Archean greenstone belt (Oliveira and Leite, 2000; Pinto and Silva, 2014; Silva, 2000). However, recent geochronological studies indicate that the sequence represent fragments of the Lower Espinhaço Supergroup (Serra de São José Group) and the IF is correlated with the Serra da Serpentina Group, defined by Rolim et al., (2016) at the Serpentina Range, deposited between the Orosirian and Statherian periods (Silveira Braga et al., 2019a).

4.3.1. Stratigraphy

The rock types mapped and identified in drill holes in the HBD area (Figure 4.1B) were grouped into five informal units, which occur in the succession shown in Figure 4.2 and described below.

4.3.1.1. Borrachudos Suite

Granite is composed of quartz, microcline, plagioclase, biotite, muscovite, hornblende and opaque minerals (magnetite and hematite). This rock presents a penetrative foliation defined mainly by biotite and is usually parallel to foliation of the metasedimentary rocks.

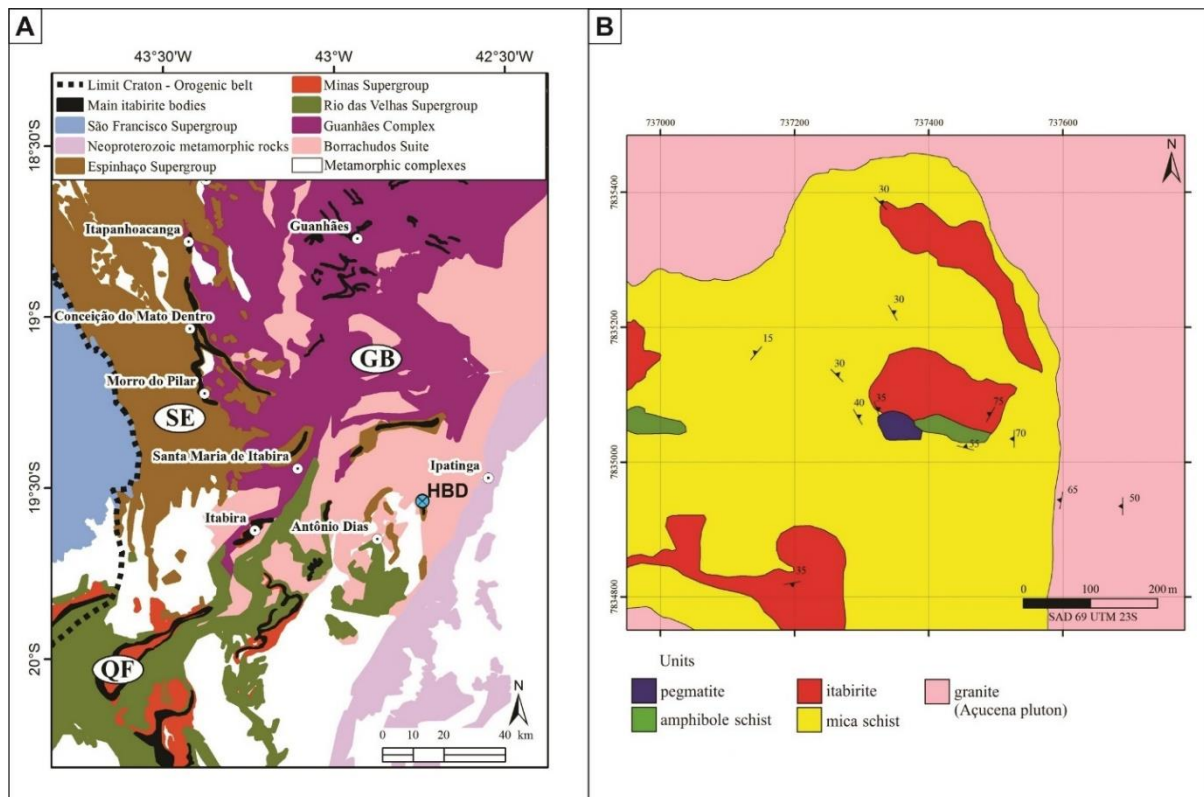


Figure 4.1: (A) Regional map of the Southern Espinhaço Range and Guanhães tectonic block, at the western border of the Neoproterozoic Araúáí belt with the distribution of the main geological units and the location of Horto-Baratinha deposit (HBD). The distribution of the geological units is based and modified from Pinto and Silva (2014). Abbreviations: SE - Serra do Espinhaço fold-thrust Block, GB- Guanhães Block, QF – Quadrilátero Ferrífero Mineral Province. (B) Geological map of HBD (Silveira Braga et al., 2019a).

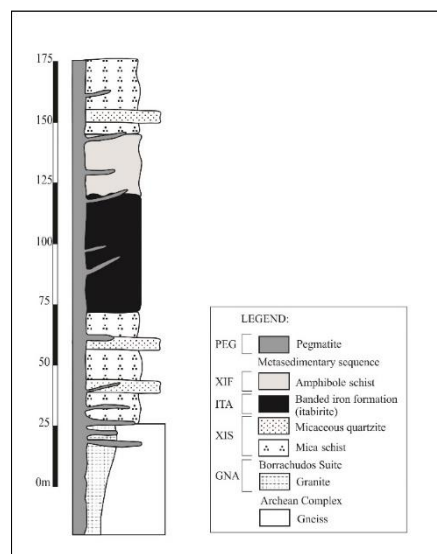


Figure 4.2 : Simplified lithostratigraphic column of HBD (Silveira Braga et al., 2019a).

4.3.1.2. Mica schist

Paraderived aluminous mica schists interlayered with quartzite layers are present at the top and bottom of the metasedimentary sequence. The main minerals are quartz, muscovite, biotite, sillimanite, garnet, tourmaline, kyanite, zoisite, cordierite, opaque minerals (mainly magnetite and hematite). The common accessory minerals are plagioclase, zircon, monazite, apatite and titanite.

4.3.1.3. Amphibole schist

It is stratigraphically located above the itabirite and below the top-micaceous schist. This unit has a scattered occurrence throughout the mapped area. The essential minerals are hornblende, tremolite-actinolite, quartz, pyrophyllite, talc, cordierite and opaque minerals (lamellar and granular hematite, magnetite).

4.3.1.4. Itabirite

Unit composed of itabirite (low-grade ore – Fe <40%) that hosts high-grade ore bodies (Fe > 60%) discontinuously distributed inside it. The itabirite is mainly composed of quartz and lamellar hematite. The high-grade iron ore bodies are metric to decametric, with a granoblastic fabric and mainly composed of granular hematite and magnetite.

4.3.1.5. Pegmatite

Centimetric to metric pegmatite dikes and sills crosscut the entire sequence. This is the only undeformed unit and is mainly composed of quartz, microcline, plagioclase, biotite, muscovite, and apatite. The intrusions have various sizes, from a few centimeters to 30 meters thick. Hydrothermal fluids associated with the pegmatite intrusions could be related to with the Si leaching from IF, crystallization of magnetite and granular hematite, and the consequent formation of high-grade iron bodies (Gomes et al., 2018; Silveira Braga et al., 2018b; Silveira Braga et al., 2019a).

4.3.2. Structures

The Horto-Baratinha sequence was affected for by progressive multiple deformation phases, associated with the collisional stage (630-560 Ma) of the Brasiliano Orogeny (Silveira Braga et al., 2019a, 2018). The early development of shear zones parallel to the lithological contacts caused transposition and obliteration of all sedimentary structures and generation of the foliation planes in the axial plane position of isoclinal intrafolial folds (Silveira Braga et al., 2019a). The sequence has further undergone flexural folding with axes trending N-S and E-W, comprising a dome and basin mesoscale refolding shape (Silveira Braga et al., 2019a).

4.4. 3D lithological modeling

The modeling process known as explicit relies on the manual definition of geological contacts and structures by digitization of 2D cross-sections that are later linked to generate 3D bodies and surfaces. The free hand design makes explicit modeling workflows time consuming and with a strong bias inherited from geological interpretation during cross-section drawing and linkage, resulting in unique and non-reproducible models. It must be viewed with caution to structural interpretation, due to its subjective and nonreproducible process (Cowan et al., 2003; Vollgger et al., 2015).

The implicit geological modeling process was introduced by Lajaunie et al., (1997) and it is based on data interpolation algorithms and firstly defines the continuous three-dimensional function, which describes the rock spatial distribution (Cowan et al., 2003; Knight et al., 2007; Rolo et al., 2017). The Radial Basis Function (RBF) is used to interpolate the lithology and grade distribution (Cowan et al., 2003). An implicit function (generic format $f(x, y, z)=0$, where x, y, and z represents the coordinates) is computed and fitted to a set of spatial data such as lithological contact points along drill holes. A scalar value is assigned to every point in space. Isovalues are extracted and used to define 3D isosurface. This function is transformed into a surface, which may represent geological contact or a fault plane, and allows the extraction of the 3D object in an automatized way, eliminating the necessity of the section by section manual digitization. A surface of any resolution could be extracted from the implicit function, depending on computational limitations. Therefore, the implicit modeling of a solid is defined by the creation of a mathematical function that is modeled from the spatially interpolated drill hole data and/or surface data (structure attitude, contacts lines), and a solid surface is obtained by triangulation of this function (Cowan et al., 2003; Knight et al., 2007). Implicit modeling also permits the direct integration and processing of planar structural measurements, producing structural isosurfaces by adjusting the gradient of the scalar field (Hillier et al., 2013; Vollgger et al., 2015).

Compared with the explicit method, implicit modeling represents one to three orders of magnitude in time savings over manual digitization and allows a rapid update when including new drill hole data (Cowan et al., 2003; Knight et al., 2007; Boyle e Latscha, 2013). Another important advantage is the possibility of testing multiple hypotheses in a reasonable amount of time by applying structural trends calculated from structural measurements, adapting boundaries, and so forth (Jessell, 2001).

The isosurfaces will always try to achieve a smooth fit due to the nature of the RBF-based spatial interpolation. Additional data may be manually introduced based on geological knowledge and experience to generate a model that complies better with the understanding at the time of creation (Vollgger et al., 2015).

4.5. 3D implicit lithological modeling of the Horto-Baratinha iron ore deposit

In our study, we aimed to construct the 3D lithological model of HBD, based on available drill hole lithological data, surface mapping and structural data collected in the field. Two different models were generated: one using only drill hole data and another combining this data with surface geological information. The surface mapping was conducted along the pits and around it, with description of 223 waypoints. The 3D lithological model aims to only resolve large-scale (decametric-scale) units shapes meaning that smaller-scale shapes, such as parasitic folds are not represented.

The Leapfrog Geo® implicit modeling software package (Cowan et al., 2002) uses different types of Contact Surfaces, which are planes that represent the geological contacts and generate the three-dimensional representation of the lithological units. The system employs RBFs to spatially interpolate large drill hole datasets in order to build a 3D geological model. The 3D models produced were extracted using 72 drill hole (5,672 m) database provided by Bemisa Company in 2015, including lithological data (drill hole logs), collar and survey data, and the digital elevation model (DEM). The data validation and composting were done using Leapfrog.

The different types of Contact Surfaces result in different shapes and cut older geologic units in different ways. The software provides four types of Contact Surface planes, as described by ARANZ Geo Limited (2016):

- Deposit: It is sheet-like and does not cut older volumes, so it appears conformably on top of older volumes.
- Erosion: It is analogous to the Deposit Contact Surface; however, it cuts away other Contact Surfaces present on the older side of the Erosion Contact Surface.
- Intrusion: It has a rounded shape, with the interior of the plane representing the intrusion lithology. This Contact Surface characteristically removes older Contact Surfaces and replaces them with the intrusive lithology.
- Vein: This Contact Surface eliminates the previous surfaces along its domain, and its boundaries are defined by hangingwall and footwall surfaces.

The choice of the surface and the relative chronological order should be determined by the geologist to control the spatial extension of the lithological volume. To generate the lithological wireframe model, it is necessary to: (1) define the type of Contact Surface of each lithology; (2) refine the Contact Surfaces according to the characteristics of the lithology, and (3) arrange them in chronological order. Then the software will use the surfaces and the chronological order to discriminate the 3D geological model into units (ARANZ Geo Limited, 2016). The refining process of the Contact Surface may be done by adding information such as the orientation of contacts, lines representing

surface contacts, surface points, lines representing the attitude of the structures, structural trends and so forth.

As described by ARANZ Geo Limited (2016) the Contact Surface should not be chosen based only on its geological origin, but it is important to consider the shape and cutting behavior of each one. The users should choose the Contact Surface for each lithostratigraphic unit based on the geological characteristics observed in the field and drill holes and then choose which Contact Surface available in the software better adapts to each situation.

The five main geological units that make up the host rocks of HBD were used to generate the 3D lithological model. The general surface resolution used to de model was 10 m, which is adaptive for each unit and defines the size of the triangles used to create a surface.

The units of HBD were modeled as the following Contact Surfaces, from the youngest to the oldest:

- Pegmatite (PEG) – Intrusion;
- Amphibole schist unit (XIF) – Intrusion;
- Itabirite and high-grade iron ore (ITA) – Vein;
- Mica schist unit (XIS) – Deposit (background);
- Granite (GNA) – Intrusion.

All the Contact Surfaces were created based on drill hole data and refined with the support of additional information: lines representing mapped surface contacts (Figure 4.3A); dip and dip direction of the contacts at the surface (Figure 4.3A); and the dip direction lines (Figure 4.3B). The dip direction lines represent a structural trend and were drawn from surface to subsurface in specified areas according to structural trends observed during the surface mapping (Figure 4.3B) based on the main structural measurements (Figure 4.3A).

The surface resolution was adapted to 5 m for the less extensive units XIF and PEG. The PEG, GNA, and XIS were modeled using a 1:1:1 ellipsoidal ratio that is the default option. The surface contact line of PEG (Figure 4.3A) was used as an input in the Contact Surface.

The amphibole schist unit was modeled as an Intrusion, due to its scattered occurrence but concordant with the other metasedimentary units, applying the same layer orientation. This was possible using the XIF dip direction lines and the surface contact as inputs in the Contact Surface (Figure 4.3), as well as a structural trend created based on the GNA surface.

The ITA was modeled as a Vein because this Contact Surface best adapted to the shape observed in the field. Lines representing the ITA footwall and hangingwall dip directions were also applied as inputs in the Contact Surface (Figure 4.3B). To check the position of high-grade bodies

inside the ITA unit and its relation with pegmatite, these intervals were posteriorly modeled as an Intrusion, using 1:1:1 ellipsoidal ratio and 5 m of resolution.

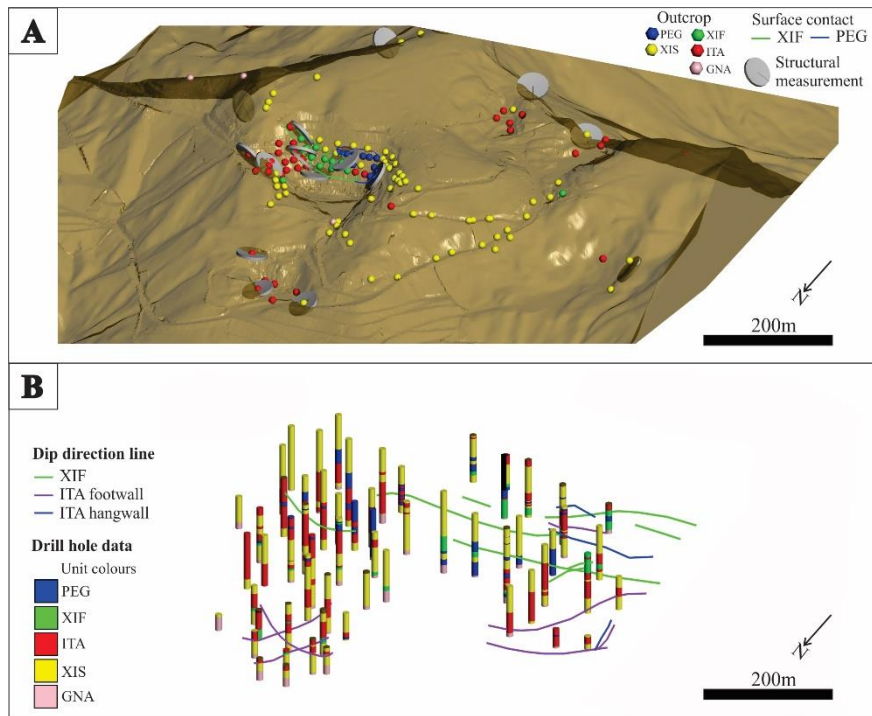


Figure 4.3: Data used to create the lithological 3D model of HBD in Leapfrog Geo®. (A) Surface data: DEM, outcrops lithology, main structural measurements of the lithological contact, XIF and PEG surface contact lines. (B) Subsurface data: drill hole lithology and dip direction lines.

4.6. Results and discussions

Figure 4.4 shows the lithological 3D model created. Every Contact Surface generated agrees with the position and attitude observed in the field. This was only possible due to the information used to refine the Contact Surface (dip direction and surface contacts lines added as inputs in the Contact Surfaces) and the use of the Contact Surfaces that best adapted to the shape of the layers. Figure 4.5 shows the lithological 3D model created using only drill hole data and the Deposit Contact Surface for all metasedimentary units. It is possible to see that most of the outcrops are not in agreement with the lithological model of Figure 4.5, but they best-fit with the model of Figure 4.4.

As demonstrated by Basson et al. (2018), although most lithologies of the deposit are sedimentary in origin, Leapfrog Geo® creates the models according to their geometry. In order to obtain realistic shapes in the present article, we adopt the Deposit Contact Surface for the more extensive metasedimentary lithology (XIS), and the discontinuous layers were modeled as Intrusion or Vein. To keep the structural trend of these less extensive layers in agreement with the other units, dip direction lines (Figure 4.3B) and structural trends were applied that made possible the modeling of XIF and ITA in agreement with the outcrop observation.

When modeled using the Deposit Contact Surface, the ITA and XIF units behaved as continuous layers throughout the area (Figure 4.5), in disagreement with the geological surface map (Figure 4.1B).

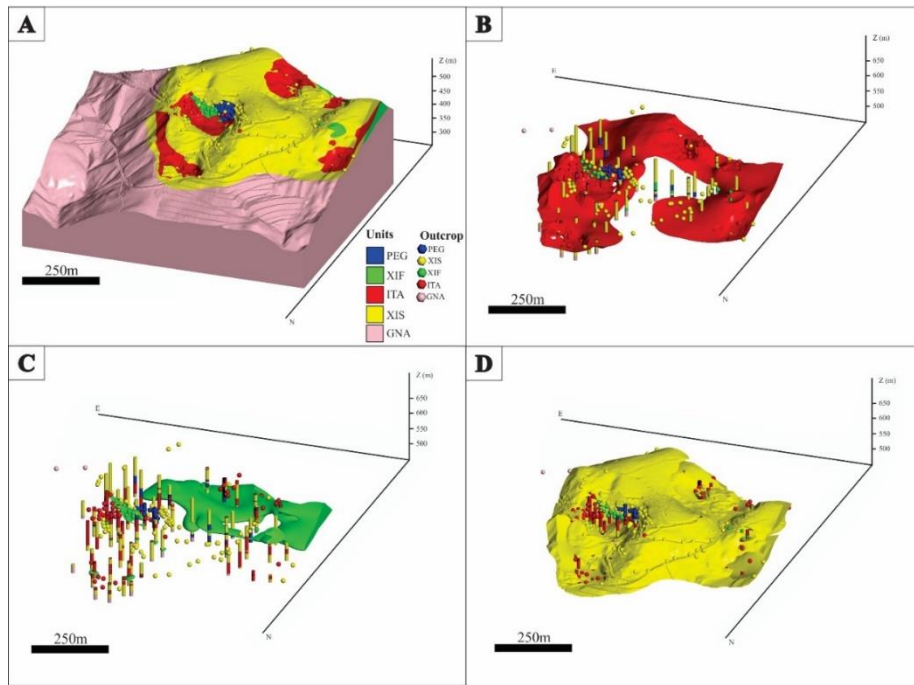


Figure 4.4: Lithological Horto-Baratinha 3D model created in Leapfrog Geo® based on surface and subsurface data. (A) Completed 3D lithological model. (B) Lithological model of ITA unit, modeled using Vein Contact Surface. (C) Lithological model of XIF unit, modeled as an Intrusion. (D) Lithological model of XIS unit, modeled as a Deposit.

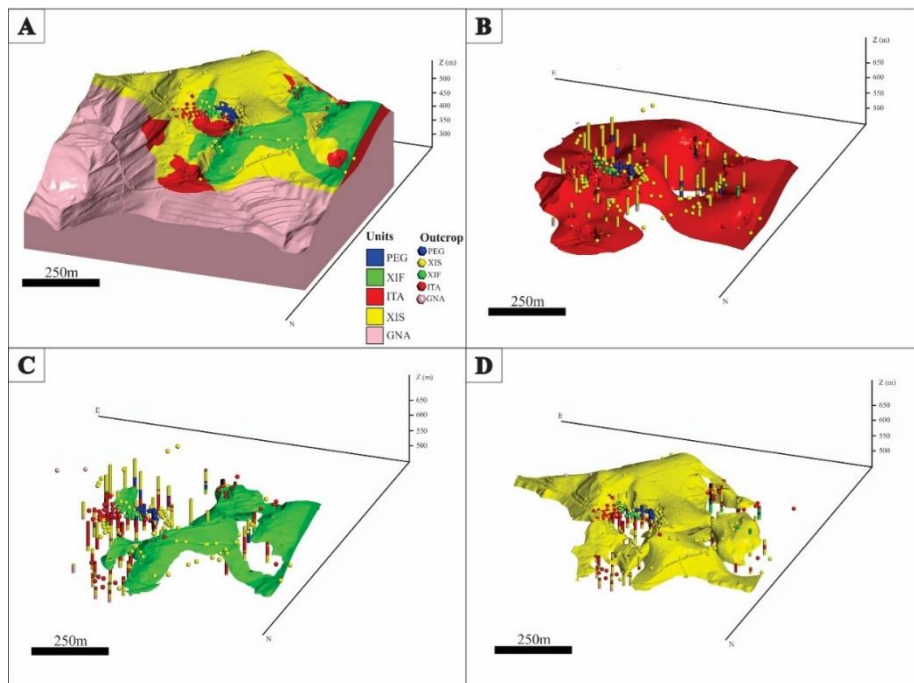


Figure 4.5: Lithological Horto-Baratinha 3D model created in Leapfrog Geo® based only in DEM and drill hole data. (A) Completed 3D lithological model. (B) Lithological model of ITA unit, modeled using Deposit Contact Surface. (C) Lithological model of XIF unit, modeled as a Deposit. (D) Lithological model of XIS unit, modeled as a Deposit.

Both models, the adapted (Figure 4.4) and the generic (Figure 4.5), present the same mesoscopic layer shapes, which look like the dome and basin refolding shape proposed by Silveira Braga et al. (2019a) for HBD. The authors compare the structural non-cylindrical refold pattern of HBD with the experimental soft model obtained by Ghosh et al. (1993) in a superposed buckling experiment. Even though the generic model is not totally in agreement with the surface mapping, it provides a coherent general geometry of the units.

The high-grade iron ore intervals were modeled based on the drill hole description to verify its relationship with the pegmatite intrusions. Figure 4.6 shows that the more extensive and continuous high-grade ore bodies are close to the biggest pegmatite intrusions.

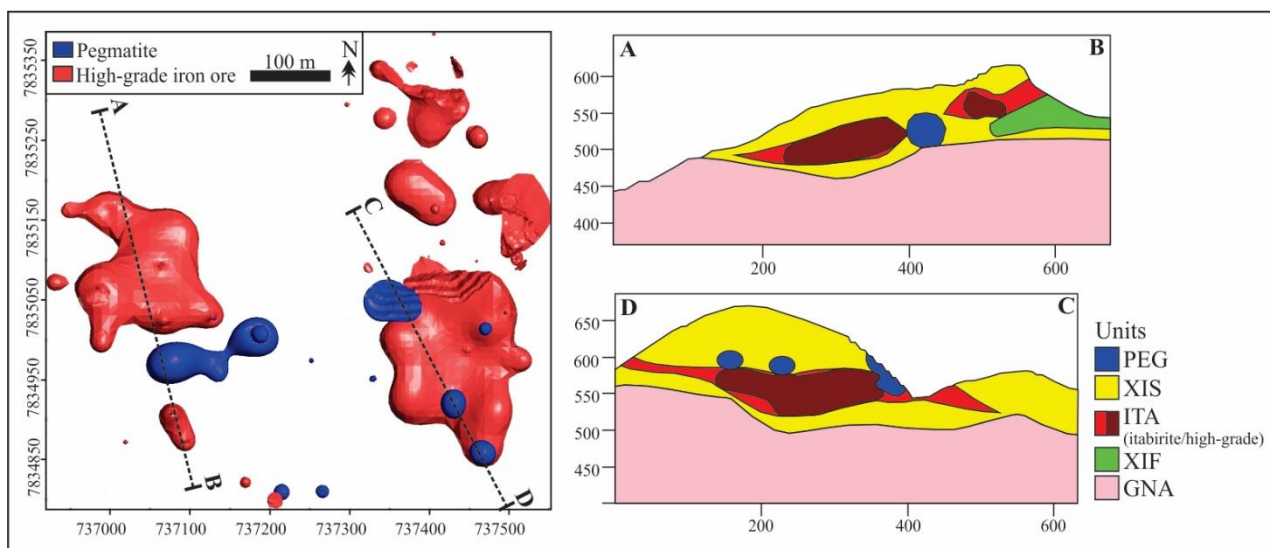


Figure 4.6: Map showing the distribution of the pegmatite intrusions and high-grade bodies at left and sections with the distribution of all units modeled at right.

4.7. Conclusion

The Leapfrog Geo® software generated a lithological 3D model by implicit modeling, which is in agreement with the shape and orientation (strike and dip) of the rock units obtained from surface mapping (Figure 4.1B) and the dome and basin refolding shape interpreted by Silveira Braga et al., (2019a). The delivered high-grade ore 3D model (Figure 4.6), points to a close spatial relationship with the pegmatite bodies, supporting the influence of the magmatic-hydrothermal fluids in the iron mineralization. The inclusion of parameters such as lines representing the contact at the surface and the general structural trend of the layers (Figure 4.3) helped to refine the outcrop pattern. Another important characteristic of the implicit modeling observed in this study case is the importance of the definition of Contact Surface based on its intersection behavior but not necessarily on the geological origin, in order to provide best fitted 3D units according to field observations.

The implicit modeling is accurate, flexible and efficient when compared with the explicit methodology, as pointed by Knight et al., (2007). In data-rich environments, the high-data density allows direct computation of boundaries and surfaces without manual, knowledge driven digitization (Vollgger et al., 2015). The implicit modeling was herein used as a semi-automatic tool since we needed to refine the modeling parameters according to the local geological characteristics. This refining was necessary mainly due to the open and irregular drill hole data throughout the modeled area. However, in the present case, the analyses of medium to low drill hole data density turned out to be sufficiently accurate in the interpretation of a non-cylindrical deposit scale geometry using Leapfrog Geo® default workflow.

4.8. Acknowledgments

The authors would like to express their gratitude to BEMISA and its team for supplying drill hole data and supporting the field work in Horto-Baratinha mine; ARANZ Geo Limited - Owners of Leapfrog, QG Consulting and the geologist Marcelo Freitas by the permission and support to the usage of Leapfrog Geo®. We also thank the anonymous reviewers for constructive criticism and Jório Coelho for editorial handling. This study was financed by the Coordenação de Aperfeiçoamento de Pessoal de Nível Superior - Brasil (CAPES) - Finance Code 001 (scholarship / Programa de Doutorado Sanduíche no Exterior / Pr. n° 88881.134959/2016-01) and Fundação de Amparo à Pesquisa de Minas Gerais (FAPEMIG/VALE CRA - RDP-00067-10-2011).

5. ARTIGO III - CUITÉ IRON ORE DEPOSIT – A TECTONIC SLICE OF LOWER ESPINHAÇO IN GUANHÃES TECTONIC BLOCK

*Flávia Cristina Silveira Braga^{ab}, Carlos Alberto Rosière^c, João Orestes Schneider Santos^d, Steffen G. Hagemann^e, Neal J. McNaughton^f, Pedro Valle Salles^{bf}

^a Graduate Program, Instituto de Geociências, Universidade Federal de Minas Gerais, Belo Horizonte, MG, Brazil

^b Faculdade de Engenharia, Universidade do Estado de Minas Gerais, João Monlevade, MG, Brazil

^c Instituto de Geociências, Universidade Federal de Minas Gerais, Belo Horizonte, MG, Brazil

^d Universidade do Estado do Amazonas, Manaus, AM, Brazil

^e Centre for Exploration Targeting, University of Western Australia, Perth, WA, Australia

^f Curtin University of Technology, Perth, WA, Australia

^g Centro Federal de Educação Tecnológica de Minas Gerais, Belo Horizonte, MG, Brazil

* Corresponding author.

E-mail addresses: flaviacsbraga@gmail.com (F.C. Silveira Braga), croisiere@gmail.com (C.A. Rosière), orestes.santos@bigpond.com (J.O.S. Santos), steffen.hagemann@uwa.edu.au (S.G. Hagemann), n.mcnaughton@curtin.edu.au (N.J. McNaughton), pedrovallesalles025@gmail.com (P.V. Salles)

5.1. Abstract

The Cuité iron formation (IF)-hosted iron ore deposit is located at the eastern border of São Francisco Craton, in the Guanhães tectonic block, comprising IF-hosted high-grade lenses (>60 wt.% Fe) associated with mica schist, enclosed by Statherian granitoids of the Borrachudos Suite and Neoarchean ortogneiss of Guanhães Complex. Concordant and discordant quartz and pegmatite veins intersect all units. Detrital zircon grains of the upper psammitic layer yielded the youngest age of 1,695 ± 15 Ma making it correlated with the Early Statherian Serra de São José Group that comprises the basal unit of the Espinhaço Supergroup. The metamorphosed IF (itabirite) has been deformed during the Brasiliano Orogeny, and the banded structure is transposed by an axial planar schistosity, defined by lamellar hematite and quartz, enveloping schistose to granular high-grade ore lenses. The lamellar hematite from IF is the oldest iron oxide generation, which was formed during the syn-deformational orogenic stage, parallel-oriented to the rock foliation. The (keno)magnetite grains from IF and iron ore developed as idioblasts that grew over the foliation formed during late and post-deformational stages. Magnetite oxidizes subsequently to martite and granular hematite during late to post-deformational stages. The three high-grade iron ore types, lamellar-granular hematitic ore (LGO), magnetitic ore (MO), and granular hematitic ore (GO) are related with syn-, late- and late to post-deformational stages respectively. During the late-collisional (Ediacaran to early-Cambrian) and post-collisional/gravitational collapse (Cambrian) of Brasiliano Orogeny the sequence was intruded by pegmatitic bodies, which are part of the Eastern Brazilian Pegmatite Province. Recrystallized regions of the detrital zircons have delivered Cambrian ages, indicating the interaction of the supracrustal units with hydrothermal fluids from the late- to post-deformational stages of Brasiliano Orogeny.

Keywords: Iron ore, Guanhães block, Espinhaço Supergroup

5.2. Resumo

O depósito de ferro de Cuité está localizado na borda leste do Cráton do São Francisco, no domínio do Bloco tectônico Guanhães, e contém lentes de minério de ferro de alto teor (>60 wt.% Fe) associado com formação ferrífera, mica xisto, cercado por granitoides estaterianos da Suite Borrachudos e ortognaisses neoarqueanos do Complexo Guanhães. Há ainda veios de pegmatitos e quartzo que cortam o todas as unidades. A camada de mica-xisto superior possui zircão detritico mais jovem com idade de 1.695 ± 15 Ma e, portanto, é correlacionada com o Grupo Serra de São José, uma das unidades que compõem a base do Supergrupo Espinhaço. A formação ferrífera (itabirito) foi deformada e metamorfizada durante a Orogênese Brasiliana, e seu bandamento sedimentar/diagenético foi transposto por uma xistosidade plano-axial, definida pela orientação de hematita lamelar e quartzo, com desenvolvimento de lentes xistosas a granulares de minérios de ferro. A hematita lamelar da formação ferrífera é a geração mais antiga de óxido de ferro, a qual foi formada durante o estágio sin-deformacional. A (keno)magnetita desenvolveu-se como idioblastos na formação ferrífera e no minério durante os estágios tardi- a pós-deformacionais. Magnetita sofreu oxidação para martite e hematita granular durante os estágios tardi- a pós-deformacionais. As três fácies de minério de ferro identificadas, minério hematítico lamelar e granular (LGO), minério magnetítico (MO) e minério hematítico granular (GO), são relacionadas com as fases sin-, tardi- e tardi- a pós-deformacional respectivamente. Durante o estágio tardi e pós-deformacional (colapso gravitacional) do orógeno Brasiliano (Ediacarano e Cambriano), a sequência foi intrudida por corpos de pegmatito, os quais fazem parte da Província Pegmatítica Oriental Brasileira. Bordas recristalizadas nos zircões detriticos apresentam idade Cambriana, indicando a interação das supracrustais com fluidos hidrotermais das fases tardia- e pós-deformacional da Orogênese Brasiliana.

Palavras chave: Minério de Ferro, Bloco Guanhães, Supergrupo Espinhaço

5.3. Introduction

Several iron formation (IF)-hosted iron ore deposits are discontinuously distributed at the east-northeast of Quadrilátero Ferrífero Mineral Province (QF), in the western part of the Neoproterozoic Araçuaí Orogenic belt (Brasiliano Orogeny), enclosed in Archean and Paleoproterozoic granitic-gneissic rocks of the Guanhães Complex (*e.g.* Horto-Baratinha, Cuité, Piçarrão, Liberdade, Guanhães, Morro do Pilar, Conceição do Mato Dentro, Morro Escuro), as shown in Figure 5.1. Some of these metasedimentary sequences have been interpreted as slivers of greenstone belts coeval with Rio das

Velhas Supergroup or Archean volcano-sedimentary unit from the Guanhães Complex (Grossi-Sad, 1997; Oliveira and Leite, 2000; Pinto and Silva, 2014; Silva, 2000). Recent geochronological studies indicate that many of them are fragments of a Statherian-Orosirian sequence correlated with the basal units of Espinhaço Supergroup (Barrote et al., 2017; Rolim et al., 2016; Silveira Braga et al., 2019a, 2015). These data opened space for the alternative interpretation that the IF sequences from Guanhães tectonic block represent tectonic enclaves of Orosirian-Statherian units such as the Serra da Serpentina and Serra de São José Groups (Rolim et al., 2016) and the gneisses of the Guanhães Block comprise metamorphic rocks of different origin and ages. Alkmim et al. (2007) interpreted the Guanhães tectonic block as a basement unit that remained as a rigid buttress during the Brasiliano collage, from Neoproterozoic to the Cambrian.

Guanhães tectonic block contains granoblastic magnetite and hematite orebodies discontinuously developed in contact with metric to decametric pegmatitic bodies (e.g. Piçarrão, Liberdade, Guanhães, Horto-Baratinha – (Barrote et al., 2017; Gomes et al., 2018; Silveira Braga et al., 2019a)). The iron deposits along the Espinhaço fold-thrust belt have IF-bearing massive iron bodies composed of platy hematite and controlled by shear zones (e.g. Morro do Pilar, Conceição do Mato Dentro, Morro Escuro – (Silveira Braga et al., 2015; Rolim et al., 2016; Gomes et al., 2018)). Cuité IF and related iron ore bodies have characteristics of both regions – with platy and granular ore.

In this paper we focus the geology, geochronology and textural features of the Cuité iron deposit, compared with other similar deposits and present an interpretation of the hypogene mechanisms of iron enrichment. This work provides a new insight of the tectonic environment and consequences for the interpretation of the Guanhães Block as an active fragment of the lower crust comprised by juxtaposed tectonic slices amalgamated and uplifted during the Brasiliano Orogeny

5.4. Geochronological methodology

Zircon grains from the mica schist were analyzed by U-Pb SHRIMP method (Sensitive High-Resolution Ion Microprobe) at the Curtin University in Perth, Australia. The samples were processed (crushing, grinding, screening, concentration, and magnetic separation) at the Instituto de Geociências of Universidade Estadual Paulista (UNESP), at Rio Claro, Brazil. After crushing, grinding and screening, the heavy fraction concentration of 60-250 mesh was realized by panning. The 60-250 mesh fraction was treated with heavy liquid (bromoform) to remove light minerals and with Frantz LB1 magnetic separator to concentrate the less magnetic minerals such as non-metamitic zircon. Zircons were handpicked and organized in an epoxy mount, which was polished and carbon-coated for SEM (Scanning Electron Microscope) study using BSE (Back-scattered images) that were taken using a TESCAN VEGA3 at the University of Western Australia in Perth, Australia.

Epoxy mounts were coated with gold for SHRIMP analyses. Most SHRIMP analytical spots were in the diameter range of 20-30 μm but the analyses of altered/recrystallized zones used a spot size of only 10 μm . Five scans were used for each 20-30 μm spot analysis and six scans for 10 μm spot size. The following masses were analyzed for zircon: ^{196}ZrO , ^{204}Pb , background, ^{206}Pb , ^{207}Pb , ^{208}Pb , ^{238}U , ^{248}ThO , ^{254}UO . The calibration was conducted using the zircon standard M257 (561.3 Ma - (Nasdala et al., 2008)) and BR266 (559 Ma, 903 ppm U - (Stern, 2001)). All data on with common lead correction greater than 1% were rejected during the first scan. The uncertainties of individual ages are quoted at the 1σ level, whereas the ages plotted are calculated at 2σ levels (about 95% confidence). SHRIMP data were reduced using SQUID software (Ludwig, 2001) and plots were prepared using ISOPLOT/Ex (Ludwig, 2003).

5.5. Geological Setting

The Guanhães and Mantiqueira complexes (Figure 5.1) comprise the Archean-Paleoproterozoic crystalline basement reworked during subsequent orogenic events during the Rhyacian (Tranzamazonian Orogeny – 2,200-2,000 Ma) and the Neoproterozoic (Brasiliano Orogeny 800-500 Ma), (Noce et al., 2007a; Silva et al., 2002). The Mantiqueira Complex consists basically of amphibolite facies mylonitic orthogneisses (Noce et al., 2007b; Peres et al., 2004) and the Guanhães Complex is comprised of TTG (tonalite-trondhjemite-granodiorite) gneisses and discontinuous strings of IF-bearing units (Dussin et al., 2000; Noce et al., 2007a). The Guanhães gneisses are intruded by alkaline granitoid plutons grouped in the anorogenic Borrachudos Suite (Dussin et al., 2000; Grossi-Sad et al., 1990b), with crystallization ages around 1,730 Ma (Dossin et al., 1993; Fernandes et al., 1994; Silva et al., 2002; Silveira Braga et al., 2019a). Both complexes are juxtaposed by a system of high-angle west-vergent thrust planes delineated by shear zones that comprise mylonitic rocks and banded gneisses. In the western border of the Guanhães Complex, the gneisses are upthrusted on the metasedimentary rocks of the Lower Espinhaco Supergroup (Carvalho et al., 2014; Gomes et al., 2018; Rolim et al., 2016; Silveira, 2016; Silveira Braga et al., 2015).

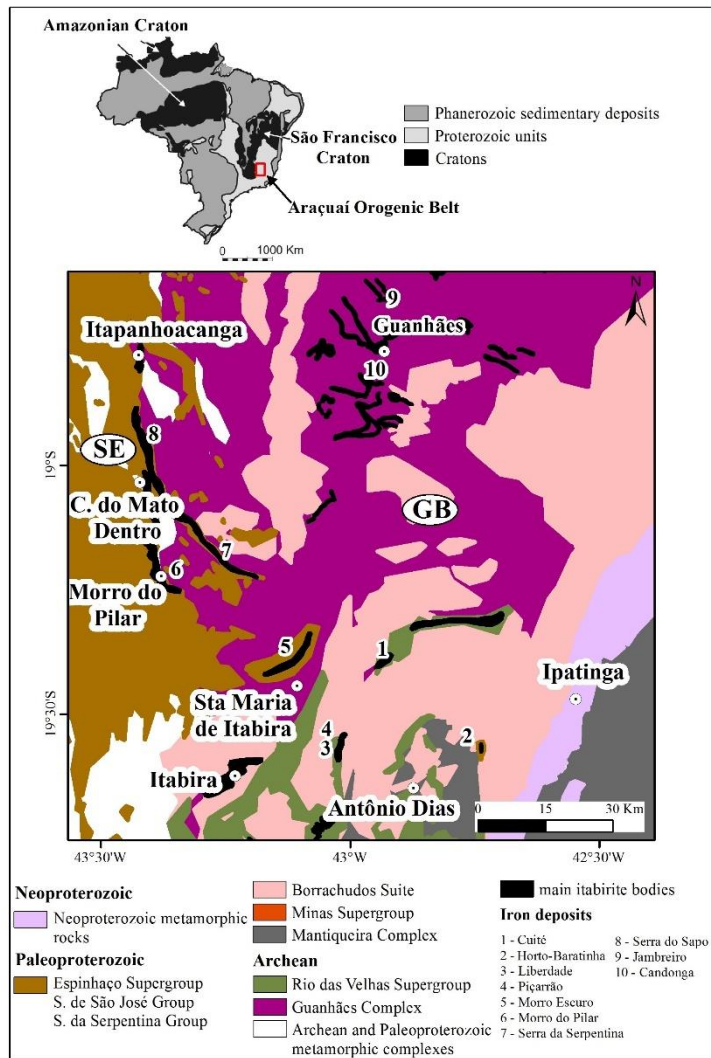


Figure 5.1: Regional map showing the location of some iron deposits and distribution of the main geological units, along the southeast border of São Francisco Craton. The distribution of the geological units is based and modified from Pinto and Silva (2014). Abbreviations: GB- Guanhães Block, SE - Serra do Espinhaço fold-thrust belt Block.

5.6. Regional Tectonic Setting

The metasedimentary sequence from Cuité is enclosed in Borrachudos Suite by SE-verging thrust faults (Oliveira and Leite, 2000), similar to observed in the itabirite-bearing sequence from Morro Escuro Ridge (Carvalho et al., 2014; Silveira Braga et al., 2015) – Figure 5.2, located at west. However, this SE-verging direction is distinct from the W-verging folds and thrust present throughout the Southern Espinhaço Range. The structures from Morro Escuro are controlled by three families of folds nucleated in three deformational phases associated with the development of a high-deformed transpressive zone during the Brasiliano Orogeny (Carvalho et al., 2014). This domain is comprehended by the eastern extension of Fundão-Cambotas system faults (FC), and the ENE-WSW Travessão shear zone (CT), (Carvalho et al., 2014), as depicted in Figure 5.2. The dextral CT shear

zone is associated with the E-W inflection of the thrust faults that juxtapose the Morro do Pilar and Serra da Serpentina itabirite-bearing sequences (Figure 5.2).

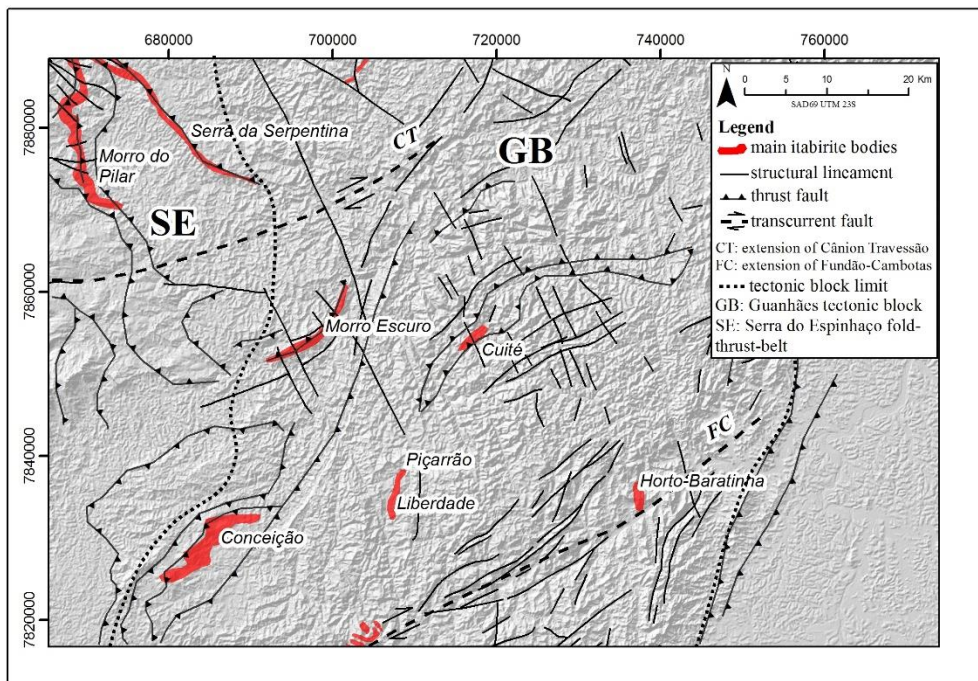


Figure 5.2: Regional structures from the main itabirite bodies between Southern Espinhaço fold-thrust belt and south portion of Guanhães tectonic block. Structures lines based on: (Carvalho et al., 2014; Grossi-Sad et al., 1997; Oliveira and Leite, 2000; Pinto and Silva, 2014; Silva, 2000).

5.7. The Cuité deposit

5.7.1. Lithostratigraphy

The sequence of the Cuité deposit is comprised by mica schist tectonically interlayered with metamorphic iron formation (itabirite) enclosed in the banded Statherian granite-gneiss of the Açucena Pluton of Borrachudos Suite and Archean gneiss of the Guanhães Complex, metamorphosed under amphibolite facies (Figure 5.3 and 5.4).

5.7.1.1. Guanhães Complex

The TTG type orthogneiss of the Guanhães Complex crops out in the surroundings of the Cuité area and displays millimetric to centimetric banding, locally interlayered with metabasic bodies and pegmatites (Oliveira and Leite, 2000). It is comprised of plagioclase, K-feldspar, quartz and biotite as main minerals and apatite, titanite, allanite, zircon, xenotime, rutile and opaque minerals as accessories (Oliveira and Leite, 2000). The crystallization ages obtained by U-Pb SHRIMP are between $2,867 \pm$

10 Ma and $2,710 \pm 6$ Ma (Silva et al., 2002). The Guanhães Complex exposes deeper crustal level with a higher metamorphic grade than the adjacent areas (Alkmim et al., 2006).

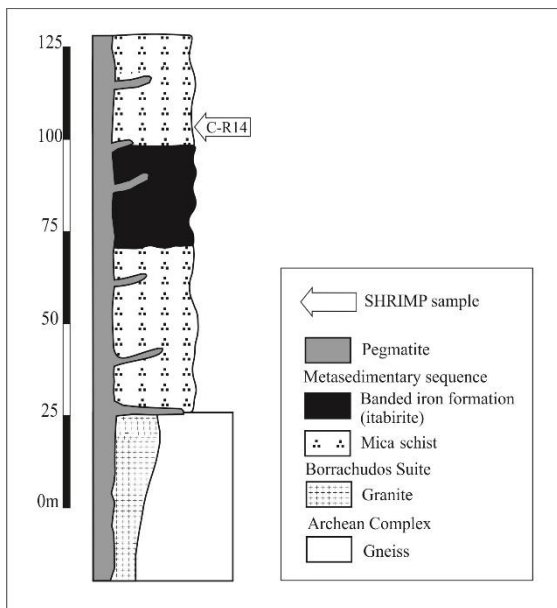


Figure 5.3: Simplified lithostratigraphic column of Cuité deposit.

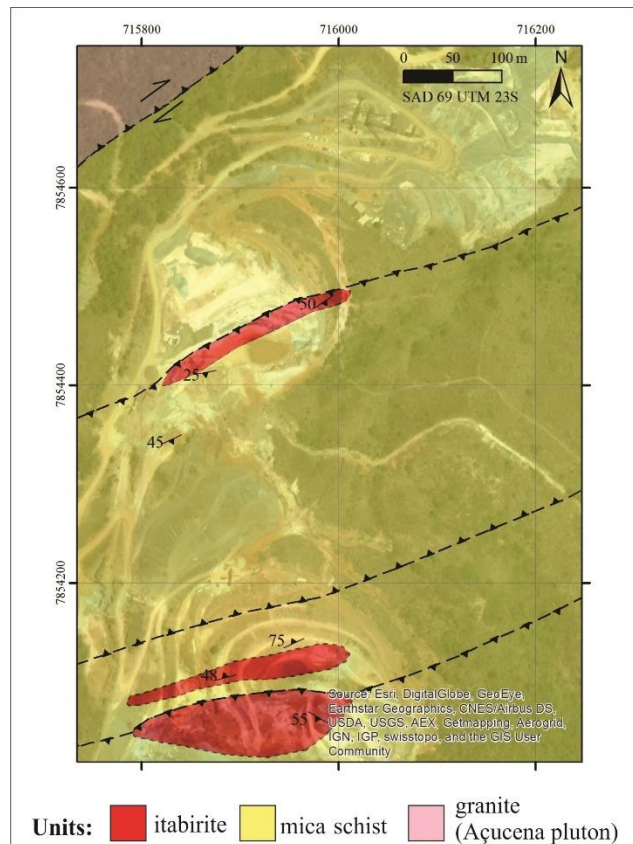


Figure 5.4: Geological sketch map of Cuité deposit.

5.7.1.2. Borrachudos Suite

The metagranitic rock of the Borrachudos Suite (Açucena Pluton) is comprised of quartz, plagioclase, K-feldspar, biotite, and hornblende as main minerals, and titanite, allanite, monazite, fluorite, apatite and opaque minerals as accessories (Oliveira and Leite, 2000). The metagranite displays a granolepidoblastic fabric with a penetrative foliation defined mainly by biotite and usually parallel to the metasedimentary schistosity. The Açucena Pluton extends between Guanhães and Ipatinga (Figure 5.1).

5.7.1.3. Metasedimentary sequence

The aluminous schists that occurs in Cuité at top and bottom of the metasedimentary sequence were grouped as a single mica schist unit (Figure 5.3). The main minerals are quartz, muscovite, biotite, sillimanite, garnet and opaque minerals (mainly hematite and magnetite). They display a lepidoblastic fabric with xenoblastic quartz grains, with the development of a tight, continuous schistosity along m-

sized shear bands close to the contact with itabirite (Figure 5.4 and 5.5). The itabirite body is 10-25 m thick and is comprised of quartz and lamellar hematite that defines the schistosity. A metamorphic layering is defined by the alternation of quartz-rich and hematite-rich bands, with the development of tight rootless isoclinal folds (Figure 5.7A). Elongated hematite grains may reach a maximum 85 μm thickness and 1.000 μm length making straight boundaries with quartz and other platy crystals.

Quartz occurs as granoblastic aggregates of medium to coarse grains (<500 μm thick and <1000 μm length) comprising millimetric lenses, parallel to the foliation, with undulatory extinction and subgrains. Chlorite, tremolite-actinolite, talc and kaolinite are accessories minerals commonly in centimetric to millimetric lenses.

5.7.1.4. Pegmatite and quartz veins

Medium to coarse-grained (>5 mm) pegmatite and quartz veins, with less than 1 m thick and metric length, develop mainly along the schistosity planes. The pegmatite is comprised mostly by quartz, microcline, plagioclase and muscovite.



Figure 5.5: Overview of the Cuité inactive south pit, with the location of the identified rocks. Red lines = lithological contacts, Yellow lines = schistosity trace.

5.7.2. High-grade iron ore bodies

The IF hosted high-grade iron ore (>60% wt. Fe) occur as 5-10 meters thick tabular bodies parallel to the schistosity. It is possible to distinguish three high-grade iron ore mineral facies depending on the dominant iron oxide (Figure 5.6 and 5.7): lamellar-granular hematitic ore (LGO), magnetitic ore (MO), and granular hematitic ore (GO). The shape and the foliation of the high-grade orebodies are controlled by the metamorphic banding of the itabirite protore.

The LGO occurs as decimetric to metric thick lenses in the shear zones (Figure 5.4). It is fine to medium grained (<1 mm to 2.5 mm) composed by lamellar hematite, kaolinite, granular hematite and quartz (Figure 5.6A). Thin lamellar hematite defines a sinuous and anastomosing penetrative schistosity commonly enveloped by kaolinite aggregates that concentrates in millimetric lenses (<0.5

cm). The kaolinite higher content of LGO (<40%) when compared with itabirite and the other ore types is the most important macroscopic feature that distinguish this ore type. Granular hematite grow as idioblasts over the platy grains (Figure 5.7B). Quartz occurs as rare millimetric lenses, displays flat grain boundaries approximately perpendicular to the lamellar hematite crystals. It is also observed undulatory extinction and subgrains of quartz, representing a diffusive mass transfer microstructure of the intracrystalline plastic deformation. Very fine quartz crystals (<10 µm) are commonly present around the medium to coarse-grained quartz (<500 µm), indicating recrystallization along the crystal rims

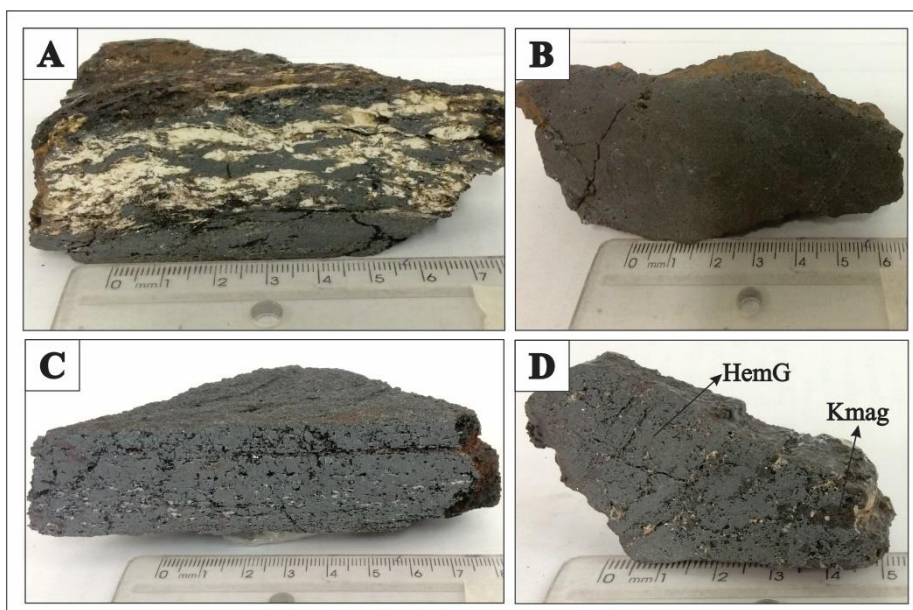


Figure 5.6: Dominant macroscopic features of the Cuité iron ore types. (A) Lamellar-granular hematitic ore, kaolinite-rich. (B) Magnetitic ore. (C) Granular hematitic with lamellar hematite. (D) Granular hematitic (HemG) ore with kenomagnetite blasts (Kmag).

The MO occurs as 0.20-2 m thick hard and massive lenticular bodies inside the granular hematitic ore (Figure 5.6B), with a very incipient foliation. Kenomagnetite occurs as medium to coarse hypidioblastic crystals (0.5 mm to >5 mm), with irregular borders due to the progressive oxidation to martite and hematite (Figure 5.7C-D, 5.8A). Ilmenite occurs as very fine (<50 µm) subeuhedral to anhedral crystals filling the fractures and as inclusion in the hematitic domains. The ilmenite in the fractures is interconnected with the ilmenite inclusions (Figure 5.7D). Some fractures and cavities in the magnetitic ore are filled by goethite (Figure 5.8A).

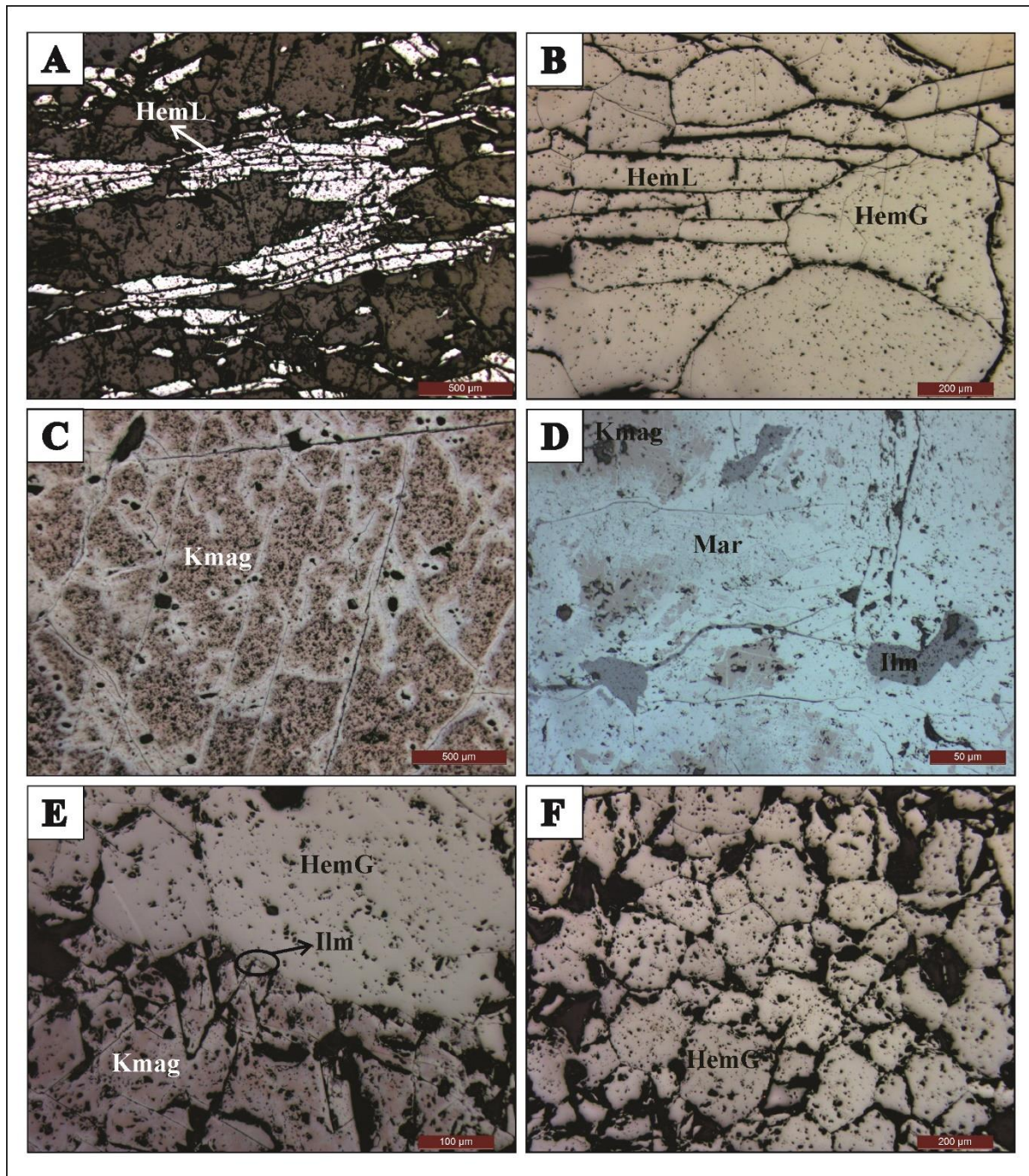


Figure 5.7: Microscopic features of iron oxides from Cuité. (A) Itabirite with alternation of lamellar hematite- and quartz-rich millimetric bands defining a plane-axial foliation. (B) Lamellar-granular hematitic iron ore. (C) Magnetitic iron ore with coarse kenomagnetite with progressive oxidation to hematite along the octahedral cleavage planes. (D) Detail in a more oxidized portion of magnetitic iron ore with ilmenite inclusion, martite, and hematite. (E) Granular hematite-rich iron ore containing kenomagnetite with progressive oxidation to hematite, and ilmenite inclusion. (F) Granular hematite-rich iron ore sample. Photomicrographs were taken under uncrossed polarized reflected light. Abbreviations: HemG – granular hematite, HemL – lamellar hematite, Kmag – kenomagnetite, Mar – martite, Ilm – ilmenite.

The GO is the dominant facies, it is medium to coarse-grained (0.2 mm to 5 mm), comprised predominantly by granular hematite (Figure 5.6C-D), with minor amount of kenomagnetite and lamellar hematite. Apatite, talc, ilmenite, quartz, sericite, kaolinite and rare monazite and carbonate

are the accessory minerals (Figure 5.7E, 5.8B, 5.9B). The ore displays discrete foliation, with polygonal fabric equigranular to inequigranular. Hematite grains may display twinning lamellae and commonly relicts of kenomagnetite, as well as apatite and talc inclusions (Figure 5.9A) comprising a subhedric, granoblastic fabric containing polygonal grains with straight boundaries (Figure 5.7E-F). The contacts have predominantly triple junctions with interfacial angles of approximately 120°, and rarely is observed curved grain boundaries. The kenomagnetite occurs as coarse grained idioblasts (Figure 5.7E) with diffuse borders due to the oxidation. There are very fine (<10 µm) ilmenite crystals along the contact between kenomagnetite and granular hematite. Sericite occurs as fine fibro-radial and oriented aggregates parallel to the foliation. Quartz commonly occur as coarse-grained millimetric thick centimetric length lenses, parallel oriented to the foliation. The granular hematitic ore commonly has millimetric cavities and fractures (Figure 5.6C-D) that are filled by fine grained talc, kaolinite and/or quartz (Figure 5.9B).

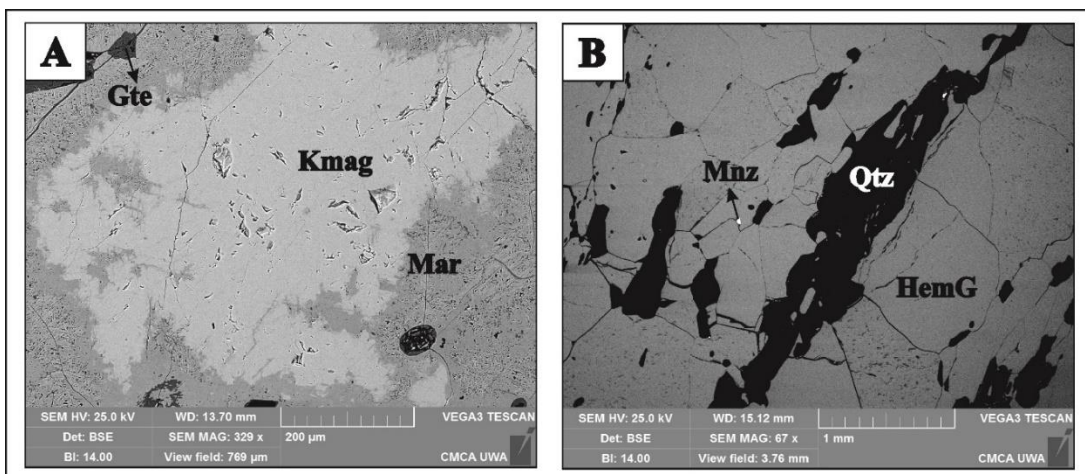


Figure 5.8: Back-scattered images (BSE) of magnetic (A) and granular hematitic (B) high-grade ore samples. Abbreviations: HemG – granular hematite, Kmag – kenomagnetite, Mar – martite, Gte – goetite, Mnz – monazite.

5.7.3. Structural Features

The ductile deformation in Cuité is characterized by a main regional foliation (S_1 —Figure 5.5), in axial plane position of tight to isoclinal millimetric to centimetric intrafolial folds, similar to other iron deposits located at Guanhães Block and in the Southern Espinhaço (Barrote et al., 2017; Rolim et al., 2016; Silveira Braga et al., 2019a, 2015). The itabirite and iron ore schistosity is defined by the orientation of lamellar hematite and quartz and in mica schist by phyllosilicates. Sigmoidal quartz centimetric lenses indicates vergence to S and SW.

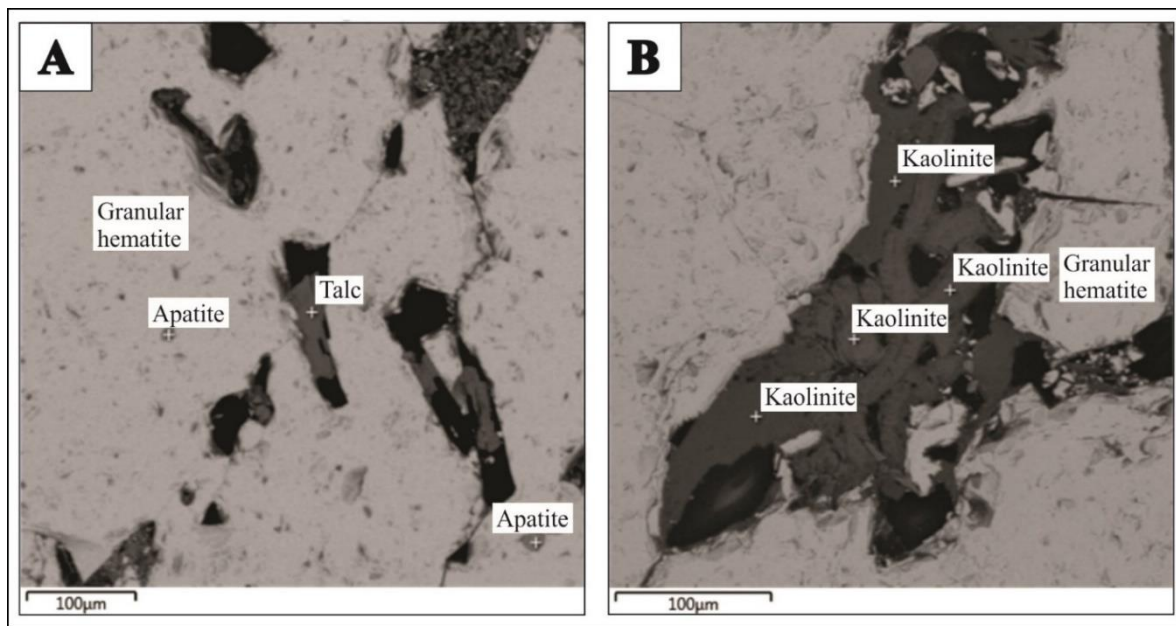


Figure 5.9: Back-scattered images (BSE) of granular hematitic high-grade ore sample C-R3 with points analyzed by EDS (Energy-dispersive X-ray spectroscopy). (A) Detail of apatite and talc inclusion in granular hematite. (B) Aluminum silicate, identified as kaolinite, filling a fracture in granular hematite.

The close to tight folds of the mica schist and itabirite are cm- to dm- scale with NW-SE to N-S axis direction. There are several cm- thick foliated kaolinite-rich lenses, parallel to S_1 , (Figure 5.10A). Close to these lenses the itabirite folds are tighter and are SW-verging. A centimetric mushroom-shaped interference refolding shape (type 2 - Ramsay (1967)) in the itabirite has NNW-SSE second axis direction (Figure 5.10B) and indicates the superposition of folds associated with shear zones. Around the mushroom-shaped fold, there are coarse-grained quartz lenses, and inside the structure, there are granular hematite bands inside the itabirite, both concordant with the structure. The NNW-SSE second axis direction is the same of many macroscopic structural lineaments observed in SRTM image (Figure 5.2).

Foliation boudinage structures with cm- to m- scale are common in the GO and mostly filled with quartz at the neck and with a fish-mouth shape (Figure 5.11). Coarse-grained quartz veins parallel oriented with the foliation boudinage are also common. Close to the quartz-neck there is a concentration of granular hematite, and outside the neck boundaries quartz and kaolinite are interlayered with the granular hematite. At the top and bottom of the quartz-neck the foliation is gently folded. The degree of the curvature of these passive folds decreases away from the quartz neck and becomes parallel to the straight external wall rock foliation.

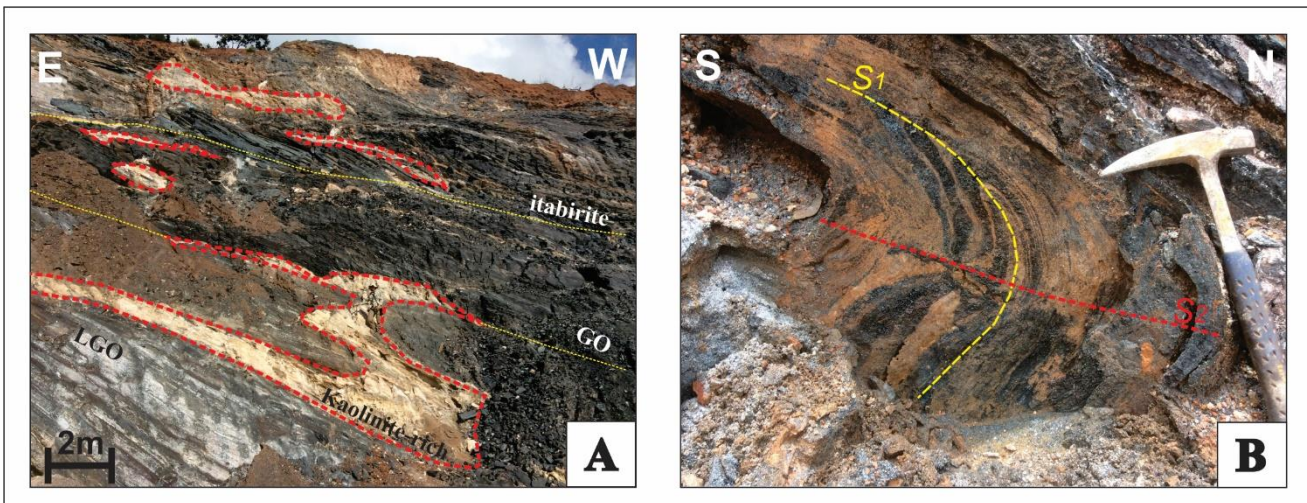


Figure 5.10: Structures from itabirite and ore zones. (A) Kaolinite-rich lenses associated with shearing (UTM 715865 / 7854071 / 924). (B) Mushroom-shaped refold outcrop showing the traces of first (S_1) and second (S_2) axial planes. Abbreviations: LGO – lamellar-granular hematitic ore, GO – granular hematitic ore.

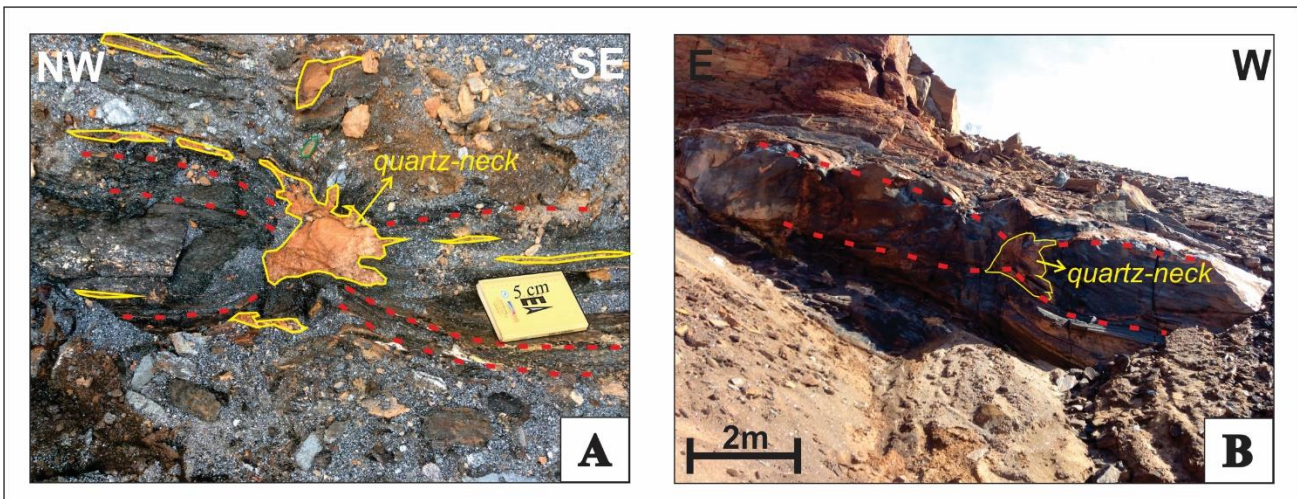


Figure 5.11: Boudin's outcrops in the Cuité ore, with quartz precipitation in the neck. (A) Centrimetric boundin (UTM 715905 / 7854113 / 931). (B) Metric boundin (UTM 715978 / 7854061 / 974).

5.7.4. *The paragenetic sequence of iron oxides generations*

The lamellar hematite is the oldest iron oxide generation identified, it defines the itabirite foliation, and was formed during the syn-deformational stage (Figure 5.7A, B). The kenomagnetite was formed during the late-deformational stage, once it is present as coarse-grained blasts, in the high-grade iron ore bodies (Figure 5.7C-D). The progressive oxidation of kenomagnetite generated the martite and granular hematite, present in the granular hematitic iron ore masses (Figure 5.7E-F, 5.8A-B, 5.12), during the late-deformational stage.

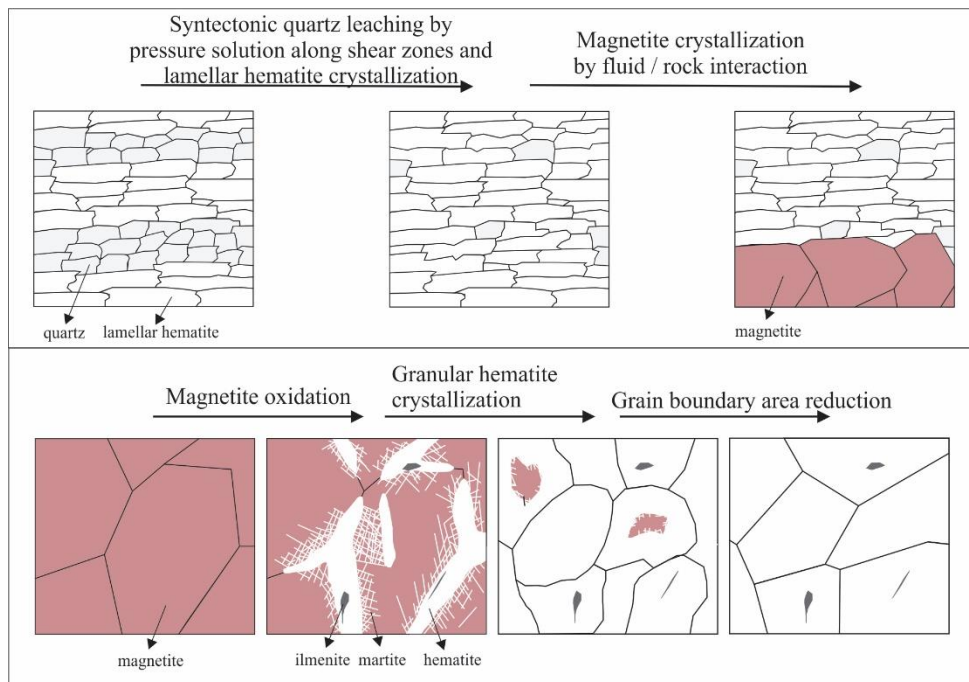


Figure 5.12: Schematic illustration of the iron oxides paragenetic sequence and their chronological.

5.7.5. U-Pb geochronology

Twenty-two analyses were performed on twenty zircon grains of the sillimanite-biotite-quartz schist sample C-R14 (Figure 5.3 and 5.5). The zircons are predominantly subrounded with low-sphericity, indicating a proximal source (Figure 5.14). Some grains display alteration/recrystallization zones, mainly in the grain rims, which are lighter in the BSE images and richer in Pb than the other areas. Twenty spots on detrital zircon core and two spots in recrystallized rim were analyzed. The results are present in Appendix 1B.

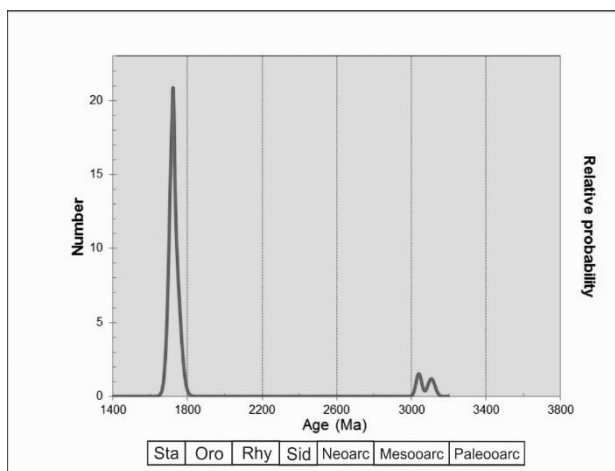


Figure 5.13: Density probability plot of SHRIMP ages of detrital zircon grains from schist sample C-R14, with 90% of Statherian and 10% of Mesoarchean ages. Abbreviations: Sta – Statherian, Oro – Orosirian, Rhy – Rhyacian, Sid – Siderian, Neoarc – Neoarchean, Mesoarc – Mesoarchean, Paleoarc – Paleoarchean.

The results obtained from the zircon core are 90% Statherian (youngest age $1,695.4 \pm 15.1$ Ma) and 10% Mesoarchean (Figure 5.13). The alteration/recrystallization rims yielded Cambrian ages (518.0 ± 31.4 Ma and 495.0 ± 38.6 Ma). The Th/U ratio in the rims is much lower than in the core (0.01-0.02 and 0.20-0.79 respectively).

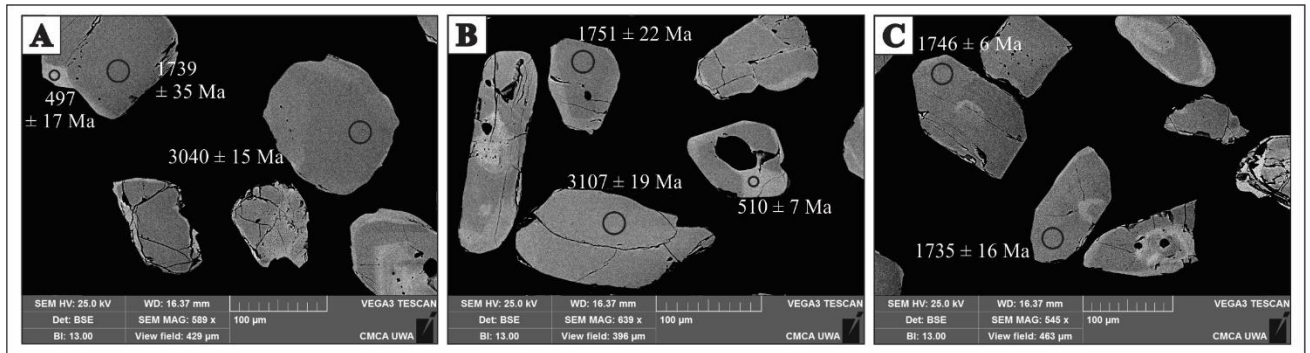


Figure 5.14: Back-scattered images (BSE) of zircons with the location of the spots analyzed and ages obtained.

5.8. Results and discussions

5.8.1. Age and correlation with other iron formation-bearing sequences

SHRIMP detrital zircon data from upper mica quartz schist unit suggest a maximum Statherian age for the supracrustal rocks. This age is much younger than the Archean Rio das Velhas greenstone belt (Hartmann et al., 2006; Machado et al., 1996; Noce et al., 2005), which is interpreted as the metasedimentary sequence of the studied region as proposed by regional maps (Oliveira and Leite, 2000; Pinto and Silva, 2014). The results indicate that the upper psammitic layer is correlated with Serra de São José Group (Figure 5.15), deposited between the Orosirian-Statherian which outcrops along the Serra da Serpentina and Serra do Sapo Ridge (Rolim et al., 2016). This is the upper unit in the IF-bearing sequence from Morro Escuro (Silveira Braga et al., 2015), Guanhães (Barrote et al., 2017) and Horto-Baratinha (Silveira Braga et al., 2019a). The Cuité itabirite seems to be correlated to the Orosirian IF from the Serra do Sapo formation (Serra da Serpentina Group - Rolim et al. (2016) – Figure 5.15).

The zircons sources are Statherian (90%) and Mesoarchean (10%). The Mesoarchean detrital zircons source is probably the TTG terrains of the Gouveia and Guanhães complexes (Noce et al., 2007a, 2007b). The source of the Statherian detrital zircons is presumably the meta-granitic rocks from the Borrachudos Suite (Rolim et al., 2016). The same age groups were found in detrital zircons from Serra da Sepentina, Serra do Sapo (Rolim et al., 2016), Guanhães (Barrote et al., 2017), Morro Escuro (Silveira Braga et al., 2015), Serro (Silveira, 2016) and Horto-Baratinha (Silveira Braga et al., 2019a). However, in these regions was also found a significant Rhyacian/Orosirian (except Horto-Baratinha)

and Paleo- Neo- Archean source. The Rhyacian/Orosirian source is attributed to the rocks from the magmatic-tectonic Minas accretionary event (Teixeira et al., 2015), related with the Rhyacian Orogeny (Brito Neves et al., 2014). The Paleoarchean source correspond to the gneissic complexes located at the southern São Francisco Craton (Hartmann et al., 2006; Machado et al., 1996). The Neoarchean grains are also attributed with TTG terrains of the Gouveia and Guanhães complexes (Rolim et al., 2016).

The ages obtained in the altered / recrystallized regions of the detrital zircons are Cambrian (518.0 ± 31.4 Ma and 495.0 ± 38.6 Ma) and probably related with the late- and post-deformational stages of Brasiliano Orogeny, which was rich in hydrothermal fluids. The low Th/U ratio indicate a possible coexistence, during the alteration/recrystallization process, with Th-rich phases (Rubatto, 2017), such as the monazite crystals found in the GO (Figure 5.8B), or result from low Th/U in the hydrothermal fluids (Ayers and Peters, 2018). However, the nature and extent of this disturbance region is currently unclear and needs further analysis. This Cambrian hydrothermal event is also registered in the Guanhães Complex (Barrote et al., 2017), in the eastern border of the Espinhaço thrust belt (Silveira Braga et al., 2015; Rolim et al., 2016); in Horto-Baratinha (Silveira Braga et al., 2019a) as well as at the eastern high-strain domain of the Quadrilátero Ferrífero in the crystallization of monazite (495.6 ± 2.2 Ma) in the Conceição iron deposit (Cabral et al., 2015).

5.8.2. Structural setting and evolution

Cuité is an IF-bearing high-grade ore deposit located at the western part of Brasiliano Orogeny, in the reworked domain of São Francisco Craton basement, between the Guanhães Block and the Espinhaço fold-and-thrust belt Block (Figure 5.1 and 5.2). The transpressive environment between CT and FC (Figure 5.2) generated a high-strain domain in Cuité, with presence of shear zones and foliation boudinage.

The intense stretching along the foliation planes promoted foliation boudinage, the partial quartz remobilization from itabirite, the formation of quartz-necks and lenses, and consequently the iron oxide concentration. The kaolinite-rich lenses parallel to S_1 , inside the itabirite, LGO and GO layers (Figure 5.10A) are associated with shearing and its origin at least in part is associated with the mica schist unit, once some lenses contain sillimanite. However, some of them could be related with sheared igneous rock. The border of some pegmatite veins are deformed, indicating that part of them could have injected the metasedimentary sequence during the late-deformational stage.

5.8.3. Tectonic fabric and mechanisms of enrichment

There are three high-grade iron ore types in Cuité: lamellar-granular hematitic ore (LGO), granular hematitic ore (GO) and magnetic ore (MO). The formation of centimetric to metric lenses of lamellar high-grade ore is described in Fe deposits along the Meridional Espinhaço fold-thrust belt and west limit of Guanhães Block, such as Morro do Pilar, Serra da Serpentina, Serra do Sapo and Morro Escuro (Gomes et al., 2018; Oliveira et al., 2017; Rolim et al., 2016; Silveira Braga et al., 2015). The genesis of these sheared high-grade orebodies as well as the LGO in Cuité are probably related to syntectonic quartz leaching by pressure solution along shear zones (Figure 5.12) during the early shear stage of the tectonic evolution (Gomes et al., 2018; Oliveira et al., 2017; Rolim et al., 2016; Silveira Braga et al., 2019a).

Horto-Baratinha contains decimetric to metric magnetic enclaves inside the metric pegmatite bodies (Silveira Braga et al., 2019a). There are small (<10 cm) magnetite-rich lenses of compact high-grade iron bodies at Guanhães, locally overprinted by granoblastic hematite (Gomes et al., 2018). The MO in Cuité, like in Horto-Baratinha, could be associated with influx of anatetic fluids from pegmatite intrusions during the late-deformational stage of the Brasiliano Orogeny.

Granular hematitic ore bodies are also observed in Horto-Baratinha (Silveira Braga et al., 2019a), Jambreiro, Candonga (Barrote et al., 2017), Piçarrão and Liberdade (Gomes et al., 2018), and mainly related with the progressive oxidation of magnetite during late- to post-deformational events.

The granular hematite texture in the GO and LGO points to a recrystallization mechanism known as low-temperature grain boundary migration or bulging, which is a process that occurs at high strain conditions (Stipp et al., 2002). The irregular grain boundaries formed during deformation are straightened to a polygonal shape (Knipe, 1989; Stipp et al., 2002). The grain boundary bulge into the crystal with high dislocation density and form new independent small recrystallized crystals as discussed by Stipp et al. (2002). The solubility of a mineral in an aqueous fluid is higher where a crystal lattice is under high stress, like at grain contacts, than at localities where stress is relatively low (Knipe, 1989).

The granular hematite recrystallized by the grain boundary area reduction and the irregular grain boundaries formed during late-deformational stage, became straight and polygonal in the post-deformational stage (Figure 5.12). The recrystallization process occurred during deformation and became dominant after deformation ceased, probably due to the presence of water along the grain boundaries as well as the relatively high temperature when deformation stopped (Knipe, 1989; Stipp et al., 2002).

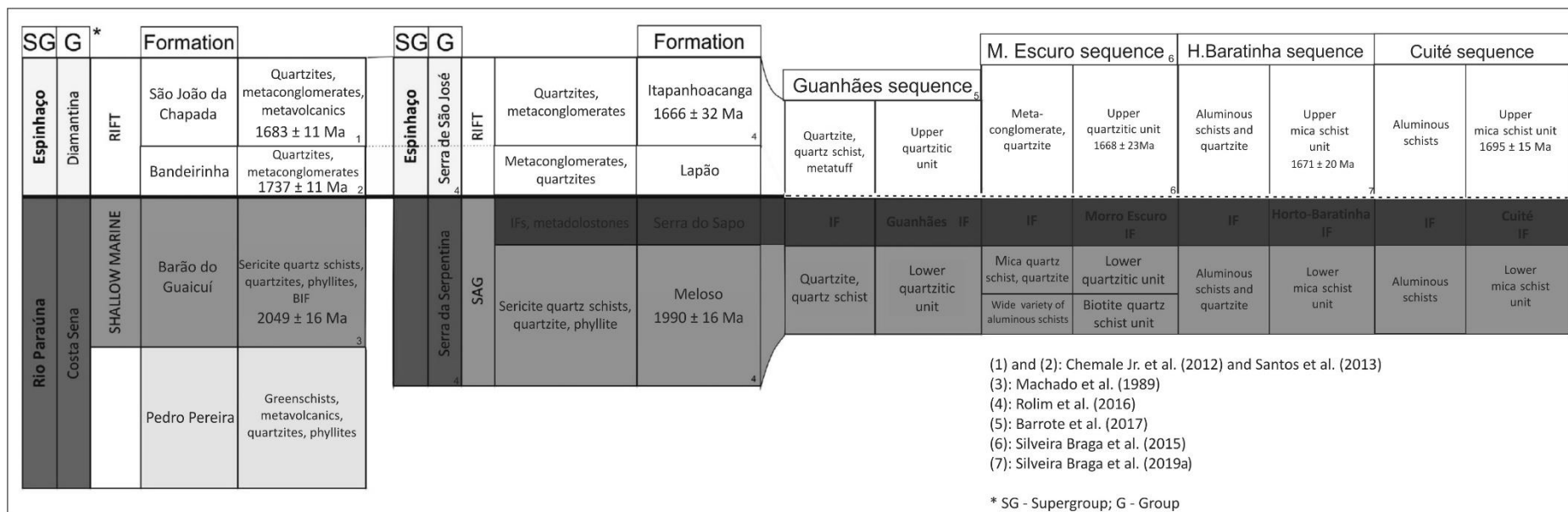


Figure 5.15: Stratigraphic chart of the Espinhaço Supergroup in the Southern Espinhaço range (Chemale et al., 2012; Martins-Neto, 2000; Santos et al., 2013) correlated with the stratigraphic chart of the Serra da Serpentina and Serra de São José groups in the Serpentina Range (Rolim et al., 2016) and to the lithostratigraphic stacking of the Guanhães (Barrote et al., 2017), Morro Escuro (Silveira Braga et al., 2015), Horto-Baratinha (Silveira Braga et al., 2019a) and Cuité (this study) iron deposits. Modified from Barrote et al. (2017) and Silveira Braga et al. (2019a).

5.9. Conclusion

According to the petrographic, structural and geochronological data of Cuité metasedimentary sequence, it is possible to conclude that:

- 1) The lithostratigraphic units that crop out in Cuité deposit comprise metagranitic-gneissic rock (Borrachudos Suite) and IF-bearing psammo-pelitic metasedimentary sequence.
- 2) SHRIMP data of detrital zircon grains of the IF-related upper mica schist has Statherian youngest age ($1,695.4 \pm 15.1$ Ma). This age is much younger than the Archean Rio das Velhas greenstone belt, which was the proposed metasedimentary sequence of the studied area (Oliveira and Leite, 2000; Pinto and Silva, 2014).
- 3) The results indicate that the upper psammitic layer is correlated with the Serra de São José Group, a rift basin tectonically active in the initial stages of the Espinhaço rift opening. The Cuité itabirite represents post-GOE (Great Oxidation Event) iron formation. The itabirite and the lower schist are related with the Serra da Serpentina Group.
- 4) The sequence was affected by oblique shear zones developed in a transpressive environment during the Brasiliano Orogeny generating thrust faults SE verging.
- 5) The intense stretching along the itabirite foliation planes promoted the foliation boudinage, the partial quartz remobilization from itabirite, the formation of quartz necks and lenses, and consequently the iron oxide concentration.
- 6) The three high-grade iron ore types, lamellar-granular hematitic ore (LGO), granular hematitic ore (GO) and magnetitic ore (MO) are related with syn-, late- and late-to-post deformational stages respectively.
- 7) The ages obtained in the recrystallized regions of the detrital zircons are Cambrian (518.0 ± 31.4 Ma and 495.0 ± 38.6 Ma) and probably related with hydrothermal fluids from the late-to post-deformational stages of Brasiliano Orogeny.

5.10. Acknowledgments

This research is part of the Ph.D. thesis of the first author at the Universidade Federal de Minas Gerais, which was financed in part by the Coordenação de Aperfeiçoamento de Pessoal de Nível Superior - Brasil (CAPES) - Finance Code 001 (Pr. 88881.134959/2016-01); Fundação de Amparo à Pesquisa de Minas Gerais (FAPEMIG/VALE CRA - RDP-00067-10-2011). The authors would like to express their gratitude to Peter C. Hackspacher (UNESP) by permission to use the preparation sample lab.

6. ARTIGO IV - CONSTRAINTS ON THE FORMATION OF ITABIRITE-HOSTED IRON ORE DEPOSITS AT THE GUANHÃES BLOCK (BRAZIL) BY CONTACT METASOMATISM WITH PEGMATITE INTRUSIONS

*Flávia Cristina Silveira Braga^{ab}, Carlos Alberto Rosière^c, João Orestes Schneider Santos^d, Steffen G. Hagemann^e, Neal J. McNaughton^f

^a Graduate Program, Instituto de Geociências, Universidade Federal de Minas Gerais, Belo Horizonte, MG, Brazil

^b Faculdade de Engenharia, Universidade do Estado de Minas Gerais, João Monlevade, MG, Brazil

^c Instituto de Geociências, Universidade Federal de Minas Gerais, Belo Horizonte, MG, Brazil

^d Universidade do Estado do Amazonas, Manaus, AM, Brazil

^e Centre for Exploration Targeting, University of Western Australia, Perth, WA, Australia

^f Curtin University of Technology, Perth, WA, Australia

* Corresponding author.

E-mail addresses: flaviacsbraga@gmail.com (F.C. Silveira Braga), crosiere@gmail.com (C.A. Rosière), orestes.santos@bigpond.com (J.O.S. Santos), steffen.hagemann@uwa.edu.au (S.G. Hagemann), n.mcnaughton@curtin.edu.au (N.J. McNaughton), pedrovallesalles025@gmail.com (P.V. Salles)

6.1. Abstract

The Horto-Baratinha (HBD) and Cuité (CTE) high-grade iron ore deposits (>60% wt. Fe) are located at the eastern margin of the São Francisco Craton bordering the Neoproterozoic Brasiliano Orogeny (Araçuaí Orogenic belt). They are hosted by metamorphic (Orosirian to early Statherian) banded iron formation (itabirite) associated with quartzite and aluminous schists that occurs as tectonic inliers in the gneissic terranes of the Guanhães Complex in Minas Gerais state, Brazil. Geochronology, lithostratigraphy and the geochemical whole-rock signature of the iron formation (IF) points to a Lake-Superior sequence type, timely correlated with the IF of the Serra do Sapo Formation exposed in the Serpentina Range on the eastern margin of the Southern Espinhaço fold-thrust belt. In the Guanhães Block the sequence is enclosed by Statherian granitoid of Borrachudos Suite (Açucena pluton) and by Neoarchean gneiss of Guanhães Complex, intruded by pegmatite of Ediacaran to Cambrian crystallization age (from 557 ± 5 to 497 ± 7 Ma). Massive irregular shaped hematite-kenomagnetite high-grade orebodies occur at the contact zone of pegmatite and display a granular fabric, contrasting with the hosting schistose quartz-hematite IF. Mineralization of IF developed in at least three distinct stages during the Brasiliano Orogeny, constrained by petrographic, microchemical and field data: (1) Syn-collisional stage (580-560 Ma) with partial enrichment along sheared zones, associated with transposition of the metamorphic layering and recrystallization of oriented lamellar hematite crystals with very low content of trace elements. (2) A late to post-collisional phase (560 – ~530 Ma) with the formation of massive kenomagnetite bodies by contact metamorphic-metasomatism with the anatetic pegmatite intrusion segregated from the Borrachudos granite. (3) A post-tectonic stage with the oxidation of kenomagnetite to martite and crystallization of granular

hematite by increased input of syn-metasomatic meteoric fluid during gravitational collapse of the orogeny (~530–490 Ma). Mineral chemistry analyses reveals a similar composition of the iron oxides from ore and pegmatite indicating its contemporaneity. Notably, Titanium and Manganese were mobile during the contact-metasomatic stages, generating Mn-rich kenomagnetite, Ti-rich hematite, and ilmenite inclusions.

Keywords: itabirite, iron ore, LA-ICP-MS, magmatic fluids, contact metasomatism

6.2. Introduction

High-grade (>60 wt. % Fe) massive, coarse-grained iron ore bodies are sparsely distributed in the gneissic terrain of the Guanhães Complex along the eastern margin of the São Francisco Craton west of the Brasiliano Orogeny, locally named as Araçuaí Orogenic belt. Together with weathered and partially enriched amphibolite facies metamorphic iron formation (itabirite, IF) they comprise several small deposits (<30 Mt each one) such as Horto-Baratinha, Cuité, Piçarrão, Liberdade, Guanhães iron deposits (Figure 6.1) interlayered with late-Paleoproterozoic psammo-pelitic units (Barrote et al., 2017; Rolim et al., 2016; Silveira Braga et al., 2019a, 2015), as tectonic slivers inserted into Archean and Paleoproterozoic orthogneissic rocks (Brito Neves et al., 2014; Noce et al., 2007b; Silva, 2000). Lens-shaped schistose high-grade ore bodies comprise the Conceição do Mato Dentro, Morro do Pilar and Morro Escuro deposits at the eastern border of the Espinhaço fold-thrust belt (Figure 6.1). These orebodies are <300 m long with maximum thickness of some tens of meters, controlled by shear zones in the more continuous tectonic outliers of the Orosirian-Statherian Serra da Serpentina Group (Rolim et al., 2016; Silveira Braga et al., 2015).

The Horto-Baratinha (HBD) and Cuité (CTE), similar to Piçarrão and Liberdade deposits (Gomes et al., 2018; Silveira Braga et al., 2019a) are located in the southernmost part of the Guanhães Complex (Figure 6.1), comprise 100 m long, <60 m thick lenticular to irregular granular hematite-kenomagnetite high-grade iron ore bodies closely associated with metric pegmatite and quartz dikes, sills and veins. Whole-rock and mineral chemistry studies from HBD and CTE supported by field mapping and geochronology delivered new and exciting findings about the origin of the ore and its tectonic implications, that distinguish them from the other deposits of the Eastern Espinhaço belt. Our results open a new perspective for the understanding of hypogene Fe-enrichment processes of iron formations (IF) the source of mineralizing fluids, and the partitioning behavior of major and trace elements.

6.3. Regional geology

The Horto-Baratinha and Cuité granular hematite and kenomagnetite-rich iron deposits are hosted by amphibolite facies IF that occur as tectonic slivers encased in the gneisses of $2,867 \pm 10$

Ma to $2,713.3 \pm 6.5$ Ma Guanhães Complex (Silva et al., 2002; Silveira Braga et al., 2019a) that, together with other deposits and occurrences widely spread in the Guanhães tectonic block. They are correlative with the Orosirian Serra da Serpentina Group that underlie the Statherian siliciclastic rift and sag sequences of the Espinhaço Supergroup, which were deposited in a number of basins over the period of 1.8 to 1.0 Ga (Chemale et al., 2012; Guadagnin and Chemale, 2015).

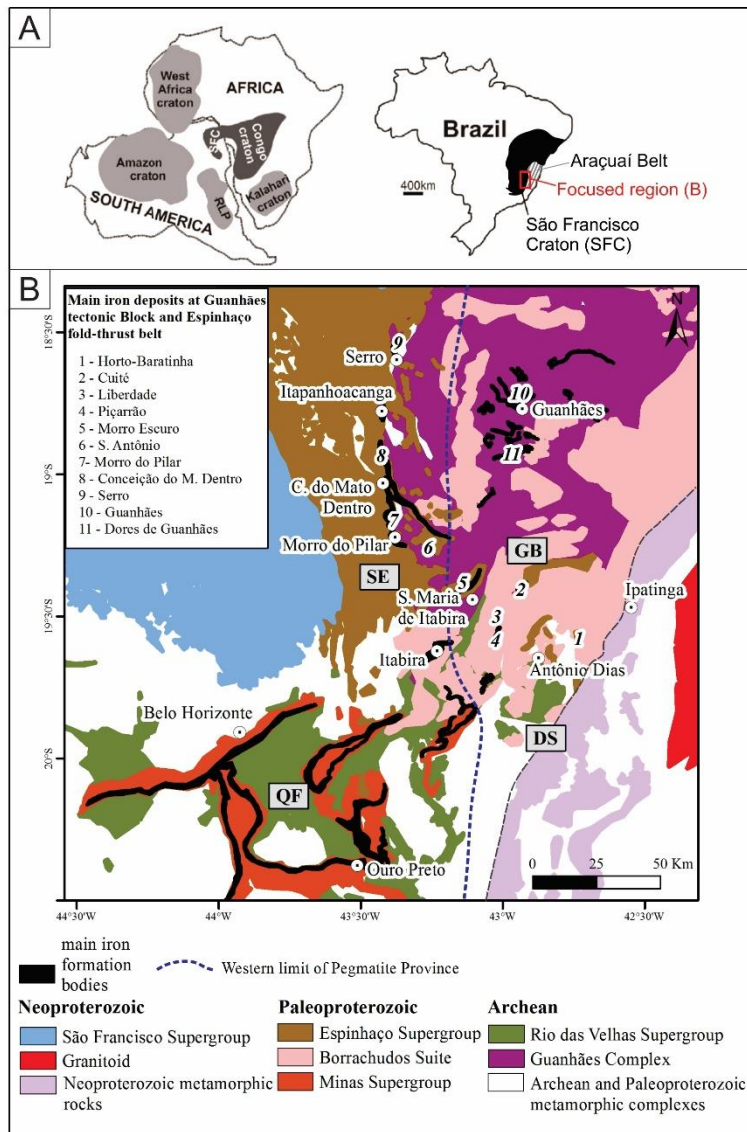


Figure 6.1: (A) Geotectonic configuration of the São Francisco-Congo Craton in the context of West Gondwana (after Alkmim et al., 2006) and SFC limit (Santos et al., 2019). (B) Simplified regional geological map of the southeast portion of São Francisco Craton and western part of Neoproterozoic Araçuaí fold-thrust belt with the distribution of the main geological units, between the Quadrilátero Ferrífero Province (composed by Rio das Velhas and Minas Supergroup) and the location of Guanhães. The distribution of the geological units is based on Pinto and Silva (2014). Abbreviations: SE - Serra do Espinhaço fold-thrust belt, GB- Guanhães Block, QF – Quadrilátero Ferrífero Mineral Province, DS – Dom Silvério shear zone.

The Guanhães Complex builds up a N-S direction elongated tectonic block that extends from the town of Santa Maria de Itabira in the southwest up to 250 km to northeast, composed mainly by

pre-Rhyacian orthogneissic rocks that enclose deformed fragments of Orosirian/Statherian metasedimentary units and anorogenic alkaline metagranitic of the Statherian Borrachudos Suite. The Borrachudos Suite is associated with a long-lived silicic igneous province developed in the interval 1,750–1,710 Ma during the Espinhaço taphrogenic event (Magalhães et al., 2018). All units are intruded by Ediacaran-Ordovician pegmatites bodies (Gomes et al., 2018; Pedrosa Soares et al., 2011; Silveira Braga et al., 2019a).

The Guanhães Complex comprises an uplifted segment of Paleoproterozoic deeper crustal roots reworked and upthrust on the tectonic shallow Espinhaço fold-thrust belt during the Brasiliano Collage in the Neoproterozoic-Cambrian boundary. To the east, the Guanhães Complex is bound by the NE-SW regional scale Dom Silvério and Abre Campo shear zones that separates the crystalline rocks from Neoproterozoic supracrustals of the Araçuaí belt (Figure 6.1). The pegmatite intrusions are late to post-tectonic features generated in the extensional of the Brasiliano Orogeny, between 630 to 480 Ma (Pedrosa Soares et al., 2011).

6.4. Methodology

6.4.1. Geochronology U-Pb SHRIMP – sample selection and methods

Zircons from pegmatite samples were analyzed by U-Pb SHRIMP method (Sensitive High-Resolution Ion Microprobe) at John de Laeter Centre for Isotope Research, Curtin University in Perth, Australia. The samples were processed with conventional crushing, grinding and screening methods at the LOPAG-DEGEO laboratory of Universidade Federal de Ouro Preto, Brazil and at the Instituto de Geociências of Universidade Estadual Paulista, in Rio Claro, Brazil. After the screening, the heavy fraction concentration of 60-250 mesh was pre-concentrated by panning. After the concentration, samples were sieved and washed to remove clay and silt size. The 60-250 pre-concentrate was purified using heavy liquid (LST, lithium heteropolytungstate or bromoform) to remove all light minerals. Then a Frantz LB1 magnetic separator was used to separate the less magnetic minerals such as non-metamictic zircons.

Zircon was handpicked and organized in an epoxy mount, which was polished and carbon-coated for SEM (Scanning Electron Microscope) study using BSE (Backscattered electrons) that were taken using a TESCAN VEGA3 at the CMCA-UWA (Centre for Microscopy, Characterization and Analysis - University of Western Australia), in Perth, Australia. Imaging of the zircon with BSE is critical for identifying internal features, such as core and rims, and to avoid areas with high common lead content (inclusions, fractures, and metamict areas).

Epoxy mounts were coated with gold for SHRIMP analysis. Most SHRIMP analytical spots were in the diameter range of 20-30 μm but some analysis used a spot size of only 10 μm . Six scans were used for each spot analysis. The following masses were analyzed for zircon: $^{196}\text{Zr}2\text{O}$, ^{204}Pb ,

background, ^{206}Pb , ^{207}Pb , ^{208}Pb , ^{238}U , ^{248}ThO , ^{254}UO . The calibration of Pb/U ratios was conducted using the zircon standards M257 (561.3 Ma - Nasdala et al. (2008)) and BR266 (559 Ma, 903 ppm U - Stern, (2001)). Data with common lead correction greater than about 1% were rejected during the first scan. The uncertainties of individual ages are quoted at the 1σ level, whereas the plotted ages are calculated at 2σ levels (about 95% confidence). SHRIMP data were reduced using SQUID software (Ludwig, 2001) and plots were prepared using ISOPLOT/Ex (Ludwig, 2003). The data obtained are present in Appendix 1C.

6.4.2. Whole-rock geochemistry

A total of 17 whole-rock samples from open pit and drill core, collected below weathering zone, were selected for major oxide element, trace element, and rare earth elements (REE) geochemistry. Samples included two iron formation and 15 iron ore samples (Table 6.1). The small number of iron formation (itabirite) samples was due to difficulties in identifying unweathered specimens.

Sample ID	Classification	Origin	Mineralogy	Fe_2O_3 content (wt.%)
B-R28	Iron formation	open pit	Qtz + HemL + HemG	62.20
B-S48	Iron formation	drill core (25.00 m depth)	Qtz + HemL + HemG + Chl + Tr-Act	46.39
B-S40	Iron ore	drill core (60.35 m depth)	HemG + Kmag + Tlc	74.54
B-S44	Iron ore	drill core (83.37 m depth)	HemG + Kmag + Tlc	79.73
B-S46	Iron ore	drill core (106.70 m depth)	HemG + Kmag + Cum-Gru	71.84
B-S31	Iron ore	drill core (38.97 m depth)	HemG + Kmag + Chl + Cb + Cum-Gru	95.45
B-S42	Iron ore	drill core (40.16 m depth)	HemG + Kmag + Cb	96.41
B-S47	Iron ore	drill core (72.05 m depth)	HemG + Kmag + Chl + Tr-Act + Ap	94.78
B-S34	Iron ore	drill core (40.65 m depth)	HemG + Kmag + Chl + Tr-Act + Tlc	95.98
B-S27	Iron ore	drill core (42.52 m depth)	HemG + Kmag + Chl	97.08
B-S28	Iron ore	drill core (47.64 m depth)	HemG + Kmag + Chl	96.07
B-R27	Iron ore	open pit	HemG + Chl + Kmag + Ap	92.42
C-R03	Iron ore	open pit	HemG + Kmag + Kln + Ap + Cum-Gru	99.31
C-R04	Iron ore	open pit	Kmag + Hem + Ilm	98.51
B-S11	Iron ore	drill core (63.10 m depth)	HemG + HemL + Chl + Bt + Qtz	90.91
B-R31	Iron ore	open pit	HemG + Kmag + Ms + Chl + Cb	92.16
B-R26	Iron ore	open pit	Kmag + HemG + Chl + Bt + Cb + Ap	88.38

Table 6.1: List of whole-rock geochemical data including details of rock classification, sample origin, mineralogy, and Fe_2O_3 content. Abbreviations: HemG – granular hematite, HemL – lamellar hematite, Hem – hematite, Kmag – kenomagnetite, Ap – apatite, Bt – biotite, Cb – carbonate (dolomite + calcite), Chl – chlorite, Cum-Gru – cummingtonite-grunerite, Tr-Act – tremolite-actinolite, Ilm – ilmenite, Kln – Kaolinite, Ms – muscovite, Qtz – quartz, Tlc – talc.

Chemical analysis was performed at the Bureau Veritas Mineral Laboratory, Canada, using the ICP-MS (Inductively Coupled Plasma Mass Spectroscopy) method. Eleven major oxides were analyzed by ICP-MS following a lithium fusion and dilute acid digestion of a 0.2 g sample pulp. Forty-six trace elements were analyzed using aqua regia digestion to precious and base metals. Analytical accuracy was tested with the international standard SO-19 from USGS, with an achieved

accuracy of $\pm 3\%$ SD. Precision was measured by the analysis of identical duplicate samples with an error of $\pm 4\%$ RSD. Whole-rock geochemical results are given in Appendix 2.

All presented REE+Y fractionation trends are normalized to post-Archean Australian shale (PAAS – McLennan, (1989), shale normalization SN) with anomalies calculated using: Eu/Eu^{*}_(SN) = Eu_(SN) / 0.66Sm_(SN) + 0.33Tb_(SN); Ce/Ce^{*}_(SN) = Ce_(SN) / 0.5La_(SN) + 0.5Pr_(SN); Y/Y^{*}_(SN) = Y_(SN) / 0.5Dy_(SN) + 0.5Ho_(SN); Pr/Pr^{*}_(SN) = Pr_(SN) / 0.5Ce_(SN) + 0.5Nd_(SN).

6.4.3. *In situ LA-ICP-MS analysis of iron oxides*

Nine samples (2 iron formation, 2 pegmatite, and 5 iron ore) were selected for in situ trace element and REE+Y mineral chemistry (Table 6.2). The SEM study using BSE and EDS (Energy Dispersive Spectrometry) was undertaken using a TESCAN VEGA3 at CMCA-UWA and at Universidade do Estado de Minas Gerais, in João Monlevade, Brazil, to better characterize the mineral texture and choose the analytical spots. The LA-ICP-MS analyses were conducted using an Agilent 7500cs ICP-MS coupled with a Resonetics Resolution ArF 193 nm Excimer laser at CODES (Centre for Ore Deposit and Earth Sciences), University of Tasmania, in Hobart, Australia. Samples were ablated in an M50 constant geometry cell (Laurin Technic, Australia) in a He atmosphere (flow rate 0.6 L/min) and the aerosol mixed with Ar carrier gas (flow rate 0.84 L/ min) for transport to the ICP-MS. Laser beam size and pulse frequencies were 30 μm and 5 Hz, with laser energy of 5.5 J/cm². The standard GSD-1G and BCR-2G from USGS (Jochum et al., 2005) were used for calibration and drift correction. The following isotopes were measured: ⁷Li, ²³Na, ²⁴Mg, ²⁷Al, ²⁹Si, ³¹P, ³⁴S, ⁴³Ca, ⁴⁵Sc, ⁴⁷Ti, ⁴⁹Ti, ⁵¹V, ⁵³Cr, ⁵⁵Mn, ⁵⁷Fe, ⁵⁹Co, ⁶⁰Ni, ⁶³Cu, ⁶⁵Cu, ⁶⁶Zn, ⁶⁹Ga, ⁷¹Ga, ⁷⁵As, ⁸⁸Sr, ⁸⁹Y, ⁹⁰Zr, ⁹³Nb, ⁹⁵Mo, ⁹⁸Mo, ¹⁰⁷Ag, ¹¹⁸Sn, ¹²¹Sb, ¹³³Cs, ¹³⁷Ba, ¹³⁹La, ¹⁴⁰Ce, ¹⁴⁶Nd, ¹⁴⁷Sm, ¹⁵³Eu, ¹⁵⁷Gd, ¹⁶³Dy, ¹⁶⁶Er, ¹⁷²Yb, ¹⁷⁵Lu, ¹⁷⁸Hf, ¹⁸¹Ta, ¹⁸²W, ¹⁹⁷Au, ²⁰⁶Pb, ²⁰⁷Pb, ²⁰⁸Pb, ²⁰⁹Bi, ²³²Th, ²³⁸U. The generated counts per second (cps) data were reduced using the SILLS software (Guillong et al., 2008). Detection limits vary depending on the selected calculation time span, which has an average of 47.5 seconds. The average detection limits per element are listed in Appendix 3, and the average and standard deviation of the LA-ICP-MS analysis separated by iron oxide generation are presented in Appendix 4.

During the manual data reduction, the mixed signals, characterized by a significant drop in the Fe spectrum and simultaneous increase of others spectra peaks (*e.g.* Si, Ca, Al, Mg, REE+Y) were excluded from the time resolved spectrum, subsequently, the data reduction was only applied to the pure signal. Calculations applied over a reduced spectrum result in a degradation of detection limits. Some analysis were excluded from the data set due to the significant mixing of mineral phases and represented analytical outliers.

Three different isotopes (^{63}Cu , ^{65}Cu ; ^{69}Ga , ^{71}Ga ; ^{95}Mo , ^{98}Mo) from the same elements were measured in order to monitor potential interference such as $^7\text{Li}^{56}\text{Fe}$ on ^{63}Cu ; $^{24}\text{Mg}^{40}\text{Ar}$ and $^{49}\text{Ti}^{16}\text{O}$ on ^{65}Cu ; $^{55}\text{Mn}^{40}\text{Ar}$ on ^{95}Mo ; $^{53}\text{Cr}^{16}\text{O}$ on ^{69}Ga ; $^{55}\text{Mn}^{16}\text{O}$ on ^{71}Ga . The differences between the two isotopes of the same element were compared with the detection limit value to monitor possible interferences. The Cu concentration in all samples are predominantly below the detection limit so this element was not used for interpretation. Any interference was verified for Ga and Mo.

Sample ID	Classification	Origin	Analyzed minerals			
			HemL	HemG	Kmag	Mar
B-R28	Iron formation	open pit	X	X		
B-R62	Iron formation	open pit	X	X	X	X
B-S27	Pegmatite	drill core (42.50 m depth)	X	X		
B-S54	Pegmatite	drill core (66.10 m depth)			X	
C-R04	Iron ore	open pit			X	X
C-R10	Iron ore	open pit	X	X		
B-R27	Iron ore	open pit		X	X	
B-S11	Iron ore	drill core (63.10 m depth)	X	X		
B-R31	Iron ore	open pit	X	X	X	X

Table 6.2: List of samples analyzed by in situ LA-ICP-MS, including details such as rock classification, sample origin, and iron oxide generation analyzed. Abbreviations: HemG – granular hematite, HemL– lamellar hematite, Kmag – kenomagnetite, Mar – martite.

The following elements presented more than 40% of analysis below detection limit: ^7Li , ^{23}Na , ^{31}P , ^{43}Ca , ^{63}Cu , ^{65}Cu , ^{88}Sr , ^{107}Ag , ^{133}Cs , ^{137}Ba , ^{139}La , ^{140}Ce , ^{146}Nd , ^{147}Sm , ^{153}Eu , ^{157}Gd , ^{163}Dy , ^{166}Er , ^{197}Au , ^{208}Pb , ^{209}Bi , ^{232}Th . The REE+Y interpretation is based on data with concentrations over detection limits.

6.5. The HBD and CTE geological setting

The Horto-Baratinha and Cuité deposits are hosted by an IF stratum between two mica schist layers. The youngest detrital zircons of the upper metasedimentary unit delivered an Statherian age ($1,671 \pm 20$ Ma - Silveira Braga et al., 2019a) indicating a contemporaneity of the IF with the Serra da Serpentina Group that has an Orosirian maximum depositional age (youngest U-Pb SHRIMP detrital zircon date is $1,990 \pm 16$ Ma; Rolim et al., 2016) or alternatively (but less probably) with the Canjica IF of the Serra de São José Group, with a maximum depositional age of $1,666 \pm 32$ Ma (U-Pb SHRIMP age for detrital zircon; Rolim et al., 2016). The sequence is laterally discontinuous, tectonically enclosed in Neoarchean orthogneiss ($1,713.3 \pm 6.5$ Ma – U-Pb SHRIMP) and intruded by an irregular shaped metagranite body of the Açucena pluton (Borrachudos Suite – Figure 6.2) with crystallization age of 1,740 Ma (Silveira Braga et al., 2019a). In HBD a layer of amphibole schist separates the upper mica schist from the IF and is increasingly iron richer at the contact zone with IF.

In both deposits the units have undergone metamorphism under prograde conditions between intermediate to high amphibolite facies during the Ediacaran-Cambrian Brasiliano Orogeny and all sedimentary structures were transposed by the early development of shear zones parallel to the lithologic contacts (Silveira Braga et al., 2019a). The CTE orebody is tabular shaped and broadly associated with ENE-WSW-trending shear zones parallel to sub-parallel to regional-scale SE- and NW-verging thrust faults (Oliveira and Leite, 2000) with the development of a low-angle dipping coarse-grained schistosity that is emphasized by quartz veining, obliterates the primary structures and raises considerable doubt about the relative stratigraphic position of the strata of the layered units. Superposed folds comprising a type 2 interference pattern (mushroom-shaped) is observed in the intrafolial isoclinal folds (Ramsay, 1967) and foliation boudinage structure of metric size are also well developed.

The HBD intrafolial folds are equally ubiquitous with the occasional observation of relictic hinges of the buckles and is hard to establish the stratigraphic sequence. In this deposit, however, the macro-structure is defined by the development of superposed open folds that overprint the foliation and build a wide dome and basin interference pattern with N-S and E-W axes (Silveira Braga et al., 2019a). Contrastingly, the orebodies occur as irregular shaped pods of variable size, <100 m long and <60 m thick, lacking any apparent tectonic control and bordered by pegmatite intrusions (Silveira Braga et al., 2019b).

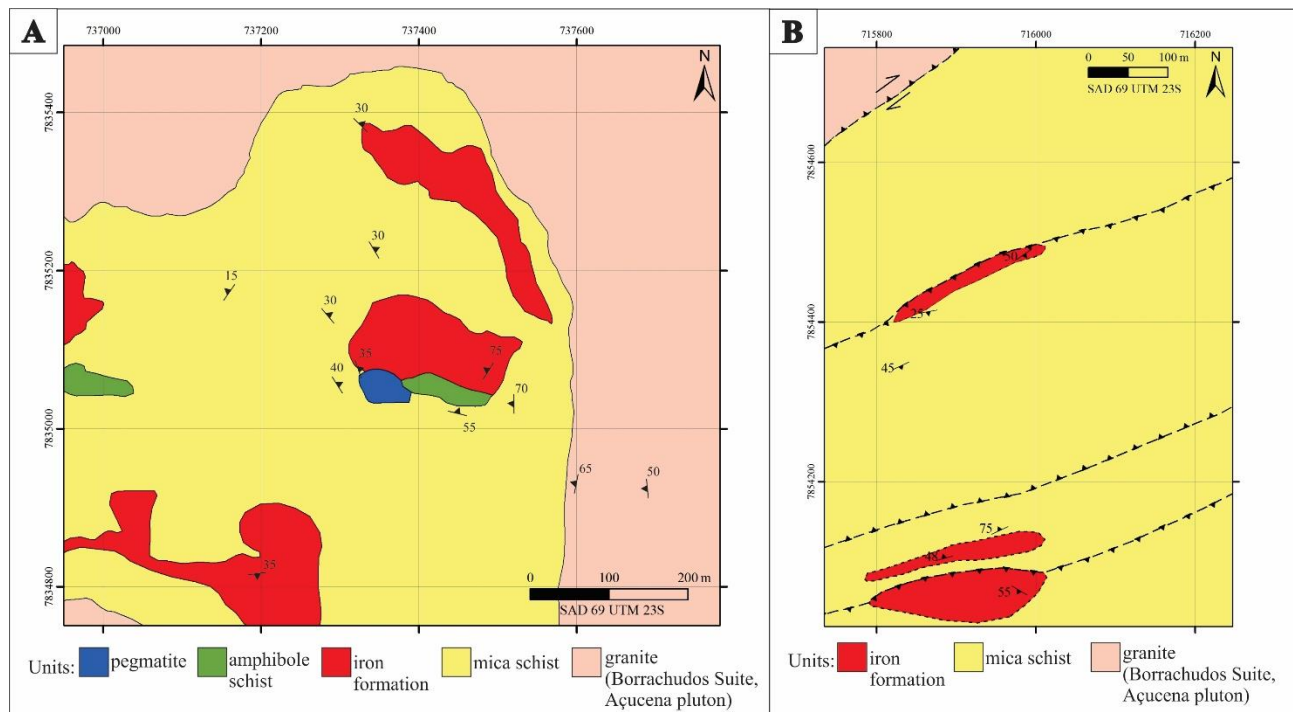


Figure 6.2: Lithological map of Horto-Baratinha (A), (Silveira Braga et al., 2019a) and Cuité (B) deposits.

In both deposits undeformed quartz veins and pegmatite bodies permeate the IF, commonly discordant and rarely concordant. The pegmatite bodies are few centimeters to 30 m thick (Figure 6.3B, C, D, F, I, J) comprised of quartz, microcline, plagioclase, biotite, muscovite, apatite and iron oxides (granular-lamellar hematite and kenomagnetite – Figure 6.3I, J and 6.6H, I). In HBD decimetric magnetic clusters occur disseminated in the largest pegmatite bodies (Figure 6.2A and 6.3C) and, it is common in the border of the bodies the presence of coarse lamellar hematite crystals randomly oriented. In contrast, the CTE pegmatites occur as relatively thin intrusion (<1 m) and are less frequent than in HBD.

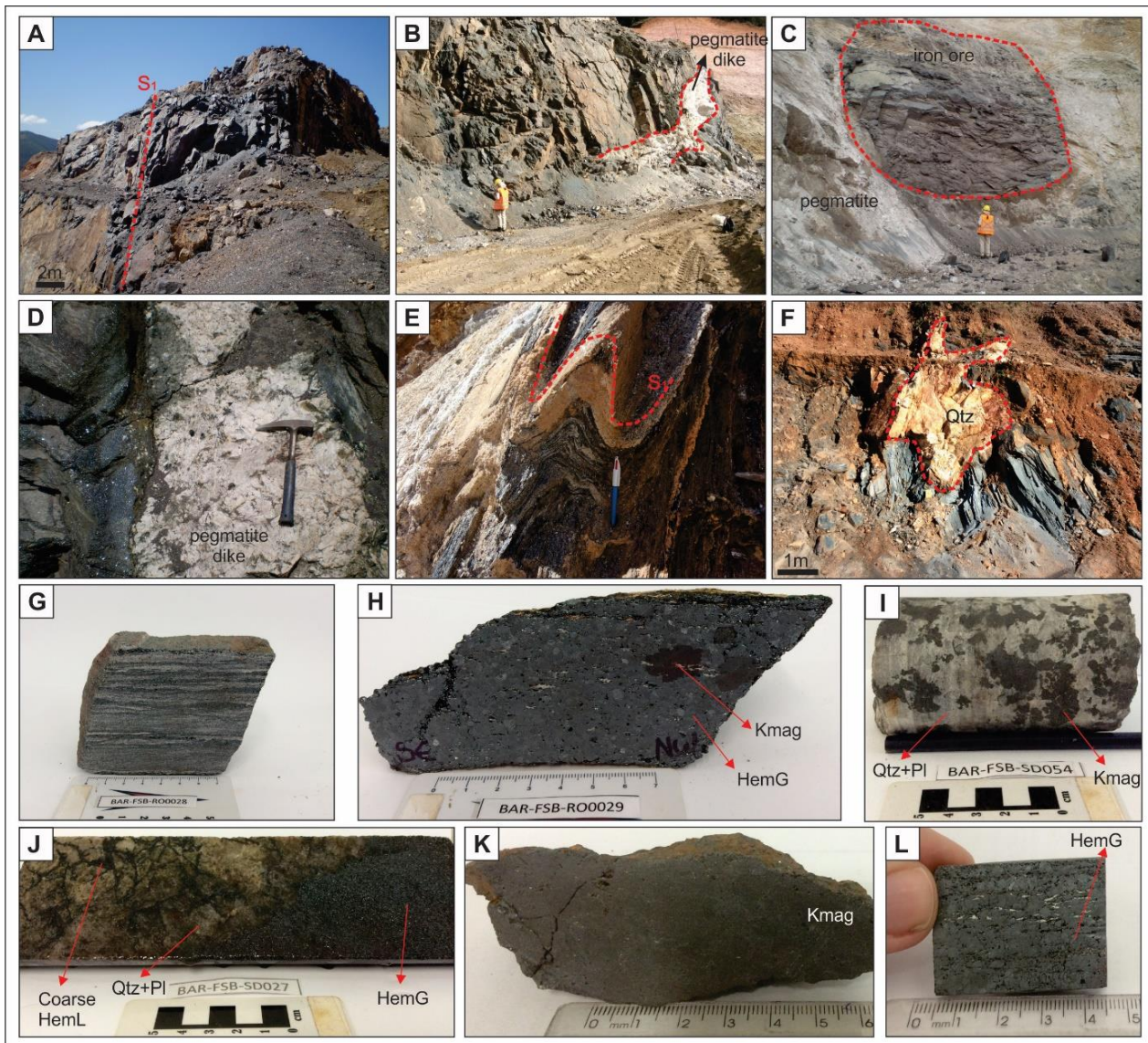


Figure 6.3: Dominant macroscopic features of HBD and CTE ore deposits. (A) Iron formation domain with sub-vertical foliation (S_1) containing decametric iron ore bodies – HBD. (B) Pegmatite crosscutting iron formation – HBD. (C) Decametric pegmatite intrusion with an iron ore body inside, as an enclave – HBD. (D) Detail of pegmatite dike containing coarse lamellar hematite close to the contact with the iron ore – HBD. (E) Slightly friable IF with folded foliation – CTE. (F) Remobilized metric quartz body inside IF – CTE. (G) Least-altered IF with characteristic micro-banding with alternating iron oxide- and quartz-rich layers – HBD. (H) Iron ore containing granular hematite, coarse-grained kenomagnetite and fine chlorite crystals – HBD. (I) Kenomagnetite-rich pegmatite – HBD. (J) Contact between pegmatite

containing coarse lamellar hematite with granular hematite-rich iron ore – HBD. (K) Kenomagnetite-rich iron ore – CTE. (L) Iron ore containing predominantly granular hematite – CTE. Abbreviations: HemG – granular hematite, HemL – lamellar hematite, Kmag – kenomagnetite, Qtz – quartz, Pl – Plagioclase, S₁ – foliation plane

6.5.1. Age of the pegmatites

Zircon grains were separated for geochronology from two pegmatite samples collected in HBD: sample B-R36 was taken from a vein hosted by the Borrachudos granite, and B-R12 from a pegmatite intersecting the IF (Figure 6.3B). The SHRIMP data is depicted in Appendix 1C. The cores of the zircons from sample B-R36 display a rounded shape and are very fractured, whereas the rims show igneous zoning, prismatic habit and are less fractured (Figure 6.4A, B, C). Two groups of ages were obtained, one Statherian and the other Cambrian (Figure 6.5A, B). The zircon cores have the oldest age of $1,740.8 \pm 4.7$ Ma (Figure 6.5A). The zircon rims have Concordia age of 503.3 ± 5.7 Ma, and low Th/U ratio (0.0058-0.0076), (Figure 6.5B). The zircons from the sample B-R12 are different from the sample B-R36. They do not have the core/rim division and are considerably metamictic and fractured (Figure 6.4C). The most homogeneous regions were dated with the smallest spot (10 µm), due to its high Pb content, and was obtained ages from 518.1 ± 3.0 to 556.7 ± 5.0 Ma with a low Th/U ratio varying between 0.0323-0.0427 (Figure 6.5C).

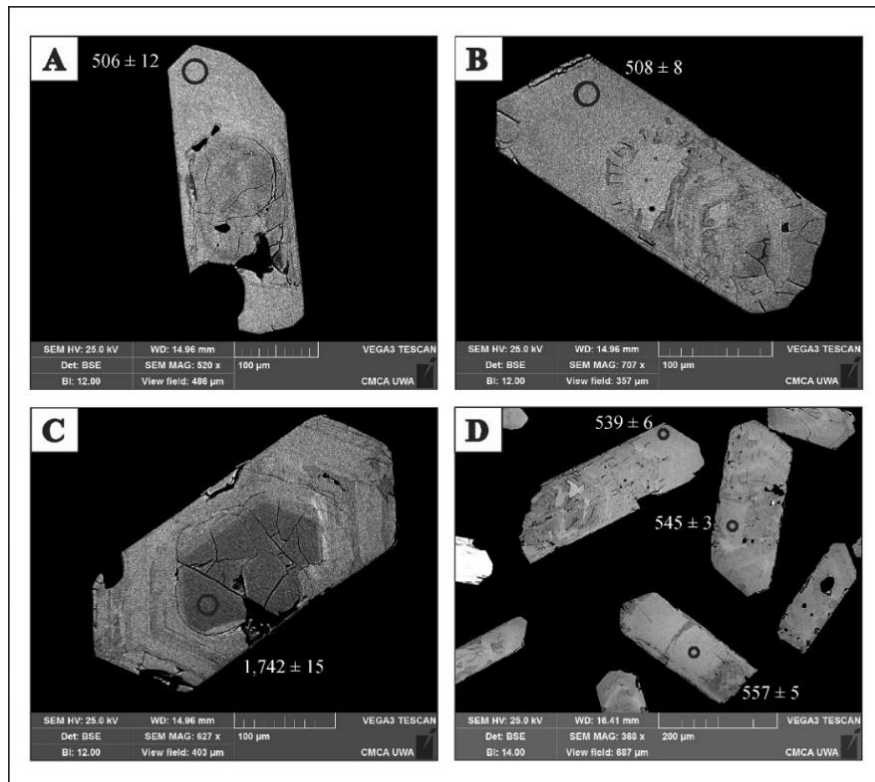


Figure 6.4: Back-scattered images (BSE) of zircons from the following pegmatite samples: (A), (B) and (C) B-R36; (D) B-R12.

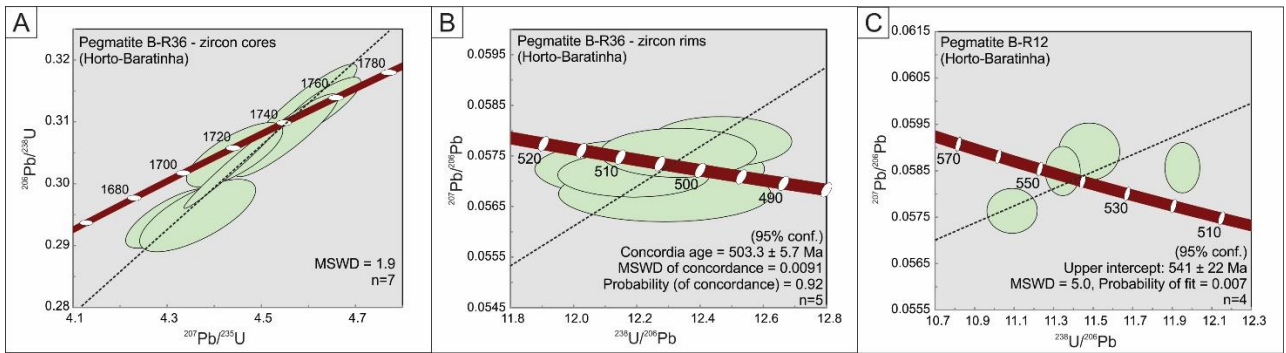


Figure 6.5: Discordia and Concordia diagrams of zircons from the following pegmatite samples: (A) B-R36 (analysis in the zircon rim); (B) B-R36 (analysis in the zircon core); (C) B-R12.

6.5.2. Iron formation

The IF that host the high-grade orebodies from HBD and CTE is monotonous and essentially comprised of quartz and lamellar hematite with a whole-rock Fe content lower than 45 wt.%. The rock displays a fine to medium grained (0.01 mm – 1.0 mm) schistosity, axial planar to rootless isoclinal folds and parallel to the lithological contacts of the layered assembly, ubiquitous in the IF slivers encased in the Guanhães Complex. The foliation which contain a shape fabric and a mineral lineation arise from the parallel arrangement of elongated hematite platelets (Figure 6.3A, E, G) clustered in lens-shaped aggregates and bands that alternate with quartz-rich domains comprised of coarser and more equant grains. (Figure 6.3G and 6.6A, B). The accessory minerals, chlorite, tremolite-actinolite, talc and kaolinite are also concentrated in millimetric spindle shaped aggregates. Idioblastic megacrystals (<200 µm) of kenomagnetite grow over the foliation. They may be partially oxidized displaying a core of kenomagnetite/maghemite and rims of martite/hematite or are otherwise completely altered to martite or recrystallized to granular hematite.

6.5.3. Hypogene iron ore

6.5.3.1. Horto-Baratinha iron ore

High-grade iron ore bodies from HBD have an irregular shape with average thickness of <60 meters and display a granoblastic, fine to coarse-grained (0.01 mm – 3.0 mm) fabric (Figure 6.3H and 6.6F, G). They are comprised mainly of granular hematite and subordinate kenomagnetite that overgrows few relicts of lamellar grains (Silveira Braga et al., 2019a). Ilmenite, quartz, carbonates (calcite and dolomite), chlorite, cummingtonite-grunerite, tremolite-actinolite, biotite, talc, apatite and muscovite occur as accessories (Silveira Braga et al., 2019a). Kenomagnetite from high-grade ore, similar to the sparse grain from the IF occur as medium to coarse crystals, hypidiomorphic, partially oxidized to hematite along the border and octahedral cleavage planes. The more extensive and continuous high-grade ore bodies from HBD are close to the largest pegmatite intrusions, as

shown by an 3D lithological model (Silveira Braga et al., 2019b). Higher concentrations of carbonate (calcite and dolomite), chlorite, cummingtonite-grunerite, tremolite-actinolite, biotite, talc, apatite and muscovite are also found near the contact with pegmatite.

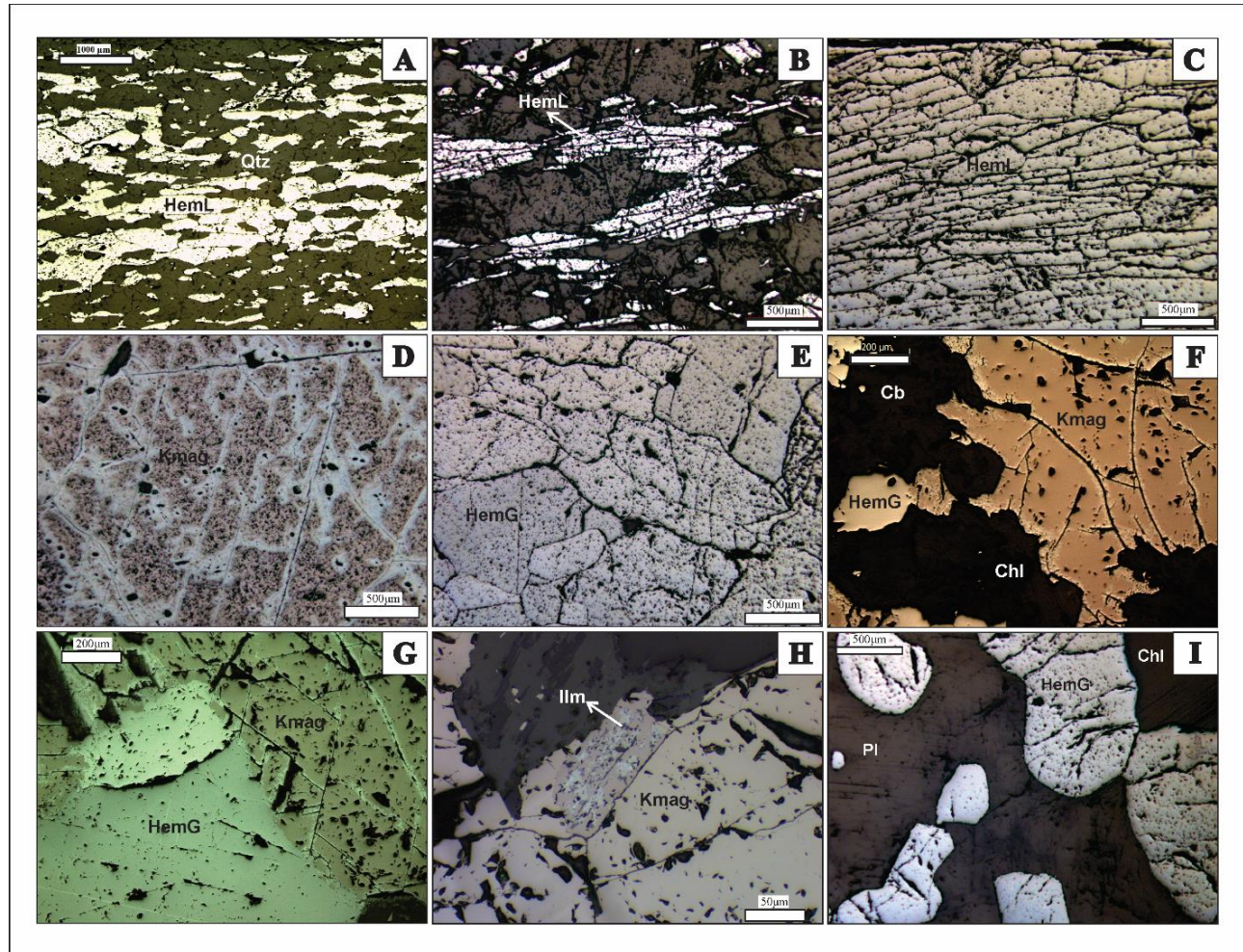


Figure 6.6: Microscopic features of iron oxides. (A) and (B) Iron formation with alternation of lamellar hematite- and quartz-rich millimetric bands defining a plane-axial foliation. (A) sample from HBD and (B) sample from CTE. (C) Lamellar-granular hematitic iron ore from CTE. (D) Magnetic iron ore from CTE with coarse kenomagnetite with progressive oxidation to hematite along the octahedral cleavage planes. (E) Granular hematite-rich iron ore sample from CTE. (F) and (G) Granular hematite-rich iron ore sample from HBD containing kenomagnetite coarse crystals. (H) Pegmatite dike from HBD containing kenomagnetite with Mn-rich ilmenite inclusion. (I) Pegmatite dike from HBD containing granular hematite associated with chlorite and plagioclase. Photomicrographs were taken under uncrossed polarized reflected light. Abbreviations: HemG – granular hematite, HemL – lamellar hematite, Kmag – kenomagnetite, Chl – chlorite, Cb – carbonate, Pl – Plagioclase, Qtz – quartz, Ilm – ilmenite.

6.5.3.2. Cuité iron ore

The high-grade ore from CTE occurs as <10 meters thick tabular bodies parallel to the schistosity. It is possible to distinguish three high-grade iron ore types depending on the abundance of the iron oxide and the fabric: lamellar-granular hematitic ore (LGO), magnetic ore (MO) and granular hematitic ore (GO). The LGO bodies (Figure 6.6C) have a maximal thickness of 4 m and

are associated with shear zones of outcrop scale. The ore is fine to medium grained (<1 mm to 2.5 mm) comprised mostly of lamellar hematite, interspersed with kaolinite and quartz. Thin platelets are commonly enveloped by kaolinite aggregates clustered in millimetric lenses (<0.5 cm) and define a sinuous and anastomosing penetrative schistosity. The high content of kaolinite in this ore type (<40%) when compared with IF and other ore types is an important macroscopic distinguishing feature. Single granular hematite grains grow as idioblasts over the platy crystals. The MO (Figure 6.3K and 6.6D) occurs as 0.20-2 m thick hard and massive lenticular bodies inside the granular hematitic ore and has an incipient foliation. Kenomagnetite occurs as medium to coarse hypidioblastic crystals (0.5 mm to 5 mm), with irregular borders frequently oxidized to hematite. Ilmenite is present as very fine (<50 µm) subeuhedral to anhedral crystals filling the fractures and as inclusion in the oxidized domains. The GO (Figure 6.3L and 6.6E) is the dominant facies and similar to the ore described in HBD. It exhibits a medium- to coarse-grained (0.2 mm to 5 mm) granoblastic hematite fabric of polygonal grains with straight boundaries, and a minor amount of kenomagnetite and lamellar hematite. Apatite, talc, ilmenite, quartz, sericite, kaolinite and rare monazite and carbonate are the accessory minerals.

6.5.4. Paragenetic sequence of the iron oxides

A comparative petrographic analysis of both deposits delivered similar results regarding the textural transformations undergone by IF and associated orebodies. The syn-tectonic platy grains of lamellar hematite oriented parallel to the foliation are ubiquitous and is considered the oldest iron oxide generation (Figure 6.7) observed in the IF from the Guanhães Block, different from the contemporaneous itabirite layers of the Serra da Serpentina and Serra de São José Groups where is possible the observation of the schistose structure partially overprinting an older, fine granoblastic hematite fabric associated to low-angle thrust planes of the Espinhaço belt. Massive hypidioblastic kenomagnetite comprises a late- and post-deformational fabric that overgrow the platy grains developed mainly at the contact zone with the pegmatite bodies. The oxidation of kenomagnetite to martite and hematite and the growth of a granoblastic hematite fabric indicate a progressive process of oxidation, recrystallization and grain growth during the late- and mainly post-deformational stage that may obliterate the tectonic fabric (Figure 6.7).

Iron oxides textures	Deformational stages of Brasiliano orogeny		
	580 Ma syn-collisional	late-collisional	480 Ma post-collisional
Lamellar hematite (HemL)	■ HemL in iron formation	■	■ Coarse HemL in pegmatite
Kenomagnetite (Kmag)		···	■
Martite (Mar)		···	■
Granular hematite (HemG)		···	■

Figure 6.7: Paragenetic sequence of the different iron oxides generations and their chronological relation with the deformational stages of Brasiliano Orogeny. Based on Silveira Braga et al. (2019a).

6.6. Whole-rock geochemistry

6.6.1. Major oxide elements

6.6.1.1. Iron formation

The SiO_2 and Fe_{total} contents in HBD IF vary from 37.42 to 44.13 wt. % and 32.45 to 43.50 wt. %, respectively. These values are in the range defined by Klein (2005) for the average bulk chemistry of unenriched Archean and Paleoproterozoic IFs (34-56 wt.% SiO_2 and 20-40 wt. % Fe_{total}) indicating a low stage of hydrothermal alteration. The Na_2O , K_2O , TiO_2 , P_2O_5 , MnO and Cr_2O_3 contents are less than 1 wt. % each one. Al_2O_3 , MgO , and CaO contents are higher than 1% in the sample B-S48 (1.37, 4.81, 1.93 wt. %, respectively), associated with the presence of chlorite and tremolite-actinolite. The Al_2O_3 , MgO , and CaO contents in itabirite from Morro Escuro, Morro do Pilar, Conceição do Mato Dentro, Liberdade, S. Antônio (Figure 6.1) are predominantly lower than 1% (Rolim, 2016; Silveira Braga et al., 2015).

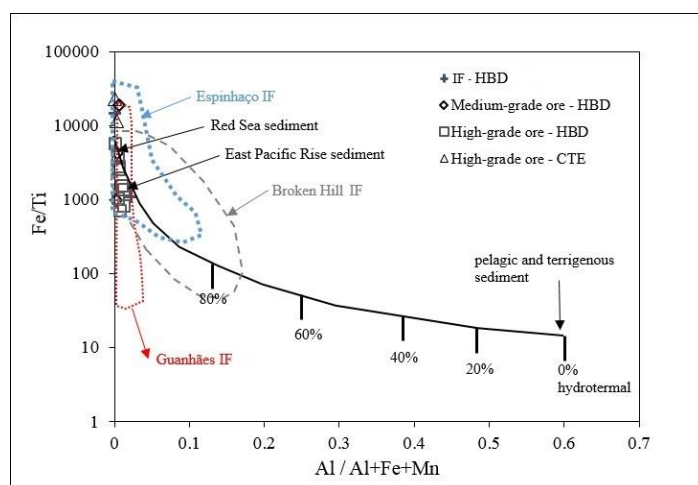


Figure 6.8: $\text{Al}/\text{Al}+\text{Fe}+\text{Mn}$ vs. Fe/Ti diagram, showing bulk compositions of IF and ore samples from HBD and CTE, modern Fe-Mn precipitate and hydrothermal sediments (modified after Bostrom, 1973). The curve represents a mixing line between compositions of hydrothermal sediments from the East Pacific Rise and average continental crust. Compositional fields: Broken Hill IF (Heimann et al., 2009); Espinhaço IF including Conceição do Mato Dentro, Morro do Pilar, Serro, Santo Antônio (Rolim, 2016) and Morro Escuro (Silveira Braga et al., 2015) data; Guanhães IF (Barrote et al., 2017).

The quartz-itabirite from Guanhães also has low Al_2O_3 , MgO , CaO contents; however, the carbonate-rich variety has higher values ($\text{Al}_2\text{O}_3 = 0.38\text{-}2.01$ wt.%, $\text{MgO} = <0.01\text{-}9.83$ wt.%, $\text{CaO} = 0.02\text{-}17.97$ wt.% - (Barrote et al., 2017)). The $\text{Al}/(\text{Al}+\text{Fe}+\text{Mn})$ vs. Fe/Ti plot (Figure 6.8) shows that all samples have pronounced hydrothermal signature and low terrigenous content.

6.6.1.2. Hypogene iron ore

Iron ore exhibits low concentrations of SiO_2 (0.19-26.28 wt.%) and high Fe_{total} (50.24-69.46 wt.%). Three ore samples (B-S40, B-S44, B-S46) from HBD were classified as medium-grade ore due to their intermediate SiO_2 and Fe_{total} content (18.05-26.28 wt.% and 50.24-55.76 wt.%, respectively). The high-grade samples from HBD and CTE have 0.19-3.22 wt.% of SiO_2 , and 61.81-69.46 wt.% of Fe_{total} . The medium-grade ore has less than 1% wt. of Na_2O , K_2O , TiO_2 , P_2O_5 , MnO , Al_2O_3 , MgO , CaO and Cr_2O_3 , except the sample B-S44 that has MgO of 1.03 wt.%, due to the presence of talc.

High-grade iron ore samples from HBD containing chlorite, cummingtonite-grunerite, tremolite-actinolite and/or carbonate (dolomite and calcite) as accessory minerals have Al_2O_3 , MgO , $\text{CaO} > 1$ wt.%. Relatively high K_2O contents (0.11-0.57 wt.%) were found in HBD high-grade ore samples from the contact zone with pegmatite intrusion (B-S11, B-S28, B-R26), which contain biotite and chlorite. The sample B-R26 has the highest P_2O_5 and MnO content (1.16 and 0.82 wt.% respectively).

The high-grade samples from CTE have a lower content of silicate and carbonates than HBD. Consequently, the content of MgO , CaO , Na_2O , K_2O , TiO_2 is also lower. However, one sample from CTE contains a significant amount of kaolinite, and consequently, a higher Al_2O_3 content, of the same order of the samples from HBD.

6.6.2. Trace and rare earth elements

The concentration of Se, Tl, Hg, Au, Ag, Bi and Cd are predominantly below detection limits. Most trace elements have concentrations below 15 ppm and very low variability between samples, except Ga, Nb, Sn, V, Zr, Y, Zn, As, Ni and $\sum\text{REE}$. The trace element content, especially Zr, Y, Zn, Ni, and $\sum\text{REE}$, is directly related to the increasing of Al_2O_3 , MgO and CaO wt. % (Figure 6.9A-E), reflecting the presence of silicates and carbonates as accessory minerals (see Table 6.1).

6.6.2.1. Iron formation

The HBD quartz-itabirite (B-R28) is the sample with the lowest content of trace elements. The sample B-S48 has significant higher proportions of V and Zr than the sample B-R28 (enrichment by the factor of 12 for both elements), probably related with the presence of chlorite and amphibole

(Table 6.1). The PAAS-normalized REE+Y profiles display the typical HREE enrichments ($\text{Pr}/\text{Yb}_{(\text{SN})}$ between 0.27-0.33) – Figure 6.10. The positive $\text{Eu}/\text{Eu}_{(\text{SN})}$ obtained (1.49-1.59) are characteristic of late-Paleoproterozoic iron formations (Planavsky et al., 2010). The Y anomalies are positive (1.41-1.57), and the Ce anomalies are slightly negative (0.74-0.91). The discriminative binary plot of $\text{Ce}/\text{Ce}^*_{(\text{SN})}$ vs. $\text{Pr}/\text{Pr}^*_{(\text{SN})}$ (Bau and Dulski, 1996) demonstrates that the values of IF, with $\text{Ce}/\text{Ce}^*_{(\text{SN})}$ close to 1 with a positive La anomaly, are consistent with most Paleoproterozoic IFs that indicates deposition in suboxic to anoxic environments (Figure 6.11A). The Y/Ho ratio are hyper-chondritic (Bau et al., 1996) and varies between 35.4 and 41.9 (Figure 6.11B), which is consistent with an overall low content of fine detrital components that is corroborated by the low content of Al_2O_3 (0.08-1.37%), Th (<0.1-1.5 ppm), Hf (<0.1-0.6 ppm), Sc (<1-3 ppm) and Zr (6.7-8.5 ppm) - Figure 6.12A.

Comparison with other IFs sequences

The REE+Y data from the HBD IF is very similar to the analytical results found in IFs from the Minas Supergroup (Mendes et al., 2016; Spier et al., 2007), Serra da Serpentina Group (Rolim, 2016; Silveira Braga et al., 2015) and other occurrences from the Guanhães Complex (Barrote et al., 2017), with a weak positive Eu anomaly, low $(\text{Pr}/\text{Yb})_{(\text{SN})}$ ratio and no significant Ce anomaly (Figure 6.13A). The Minas Supergroup itabirite has early-Paleoproterozoic age (Babinski et al., 1995; Machado et al., 1996; Mendes et al., 2014) and the others are from late-Paleoproterozoic, all of them deposited on a platformal environment.

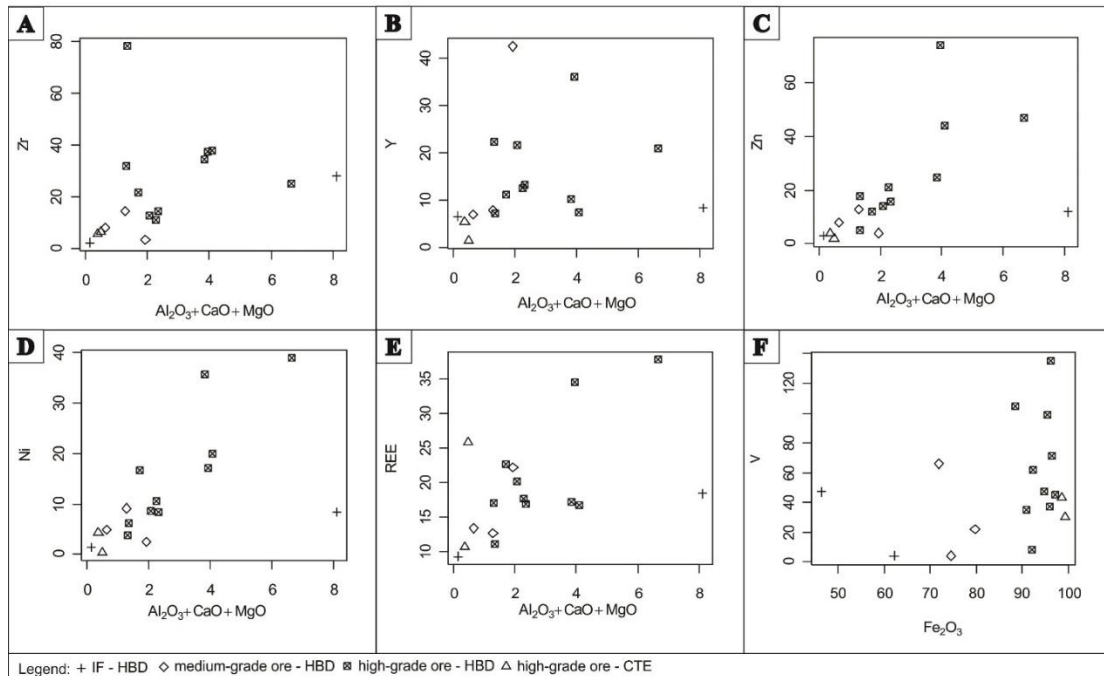


Figure 6.9: Graph $\text{Al}_2\text{O}_3+\text{MgO}+\text{CaO}$ versus (A) Zr, (B) Y, (C) Zn, (D) Ni and (e) rare earth elements. Graph Fe_2O_3 vs. V (F).

The obtained REE+Y profiles are also similar to the late-Archean Witwatersrand, the early-Paleoproterozoic Brockman, Kuruman and the late-Paleoproterozoic Biwabik (Figure 6.13B) iron

formations, and in contrast with the Algoma IFs (Carajás and Isua - (Figueiredo e Silva et al., 2008; Polat and Frei, 2005)), and Rapitan-type Neoproterozoic IF from Urucum district (Klein and Ladeira, 2004).

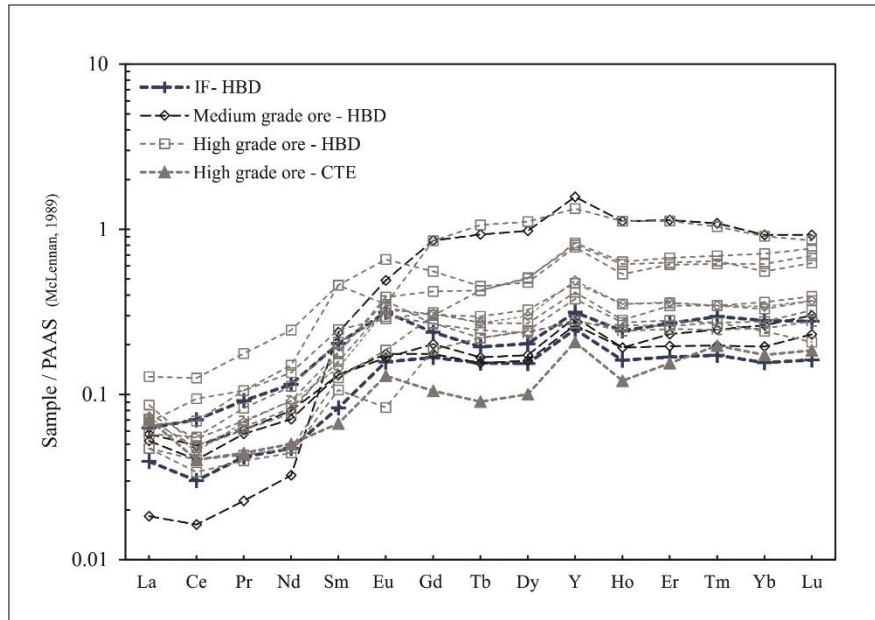


Figure 6.10: Distribution pattern of the REE+Y values of the iron formation (IF) and ore from HBD and CTE normalized to PAAS.

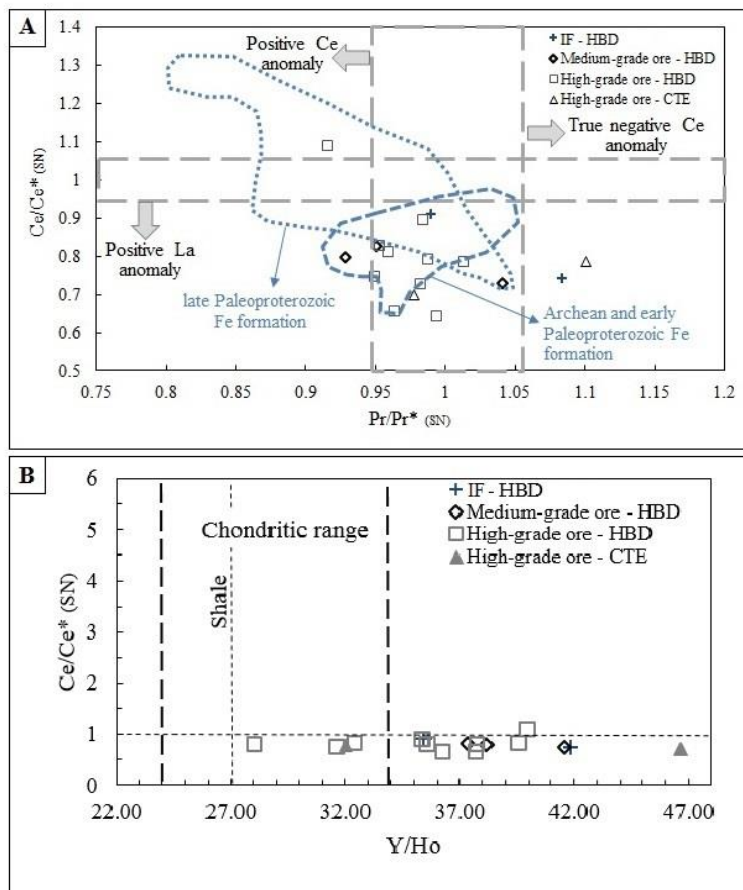


Figure 6.11: (A) Discriminative diagram of $\text{Pr}/\text{Pr}^*(\text{SN})$ vs $\text{Ce}/\text{Ce}^*(\text{SN})$ for La and Ce anomalies (Bau and Dulsky, 1996). Compositional fields of Fe formations extracted from Planavsky et al. (2010). (B) Y/Ho vs. $\text{Ce}/\text{Ce}^*(\text{SN})$ diagram (Pecoits, 2010).

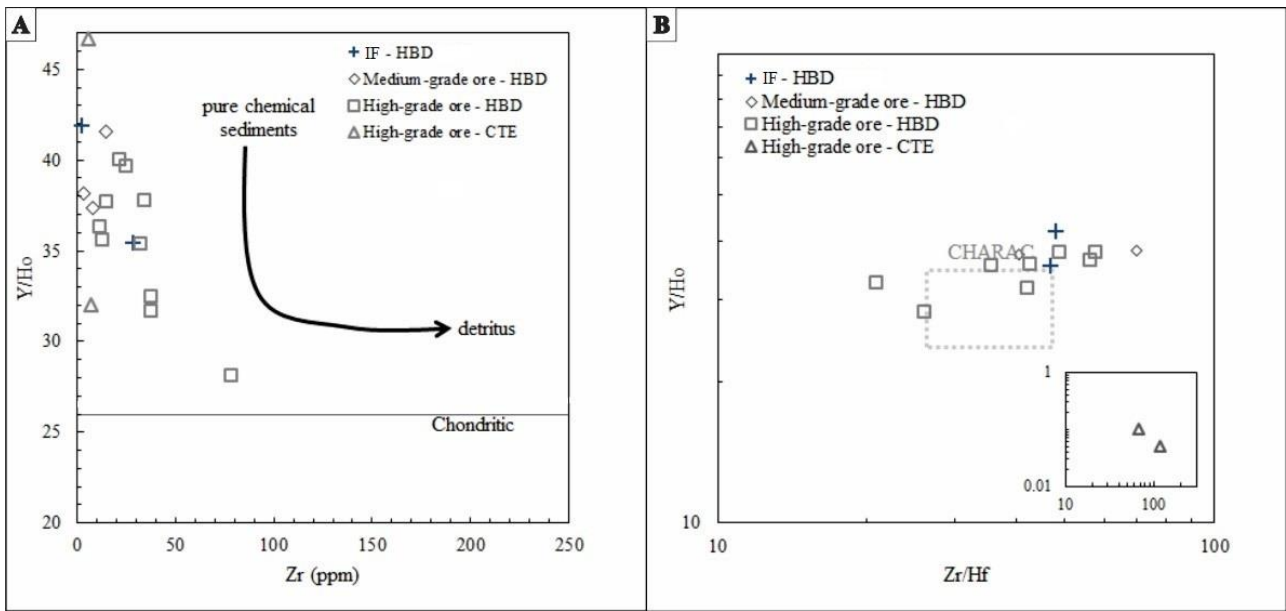


Figure 6.12: Relation between Zr, Hf, Y and Ho content of whole-rock chemistry of IF and iron ore. (A) Y/Ho vs. Zr. (B) Y/Ho vs. Zr/Hf with CHARAC field.

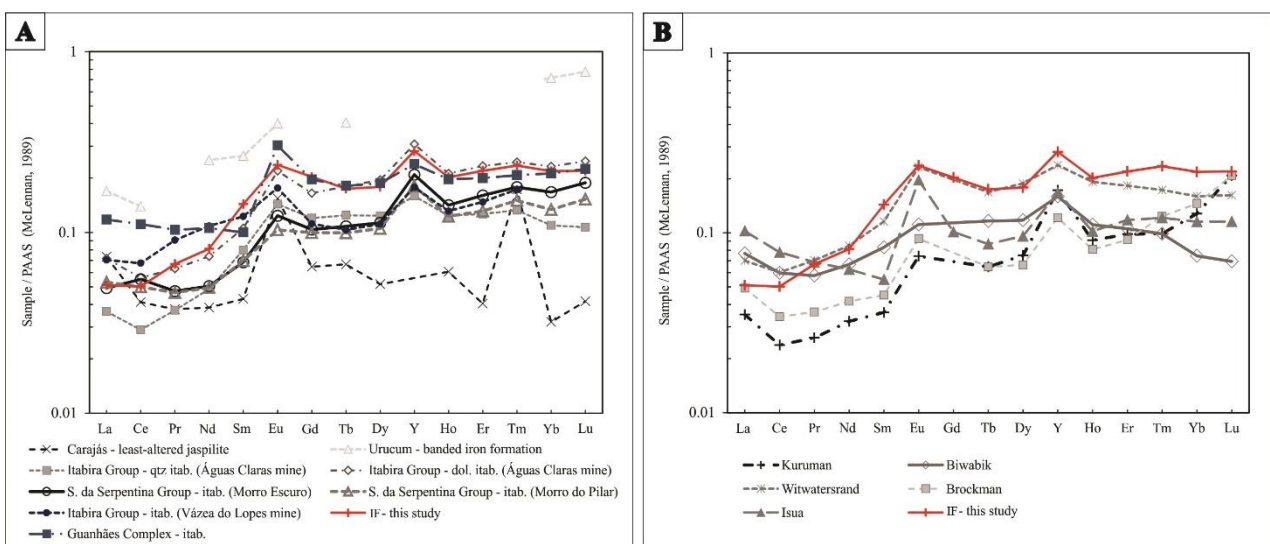


Figure 6.13: (A) An average (REE+Y)_{SN} spidergrams from the following Brazilian IFs: Carajás (Figueiredo e Silva et al., 2008); Urucum (Klein and Ladeira, 2004); Serra da Serpentina Group near Morro do Pilar and Morro Escuro deposits (Silveira Braga et al., 2015); Cauê Formation of the Itabira Group, Quadrilátero Ferrífero district, Águas Claras mine (Spier et al., 2007) and Várzea do Lopes mine (Mendes et al., 2016); Guanhães Complex (Barrote et al., 2017). (B) Comparative plot of REE+Y spidergrams from the study area and IFs worldwide: Isua, Greenland (Polat and Frei, 2005); Witwatersrand Supergroup, South Africa; Kuruman, South Africa; Brockman, Western Australia; Biwabik, USA (Planavsky et al., 2010).

6.6.2.2. Hypogene iron ore

The HBD high-grade ore sample B-S28, collected at the contact with pegmatitic intrusion, stands out due to the high concentration of Ga (53.7 ppm), Nb (566.4 ppm), Sn (197.0 ppm), V (135 ppm) and Zr (78.2 ppm), which represent enrichments in these elements by factors of 2 to 1,888 (23-

215 for Ga, 298-1888 for Nb, 33-394 for Sn, 2-17 for V and 2-13 for Zr) relative to iron ores located in more distal areas to the pegmatite.

There is a significant relationship between the increase of Ni and V in high-grade ore ($\text{Ni}=0.04\text{-}38.8\text{ ppm}$; $\text{V}=8\text{-}135\text{ ppm}$) compared with medium-grade ore and IF ($\text{Ni}=1.40\text{-}9.10\text{ ppm}$; $\text{V}=4\text{-}66\text{ ppm}$), (Figure 6.9F).

Individual PAAS-normalized REE+Y profiles are in general uniform with the typical HREE enrichment for the majority of samples ($\text{Pr}/\text{Yb}_{(\text{SN})}$ variation is 0.02-0.31 in medium-grade ore, 0.06-0.32 in high-grade ore). The granular-rich ore sample from CTE (C-R03) is most affected by supergene alteration (goethite and kaolinite enrichment) and not discussed further.

The Eu anomalies are commonly positive (1.06-1.28 in medium-grade ore, 1.14-1.85 in high-grade ore), except in the HBD high-grade ore samples B-S27, B-S28, B-S11 collected at the contact with pegmatite, which show weak negative values (0.83, 0.58 and 0.54 respectively).

The Y anomalies are mostly positive ranging from 1.49-1.60 in medium-grade ore and 0.90-1.87 in high-grade ore. The samples have slightly negative Ce anomalies (0.73-0.83 in medium-grade ore, 0.64-0.89 in high-grade ore) with the exception of one HBD sample (high-grade ore B-S42), which has a weak positive anomaly ($\text{Ce}/\text{Ce}^*_{(\text{SN})} = 1.09$).

The discriminative binary plot of $\text{Pr}/\text{Pr}^*_{(\text{SN})}$ vs. $\text{Ce}/\text{Ce}^*_{(\text{SN})}$ (Bau and Dulski, 1996) demonstrates general similar behavior between iron formation and ore samples, with $\text{Ce}/\text{Ce}^*_{(\text{SN})}$ values close to 1 with predominantly positive La anomalies (Figure 6.11A). Four Y/Ho values from high-grade ore samples fall in the chondritic range ($24 < \text{Y/Ho} < 34$) in the plot Y/Ho vs. $\text{Ce}/\text{Ce}^*_{(\text{SN})}$, and all are outside shale contamination field (Figure 6.11B). Three of them were collected near pegmatite intrusion in HBD, and one (CTE) is slightly weathered and kaolinite-rich.

A plot of Y/Ho ratio (as an indicator for seawater-like REE+Y features) vs. Zr concentration (as an indicator for detritus content) allows to evaluate the impact of detrital aluminosilicates on the REE+Y budget of pure chemical sediments (Viehmann et al., 2016). The ore samples, similar to the IF, present hyper-chondritic Y/Ho ratios and low Zr content indicating overall low detrital contribution (Figure 6.12A). Most samples plot outside the CHARAC field in the Zr/Hf vs. Y/Ho diagram (Figure 6.12B) with Zr/Hf varying from 20.89-146.00, except the HBD high-grade ore samples B-S27 and B-S28, collected close the pegmatite contact, with the Zr/Hf values of 26.07 and 35.67, respectively.

6.7. Iron oxide LA-ICP-MS chemistry

6.7.1. Mineral chemistry of iron oxides from iron formation

6.7.1.1. Lamellar hematite

Lamellar hematite has the lowest abundances of most trace elements, with moderate contents of Al (564-713 ppm), Si (59-374 ppm), Ti (9-127 ppm), V (16-21 ppm), Mn (21-39 ppm), Sb (10-14 ppm) and W (7-11 ppm) – Figure 6.15. The REE+Y content is predominantly below detection limit, with sum below 0.5 ppm. The PAAS-normalized REE+Y pattern (Figure 6.16A) displays enrichment in HREE relative to LREE.

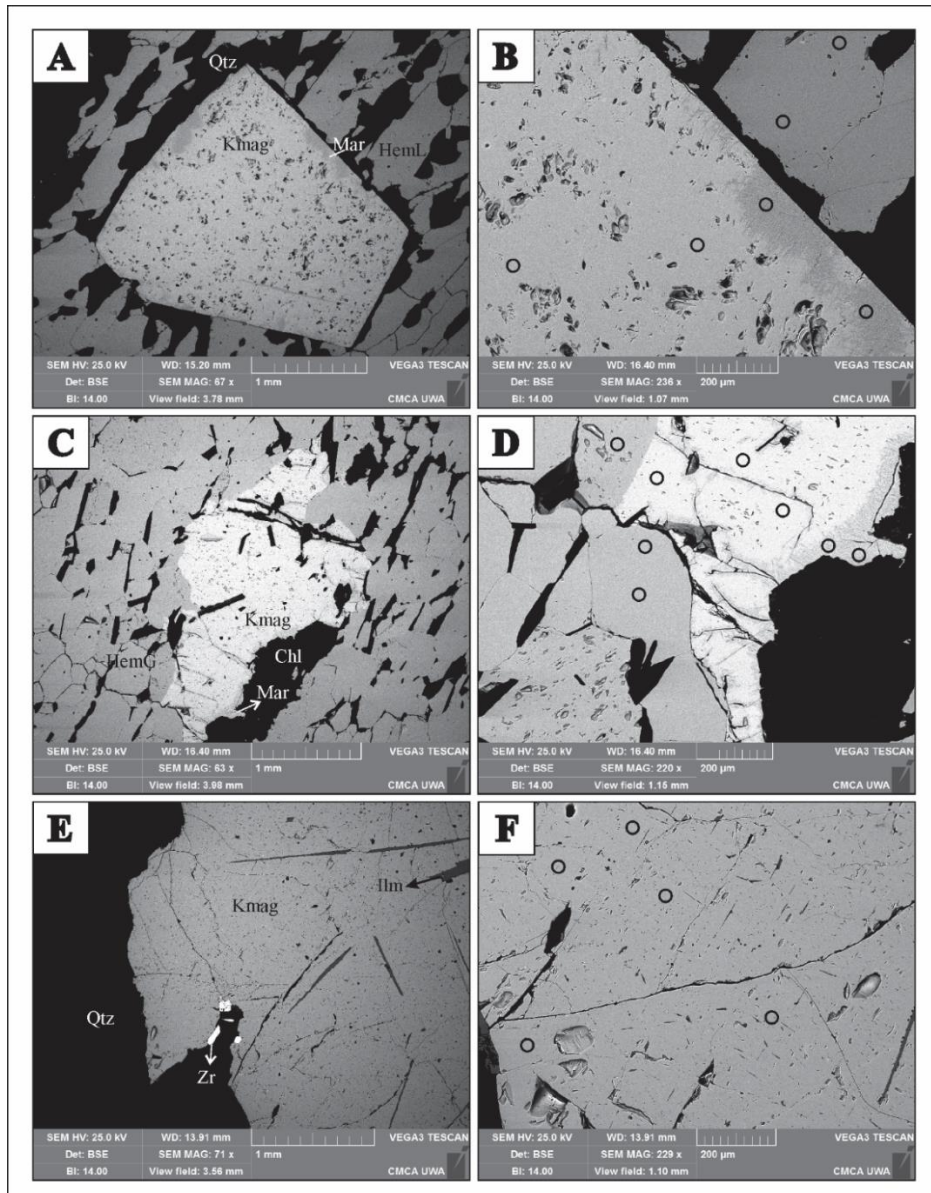


Figure 6.14: Back-scattered images (BSE) of iron oxide generations analyzed by LA-ICP-MS (the dark circles indicates the spots analyzed). (A) Sample B-R62 – Iron formation containing lamellar hematite, quartz and a granoblastic kenomagnetite with core oxidized to martite. (B) Zoom in the sample B-R62 showing some of the spots analyzed. (C) Sample B-R31 – iron ore containing chlorite, granular hematite and kenomagnetite with core oxidized to martite. (D) Zoom in the sample B-R31 showing some of the spots analyzed. (E) Sample B-S54 – pegmatite containing quartz, zircon,

coarse-grained kenomagnetite with ilmenite inclusion. (F) Zoom in the sample B-S54 showing some of the spots analyzed. Abbreviations: Kmag – kenomagnetite, Mar – martite, HemL – lamellar hematite, HemG – granular hematite, Chl – chlorite, Cb – carbonate, Ilm – ilmenite, Qtz – quartz, Zr – zircon.

6.7.1.2. Kenomagnetite

The kenomagnetite relics display considerable content of Mn (1,292-1,765 ppm), Ni (645-663 ppm), Zn (354-581 ppm), Si (239-309 ppm), Al (100-263 ppm), Co (83-85 ppm), Mg (55-83 ppm) and V (6-7 ppm) – Figure 6.15. It also has a distinct lower Ti content (<1 ppm) than the kenomagnetite from ore and pegmatite. The REE+Y content is also very low and predominantly below the detection limit (Σ REE+Y below 0.03 ppm), being only possible to confirm a relative enrichment in HREE (Figure 6.16B).

6.7.1.3. Martite

The oxidized martite rims (Figure 6.14A and B) have high concentration of Si (377-567 ppm), Mg (32-55 ppm), Mn (1,624-1,932 ppm), P (787-1,211 ppm), Al (369-693 ppm), Zn (292-421 ppm), Ni (652-732 ppm) and considerable content of V (6-9 ppm), Cr (2-3 ppm), Co (80-92 ppm), As (5-9 ppm), Y (6-12 ppm), Pb (62-116 ppm) and U (63-131 ppm). The REE+Y content is the highest compared to the other iron oxides (Figure 6.16C) with a relative enrichment in HREE, positive Eu anomaly (1.4-1.6), negative Ce anomaly (0.66-0.78) and Y/Ho ratio varying from 25 to 31.

6.7.1.4. Granular hematite

Similar to the lamellar hematite, the granular hematite grains from IF have low abundances of the majority of trace elements, with moderate content of Al (586-699 ppm), Si (141-324 ppm), Ti (11-97 ppm), V (17-20 ppm), Mn (12-28 ppm), Sb (9-14 ppm) and W (7-8 ppm) – Figure 6.15. The REE+Y content is also very low and predominantly below the detection limit (Σ REE+Y below 0.05 ppm), and PAAS-normalized REE+Y patterns showing enrichment in HREE (Figure 6.16D). The Y/Ho ratios vary from 1.0 to 8.0.

6.7.2. Mineral chemistry of iron oxides from hypogene iron ore

6.7.2.1. Lamellar hematite

In general, all the lamellar hematite in ore has considerable content of Al (1,619-3,113 ppm), Si (110-320 ppm), V (42-73 ppm), Cr (6-144 ppm). The lamellar hematite from HBD has also considerable contents of Mg (35-86 ppm), Ti (391-4,429 ppm), Mn (48-269 ppm), Ga (3-30 ppm), Zr (33-45 ppm) and Nb (2-297 ppm). As the lamellar hematite from IF, the REE+Y content is predominantly below the detection limit (Σ REE+Y below 2 ppm), with enrichment in HREE relative to LREE (Figure 6.16A), and variable Y/Ho ratio (4-26).

6.7.2.2. Kenomagnetite

The kenomagnetite from ore (Figure 6.14C, D) has considerable content of Mg (1,457-5,641 ppm), Si (140-480 ppm), Al (58-416 ppm), V (23-69 ppm), Cr (6-23 ppm) in all samples (Figure 6.15). This iron oxide generation has distinct high content of Mn (552-612 ppm CTE, 7,466-17,097 ppm HBD), Co (2 ppm CTE, 90-214 ppm HBD), Ni (6-7 ppm CTE, 228-917 ppm HBD) and Zn (2-14 ppm CTE, 775-1,067 ppm HBD) in HBD compared with CTE. The REE+Y content is very low (Σ REE+Y below 0.05 ppm), and is only possible do recognize a relative enrichment of HREE (Figure 6.16B).

6.7.2.3. Martite

The martite pseudomorphs (Figure 6.14C and D) have higher concentration of Si (279-1,524 ppm), Mg (530-1,941 ppm), Mn (506-12,847 ppm), P (34-1,542 ppm), Al (38-460 ppm), Zn (3-1,176 ppm), Ni (6-334 ppm) and considerable content of V (26-74 ppm), Cr (9-24 ppm), Co (2-135 ppm), As (1-16 ppm), Y (0.1-29 ppm), Pb (2-28 ppm) and U (0.3-28 ppm). The martite from ore is richer in Mg, Si, V, Cr, Mn, Pb and U than the martite from IF. The martite from HBD has a higher content of Si, Mn, Co, Ni, and Zn than martite from CTE, which has a greater concentration of P (Figure 6.15).

The REE+Y content has similar behavior in martite of CTE and HBD, with an enrichment of HREE relative to LREE (Figure 6.16C), positive Eu anomaly (1.3-2.6), predominate low negative to low positive Ce anomaly (0.68-1.75) and Y/Ho ratio varying from 22 to 31.

6.7.2.4. Granular hematite

All the granular hematite grains from ore (Figure 6.14C, D) display a considerable amount of Mg (2-85 ppm), Al (959-3,658 ppm), Si (124-379 ppm), V (31-84 ppm), Zr (8-50 ppm). However, the amount of the following elements are higher in the ore samples of HBD compared with CTE: Ti (71-414 ppm CTE, 251-5,128 ppm HBD); Cr (9-42 ppm CTE, 4-134 HBD); Mn (12-53 ppm CTE, 20-294 ppm HBD); Zn (0.2-0.4 ppm CTE, 0.2-29 HBD); Ga (1-3 ppm CTE, 2-30 ppm HBD); Nb (<1 ppm CTE, 1-497 ppm HBD); Sn (<1 ppm CTE, 1-544 HBD). The REE+Y results are very low (Σ REE+Y below 1 ppm) but exhibit an enrichment of HREE relative to LREE (Figure 6.16D), and Y/Ho ratio varying from 1 to 31.

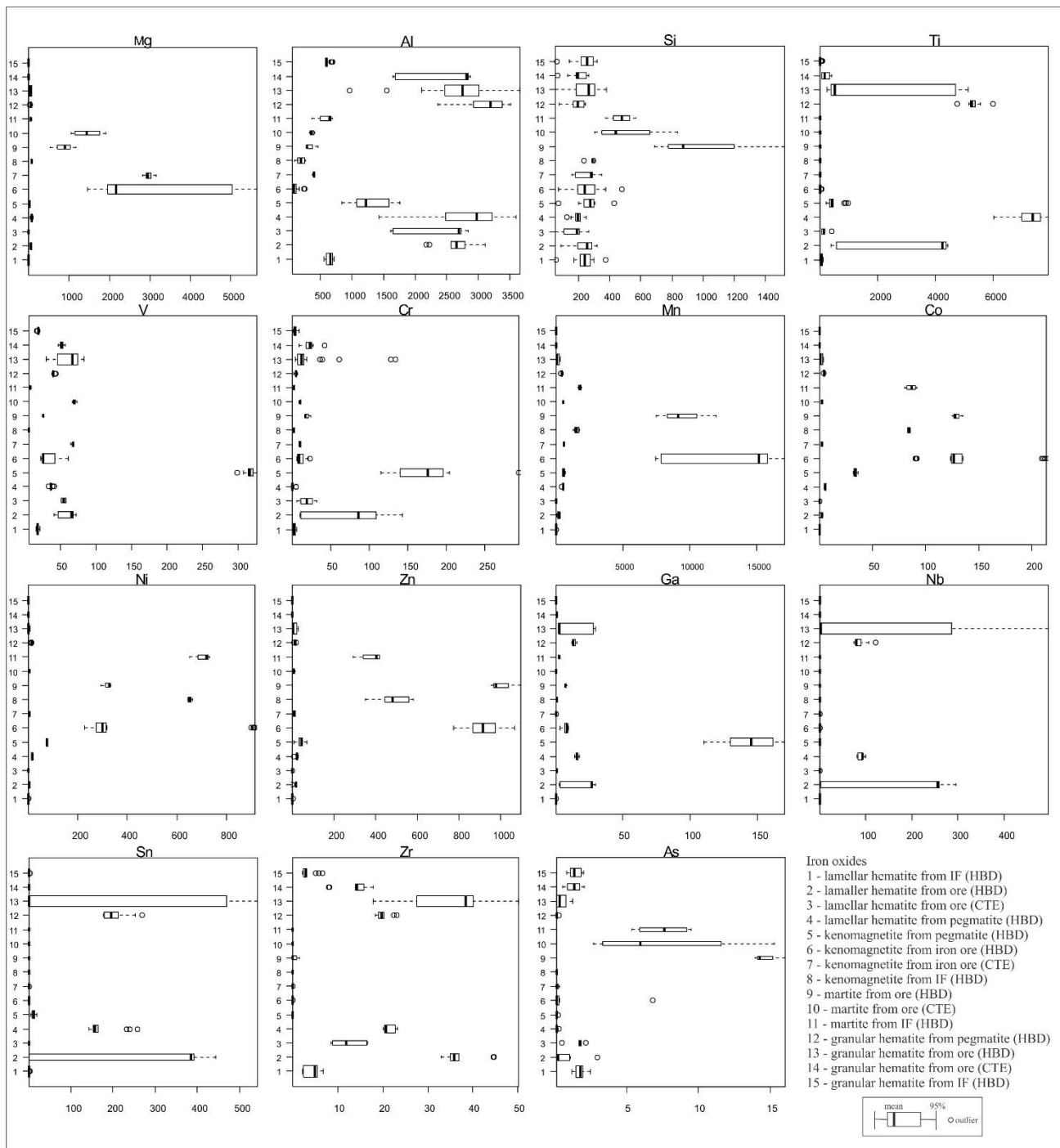


Figure 6.15: Box-and-whisker plots, derived from mineral chemistry LA-ICP-MS data, of minor and trace elements in ppm grouped by iron oxide generation. The upper and lower margins of the box represent the upper and lower 50 percentile of the data. The whiskers represent the upper and lower threshold values (95 percentile of the data). Median values are shown as solid black lines and mean values as solid black circles.

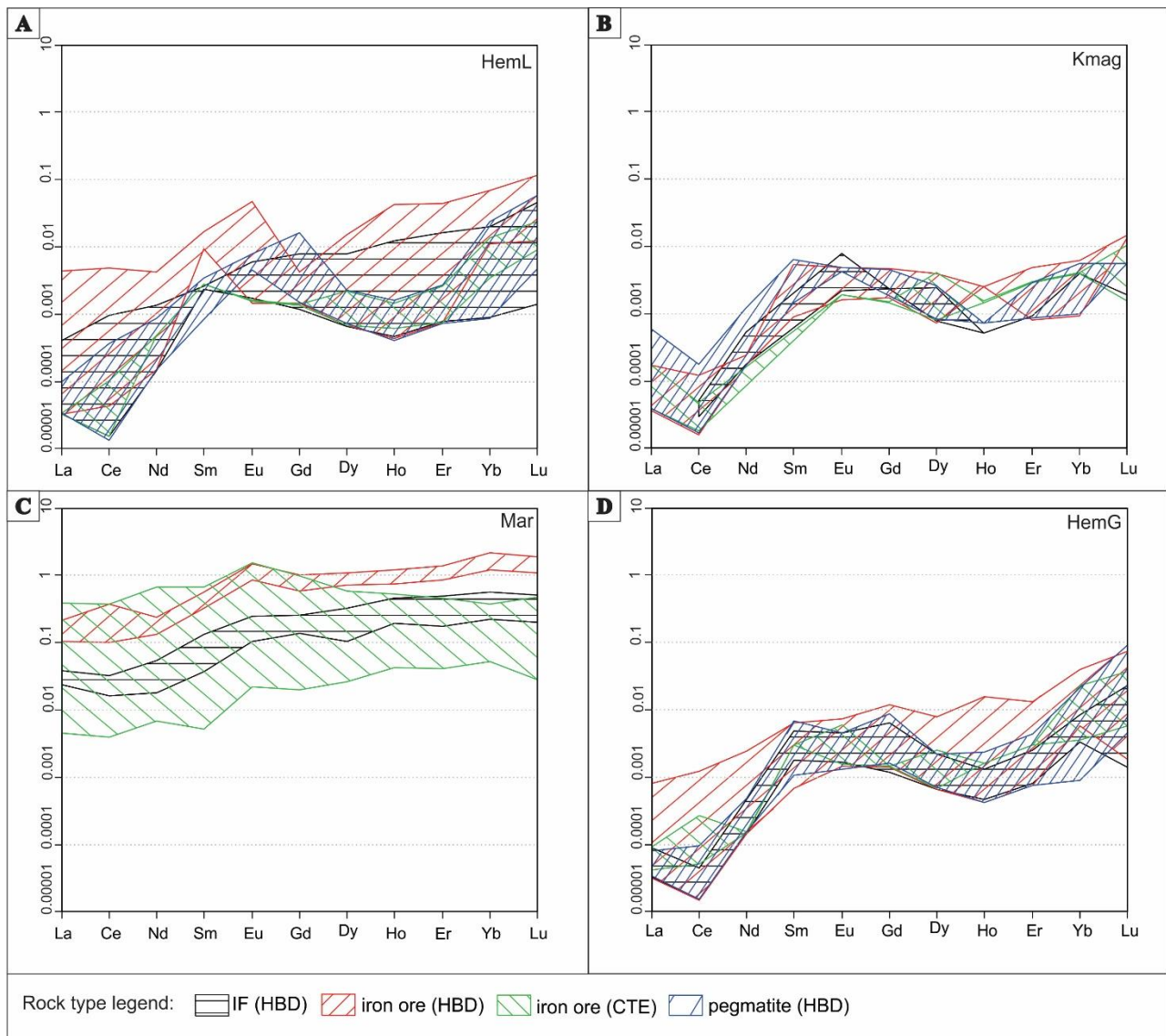


Figure 6.16: Spider diagram fields of PAAS-normalized (McLennan, 1989) LA-ICP-MS analyses of REE abundances of (A) lamellar hematite, (B) kenomagnetite, (C) martite and (D) granular hematite.

6.7.3. Mineral chemistry of iron oxides from pegmatite

6.7.3.1. Lamellar hematite

This iron oxide generation has high content of Ti (6,040-7,929 ppm), Al (1,429-3,602 ppm), Mn (432-571 ppm), Si (130-254), Sn (143-258 ppm) and Nb (81-100 ppm), and considerable content of Mg (34-118 ppm), Sc (6-8 ppm), V (34-41 ppm), Ni (13-18 ppm), Zn (8-31 ppm), Ga (15-18 ppm), Zr (20-23 ppm) – Figure 6.15. The low content of REE+Y (Σ REE+Y below 0.2 ppm) exhibit low Y/Ho ratios (3-14) and PAAS-normalized diagram (Figure 6.16A) with HREE enrichment trend.

6.7.3.2. Kenomagnetite

The kenomagnetite from pegmatite (Figure 6.14E, F) has high content of Al (836-1,764 ppm), Mn (469-686 ppm), V (300-327 ppm), Ti (227-995 ppm), Si (204-433 ppm), Cr (115-295 ppm) and

considerable amount of Ga (110-170 ppm), Ni (72-79 ppm), Co (32-36 ppm), Zn (7-72 ppm), Sn (5-19 ppm) and Mg (8-25 ppm) – Figure 6.15. The REE+Y content is very low (Σ REE+Y below 0.1 ppm), with enrichment in HREE relative to LREE (Figure 6.16B).

6.7.3.3. Granular hematite

The granular hematite has considerable content of Ti (4,751-6,008 ppm), Al (2,361-3,516 ppm), Mn (379-440 ppm), Si (156-248 ppm), Sn (177-269 ppm), Nb (74-122 ppm), Mg (25-78 ppm) and V (38-44 ppm) – Figure 6.15. The low content of REE+Y (Σ REE+Y below 0.1 ppm) exhibit enrichment of HREE in the PAAS-normalized diagram (Figure 6.16 D) and low Y/Ho ratios (4-13).

6.7.4. The main chemical changes related to hydrothermal alteration

With the purpose to evaluate the chemical changes undergone by the iron formation due to the contact alteration and kenomagnetite mineralization in the pegmatite aureole, the chemical composition of kenomagnetite and subsequent generations were normalized with the trace element values obtained from lamellar hematite, delivering a consistent positive balance for the following elements: Mg, V, Cr, Mn, Co, Ni, Zn and Ga (Figure 6.17A).

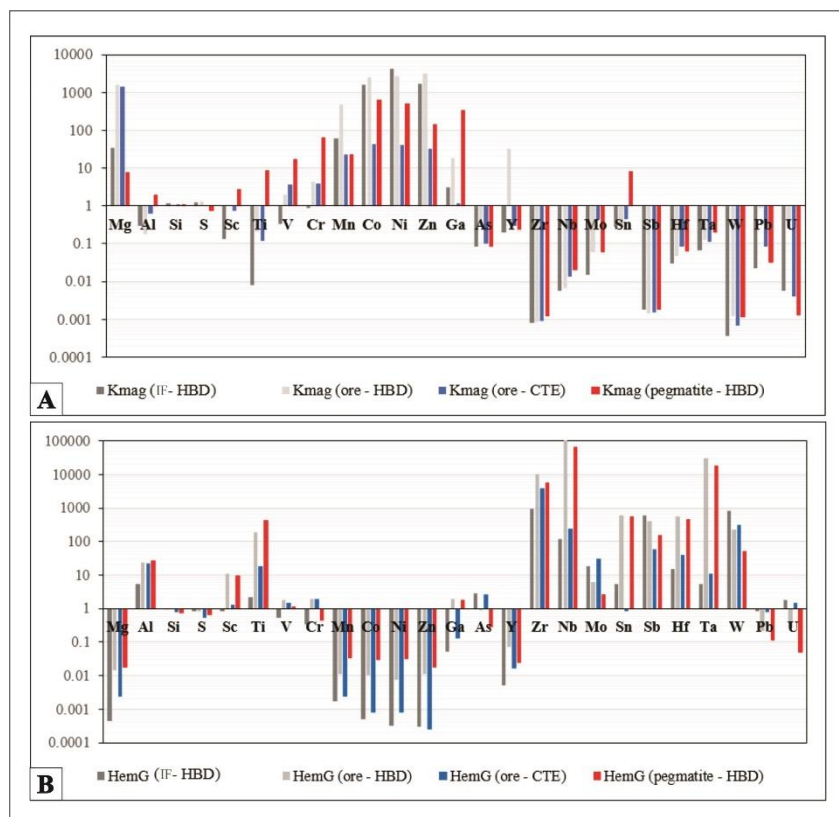
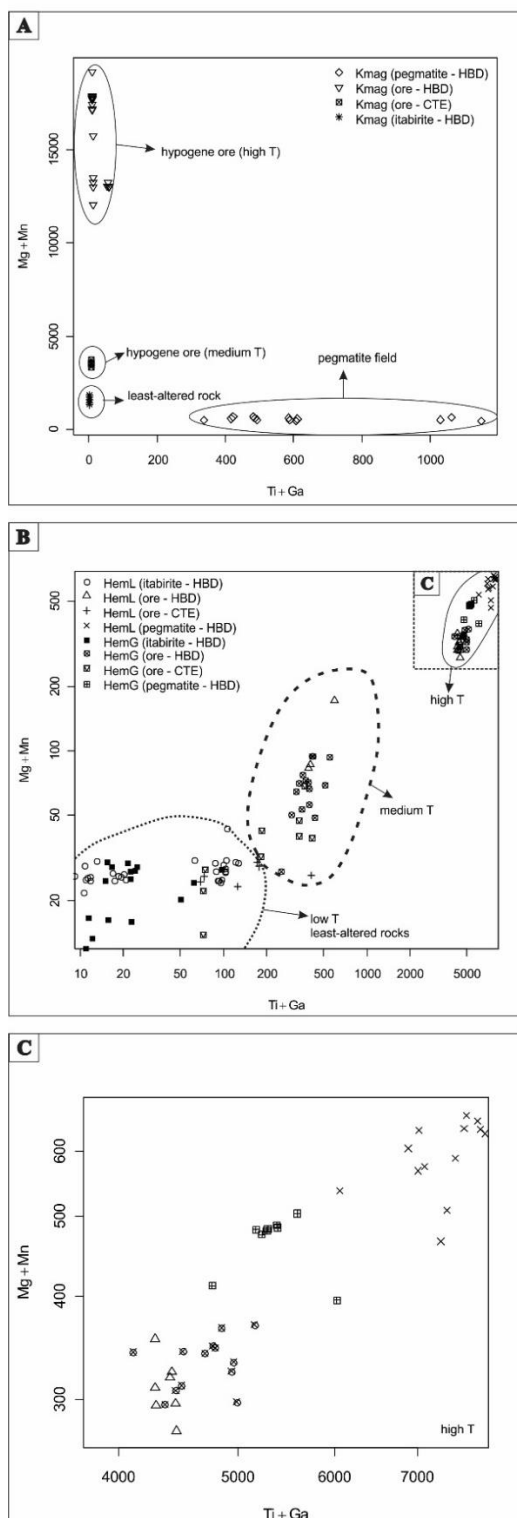


Figure 6.17: Mass balance calculations of average iron oxides in situ analysis. (A) Kenomagnetite normalized to lamellar hematite from HBD iron formation. (B) Granular hematite normalized to kenomagnetite from HBD iron ore.

Comparing composition of kenomagnetite of associated rocks, the crystals from pegmatite are typically richer in Al, Ti, V, Cr, and Ga, whereas in the HBD and CTE ores they show higher contents of Mg, Mn, Co, Ni, and Zn being depleted in Ti (<2%), Al (<1%), and others HFSE elements, such as Zr, Hf, Nb, Ta and Sc (Figure 6.15) indicating a hydrothermal origin (Dare et al., 2014).



Normalizing the kenomagnetite with martite is noted an increase in the content of Al, Si, As, Y, REE, Zr, Nb, Mo, Sn, Sb, Ta, W, Pb, and U and granular hematite is enriched in Al, Ti, Zr, Nb, Mo, Sn, Sb, Hf, Ta and W when compared with martite. Normalizing the composition of granular hematite with the kenomagnetite is observed the increasing content of Al, Sc, Ti, As, Zr, Nb, Mo, Sn, Sb, Hf, Ta and W (Figure 6.17B).

The REE+Y have predominant very low content with more than 40% of analyses below detection limit and with Σ REE+Y below 2 ppm, except martite that exhibit the highest values, containing Σ REE+Y below 100 ppm (Figure 6.16).

The iron oxides appear grouped in different fields in the graph Ti+Ga vs. Mg+Mn. The pegmatic kenomagnetite grains have the highest Ti+Ga content, very distinct from the values obtained in the HBD iron ore that delivered the highest Mg+Mn contents (Figure 6.18A). Among the hematite generations, there is a positive correlation between Ti+Ga vs. Mg+Mn (Figure 6.18B and C) with the lowest content in the least-altered rocks and highest content in ore and pegmatite samples.

Figure 6.18: Mineral chemistry discrimination diagrams for iron oxides from HBD and CTE. (A) Ti+Ga vs. Mg+Mn in (keno) magnetite. (B) Ti+Ga vs. Mg+Mn in hematite. (C) Zoom in the graph of letter B.

6.7.5. Kenomagnetite chemistry and discrimination diagrams

Magnetite is oxidized to the defective form kenomagnetite/maghemite and occur in three different settings: a) as isolated hypidioblasts grown over the foliation in the iron formation, b) single crystals eventually clustered in pegmatite bodies up to few centimeters distant from iron ore contact, c) single grains and coarse-grained clustered in iron ore.

Dare et al. (2014) proposed a discrimination diagram to distinct magmatic and hydrothermal magnetite of felsic host rocks (such as I-type granite) based on the Ti content and Ni/Cr ratio. According to the authors, in silicate magmas, the Ni and Cr behavior is coupled, with Ni/Cr ratios ≤ 1 , as both behave compatibly during fractionation of intermediate and felsic melts. However, in many hydrothermal settings, their behavior is decoupled and the Ni/Cr ratio of magnetite is typically higher, probably due to a higher solubility of Ni compared to Cr in fluids (Figure 6.19). Despite their highest Ni/Cr ratio (255.9-321.4) the kenomagnetite from IF plot outside the scale of the graph of Figure 6.19A due to its very low Ti content (<1 ppm). The kenomagnetite from pegmatite plot in the hydrothermal field, close to the magmatic field. The kenomagnetite grains from ore samples have higher Ni/Cr ratio, and plot in the hydrothermal field (Figure 6.19A).

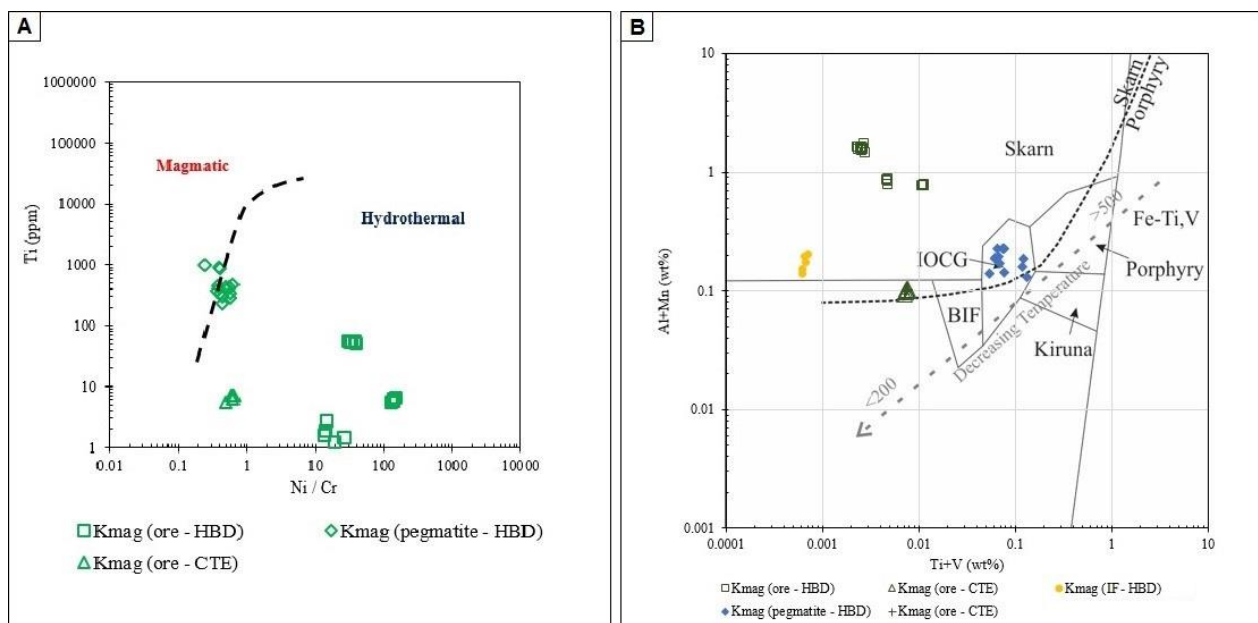


Figure 6.19: (A) Plot of Ti (ppm) vs. Ni/Cr ratio of magnetite to distinguish between magmatic (red) and hydrothermal (blue) formation settings (Dare et al., 2014). (B) Ti + V vs. Al + Mn (wt. %) diagram for magnetite with deposit fields (Dupuis and Beaudoin, 2011; Nadoll and Koenig, 2011).

Dupuis and Beaudoin (2011) proposed that Ti+V vs. Al+Mn (wt. %) diagram for magnetite composition may be used to discriminate among a wide variety of mineral deposits, including iron oxide–copper–gold (IOCG), banded iron formation (BIF), porphyry Cu, Fe–Cu skarn, Ni–Cu–PGE, Cu–Zn–Pb volcanogenic massive sulfide (VMS), and Archean porphyry Cu–Au. The kenomagnetite

from pegmatite plot in the IOCG field whereas the others plot in the skarn field (Figure 6.19B). The temperature dependence of Ti, V, Al, Mn, and Ga in magnetite composition can distinguish between low and high T mineral systems, as shown in Figure 6.19B (Nadol et al., 2014). Figure 6.19B shows that the kenomagnetite from pegmatite has the highest temperature system.

6.7.6. Comparisons with other iron ore deposits

Figure 6.20 shows the average content of Ti, V, Cr, Mn, Co, Ni and Zn of different iron oxides from the following iron ore bodies present in Espinhaço fold-thrust belt and Guanhães Block:

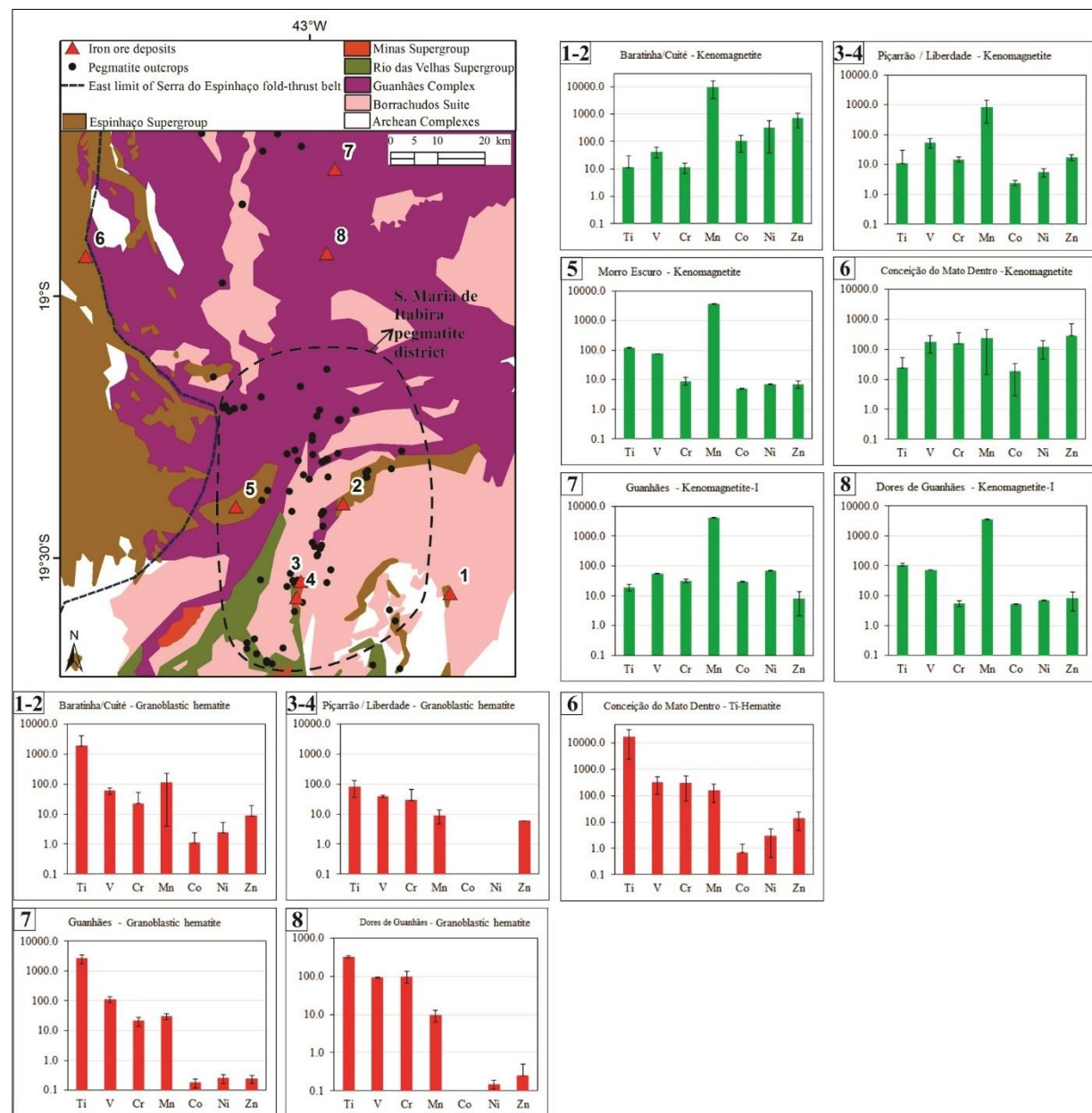


Figure 6.20: Map with the location of the main iron ore deposits along the east border of São Francisco Craton in Espinhaço fold-thrust belt and Guanhães Block, labeled from 1 to 8, with graphs showing the average mineral content of Ti, V, Cr, Mn, Co, Ni and Zn in the iron oxides presents in these ore bodies. 1-Horto-Baratinha, 2-Cuité, 3-Liberdade, 4-Piçarrão, 5-Morro Escuro, 6-Conceição do Mato Dentro, 7-Guanhães, 8-Dores de Guanhães. Microchemical data source: 1,2-this article; 3,4,5,7,8-(Gomes et al., 2018); 6-(Teodoro, 2018). The Santa Maria de Itabira pegmatite district limit (Pedrosa-Soares et al., 2011) indicated in the map is part of the Eastern Brazilian Pegmatite Province.

- Morro Escuro and Conceição do Mato Dentro deposits are hosted by the late-Paleoproterozoic Serra da Serpentina itabirite. The high-grade ore bodies are associated with shear zones, they have few centimeters thick and contain predominantly platy hematite (Silveira Braga et al., 2015; Teodoro, 2018). Rare centimetric high-grade lenses kenomagnetite rich are found in Morro Escuro (Gomes et al., 2018).
- In Guanhães and Dores de Guanhães, similar to Baratinha IF-bearing sequences and magnetite-rich high-grade orebodies are exposed as isolated segments within the TTG gneiss of the Guanhães Complex (Barrote et al., 2017; Gomes et al., 2018). Barrote et al. (2017) suggested a correlation between the Guanhães itabirite-bearing metasedimentary sequence and Serra da Serpentina Group based on the similar age distributions of detrital zircons. The deposits comprise small (<10 cm) lenses of high-grade iron bodies where the kenomagnetite is the major component and is locally overprinted by granoblastic hematite (Gomes et al., 2018).
- Piçarrão and Liberdade Deposits are also comprised by itabirite-hosted high-grade ore bodies in the TTG Guanhães Complex (Gomes et al., 2018). The 5–30 m-thick ore bodies are positioned at the contact with pegmatite intrusions and are composed predominantly of granoblastic hematite and martite with relative few relics of kenomagnetite (Gomes et al., 2018).

The titanium content is anomalously high in the hematite grains from HBD/CTE, Conceição do Mato Dentro and Guanhães. In Conceição do Mato Dentro deposit Ti-hematite has a platy habitus occurring in isolated centimetric to millimetric shear bands, apparently associated with kenomagnetite (Teodoro, 2018). In Guanhães the Ti-rich variety comprise a granoblastic fabric commonly in the high-grade lens (Gomes et al., 2018).

Vanadium is quite similar in all deposits and slightly higher in Conceição do Mato Dentro iron oxides. Chromium is slightly higher in Conceição do Mato Dentro kenomagnetite and hematite than in the other deposits. Kenomagnetite from HBD/CTE, Piçarrão, Morro Escuro, Guanhães, and Dores is Mn-rich. Cobalt has general low content, especially in the hematite grains from Guanhães, Dores de Guanhães, and Piçarrão. Nickel has highest content in kenomagnetite from HBD/CTE, Guanhães and Conceição do Mato Dentro and Zn is higher in kenomagnetite from HBD/CTE and Conceição do Mato Dentro.

6.8. Discussion

6.8.1. Origin of the Pegmatite

The pegmatite bodies from the HBD and CTE belong to the swarm that run through the southern Guanhães Complex and comprise the Santa Maria de Itabira Pegmatite District (Figure

6.20). According to Pedrosa-Soares et al. (2011) the pegmatites from this district crystallized from fluids developed by anatexis of gneissic rocks. Oliveira et al. (2017) consider these anatetic fluids also responsible for the formation of S-free Au-PGE quartz veins (“Jacutinga-type”) in Itabira deposits (Figure 6.1) and Gomes et al. (2018) associated them with the high-grade ore bodies from Piçarrão and Liberdade deposits (Figure 6.20).

The U-Pb dating of pegmatite zircons from Horto-Baratinha indicates crystallization ages between 557 ± 5 to 497 ± 7 Ma. Some of the grains exhibit inherited cores dated at $1,740.8 \pm 4.7$ Ma, same age obtained by several authors (*e.g.* Silva et al., 2002 ; Dossin et al., 1993 ; Silveira Braga et al., 2019a) for the granitoids of the Borrachudos Suite (Açucena Pluton) that surround the studied iron deposits (Figure 6.1). These data lead to the conclusion that the pegmatitic bodies associated with the hematite-kenomagnetite massive orebodies formed by anatetic melting of the Açucena granite during the Ediacaran and Cambrian and is a potential source of mineralizing fluids. The pegmatites were apparently separated from their site of formation by mechanisms such as filterpressing and seismic-pumping probably by the end of the collisional phase of the Brasiliano Orogen, once they are found as mobilized and immigrating intrusion into an environment different from their birthplace (Dill, 2015).

6.8.2. *Chemical and textural changes during iron mineralization*

In the late Neoproterozoic-Cambrian Brasiliano Collage, the paleoproterozoic IF-bearing supracrustal successions of the Serra da Serpentina and Serra do Sapo Groups and the Espinhaço Supergroup, deposited at the margins of the São Francisco craton, developed to a north-south trending fold and thrust belt incorporating the crystalline basement, as a response to the propagation of the deformation of the Araçuaí Orogen. Granitic gneissic rocks, metavolcanic and metasedimentary units of distinct metamorphic grades and structural levels, were tectonically uplifted and juxtaposed with the development of extensive shear zones. In the IF of the basal sequences the intensive deformation caused recrystallization and transposition of the banded structure with the development of a continuous schistosity. The anisotropic fabric is defined by more or less equant quartz grains clustered in narrow aggregates between elongated lamellar hematite platelets that exhibit a dimensional and crystallographic preferred orientation and locally evolves to a domanial type of cleavage with differentiated iron-rich domains probably by removal solution of quartz. These partially enriched domains may evolve to lamellar hematite-rich lenses of several tens of meter as consistent elongated high-grade “ore shoots” in the IF (Gomes et al., 2018; Rolim et al., 2016; Silveira Braga et al., 2015).

Irregular shaped hematite-kenomagnetite high-grade iron ore pods in the IF exhibit a granoblastic fabric at the contact with the pegmatitic intrusions contrasting with the foliated structure of the host as described by Silveira Braga et al. (2019b) that identified a close spatial relationship

between these rocks in the lithological 3D model of the Horto-Baratinha Deposit. The ore also displays higher proportion of interstitial silicates and carbonates that is observed mainly but not necessarily near the contact with pegmatite, together with the increasing content of Al_2O_3 , MgO and CaO and the trace elements Zr, Y, Zn, Ni, and ΣREE in whole-rock analysis. At the contact zone with the pegmatite intrusions samples B-S11, B-S27, B-S28 (HBD) also displayed an anomalous enrichment of some trace elements such as Ga, Nb, Rb, Sn, Ta, As, K_2O , P_2O_5 .

The whole-rock REE+Y analytical results from IF and hematite-kenomagnetite ore collected from HBD and CTE indicate that the mineralization process did not affect the general signature of the iron formation (Figure 6.10); although a weak HREE enrichment ($\text{Pr}/\text{Yb}_{(\text{SN})}$ between 0.27-0.33 in IF, 0.02-0.32 in hypogene ore) and a decrease of the europium anomaly were noted in some samples ($\text{Eu}/\text{Eu}_{(\text{SN})}$ between 1.49-1.59 in IF, 1.06-1.85 in hypogene ore). The similarity of REE+Y composition between IF and compact iron ore was also described by many authors in deposits of different ages and characteristics such as Mendes et al. (2016) in the QF, and Gomes et al. (2018) in the Piçarrão/Liberdade and Guanhães deposits, indicating that hypogene mineralization in many cases does not significantly affect the original IFs geochemical signature (Figure 6.1). Hensler et al. (2017) show that the intense SiO_2 leaching of hypogene Pau Branco ore deposit in the QF caused an apparent enrichment in REE but preserving the IF signature.

6.8.3.1. Kenomagnetite crystallization

The analyses of the trace elements of kenomagnetite, normalized to the values obtained from lamellar hematite, indicates a consistent increase of trace elements, mainly V, Cr, Mn, Co, Ni, Zn and Ga (Figure 6.17).

Kenomagnetite from high-grade ore exhibit a lower content of Al, V, Ti, Cr, Ga and Sn but higher Mn, Ni, Co, Zn and Mg than the crystals sampled from pegmatite (Figure 6.15). Despite these chemical differences both plot in the hydrothermal magnetite field in Ni/Cr vs. Ti diagram (Figure 6.19A) due to its high Ni content. Nevertheless, the pegmatite hosted crystals plot closer to the magmatic field (Figure 6.19A), indicating the influence of igneous components during its crystallization.

When plotted in $\text{Ti} + \text{V}$ vs. $\text{Al} + \text{Mn}$ graph all the kenomagnetites grains from ore and IF samples plot in the skarn field (Figure 6.19B), mainly due to its high Mn content. According to Nadoll et al. (2014) hydrothermal magnetite commonly incorporates Mn and Zn at levels above 100 ppm and the high Mn and Mg concentrations in hydrothermal magnetite from skarn deposits is a consequence of extensive fluid/rock interactions. Kenomagnetite from IF plot more to the left coinciding with the hydrothermal-metamorphic BIF-Iron ore magnetite field from Nadoll et al. (2014). The kenomagnetite from pegmatite plot in the IOCG field indicating hydrothermal fluids of

higher temperatures (Figure 6.19B) than the kenomagnetites from ore and IF. Similar relative Mg and Mn enrichment is observed by Gomes et al. (2018) in kenomagnetites from Dores de Guanhães, Guanhães and Morro Escuro deposits (Figure 6.20). According to Dare et al. (2014), magnetite forming from high-temperature hydrothermal fluids (~500–700 °C) associated with a magmatic-hydrothermal source is typically enriched in Ni, V, Co, Zn, Mn, and Sn, that is observed in the analyzed kenomagnetite crystals from ore, particularly in HBD.

Kenomagnetite commonly have Mn-rich ilmenite and rutile inclusions (Figure 6.6 H and 6.14E) because during the system cooling and crystallization of magnetite, Ti, Al, and Mg, which were originally in the solid solution, were separated from the solution as independent mineral phases (Borisenko et al., 1969).

The greater concentrations of Al and Ti in kenomagnetite compared to the others also indicates hotter temperatures systems (Nielsen et al., 1994). The data point out that kenomagnetite crystallization as a product of contact metasomatism of pegmatite with IF, with extensive fluid interaction.

The crystallization of kenomagnetite is associated with reducing environment, once that non-redox reaction of hematite to magnetite generate a high volume change, which is possible to occur only in unlithified sediments (Mücke and Cabral, 2005).

A consistent very low content of REE in kenomagnetite and granular hematite, which have a REE+Y PAAS-normalized general trend similar to the lamellar hematite from IF (Figure 6.16), may suggest an intensive fluid-rock interaction coupled with excessive REE exchange, with precipitation into other mineral phases (e.g., monazite, xenotime) during recrystallisation metasomatic-metamorphic contact processes. Therefore, the local co-precipitation of accessory mineral phases in iron ore and the preferential uptake of REE in these gangue minerals, may have led to a depletion of these elements in the fluid and, therefore, to REE fractionation trends in the iron oxide.

6.8.3.2. Chemical changes during oxidation of magnetite to martite

Martite pseudomorphs represent a transitional phase to the crystallization of granular hematite appearing as relicts in this phase. Martite relics exhibit higher content of Al, Si, As, Y, REE, Zr, Nb, Mo, Sn, Sb, Ta, W, Pb and U than kenomagnetite probably occupying the Fe²⁺ free sites. Differently from other mineral phases it exhibits extensively high contents of Zr, Hf, REE+Y, over the detection limit. When plotted in the Zr/Hf versus Y/Ho graph (Bau 1996 - Figure 6.21) the points fall mostly outside the CHARAC (CHArge-and-RAdius-Controlled) field suggesting a transitional system between pure silicate melts (basic to intermediate) and hydrothermal fluids during the crystallization, characterized by high-silica magmatic systems, rich in H₂O, Li, B, F, P, and/or Cl. In this system,

non-CHARAC behavior of high field strength elements may be due to its chemical complexation with a wide variety of ligands (Bau, 1996).

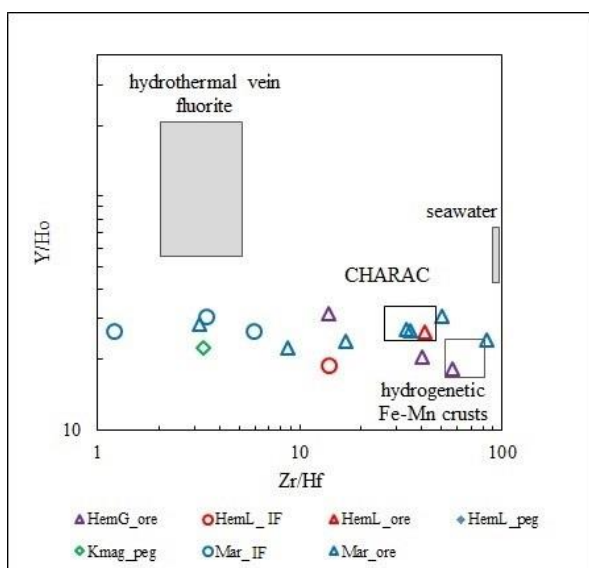


Figure 6.21: Plot of Y/Ho vs. Zr/Hf schematically showing fields of seawater, hydrogenetic marine Fe-Mn crusts, hydrothermal fluorite vein and CHARAC field, proposed by Bau (1996). It plots only the samples that have Zr , Hf , REE+Y results over the detection limit. The majority of plots are characterized by non-CHARAC behavior indicating aqueous systems.

6.8.3.3. Origin of Ti-rich hematite

The hematite crystallization in HBD and CTE seems to be a consequence of redox changes, once that non-redox reaction of magnetite to hematite generate a high volume decrease, and the newly formed hematite should have porous appearance and abundant shrinkage cracks (Mücke and Cabral, 2005). The pseudomorphic replacement of magnetite by hematite related to oxidation follows the (111) planes of primary magnetite and results arrangement of the newly formed hematite as martite-textured (Mücke and Cabral, 2005), what is observed in the analyzed samples.

Granular hematite is enriched in Al, Ti, Zr, Nb, Mo, Sn, Sb, Hf, Ta and W when compared with martite. The granular hematite has greater Al, Sc, Ti, As, Zr, Nb, Mo, Sn, Sb, Hf, Ta and W than kenomagnetite (Figure 6.18B). Hematite grains hosted by the pegmatite exhibits a very similar chemical composition to high-grade ore grains, indicating that both were formed in equilibrium with the same environment, during the reaction between intrusion and country rock. The few compositional differences are attributed to the highest temperature and melt interaction of the iron oxides from pegmatite.

An erratic but anomalously high content in Ti is characteristic for many deposits in the eastern border of the Espinhaço belt and Guanhães Block (Gomes et al., 2018; Teodoro, 2018), as shown in Figure 6.20. A residual origin for the Ti enrichment must be discarded as the analyzed values obtained in the HBD and CTE do not exhibit consistent depletion of most of the mobile trace elements such as

Al, Si, V, Cr, Ga, Nb, Sn, Zr and As but are consistent with analytical results from the pegmatitic bodies (Figure 6.15 and 6.17) suggesting a magmatic/hydrothermal source for this element. It is observed a depletion in Mg content during recrystallization of kenomagnetite/martite to granoblastic hematite, which is a result of the weak compatibility of Mg^{2+} , substituting Fe^{2+} , in hematite compared to magnetite (Hensler et al., 2015).

In the CTE deposit, on the other hand, granular hematite grains exhibit a relative lower proportion of Ti and other trace elements (Cr, Mn, Zn, Ga, Nb, and Sn - (Figure 6.15 and 6.22), probably due to the limited influence of the pegmatite fluids in the mineralization as indicated by the relative inexpressive of pegmatite bodies compared with HBD.

Although Titanium is usually an immobile element in hydrothermal solutions (Dare et al., 2014), high Ti transportability is reported for high-temperature environments such as in magnetite skarns, due to high salinity of F^- , Cl^- , SO_4^{2-} and/or CO_3^{2-} -bearing hydrothermal fluids (Purtov and Kotelnikova, 1993; Van Baalen, 1993).

The LA-ICP-MS results obtained by Hensler et al. (2015) in granoblastic hematite of the Águas Claras and Pau Branco iron ore bodies from the QF also reveal a significant Ti-enrichment and a consistent depletion in Mg when compared to magnetite and martite raising the suspicion of the influence of Brasiliano fluids in the recurrent mineralization of these deposits as indicated by our recent observations.

6.8.3. Mineralization process in HBD and CTE

The mineralization process could be divided into three main phases (Figure 6.22):

- 1) Iron enrichment by shear-zone controlled selective solution removal of quartz assisted by the hydrothermal fluids during the syn-collisional and late-collisional stages (580 – 560 Ma) of the Brasiliano Orogeny. This stage is of regional importance as described by several authors (Gomes et al., 2018; Oliveira et al., 2017; Rolim et al., 2016; Silveira Braga et al., 2015), but it seems not to be effective in the Horto-Baratinha as in Cuité and the deposits located in the thrust fronts along the Serra do Sapo and Serpentina Ridges that exhibit tabular-shape sheared high-grade orebodies (LGO) (Figure 6.3F). Hematite crystals grow as oriented plates with the development of a grain shape and crystallographic preferred orientation by strain-controlled, fluid assisted small scale diffusion and crystallization (Rosière et al., 2013).
- 2) Contact-metasomatic/contact-metamorphic alteration related to the emplacement of anatectic pegmatites with the formation of kenomagnetite. Pegmatites were originated by the partial melting of the Borrachudos granite during the late-collisional and post-collisional/gravitational collapse of the orogeny (560 – 490 Ma) associated with the uplift of

the sequence (Figure 6.22). Magmatic fluids (high temperature, high salinity) intruded the sequence in a reducing environment, resulting in the formation of kenomagnetite.

- 3) Quartz solubility is sensitive to pressure, temperature, pH and salinity (Evans et al., 2013; Hagemann et al., 2016). High magmatic fluid temperature, associated with high pressure, pH and salinity could be responsible by Si-leaching of IF. The leached Si precipitated as pegmatite intrusions and quartz veins.
- 4) An mixing of low-temperature, low-salinity meteoric waters and higher-temperature, higher-salinity brines related to anataxis was identified by Gomes et al. (2018) in fluids inclusion of quartz veins from Piçarrão iron deposit. This fluid mixing is associated with the final stage of gravitational collapse of the orogeny (Figure 6.22) and related with the progressive oxidation of kenomagnetite to martite and granular hematite crystallization (Gomes et al., 2018; Oliveira et al., 2017).

6.9. Conclusions

According to the geochronological, whole-rock and in situ LA-ICP-MS chemical data, it is concluded that:

- 1) The pegmatitic bodies associated with the hematite-kenomagnetite massive orebodies formed by anatetic melting of the Borrachudos Suite (Açucena Pluton) during the Ediacaran and Cambrian (from 557 ± 5 to 497 ± 7 Ma) and is a potential source of mineralizing fluids.
- 2) The iron formation-bearing sequence from HBD and CTE deposited at the margin of the São Francisco craton during Orosirian-Statherian, and is associated with supracrustals sucessions of the Serra da Serpentina and Serra do Sapo Groups.
- 3) The iron oxides generation and mineralization process at HBD and CTE could be divided into three phases (Figure 6.22):
 - a. syn-collisional (580 – 560 Ma):
 - i. Metamorphic recrystallization and transposition of the sedimentary structures.
 - ii. Generation of lamellar hematite in iron formation.
 - iii. Partial Si-leaching along shear zones.
 - b. late-collisional and post-collisional/gravitational collapse of the orogeny (560 – ~530 Ma):
 - i. Partial melting of the Borrachudos granite with generation of pegmatitic magma causing contact-metasomatic/contact-metamorphic processes with country rocks.
 - ii. The contact-metasomatic process resulting in crystallization of kenomagnetite hypidioblasts and Si-leaching.

c. final stage of gravitational collapse of the orogeny (~530 – 490 Ma):

- Last pegmatite intrusions and final uplift of Guanhães Block.
- A mixing of low-temperature, low-salinity meteoric waters and higher-temperature, higher-salinity brines related to anataxis promoted the progressive process of oxidation, recrystallization and grain growth generating granular hematite.

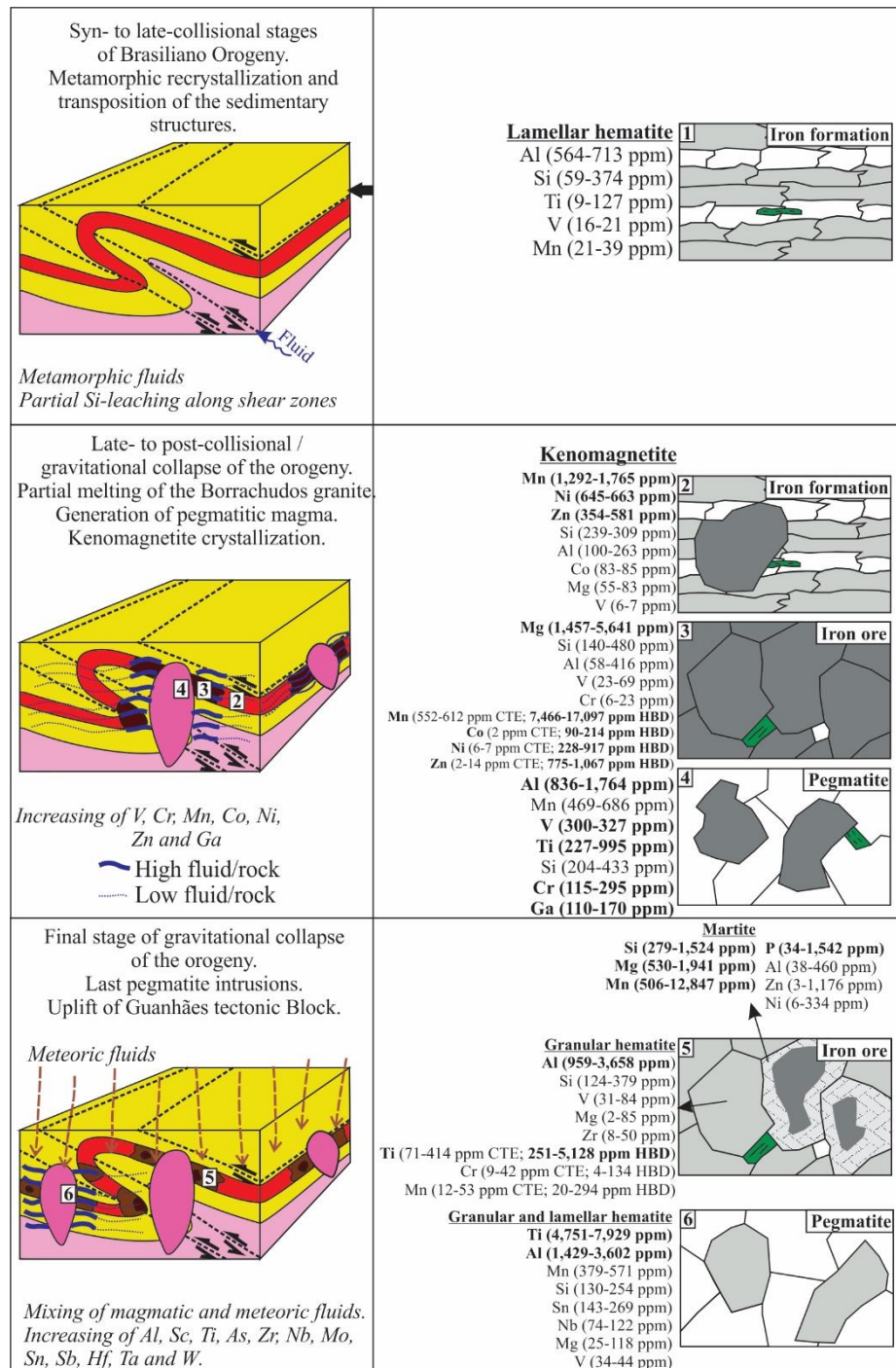


Figure 6.22: Genetic model and mineral chemical evolution of the HBD and CTE iron ore deposits.

- 4) The compositional variation between IF and ore bodies in whole-rock chemistry indicates strong SiO₂ leaching and enrichment of Fe₂O₃, TiO₂, As, Sb, W, Ni, Zr, and V.
- 5) Titanium and manganese behaved as mobile elements during the contact-metasomatic process, generating Mn-rich kenomagnetite, Ti-rich hematite and ilmenite inclusions.

Acknowledgments

The authors would like to express their gratitude to BEMISA and its team for supplying drill hole data and supporting the field work in Horto-Baratinha mine. We also thank Leonid Danyushevsky, Paul Olin, and Ivan Belousov (University of Tasmania) for the supporting with LA-ICP-MS. This study was financed by the Coordenação de Aperfeiçoamento de Pessoal de Nível Superior - Brasil (CAPES) - Finance Code 001 (scholarship / Programa de Doutorado Sanduíche no Exterior / Pr. n° 88881.134959/2016-01) and Fundação de Amparo à Pesquisa de Minas Gerais (FAPEMIG / CRA-APQ 01178-15).

7. ARTIGO V - EDIACARAN-CAMBRIAN FAR-FIELD HYDROTHERMAL EVENT IN THE SOUTHEAST BRAZIL: EVIDENCE FROM ZIRCON U-PB SHRIMP, TRACE ELEMENTS, LU-HF AND OXYGEN ISOTOPES

*Flávia Cristina Silveira Braga^{ab}, João Orestes Schneider Santos^c, Carlos Alberto Rosière^d, Vassily K. Rolim^e, Malcolm P. Roberts^f, Noreen J. Evans^g, Steffen G. Hagemann^f

^a Graduate Program, Instituto de Geociências, Universidade Federal de Minas Gerais, Belo Horizonte, MG, Brazil

^b Faculdade de Engenharia, Universidade do Estado de Minas Gerais, João Monlevade, MG, Brazil

^c Universidade do Estado do Amazonas, Manaus, AM, Brazil

^d Instituto de Geociências, Universidade Federal de Minas Gerais, Belo Horizonte, MG, Brazil

^e PRCZ Consultores Associados Ltda, Belo Horizonte, MG, Brazil

^f University of Western Australia, Perth, WA, Australia

^g School of Earth and Planetary Science, John de Laeter Centre, Curtin University, Perth, WA, Australia

* Corresponding author.

E-mail addresses: flaviacsbraga@gmail.com, flavia.braga@uemg.br (F.C. Silveira Braga), crosiere@gmail.com (C.A. Rosière), orestes.santos@bigpond.com (J.O.S. Santos), vassily.rolim@gmail.com (V. K. Rolim), malc.roberts@uwa.edu.au (M. Roberts), noreen.evans@curtin.edu.au (N.J. Evans), steffen.hagemann@uwa.edu.au (S.G. Hagemann)

7.1. Abstract

Iron formation-bearing sequences from two tectonic blocks of the Southeastern São Francisco Craton (Guanhães and Southern Espinhaço blocks) were affected by the Neoproterozoic-Cambrian Brasilian Orogeny (locally manifest as the Araçuaí Orogenic belt). The rocks of the Guanhães Block were deformed and upthrust onto the Statherian metasedimentary units of the Lower Espinhaço Supergroup during the orogenic event. The two blocks are associated with iron formation-bearing sequences containing high-grade iron ore bodies (Horto-Baratinha, Cuité, Morro Escuro and Morro do Pilar deposits). In order to characterize the temporal and geochemical evolution of the hydrothermal event associated with the late orogenic event, three different types of zircon were studied: detrital zircon (Lower Espinhaço Supergroup – Orosirian-Statherian maximum depositional age), zircon from gneissic basement (Archean Guanhães Complex), and zircon from meta-granitoids (Statherian Borrachudos Suite). All populations include zircon with <5µm to 50µm wide areas that are brighter in BSE images (mainly rims). These zones are much younger than the rest of the grain (U-Pb SHRIMP ages from 492 Ma to 554 Ma) and display higher U contents and lower Th/U ratios. Dated zircons from pegmatites that crosscut the Paleoproterozoic sequence have similar ages, high U contents and low Th/U. Some of the pegmatite zircons have inherited cores from the Borrachudos Suite. Comparing the chemical composition of core and rims it is possible to note a general ZrO₂, SiO₂ and Th depletion and U, Pb, Hf, Mg, Ca, Fe, Yb and P enrichment in the rim. There is a decreasing trend of $\epsilon_{\text{Hf(t)}}$ and increasing of $^{176}\text{Hf}/^{177}\text{Hf}_{(t)}$ from core to rim. Higher $\delta^{18}\text{O}$ values (above

7‰) were found in BSE brighter area of detrital and pegmatite zircons, approximately 1‰ greater than the dark areas, indicating low-temperature water-rock interaction. During the late- and mainly post-collisional stages of the Brasilian Orogeny (560-490 Ma) uplifting and juxtaposing of Neoarchean gneissic rocks of eastern São Francisco Craton, Statherian granites and metamorphic supracrustal units occurred. Uplift and decompression promoted partial melting of the Borrachudos Suite, generating pegmatite intrusions and delivering magmatic-hydrothermal fluid that affected the entire sequence. Zircons from metasedimentary rocks, granite, and gneiss were recrystallized at sub-solidus conditions during interaction with the moderate- to low-temperature hydrothermal fluid. A concentric porous fabric present in some grains indicates the fluid path during crystal alteration and recrystallization. The zircon recrystallization process deeply affected the chemical and isotopic composition. The pegmatite zircons represent an anatetic new zircon growth, or overgrowth, in the presence of fluid and melt.

Keywords: zircon, overgrowth, recrystallization, hydrothermalism

7.2. Introduction

Zircon occurs in a wide variety of sedimentary, igneous, and metamorphic rocks as a common accessory mineral. It incorporates an assortment of minor and trace elements, so it retains significant chemical and isotopic information. The chemical and mechanical durability of zircon during weathering, igneous and hydrothermal process makes it an ideal mineral for studies related to the evolution of Earth's crust and mantle. Textural imaging using back-scattered electrons (BSE) and in situ microchemical and isotopic analysis has revealed many cases where single zircon crystals contain a record of multiple geologic events, which can either be zircon-consuming, zircon-altering, or zircon-forming (Hoskin and Schaltegger, 2003).

Magmatic, hydrothermal and metamorphic zircons are described extensively in the literature. Hydrothermal zircon or zircon crystallized from fluid-saturated melts can be used to date and characterize fluid-infiltration events and water-rock interaction (Hoskin, 2005). Metamorphic zircons can be formed by distinct process - alteration, replacement/recrystallization, new zircon growth - that affects zircon trace elements chemistry and Hf isotope composition in different ways (Rubatto, 2017). The altered zircon can partially overprint and disturb the relict mineral, while relict textural and chemical vestiges are preserved (Rubatto, 2017). Replacement/recrystallization occurs under sub-solidus conditions with evidence of complete resetting of the chemical/isotopic system, a sharp boundary with inherited domains, and lack of regular growth textures (Hoskin and Black, 2000; Rubatto, 2017). However, due to inheritance, recrystallized zircons often display a Hf isotope composition similar to the relict core (Ge et al., 2013). New zircon growth (or overgrowth) is related to dissolution and re-precipitation of pre-existing zircon during crystallization from a melt or

precipitation from a fluid (Geisler et al., 2007; Schaltegger et al., 1999), and usually shows sharp boundaries, and distinct chemical and isotopic compositions relative to the relict (Rubatto, 2017). Zircon overgrowth represents a new crystal domain (Rubatto, 2017) and commonly show elevated initial $^{176}\text{Hf}/^{177}\text{Hf}$ values relative to their relict cores (Chen et al., 2015; Xia et al., 2009). The zircon metamorphic growth could be also associated with metamorphic reactions that release sufficient Zr (Sláma et al., 2007; Vavra et al., 1996).

Despite of the several improvements in zircon chemical and isotopic studies, distinguishing between hydrothermal, magmatic and metamorphic crystals is somewhat unclear. Hydrothermal zircon may possess a range of geochemical and textural characteristics resulting from distinctive fluid compositions or zircon/fluid fractionation effect, and consequently its potentially significant petrogenesis is little known (Ayers and Peters, 2018; Hoskin, 2005; Hoskin and Schaltegger, 2003; Zhong et al., 2018). The term hydrothermal zircon is generic because it refers to all zircons crystallized from, or altered by an aqueous fluid (Hoskin, 2005). This paper aims to contribute with the hydrothermal zircon characterization, studying different zircons source affected by the same hydrothermal event.

In this study, our focus is the discrimination between, and characterization of, U-rich zircon rims and original cores, which is critical for understanding the temporal and geochemical evolution of the hydrothermal event associated with the Neoproterozoic-Cambrian Late Brasilian Orogeny. This study contributes to our understanding of the tectonometamorphic and hydrothermal history of poly-deformed regions, particularly of medium- to high- grade metamorphic terrains, such as the Araçuaí Orogen (part of Brasilian Orogeny) and associated hydrothermal deposits. The textural and chemical zircon features allow the establishment of a relationship between the formation of hydrothermal minerals, tectonic deformation and fluid interaction.

7.3. Geological Setting

The area is located in the southeastern portion of the São Francisco Craton, neighbouring the Cambrian-Neoproterozoic Brasilian Orogenic belt to the east (Figure 7.1) that, together with associated cratonic blocks, resulted from the assembly of the West Gondwana. The eastern margin of the craton was reworked by the Brasilian Orogeny and is locally named the Araçuaí belt or Araçuaí Orogen (Pedrosa Soares et al., 2001). The Araçuaí Orogen extends from the eastern edge of the São Francisco Craton to the Atlantic margin, in southeastern Brazil (Alkmim et al., 2006; Pedrosa Soares et al., 2011, 2001) – Figure 7.1.

The cratonic basement is mainly represented by Archean and Paleoproterozoic units such as the Mantiqueira (Rhyacian) and Guanhães (Neoarchean) Complexes, the Rio das Velhas greenstone

belt (Neo- and Mesoarchean), the Siderian Minas Supergroup, the Statherian Borrachudos Suite and Statherian to Mesoproterozoic Espinhaço Supergroup.

Archean and Paleoproterozoic units comprising the Mantiqueira and Guanhães Complexes make up the continental crust reworked by Brasilian (Neoproterozoic-Cambrian) and Trans-Amazonian (Rhyacian) orogenic events. The Guanhães Complex is comprised of TTG (tonalite-trondjemite-granodiorite) gneisses, migmatites, and granitic bodies, commonly displaying mylonitic fabric that includes discontinuous strings of metavolcanic and iron formation-bearing metasedimentary rocks (Dussin et al., 2000; Noce et al., 2007a), constitute the main unit of the Guanhães tectonic block (Figure 7.1). This tectonic block exposes a deeper crustal level with a higher metamorphic grade than the adjacent blocks, such as the Serra do Espinhaço fold-thrust belt block located to the northwest (Alkmim et al., 2006). The studied area is located in the Guanhães tectonic block at the southern limit of the Serra do Espinhaço belt (Figure 7.1).

The Archean and Paleoproterozoic crust from Guanhães block, Espinhaço belt and the eastern QF (Figure 7.1) is considered a metacratonization zone, resulted of the craton basement remobilization during the Brasilian orogenic event (Liégeois et al., 2013; Oriolo et al., 2017; Silva et al., 2005).

A rift system is interpreted during the Late Orosirian and Statherian, with emplacement of the Borrachudos anorogenic plutons around 1,740 Ma and deposition of the lower volcano-sedimentary Espinhaço Supergroup sequence (Dossin et al., 1993; Fernandes et al., 1994; Silva et al., 2002). The felsic rocks associated with the Espinhaço taphrogenic event are interpreted as integrating the long-lived Statherian silicic large igneous province (1,750–1,710 Ma) characterizing the major magmatic event recorded throughout the whole Espinhaço rift system (Magalhães et al., 2018).

The Espinhaço Supergroup is interpreted by Chemale et al. (2012) as being deposited in two distinct intraplate basins: lower volcano-sedimentary strata deposited between 1,680-1,800 Ma, and the upper rift-sag with a 1,192 Ma maximum deposition age. The shallow marine sedimentary rocks from the Lower Espinhaço Basin are underlain by metamorphosed iron formation-bearing psamopelitic units and ultramafic rocks, and were grouped into two main units by Rolim et al. (2016); Serra da Serpentina and Serra de São José Groups. The metasedimentary sequence identified in Horto-Baratinha, Cuité, Morro Escuro and Morro do Pilar iron deposits (Silveira Braga et al., 2019a, 2015) is correlated with the groups defined by Rolim et al. (2016).

The evolution of the Araçuaí Orogen, with a precursor rift-related to distal passive margin and oceanic successions, is recorded by magmatic arc-related rocks and collisional to post-collisional igneous supersuites (Alkmim et al., 2006). Orogenic igneous rocks, formed from c. 630 to c. 480 Ma, cover one-third of this orogenic area, building up the Eastern Brasilian Pegmatite Province, the most important dimension stone province worldwide. The province is subdivided into districts (Figure 7.1)

encompassing the most important pegmatite populations, based on their main mineral resources, pegmatite size, type, class, and relationship with parent and host rocks (Pedrosa Soares et al., 2011).

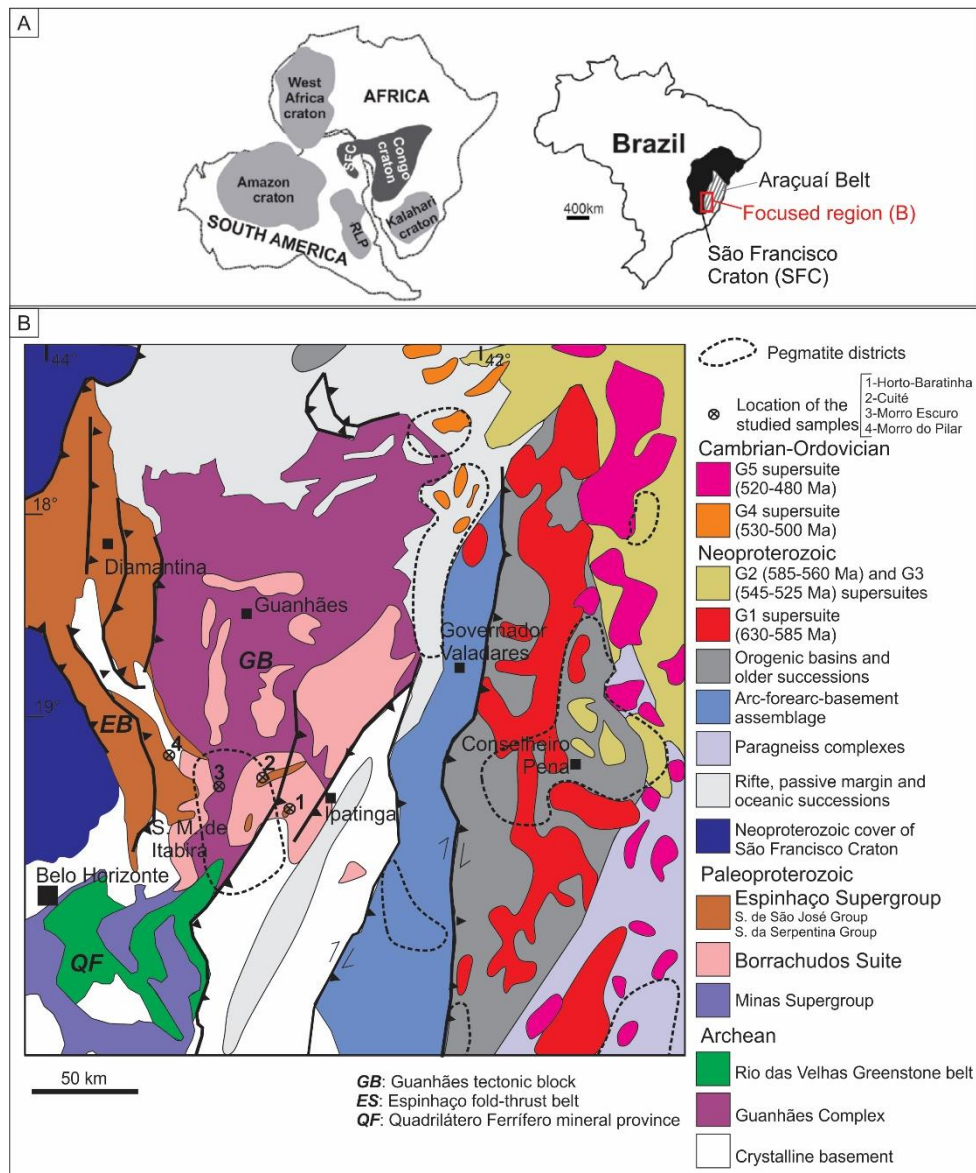


Figure 7.1: (A) Geotectonic configuration of the São Francisco-Congo Craton in the context of West Gondwana and SFC limit (after Alkmim et al., 2006). (B) Simplified geological map from part of the Araçuaí Orogen (modified from Pedrosa Soares et al. (2011) showing the location of the studied samples.

The supersuites are named G1 to G5 and represent different magmatic events within the Araçuaí Orogeny (Alkmim et al., 2007; Pedrosa Soares et al., 2011, 2007, 2001; Silva et al., 2002). The G1 supersuite (630–585 Ma) represents a continental calc-alkaline magmatic arc. The G2 supersuite formed during the syn-collisional stage (585–560 Ma) and generally includes S-type granites. The G3 supersuite (545–525 Ma) has autochthonous patches and veins of non-foliated garnet-cordierite leucogranites. The S-type G4 and I- A-type G5 supersuites, formed during the post-collisional stage (530–480 Ma).

Two main types of pegmatites are described in the Eastern Brasilian Pegmatite Province: pegmatites from granitic residual melts and anatetic pegmatites from partial melting of gneissic basement. The studied area is located in the Santa Maria de Itabira (or Nova Era–Itabira–Ferros) district, which contains anatetic pegmatites associated with a hydrothermal system (Pedrosa Soares et al., 2011). The widespread, undeformed pegmatites of this district were dated at 477 ± 14 Ma by Rb-Sr (Preinfalk et al., 2002), at 519 ± 10 Ma by muscovite K-Ar age (Marciano, 1995), and 474 ± 8 Ma using ion microprobe U-Th-Pb analysis (Ferreira, 2017). Hydrothermal coarse-grained quartz-feldspar veins hosted by ultramafic schists and banded iron formations from this district host significant deposits of emerald, alexandrite, and aquamarine (Pedrosa Soares et al., 2011).

The residual pegmatites are considered much more economically important than the anatetic variety, and their parent rocks belong to the syn-collisional G2 and post-collisional G4 and G5 supersuites (Pedrosa Soares et al., 2011) – Figure 7.1.

During the Araçuaí Orogen evolution, the region was affected by the development of an hydrothermal system, as registered by several authors (e.g. Barrote et al., 2017; Cabral and Zeh, 2015; Gomes et al., 2018; Gonçalves et al., 2019; Martins et al., 2016; Oliveira et al., 2017; Rolim et al., 2016; Silveira Braga et al., 2019a, 2015). The hydrothermal event is better described in the lower-grade external fold-and-thrust belt and its Foreland Domain, close to the eastern margin of the adjoining São Francisco craton (Gonçalves et al., 2019). However, example of hydrothermalism associated with this period is also described in the cratonic basement domain (Cabral and Zeh, 2015; Martins et al., 2016). In this study, the geochemical and isotopic data compilation of hydrothermal altered zircons from iron deposits located in the eastern margin of craton up to west, in the basement-reworked domain (Guanhães tectonic block) provide an important overview of this regional hydrothermal event.

7.2.1. Hydrothermalism associated with Brasilian Orogeny

Several authors have described the hydrothermalism associated with the Brasilian Orogeny throughout the Southern Serra do Espinhaço Block, Guanhães Block and also in the Quadrilátero Ferrífero (QF) Fe-Au mineral province (e.g. Cabral et al., 2015; Silveira Braga et al., 2015; Martins et al., 2016; Rolim et al., 2016; Barrote et al., 2017; Oliveira et al., 2017; Gomes et al., 2018; Silveira Braga et al., 2019a). In addition to the emerald, alexandrite, and aquamarine associated with hydrothermal quartz-feldspar veins, there are also Neoproterozoic-Cambrian hydrothermal record in iron and gold deposits.

The schistose iron ore types hosted in the Minas Supergroup (Figure 7.1) in the eastern part of QF has been interpreted as having formed during the Neoproterozoic Brasilian Orogeny, implying that iron ore formation took place during two compressive tectonic events of noticeably distinct age.

The first was the Paleoproterozoic Trans-Amazonian event (~2100 Ma) – considered the main Fe and Au mineralization event along QF – and the second was the Neoproterozoic Brasilian event (Rosière et al., 2008; Rosière and Rios, 2004).

A U-Pb age for iron formation-hosted gold vein mineralization (locally referred to as the Jacutinga lode) was obtained on monazite grains recovered from the Conceição iron ore deposit and yielded a precise Late Cambrian age of 495.6 ± 2.2 Ma (Cabral et al., 2015). Xenotime crystals from tourmaline-rich hydrothermal pockets in the auriferous lode of Passagem de Mariana, a world-class gold deposit located south-east QF, delivered a Concordia age of 496.3 ± 2.0 Ma. There is also a register of this Cambrian hydrothermal event in the north-west of QF, where xenotime was dated at 518.5 ± 9 Ma, suggesting a Cambrian imprint on the Lamego lode gold deposit (Martins et al., 2016). However, according to the authors, no gold input was associated with this event.

This Cambrian hydrothermal event is registered in the U-rich zones along zircon rims and fractures ubiquitously found in iron formation-bearing sequences of the Guanhães Complex and in the eastern border of the Espinhaço belt (Barrote et al., 2017; Rolim et al., 2016; Silveira Braga et al., 2019a, 2015).

7.4. Methodology

Four type of analyses were conducted in the zircon grains: U-Pb, electron microprobe, Lu-Hf, and $^{18}\text{O}/^{16}\text{O}$. The samples were collected from four iron ore deposits: Horto-Baratinha, Cuité, Morro Escuro, and Morro do Pilar (Figure 7.1). Summarized details of the location and analysis of the samples are presented in Table 7.1. Analytical procedures are described in Appendix 5, and the results are in Appendix 6. Multiple measurements were performed on the same domain, and where possible, at the same spot location.

Given the complexity of zircon textures, trace-element analysis is widely applied as a complementary tool for more assertive petrogenetic interpretation. Several *in situ* techniques are used, such as secondary ion mass spectrometry (SIMS), laser-ablation inductively coupled plasma mass spectrometry (LA-ICP-MS), and electron microprobe (EMP), each with different analytical volumes, detection limits and analytical precision. The EMP has higher detection limits than the other techniques, however, it utilizes the smallest spot size, avoiding accidental analysis of inclusions, or mixing analysis of texturally distinct areas within single crystals. . The zircon rims are too narrow (around 10 um) to be analyze by LA-ICP-MS. Thus, only the EMP method with spot size of <2 um was chosen for elemental analysis.

Sample ID	Lithotype	Location	UTM (E / N) meters	Number of Analyses (spots)			
				U-Pb	Lu-Hf	WDS	$^{18}\text{O}/^{16}\text{O}$
B-R66	Gneiss	Horto-Baratinha	733405 / 7837473	7	5	12	-
B-R49	Granite	Horto-Baratinha	739922 / 7835917	8	5	7	-
B-R63	Granite	Horto-Baratinha	733710 / 7837868	9	4	24	13
B-R12	Pegmatite	Horto-Baratinha	737497 / 7835093	4	4	6	6
B-R36	Pegmatite	Horto-Baratinha	737712 / 7834508	15	8	28	-
B-S54	Pegmatite	Horto-Baratinha	737331 / 7834953	0	0	5	-
B-R54	Paraschist	Horto-Baratinha	737345 / 7835201	20	9	20	-
B-R56	Paraschist	Horto-Baratinha	737331 / 7835386	20	12	21	12
B-S15	Paraschist	Horto-Baratinha	737363 / 7835194	5	3	4	-
C-R14	Paraschist	Cuité	715909 / 7854122	20	12	21	7
C-R23	Paraschist	Cuité	716023 / 7854091	6	5	5	-
C-R20	Pegmatite	Cuité	715938 / 7854212	-	-	8	-
6666	Quartzite	Morro do Pilar	672788 / 7870977	34	-	8	-
6670	Metaconglomerate	Morro Escuro	697903 / 7854995	32	-	9	-

Table 7.1: Summarized details of the samples. Notes: UTM - Universal Transverse Mercator; CM (Central Meridian) - 45°W, zone 23. WDS - Wavelength Dispersive Spectroscopy

Table 7.2 shows the main trace element characteristics of magmatic, metamorphic, hydrothermal and altered zircons (based on Ayers and Peters, 2018). A common diagnostic feature is the Th/U ratio, which is frequently low in metamorphic and hydrothermal zircons. Hydrothermal (and hydrothermalized) zircons are also characterized by high U and REE content. Zircon is more likely to recrystallize and achieve trace element partitioning equilibrium in fluids in which its solubility is enhanced (Ayers and Peters, 2018). The higher silica content in the fluid, and (to a lesser extent) the higher pH, the greater zircon aqueous solubility, which is relatively low at crustal and upper mantle conditions in most fluid compositions (Ayers et al., 2012).

Type	Trace element concentration / pattern depend on...	Diagnostic trace elements
Magmatic	Melt concentration and $D_{\text{zircon/melt}}$	High Th/U – 0.3-0.8
Metamorphic	Rock concentration and $D_{\text{zircon/rock}}$	Low Th/U=0.01-0.1, low U
Hydrothermal	Fluid concentration and $D_{\text{zircon/fluid}}$	Low Th/U; high U; high REE, Nb, Hf, U, Ti
Altered or secondary domains (affects metamict zircons at low T)	Composition of altering fluid, kinetics?	High Th/U, LREE; low REE, Th, U; high Hf, Ca, Al, Fe

Table 7.2: Definition of zircon growth types. Source: Ayers and Peters (2018) and references therein.

7.5. Results

7.5.1. Textural characterization

7.5.1.1. Zircon from metasedimentary rocks (B-R54, B-R56, B-S15, C-R14, C-R23, 6666, 6670)

All the zircon grains show a subrounded to rounded habit. The recrystallized zones are mainly along the rims, sometimes along the fractures or in the interior of crystals, which are brighter in BSE images and varying in width from <5 um to 50 um (Figures 7.2 and 7.3). These zones are often texturally homogeneous, show sharp boundaries with the core, and no internal zoning. Some grains exhibit a concentric porous fabric with discrete recrystallized zone positioned in the interior of the zircon (Figure 7.2). Some zircons from Morro do Pilar and Horto-Baratinha have xenotime inclusions in recrystallized zones.

The BSE brighter areas are more common in the zircons from Horto-Baratinha and Cuité, but also occur in zircons from Morro do Pilar and Morro Escuro (Figure 7.3).

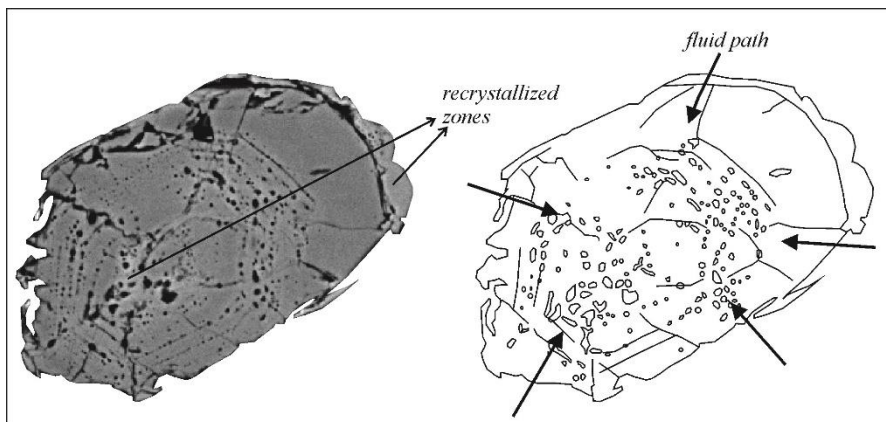


Figure 7.2: Back-scattered electron image of detrital zircon from sample C-R14 showing concentric porous fabric, which is indicative of the fluid path affecting altered areas along zoning planes.

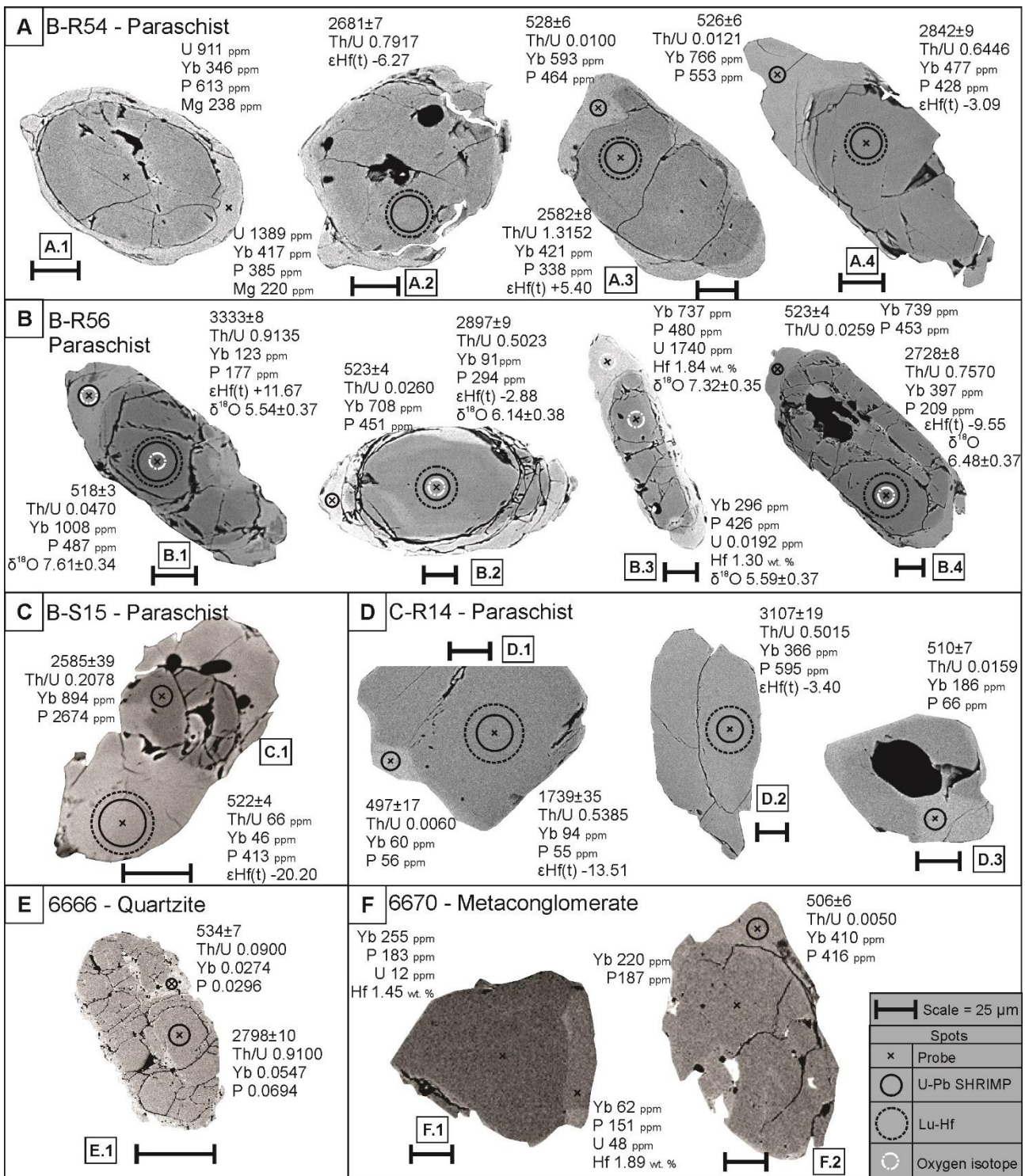


Figure 7.3: Back-scattered electron images of representative detrital zircon grains including U-Pb ages and some chemical and isotopic data.

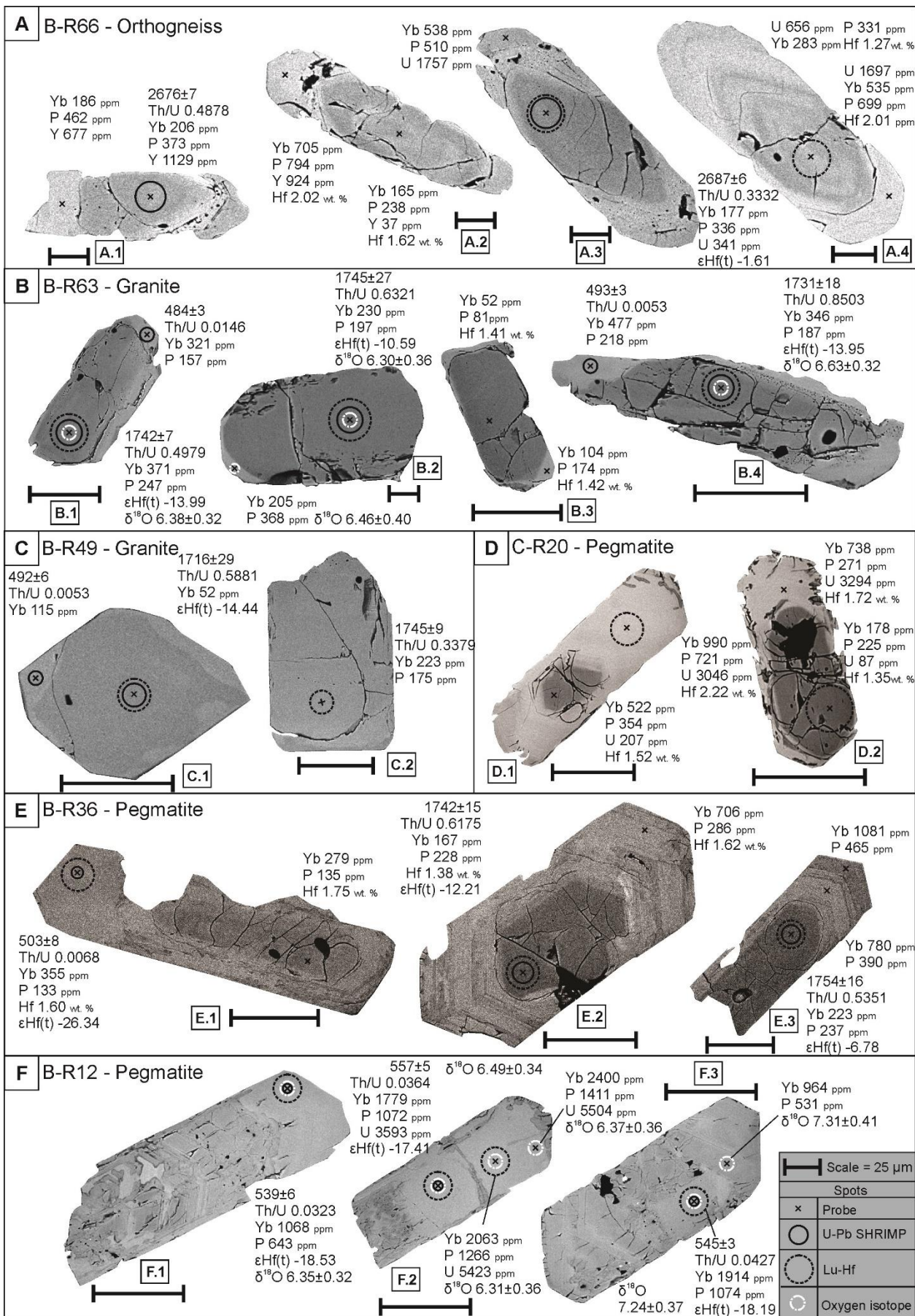


Figure 7.4: Back-scattered electron images of representative igneous zircon grains including U-Pb ages and some chemical and isotopic data.

7.5.1.2. Zircon from meta-igneous rocks (B-R49, B-R63, B-R66)

The zircons from orthogneiss and meta-granitoid are predominantly long prismatic, subhedral, with length to width ratios around 2:1 and 3:1 (Figure 7.4). Some show internal zoning, associated with the igneous crystallization process. Similar to the zircons from metasedimentary rocks, these crystals sometimes show recrystallized zones, mainly in the rims, rarely along some fractures or in the interior of grains, which are brighter in BSE images and vary from $<5\mu\text{m}$ to $25\mu\text{m}$ thick (Figure 7.4).

These zones are often texturally homogeneous, with no internal zoning. However, different from detrital zircons, the contact core/rim is gradual (Figure 7.4). The interfaces recrystallized rim/core are frequently more porous (Figure 7.4).

7.5.1.3. Zircon from pegmatites (B-R12, B-R36, B-S54, C-R20)

The zircons from pegmatites show long prismatic lengths of 75-125 μm and aspect ratios around 3:1. Zircons from samples B-R36 and C-R20 show two different textural zones. The internal zone of zircon from these samples are intensively fractured, without zoning, and shows a rounded shape (Figure 7.4). The external zone shows well-developed magmatic-style oscillatory igneous zoning, is brighter and shows fewer fractures than the internal zone. The crystal boundaries are prismatic (Figure 7.4).

Zircons from sample B-R12 are highly metamict, with relicts of igneous zoning, and amorphous domains with a rounded shape along the fractures (Figure 7.4). These crystals are much brighter in BSE images than those previously described.

7.5.2. Zircon U-Pb ages

Here we integrate new zircon U-Pb ages (samples B-R12, B-R36, B-S54, B-S15, C-R14, C-R23, C-R20 – see Table 7.1) with previously published ages for Morro Escuro (Silveira Braga et al., 2015), Morro do Pilar (Rolim et al., 2016) and Horto-Baratinha (Silveira Braga et al., 2019a) – (samples B-R66, B-R63, B-R49, B-R54, B-R56, 6666 and 6670).

The analyses of detrital zircon yielded Statherian ages for the youngest populations, indicating deposition synchronous with the base of Espinhaço Supergroup (Chemale et al., 2012; Rolim et al., 2016; Silveira Braga et al., 2019a, 2015). Two samples (B-R54 and B-R56, Figure 7.5A and B) show dominant Neoarchean peaks whereas one samples (C-R14) lacks Archean grains, where the main peak is Statherian (Figure 7.5C). The majority of Archean peaks are Neoarchean, and the Rhyacian peaks are presents only in samples from Morro Escuro and Morro do Pilar. Discussion about zircon source can be found in Silveira Braga et al. (2015, 2019a) and Rolim et al. (2016). The U content varies between 25 ppm and 1614 ppm and Th/U values are 0.17-2.99. The BSE brighter areas over

detrital zircon rims show $^{206}\text{Pb}/^{238}\text{Pb}$ ages from 494 ± 3 to 541 ± 17 , U content between 724-2689 ppm, and Th/U of 0.001-0.24.

Igneous zircons from orthogneiss generated a Pb-loss Discordia (Figure 7.6) with an upper intercept at $2,713.3 \pm 6.5$ Ma (MSWD = 5.4), interpreted as the crystallization age of the sample (pre-metamorphism), and a lower intercept at 540 ± 20 Ma (Silveira Braga et al., 2019a). The U content is 316-1331 ppm and Th/U from 0.124 to 0.488. The rim analysis resulted in discordant ages that are not discussed further.

Igneous zircons core analysis from two granite samples delivered Statherian crystallization ages (Figure 7.6A and B). The two Discordia provided upper intercepts at $1,746 \pm 10$ (MSDW = 2.9) and $1,740 \pm 10$ (MSWD = 1.6), and lower intercept at 492 ± 6 and 495 ± 6 (Figure 7.6A and B). The U content is 30-1066 ppm and Th/U is 0.142-0.915. The rim analyses resulted in ages between 484 ± 3 Ma and 525 ± 5 Ma, U content between 580-1897 ppm and a Th/U of 0.005-0.072.

Pegmatite (B-R36) shows core relicts of Statherian age ($1,741 \pm 5$ Ma - Figure 7.7A), indicating that they possibly were inherited from the Açuçena host rock pluton (Borrachudos Suite) and were partially consumed during partial melting. The U content in these zones varies between 53-672 ppm and Th/U ranges from 0.341 to 0.867. The rim analysis yielded much younger concordant ages, indicating a crystallization age of 503 ± 6 Ma with U much higher content (3320-5899 ppm) and lower Th/U ratios of 0.058 to 0.068 (Figure 7.7A). Zircons from other pegmatite (samples B-R12 – Figure 7.7C) do not have core/rim textures and are much more metamictic and fractured than zircons from sample B-R36. The homogenous and less metamict zones were dated with the smallest spot (10 μm), due to the high Pb content, and the concordant ages obtained vary from 518 ± 3.0 to 557 ± 5.0 Ma, Figure 7.7. The U content is between 3315-4523 ppm and Th/U is 0.032-0.043.

It is recognized in Figure 7.7A a considerable increase in U content, and consequent decrease in Th/U ratio (Figure 7.7B), in the younger zircon areas when compared with the older ones. The same behavior is observed for the igneous zircons (Figure 7.7). Comparing the concordant ages obtained in the BSE brighter areas of detrital zircons and pegmatites, it is possible to recognize various peaks between 490 Ma to 560 Ma in both zircon types (Figure 7.8). The most pronounced pegmatite zircon peak is at 504 Ma and the BSE brighter area of detrital zircons has a peak at 534 Ma (Figure 7.8).

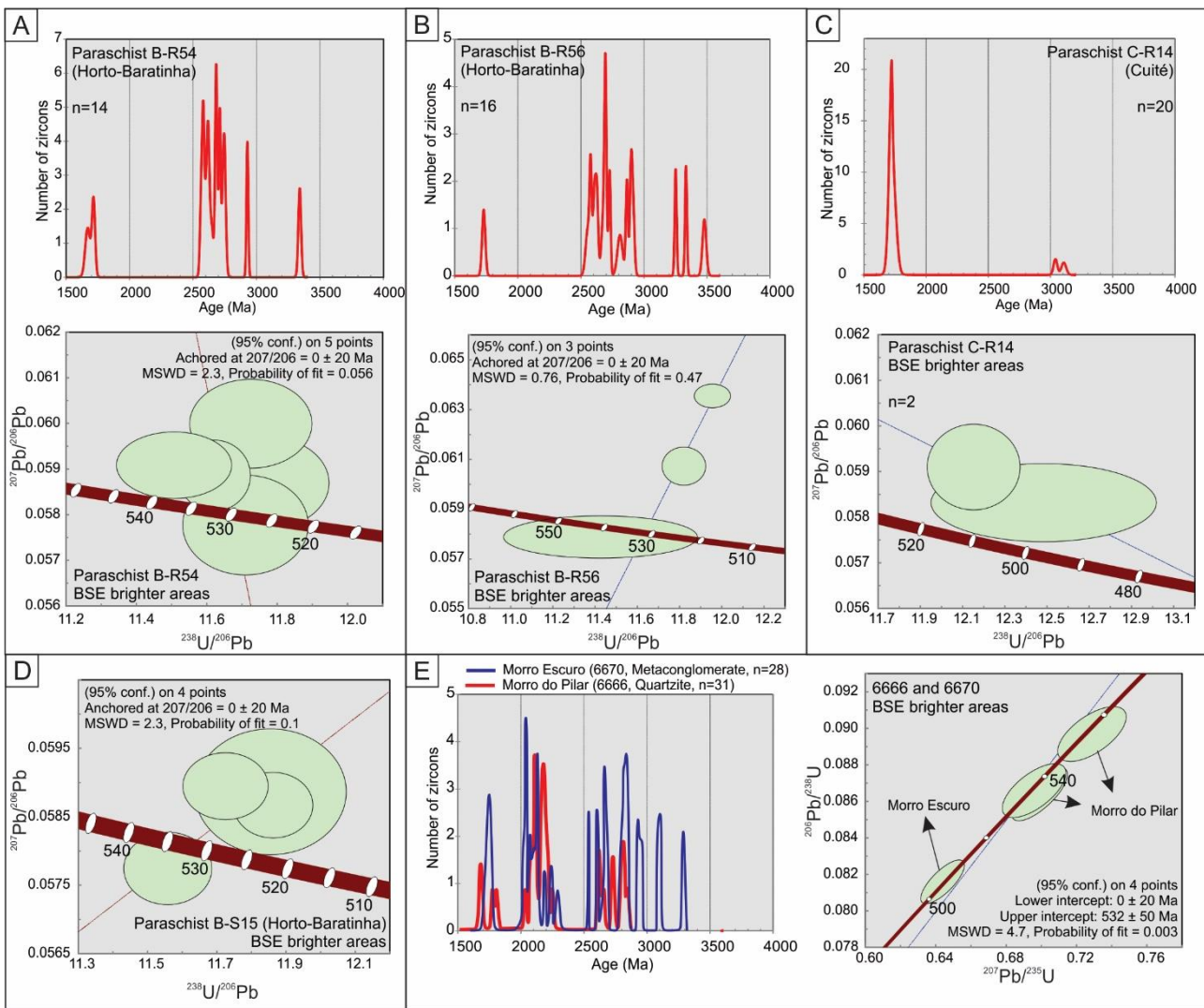


Figure 7.5: Density probability plot of the ages of detrital zircon cores and concordia/discordia diagrams of zircon rim ages from samples: (A) B-R54; (B) B-R56; (C) C-R14; (D) B-S15; (E) 6666 and 6670.

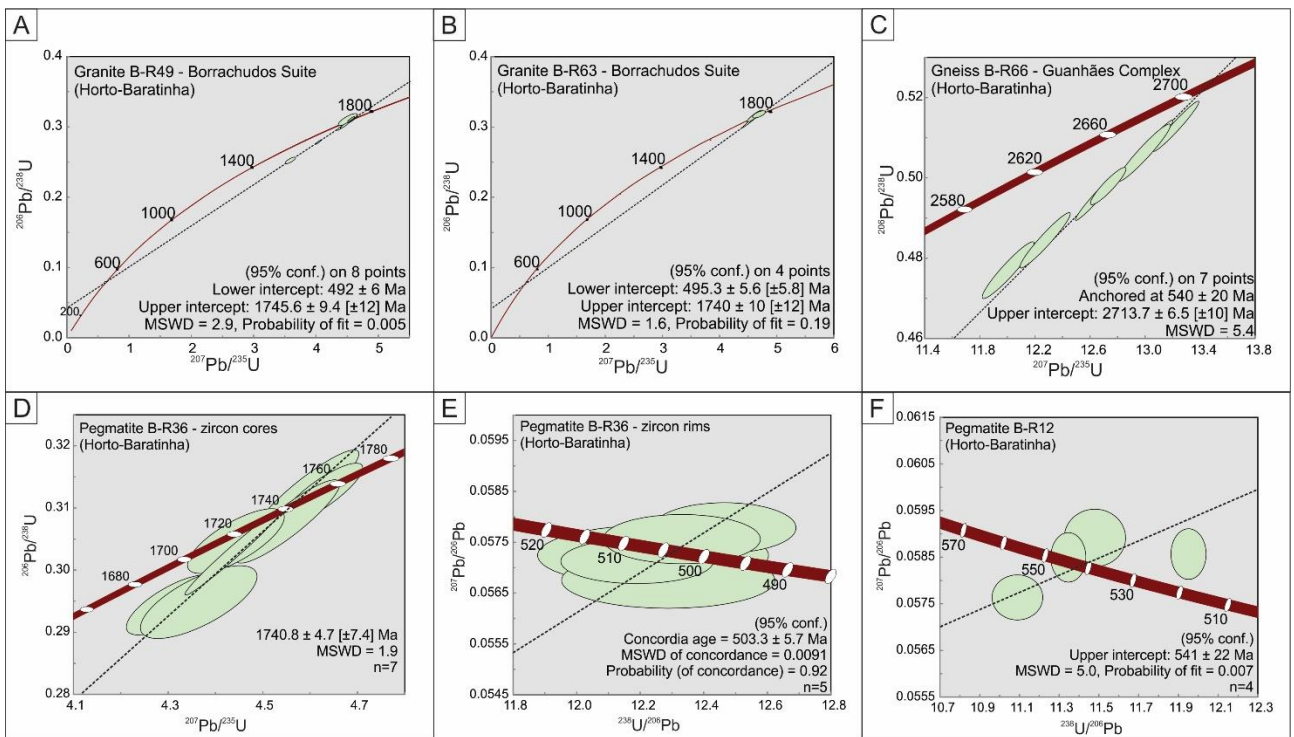


Figure 7.6: Discordia diagrams of zircon ages from samples: (A) B-R49; (B) B-R63; (C) B-R66; (D) B-R36 (inherited core); (E) B-R36 (rims); (F) B-R12

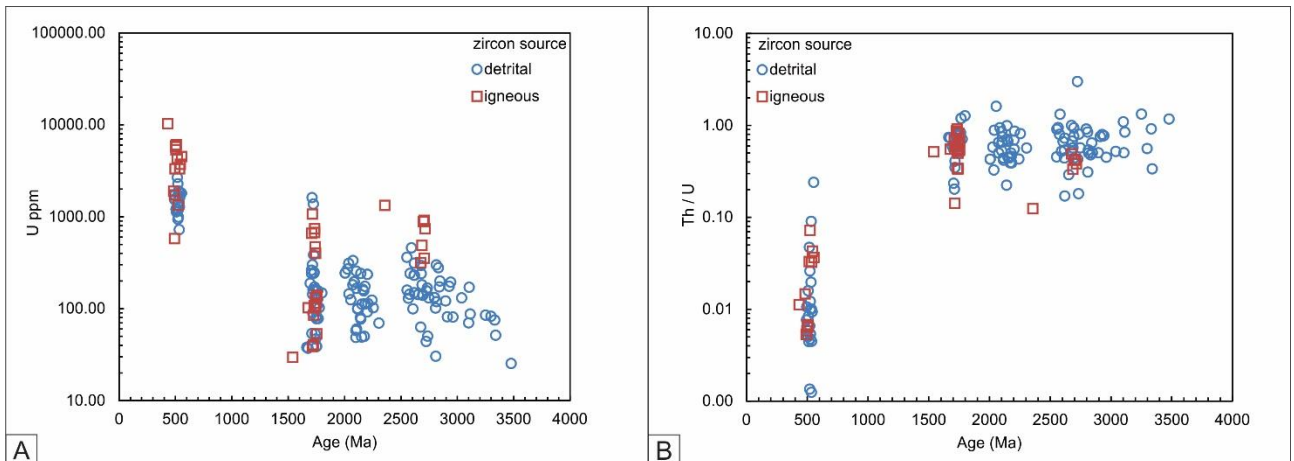


Figure 7.7: Plot of Age vs. U content (A) and Th/U ratio, showing the distinct values found in the Neoproterozoic-Cambrian zircon zones.

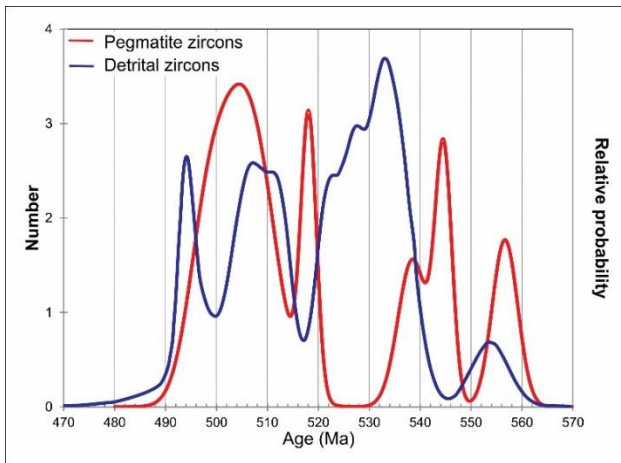


Figure 7.8: Density probability plot of the concordant ages of BSE brighter areas of detrital zircon and pegmatite.

7.5.3. Chemical composition

Analytical data are presented in Appendix B as the mean (\pm SD) for zircons of each rock type. These data provide a summary of the absolute levels of each element and the range of variation. The box-plots of Figure 7.9 show the concentration of some elements.

Silica ranges from 31.67% to 37.07% SiO₂ and ZrO₂ from 58.35% to 66.74%. The SiO₂ and ZrO₂ content in the core is higher than in the rim in the majority of samples, except in the detrital zircons from Morro do Pilar and Morro Escuro (Figure 7.9). More than 30% of the Na, Ca, Ti, Gd, Ta and Nb results are below the detection limit (particularly Ti, Ta, and Nb with lower detection limit of 2.3, 9.0 and 10.6 ppm respectively) and are not discussed below.

Hafnium concentration ranges from 1.08 to 3.14 wt% (Figure 7.9). The highest Hf values are in pegmatite zircons from sample B-R12 (mean 2.68%). Enrichment in Hf in BSE brighter rims is evident in all samples when compared with the cores (Figure 7.9).

The Mg content is higher in the BSE brighter areas of Morro Escuro hydrothermalized detrital zircon (303-798 ppm), a pattern also observed in hydrothermalized detrital zircons from Morro do Pilar, Baratinha, Cuité, and in zircons from pegmatite (Figure 7.9). The Ca content is above the detection limit only in few analyses, varying from 17 to 207 ppm, with a marked enrichment in the ortogneiss zircon rims.

Approximately 60% of the Fe analyses are below the detection limit; however, it is possible to distinguish a slight rim-enrichment in the detrital zircons (rim max. 562 ppm, core max. 396 ppm) and in zircons from gneiss (rim max 57 ppm).

The Th content in the granite and detrital zircons from Morro Escuro and Morro do Pilar are very low. In general, the Th content in the zircon rim is lower than that in the core, except in detrital zircons from Cuité.

The U content is higher in the zircons from pegmatite, mainly in the rim (core: 101-1380 ppm, rim: 895-8312 ppm). There is a clear U-enrichment in the zircon rims of all samples (Figure 7.9). The

lowest U content was identified in the zircons from Baratinha granite. The Pb content is higher in pegmatite zircon rims (219-887 ppm), and in gneiss zircon rims (585-2021 ppm). The Pb rim-enrichment is clear in zircons from some metasedimentary rocks, pegmatite, and orthogneiss.



(continued on next page)

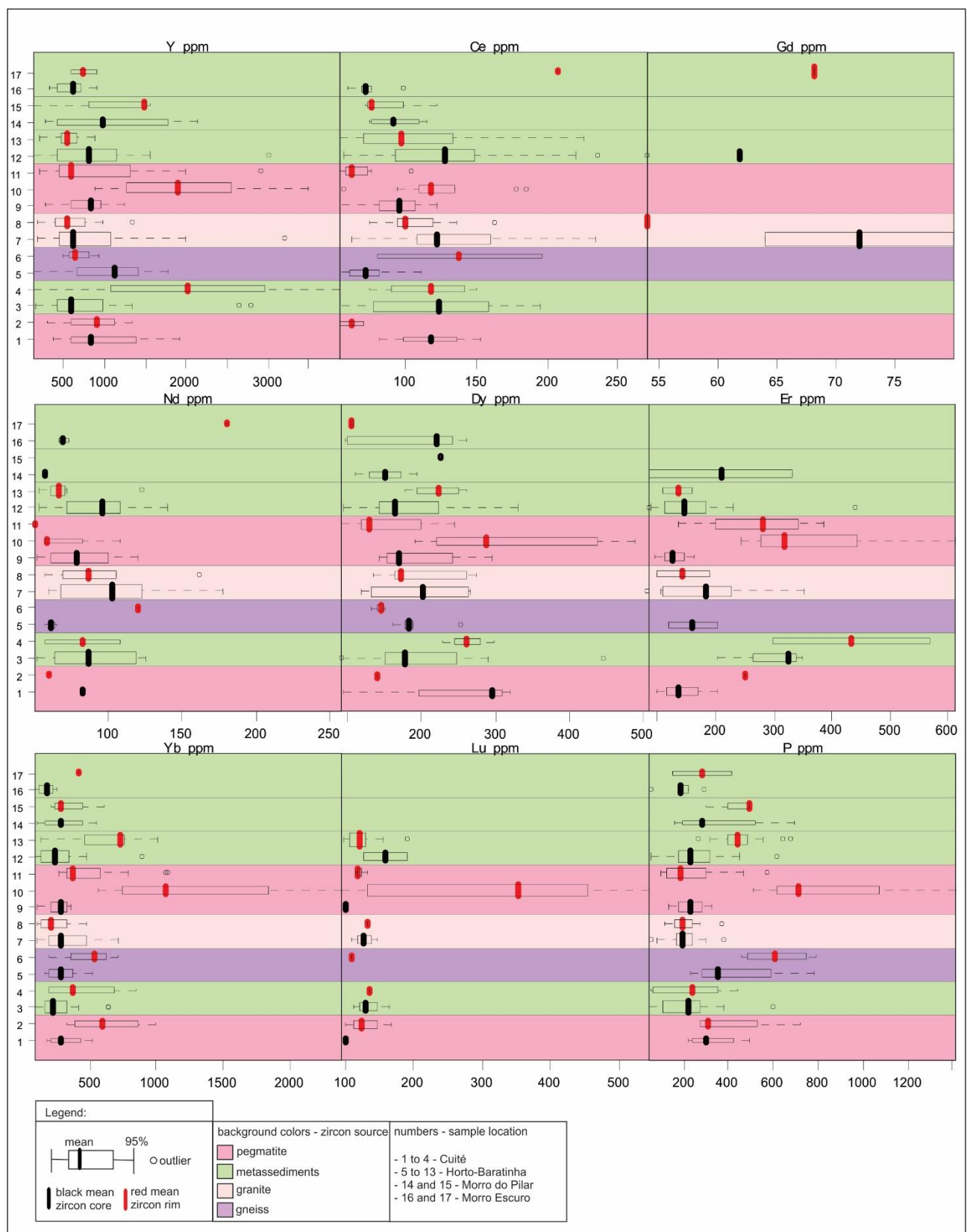


Figure 7.9: Box-plots of main and trace elements from zircon microanalyses by electron microprobe.

The Zr/Hf ratio is inversely proportional to the U content (Figure 7.10A), and the highest U values, found in zircon rims, corresponds to the lowest Zr/Hf ratio. There is also a moderate proportional relationship between Hf and Th/U, with the lowest ratio values in the rims of zircon of pegmatite (Figure 7.10B).

The rim-core Y content shows distinct behavior among the samples (Figure 7.9). There is a Y rim-enrichment in detrital zircons from Morro Escuro and Morro do Pilar, and a slight enrichment in Y in the Baratinha pegmatite zircon rims. The other samples show a Y enrichment in the core. Xenotime was identified in zircon rims from Morro Escuro, Morro do Pilar, and in Baratinha pegmatite, indicating that the fluid could be Y-rich. Xenotime from Morro do Pilar was dated by U-Pb SHRIMP giving ages between 536 ± 6 and 544 ± 5 (Rolin, 2016).

The following REE were analyzed: Ce, Gd, Nd, Dy, Er, Yb and Lu (Figure 7.9). The light REE content (LREE) is lower than the heavy REE content (HREE), with is typical of zircon (Hanchar et al., 2001). The Ce average values are very similar in all samples, however, the rim-core relationship shows some variation among the samples. Zircons from Baratinha pegmatite, granite and schist show higher Ce values in the core. The detrital zircons from Morro Escuro show a Ce enrichment in the rim. The majority of Gd analyses are below the detection limit. The Nd content is very low and relatively homogeneous, with a maximum of 259 ppm and generally shows consistent concentration in the majority of sample. However, it is possible to recognize a slight rim depletion, except in Baratinha gneiss and detrital zircon from Morro Escuro. Ytterbium is the most enriched REE (87-2400 ppm) with the highest Yb values in the pegmatite zircons rims. A slight Yb enrichment is recognized in the rim compared with the core in all samples. The Lu content is also very low (93-544 ppm) with clear rim enrichment in pegmatite. The Er and Dy contents are very low in all samples (87-611 ppm and 91-507 ppm respectively).

The P content is highest in the pegmatite zircon rims (97-1411 ppm). P-enrichment in the rim is commonly observed, mainly in orthogneiss and detrital zircons from Baratinha, Morro Escuro, and Morro do Pilar. The P content is proportional to U and Hf, as shown in Figure 7.10 (C and D).

7.5.4. *Lu-Hf signature*

In order to characterize and trace potential primary magmas using detrital and igneous zircons, as well as describe the influence of hydrothermal fluids, Lu-Hf isotope ratios were obtained from a selection of concordant U-Pb zircons previously analyzed. Distinct $^{176}\text{Hf}/^{177}\text{Hf}$ signatures are expected if zircon domains formed during different episodes of a rock evolution (Rubatto, 2017). Epsilon $\text{Hf}_{(\text{t})}$ and $^{176}\text{Hf}/^{177}\text{Hf}_{(\text{t})}$ versus age of the zircons rim and core are presented in Figure 7.11.

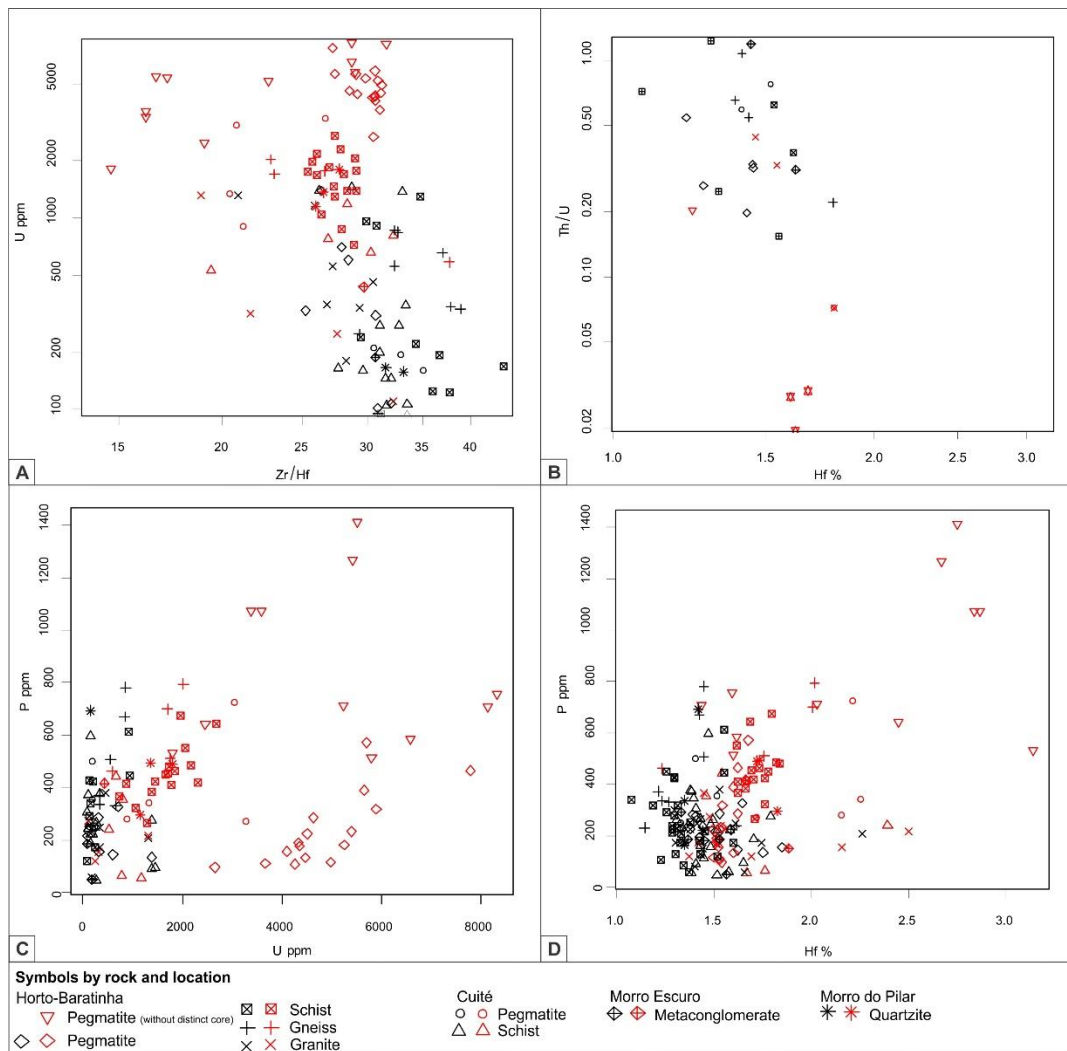


Figure 7.10: Plots of microanalysis data from electron microprobe: (A) Zr/Hf vs. U (ppm); (B) Hf (wt. %) vs. Th/U; (C) U(ppm) vs. P (ppm); Hf (wt. %) vs. P (ppm).

The detrital zircon grains of Cuité and Horto-Baratinha exhibit decreasing $\epsilon\text{Hf(t)}$ from older to younger grains, and between the core and BSE brighter rim (from -28.07 to 17.69 units), and decreasing $^{176}\text{Hf}/^{177}\text{Hf}_{(t)}$, yielding T_{DM} model ages between 2364-3592 Ma in the core and 1513-2001 Ma in the rim (Figure 7.11). The Archean grains show sub-chondritic $\epsilon\text{Hf(t)}$ clustering, with values between -17.62 to 17.69 and T_{DM} varying from 2,628 and 3,592 Ma. The Paleoproterozoic analysis shows negative $\epsilon\text{Hf(t)}$ (-28.07 to -5.79) and T_{DM} model ages from 2,364 to 3,184 Ma. The T_{DM} and $\epsilon\text{Hf(t)}$ values from the BSE brighter rims are lower than the values from the Paleoproterozoic and Archean cores (Figure 7.11).

The zircon core analyses of orthogneiss (B-R66) show $\epsilon\text{Hf(t)}$ between -4.64 to 1.61, $^{176}\text{Hf}/^{177}\text{Hf}_{(t)}$ from 0.2809-0.2801 and T_{DM} model ages between 3018 and 3152 Ma (Figure 7.11). Zircon core analyses from Borrachudos granite (B-R63 and B-R49) exhibit $\epsilon\text{Hf(t)}$ between -16.10 to -10.59, $^{176}\text{Hf}/^{177}\text{Hf}_{(t)}$ of 0.2813-0.2814 and T_{DM} model ages between 2534 and 2686 Ma (Figure 7.11).

The $\epsilon\text{Hf(t)}$, $^{176}\text{Hf}/^{177}\text{Hf}_{(t)}$ and T_{DM} values of Borrachudos granite are within the range of the Statherian detrital core analysis.

The zircon core analyses from pegmatite (B-R36) show $\epsilon\text{Hf(t)}$ between -13.49 to -6.78, $^{176}\text{Hf}/^{177}\text{Hf}_{(t)}$ between 0.2813-0.2815 and T_{DM} model ages between 2,422 and 2,666 Ma, similar to the pattern found in zircons of Borrachudos granite (Figure 7.11). Zircon rim analyses exhibit lower values, with $\epsilon\text{Hf(t)}$ varying from -28.49 to -17.41 and T_{DM} model ages from 1,948 to 2,170 and higher $^{176}\text{Hf}/^{177}\text{Hf}_{(t)}$ ratio between 0.2817-0.2819 (Figure 7.11). These values are similar to those found in the BSE brighter areas of hydrothermalized detrital zircons (Figure 7.11).

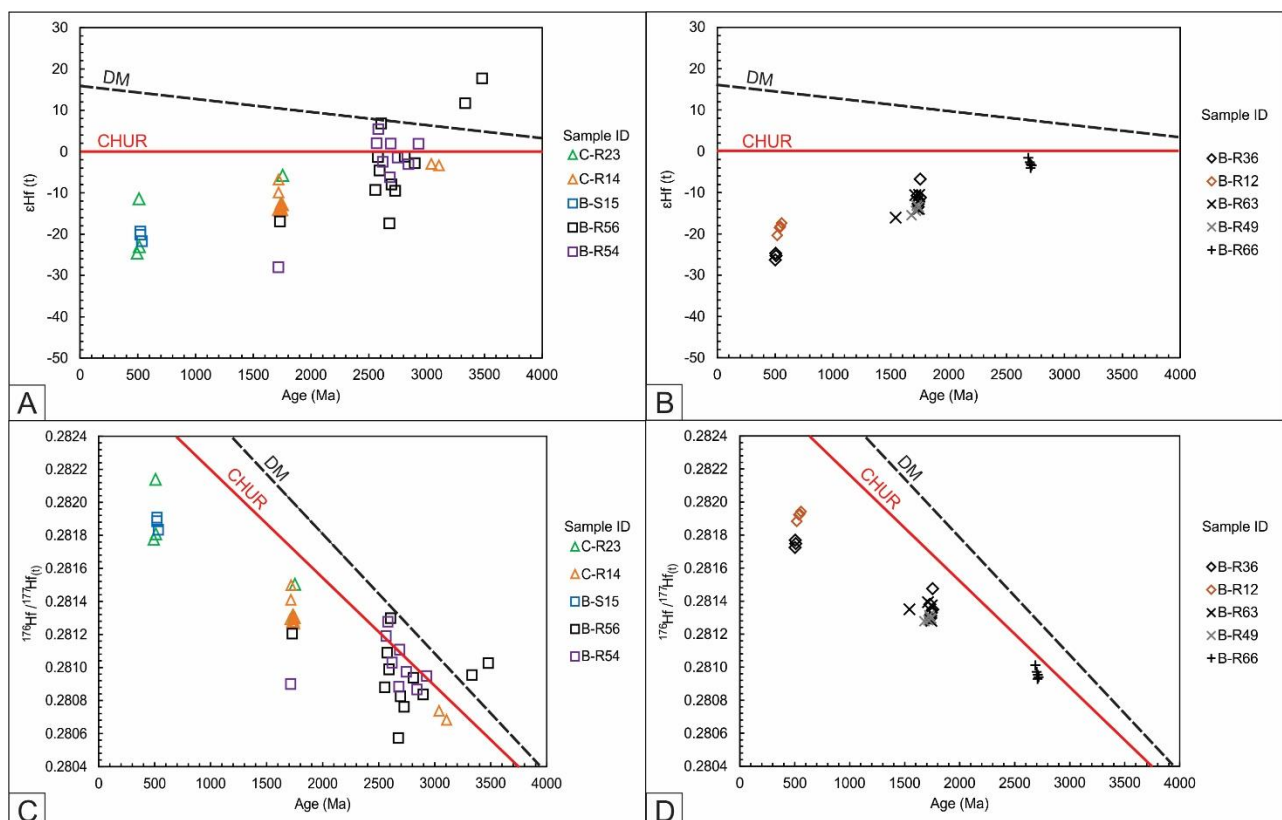


Figure 7.11: Plot Age (Ma) vs. $\epsilon\text{Hf}_{(t)}$ of detrital (A) and igneous (B) zircons. Age (Ma) vs. $^{176}\text{Hf} / ^{177}\text{Hf}_{(t)}$ of detrital (C) and igneous (D) zircons. The errors are too small to show in the graph. DM-depleted mantle; CHUR-chondritic uniform reservoir.

7.5.5. Oxygen isotope signatures

The zircon zones that are brighter in BSE images are typically narrower than the SIMS spot diameter and are commonly much fractured, which is not ideal for oxygen analysis. For this reason, only a small number of analyses were conducted in these areas. All oxygen isotope results are presented in Figure 7.12. Figure 7.13 shows the $\delta^{18}\text{O}$ results of spots that were also dated by SHRIMP, with the corresponding ages plotted. Despite the small number of analysis in the zircon rims, it is

possible to recognize that these zones appear to have slightly higher $\delta^{18}\text{O}$ values, $\sim 1\text{\textperthousand}$, above core (Figure 7.12 and 7.13).

Statherian detrital zircons of sample C-R14 show $\delta^{18}\text{O}$ values ranging from 5.08 to 5.89. The lowest value was found in a zone that is brighter in BSE images, however, the U-Pb results revealed an age of $1,724 \pm 5$ Ma. Thus, this low value could be the result of partial isotopic disorder.

The $\delta^{18}\text{O}$ results of detrital zircon core from sample B-R56 yields values between 5.12 and $6.48\text{\textperthousand}$. The lowest values were found in the Archean zircons, which is in accordance with the average value of $5.3 \pm 0.3\text{\textperthousand}$ proposed by Valley (2003) for Archean magmatic zircons, and indicates equilibrium with mantle signature. However, some Archean zircons show values higher than 5.3. The BSE brighter areas results range from 5.10 to $7.61\text{\textperthousand}$. The lowest value corresponds to the narrowest rim analyzed ($10\mu\text{m}$, $22\mu\text{m}$ and $25\mu\text{m}$ – rims thick analyzed) so this analysis could have experienced contamination by the zircon core. The $\delta^{18}\text{O}$ results of magmatic zircon core from the granite (B-R63) range from 6.08 to $6.68\text{\textperthousand}$. The rims results are similar to slightly lower than the core and varies from 5.96 to $6.46\text{\textperthousand}$.

The $\delta^{18}\text{O}$ results of magmatic zircon from pegmatite (B-R12) varies from 6.31 to $7.31\text{\textperthousand}$, which are similar to those found on the BSE brighter areas of detrital zircon (values above 7\textperthousand) and in the granite (values $\sim 6.3\text{\textperthousand}$).

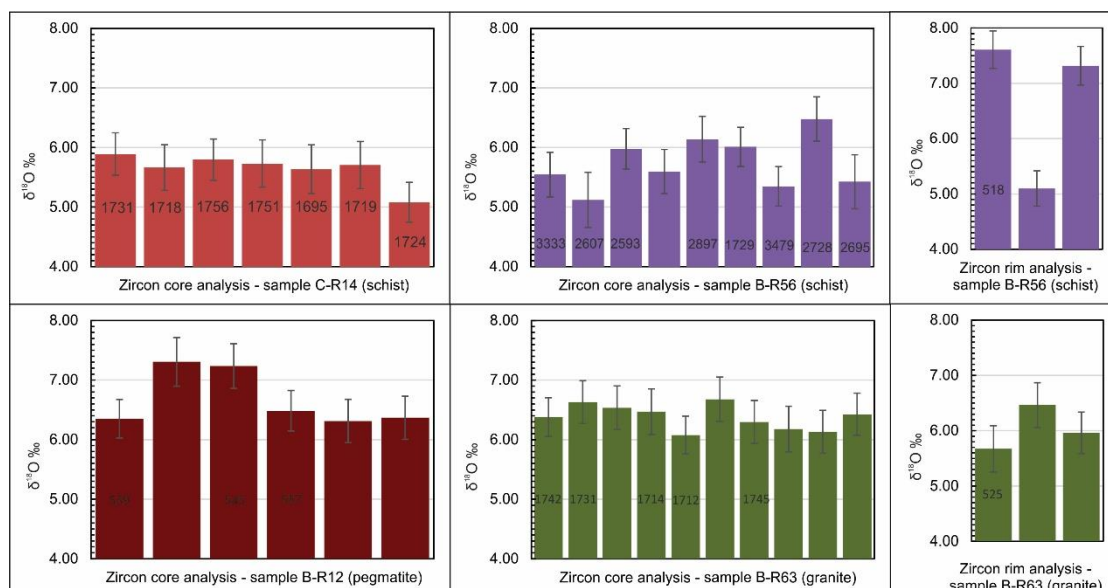


Figure 7.12: Box-plots with SD of all $\delta^{18}\text{O}\text{\textperthousand}$ results obtained.

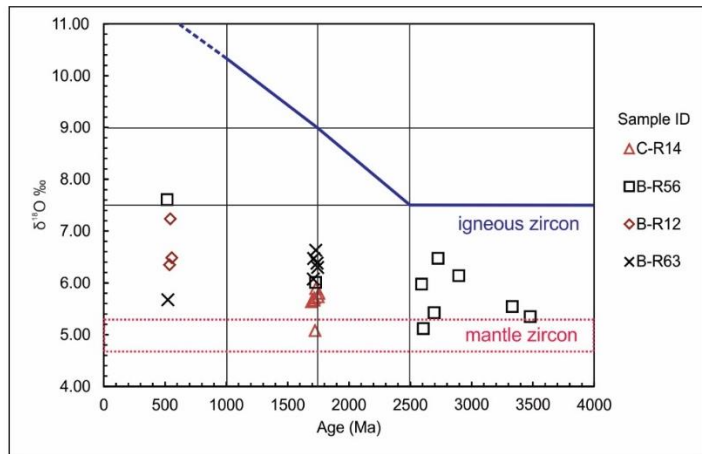


Figure 7.13: Age (Ma) vs. $\delta^{18}\text{O}\text{\textperthousand}$. Igneous and mantle unaltered zircon fields based on Valley et al. (2005).

7.6. Discussion

The detrital zircons from the Guanhães tectonic block and Southern Espinhaço block exhibit BSE brighter zones, mainly located in the crystal rims, with higher U-content and lower Th/U ratios, and yielding concordant Ediacaran to Cambrian ages (Barrote et al., 2017; Rolim et al., 2016; Silveira Braga et al., 2019a, 2015). It has been reported that the higher U and Hf contents are always correspond to bright BSE images (e.g. Gagnevin et al., 2010; Hoskin, 2005; Xia et al., 2009). However, radiation damage may also influence the BSE signal (Nasdala et al., 2006).

All the zircon detrital grains show a subrounded to rounded habit, indicating a larger transport distance from the source. Similar U-rich zones are observed in some igneous zircons from the Archean gneissic crystalline basement, and in the Statherian metagranitoids from the Borrachudos Suite (Silveira Braga et al., 2019a).

The U-rich zones vary from $<5\mu\text{m}$ to $50\mu\text{m}$ thick in the detrital zircons and igneous zircons from granite and gneiss. They are often texturally homogeneous, show sharp boundaries with the core, and show no internal zoning. A texture indicative of fluid interaction is concentric porous fabric present in some grains (Figure 7.2) demonstrating fluid path during crystal alteration and recrystallization. The pegmatite zircons show the typical well-developed magmatic-style oscillatory zoning and are also U-rich. Some crystal have a core inherited from the Borrachudos granite, which is rounded, intensely fractured, with no internal zoning, and with less U than the rim. The presence of relict zircon cores with rounded grains and/or resorbed features indicates partial dissolution of the grains during melting.

7.6.1. Age of the hydrothermal event

The BSE brighter areas of detrital zircons and zircons from meta-granite yield concordant ages (492 Ma to 554 Ma) that are much younger than the unaltered cores (1666 Ma to 3479 Ma).

Pegmatite crystallization also occurred at this time. The inherited core from pegmatite crystals delivered Statherian ages (1741 ± 5 Ma – Figure 7.6), indicating they were inherited from the Açuena pluton (Borrachudos Suite) and were partially consumed during partial melting. The dissolution modeling of zircon in anatetic melts as a function of water content, temperature and melt composition, shows that only the largest crystals (>50-100 μm) would survive crustal fusion and incorporation into a >2 wt. % H_2O , 750-850°C zircon-undersaturated melt (Watson, 1996).

The age of the BSE brighter zircon zones is associated with the age of orogenic igneous rocks from Araçuaí belt, formed between 630 Ma to 480 Ma, and grouped into five units (supersuites G1, G2, G3, G4, and G5) – Figure 7.1. The G4 and G5 suites are associated with a post-collisional stage (530–480 Ma). The G5 Suite is composed of a variety of rocks that have been classified as I- and A-type granitoid plutons, including metaluminous to slightly peraluminous, high-K-Fe calc-alkaline to alkaline granitic and/or charnockitic to dioritic/noritic intrusions, originating in the lowermost continental crust with an important mantle contribution (Pedrosa Soares et al., 2011, 2001). One of the most important pegmatitic regions worldwide, the Eastern Brasilian Pegmatite Province (Figure 7.14) is located at the western margin of the Araçuaí Orogenic belt, and its pegmatite bodies are correlated with the post-deformational stage of orogenic igneous activity (Pedrosa Soares et al., 2011, 2001).

7.6.2. Th/U ratio

The BSE brighter zones of detrital zircons and zircons from orthogneiss, meta-granite and pegmatite present higher U content and lower Th/U ratio than the unaltered BSE dark cores. These are typical chemical characteristics of hydrothermal zircons (Table 2). The low Th/U in hydrothermal zircon is inherited from the fluid (Ayers and Peters, 2018) and/or associated with crystallization of Th-rich minerals such as monazite and allanite in crustal metamorphic rocks (Rubatto, 2017).

Kirkland et al. (2015) observed a general decrease in zircon Th/U ratio with increasing whole rock SiO_2 content. However, within a fractionating magma, Ti-in-zircon thermometry indicate lower zircon Th/U in cooler melts, which is associated with zircon growth under non-equilibrium conditions, with greater incompatibility of Th relative to U and the removal and segregation of mineral precipitates (Kirkland et al., 2015). According to Kirkland et al. (2015) these observations can be used as a tool to determine whether zircon growth occurred in a liquid of similar composition to the observed whole rock, indicating therefore an equilibrium condition. The lower Th/U in pegmatite zircons rims compared with the considered inherited core may indicate zircon growth in pegmatite under non-equilibrium conditions.

7.6.3. Trace elements and isotopic changes associated with hydrothermalism

A general ZrO₂, SiO₂ and Th depletion and common U, Pb, Hf, Mg, Ca, Fe, Yb and P enrichment is noted in zircon BSE brighter areas relative to unaltered zones. Yttrium content shows distinct behavior among the samples. Xenotime was identified in zircons rims from Morro Escuro, Morro do Pilar and in Baratinha pegmatite, indicating that the fluid could have been Y-rich. Xenotime from Morro do Pilar quartzite was dated by U-Pb SHRIMP, giving ages between 536 ± 6 and 544 ± 5 Ma (Rolim, 2016). The enrichment of foreign elements such as Ca, Al, and Fe in zircon is probably associated with diffusion-reaction process and highly unlikely to occur during a coupled dissolution–reprecipitation because, during this process, the parent zircon dissolves completely before new crystalline zircon precipitates (Geisler et al., 2007).

The Lu-Hf isotopes results for granite zircons shows negative $\epsilon\text{Hf}_{(t)}$ (-16.10 to -10.59) and T_{DM} model ages between 2,534 and 2,686 Ma, similar to the results obtained by Magalhães et al. (2018) in zircons from Sthaterian anorogenic meta-rhyolite associated with the taphrogenetic event in the São Francisco-Congo paleocontinent. These values indicate that the Sthaterian anorogenic igneous rocks (metarhyolites and granites) were generated with the involvement of Archean and possibly Siderian to Orosirian rocks during magma genesis (Magalhães et al., 2018), with considerable crustal contamination. Analyses of the core of zircon from the orthogneiss basement yielded $\epsilon\text{Hf}_{(t)}$ between -4.64 and 1.61, and T_{DM} model ages between 3,018 and 3,152 Ma, indicating an older magma source and less crustal contamination than the Borrachudos granite. Comparing the core and rim analyses obtained in the detrital zircons, a trend can be recognized of decreasing $\epsilon\text{Hf}(t)$ between unaltered core and altered U-rich rim zones, and also between older to younger cores. The T_{DM} model ages obtained on the rim (1513-2001 Ma) are younger than those on the core (2364-3592 Ma), indicating that the process that generated the U-rich rims also affected the Lu-Hf zircon signature. The data indicates that the crust was derived by remelting of older crust, as the $\epsilon\text{Hf}_{(t)}$ is predominantly negative and T_{DM} model ages are much older than the crystallization ages (Kinny and Maas, 2003).

The analyses of zircon cores from the pegmatite delivered similar results to those obtained on granite zircon cores. The pegmatite zircon rim had lower $\epsilon\text{Hf}_{(t)}$ than the inherited core, similar to the values obtained in the detrital rims, indicating that they probably were generated during interaction with fluids of similar composition, and as indicated by U-Pb SHRIMP results, at the same time interval.

The increase in the $^{176}\text{Hf}/^{177}\text{Hf}_{(t)}$ of the pegmatite zircon rims compared with the core could reflect partial melting reactions involving the breakdown of biotite, which releases a significant

amount of Zr with elevated $^{176}\text{Hf}/^{177}\text{Hf}$ ratios into the system, as concluded by Melo et al., (2017) who studied zircons from S-type granites from the Carlos Chagas (G2 supersuite). According to these authors, reactions associated with the dissolution of relict zircon grains (inherited/magmatic) during anatexis probably led to new zircon growth in the S-type granite. The fluid generated by the anatexis probably also affected the metasedimentary sequence, given that similar $^{176}\text{Hf}/^{177}\text{Hf}_{(\text{t})}$ values are found in the altered detrital zircon rims.

The $\delta^{18}\text{O}$ lowest values were found in the Archean detrital zircons (5.35-5.98 ‰), indicating equilibrium with the mantle. The higher values ($> 7\text{\textperthousand}$) were found in the altered detrital zircon areas and in the pegmatite zircons, approximately 1‰ higher than values measured on the core, indicating low-temperature water-rock interactions. $\delta^{18}\text{O}$ values higher than the mantle value ($5.3 \pm 0.3\text{\textperthousand}$ - Valley, 2003) are considered as a direct or indirect result of intra-crustal recycling, magma interaction with supracrustal materials, considering that oxygen isotope fractionation is larger during low-temperature processes on or near the surface of the Earth (Valley et al., 2005). The bulk melting of igneous rocks mixed with 5% metasediments could raise $\delta^{18}\text{O}$ by 1‰ (Valley et al., 2005). The meta-rhyolite zircons analyzed by Magalhães et al. (2018) show $\delta^{18}\text{O}$ values varying from 6.8 to 8.0, higher than the values obtained here, probably due to the more intense supracrustal contamination and lower temperature processes near the surface.

7.6.4. Tectonic setting, hydrothermalism and zircon changes implications

The basement domain of Brasilian orogen is intimately related to crustal reworking processes and is significantly overprinted by deformation, magmatism, metamorphism and hydrothermal activity (Oriolo et al., 2017). Most of the Brasilian Pan-African magmatism was related to metacratonization processes, which leads to craton remobilization during orogenic event (Oriolo et al., 2017).

During the late- and mainly post-collisional stage of the Brasilian Orogeny (560–490 Ma) occurred the uplift and juxtaposition of Neoarchean gneissic rocks with Statherian granites and amphibolite facies supracrustal units (Orosirian- Statherian maximum depositional ages). This period is temporally similar to the Pan-African III (collisional peak at 590–540 Ma) and Brasiliano III climaxes between 590–560 Ma (Araçuaí Orogen) and 520–500 Ma (Búzios Orogen), all characterised dominantly by crustal recycling processes (Oriolo et al., 2018, 2017; Silva et al., 2005). Silva et al. (2005) reinforce the correlation between northernmost Araçuaí Orogen and the West Congo Orogen, both belonging to the system Brasiliano/Pan-African III. An important tectonothermal event immediately after the peak of the Pan-African and Brasilian compression leaded the progressive accumulation of thermal energy in the lithospheric mantle along the border of proto-West Gondwana,

between 530 and 510 Ma (Heilbron et al., 2008; Teixeira et al., 2010). The alignment of Lu-Hf data of magmatic units presented in Figure 7.11 (B, D) also points to the crustal reworking.

The crustal uplifting and decompression promoted partial melting of wall rocks (mainly granites from the Borrachudos Suite), generating pegmatite intrusions and magmatic-hydrothermal fluid (Figure 7.14). The pegmatites and associated hydrothermal fluid were probably separated from their site of formation by mechanisms such as filterpressing and seismic-pumping (Dill, 2015) by the end of collisional phase of the Brasiliiano Orogeny.

The hydrothermal fluid interacted with the entire sequence, producing U-rich zones in zircons, which have different chemical and isotopic signatures in relation to the non-affected zones (Figure 15). Zircons from metasedimentary rocks (Espinhaço belt), granite (Borrachudos Suite), and orthogneiss (Guanhães Complex) suffered recrystallization at sub-solidus conditions, due to interaction with the hydrothermal fluid (Figure 7.15). The pegmatite zircons represent an anatetic new zircon grow, or overgrowth, in the presence of fluid and melt (Figure 7.15).

7.7. Conclusions

- 1) The detrital and igneous zircons from Guanhães tectonic block and Southern Espinhaço block, associated with iron formation-bearing sequences containing high-grade iron ore bodies (>60 wt.% Fe) exhibit zones (mainly in crystal rims) with higher U-content and lower Th/U ratios relative to the core. The Ediacaran to Cambrian rim ages are much younger than the age of the corresponding core.
- 2) The detrital zircon U-rich zones and the pegmatite zircons have ages between 492 Ma to 557 Ma.
- 3) The U-rich zones are brighter in BSE images, <5µm to 50µm thick in the detrital and igneous zircon from granite and gneiss, often texturally homogeneous, form sharp boundaries with the core, and contain no internal zoning. A concentric porous fabric present in some grains indicates the fluid path during crystal alteration and recrystallization.
- 4) Comparing the chemical composition of altered and unaltered zones it is possible to note a general ZrO₂, SiO₂ and Th depletion in the altered area and common U, Pb, Hf, Mg, Ca, Fe, Yb and P enrichment.
- 5) There is a decreasing trend of $\epsilon\text{Hf(t)}$ and increasing of $^{176}\text{Hf}/^{177}\text{Hf}_{(t)}$ between unaltered and altered zones. The T_{DM} model ages obtained on the rim are younger than those of the core. Therefore, the process that generated the U-rich rims also affected the Lu-Hf zircon signature.

- 6) Slightly higher $\delta^{18}\text{O}$ values (above 7‰), were found in the detrital U-rich zones and pegmatite zircon, approximately 1‰ higher than those of unaltered zircon areas, indicating the low-temperature water-rock fluid interaction.

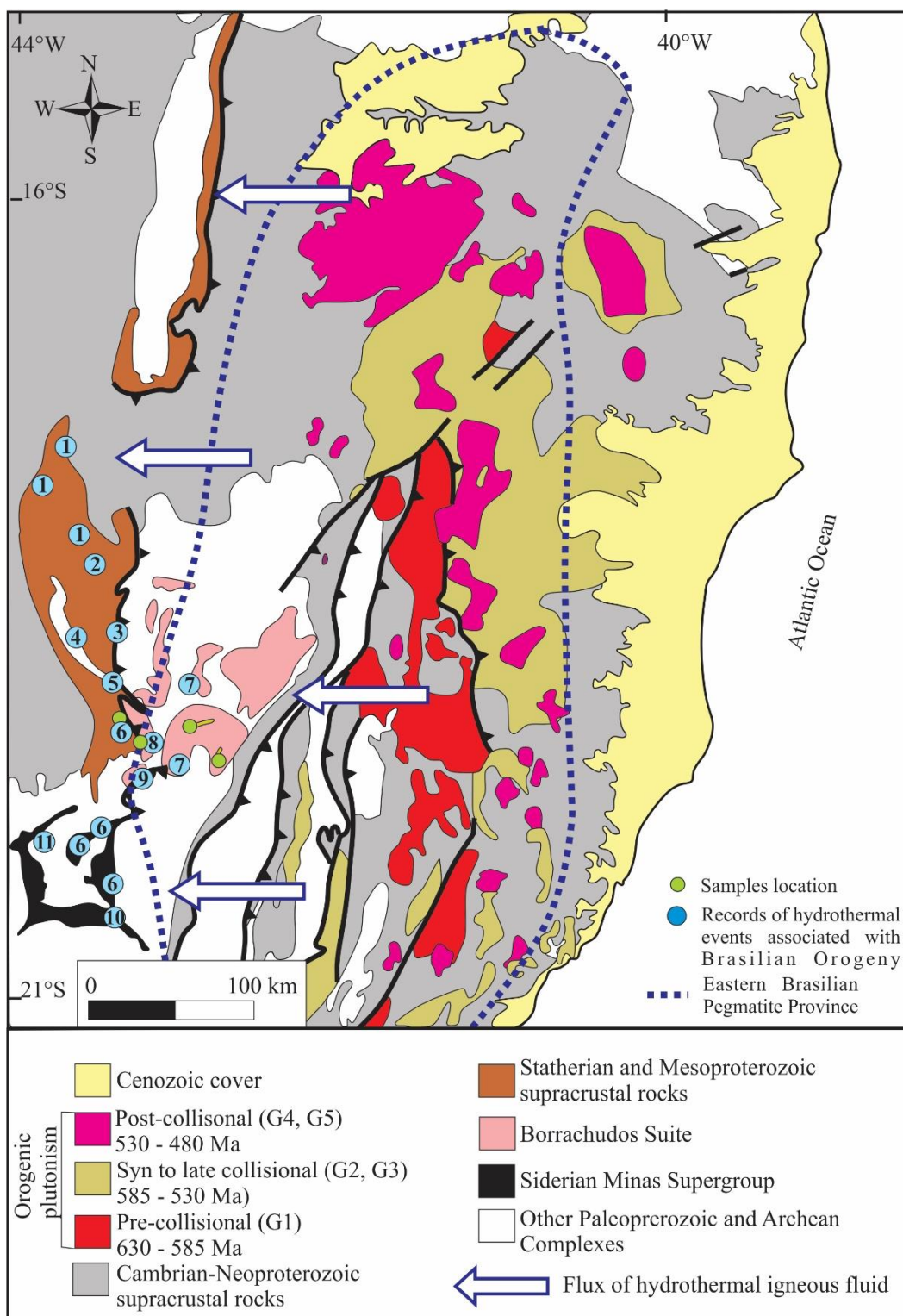


Figure 7.14: Simplified geological map (modified from Silva et al. (2011)) of the Brasilian Orogen (locally named as Araçuaí Orogen) at the southeast border of the São Francisco Craton, showing assigned hydrothermal

events. 1- (Chaves et al., 2010), 2-(Cabral et al., 2013), 3-(Cabral et al., 2011), 4-(Ronchi et al., 1992), 5-(Rolin et al., 2016), 6-(Oliveira et al., 2017), 7-(Gomes et al., 2018), 8-(Silveira Braga et al., 2015), 9-(Cabral et al., 2015), 10-(Cabral and Zeh, 2015), 11-(Martins et al., 2016).

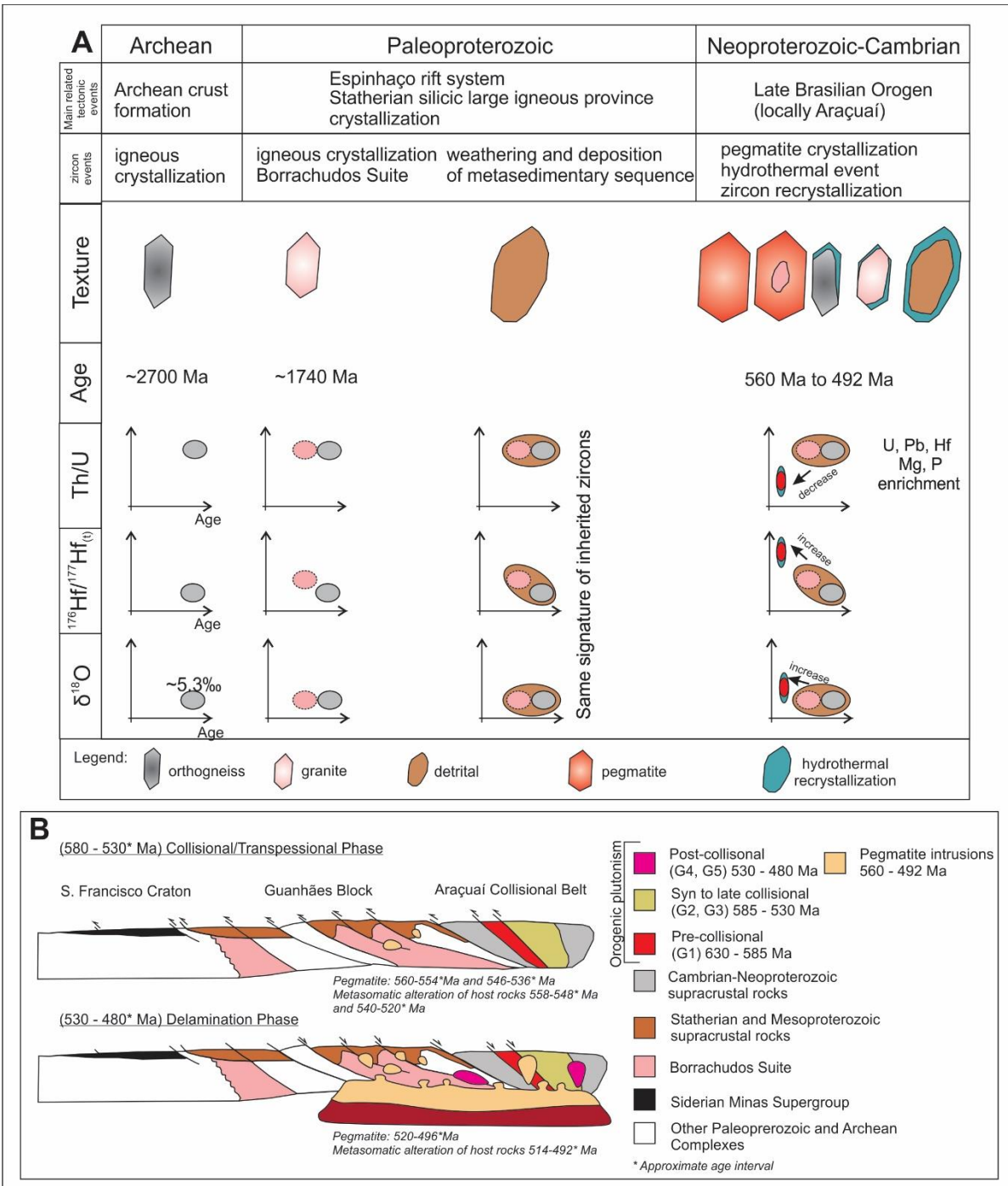


Figure 7.15: (A) Schematic diagram illustrating the processes of zircon recrystallization and growth from the Serra de São José Group (Lower Espinhaço Supergroup), Guanhães Complex, Borrachudos Suite and pegmatite bodies (Santa Maria de Itabira pegmatitic district) during the tectono-metamorphic evolution of the Late Brasilian Orogeny. (B) Schematic W-E cross section showing pegmatite pulses.

- 7) During the late- and mainly post-collisional stages of the Brasilian Orogeny (560–490 Ma) uplift and juxtaposition of Neoarchean gneissic rocks, Statherian granites and metamorphic supracrustal units (Orosirian- Statherian maximum depositional ages) occurred. This uplift and decompression promoted partial melting of the Borrachudos granite in the study area, generating pegmatite intrusion and delivering magmatic-hydrothermal fluid that affected the entire sequence.
- 8) Zircons from metasedimentary rocks, granite, and orthogneiss suffered recrystallization at sub-solidus conditions after interaction with the moderate to the low-temperature hydrothermal fluid. The pegmatite zircons represent an anatetic new zircon grow, or overgrowth, in the presence of fluid-saturated melt.

7.8. Acknowledgements

This study was supported by the Coordenação de Aperfeiçoamento de Pessoal de Nível Superior - Brasil (CAPES) - Finance Code 001 (scholarship / Programa de Doutorado Sanduíche no Exterior / Pr. n° 88881.134959/2016-01) and Fundação de Amparo à Pesquisa de Minas Gerais (FAPEMIG CRA-APQ 01178-15). The authors would like to acknowledge the Australian Microscopy & Microanalysis Research Facility, AuScope, the Science and Industry Endowment Fund, and the State Government of Western Australian for contributing to the Ion Probe Facility at the Centre for Microscopy, Characterisation and Analysis at the University of Western Australia and Heejin Jeon for all support. GeoHistory Facility instruments in the John de Laeter Centre, Curtin University were funded via an Australian Geophysical Observing System grant provided to AuScope Pty Ltd. by the AQ44 Australian Education Investment Fund program. The NPII multi-collector was obtained via funding from the Australian Research Council LIEF program (LE150100013).

8. CONCLUSÕES

A partir dos cinco artigos apresentados neste volume, as seguintes conclusões acerca da gênese dos depósitos de ferro do Bloco Guanhães, em especial Horto-Baratinha e Cuité, podem ser estabelecidas:

Idade da sequência metassedimentar: Os dados de geocronologia por U-Pb SHRIMP em zircões detritico dos mica xistos superiores presentes nos depósitos de Horto-Baratinha e Cuité resultaram em idades estaterianas nos zircões mais jovens (1.671 ± 20 Ma e 1.695 ± 15 Ma respectivamente). Esta idade é semelhante à encontrada em metassedimentos de outros depósitos de ferro localizados no Bloco Guanhães e na Serra do Espinhaço Meridional (Barrote et al., 2017; Gomes et al., 2018; Rolim et al., 2016; Rosière et al., 2017). Essas idades indicam que a porção superior da pilha de metassedimentos é cronocorrelata ao Grupo Serra de São José, definido por Vassily et al. (2016) na região da Serra da Serpentina. A camada de itabirito é aqui tentativamente correlacionada com a formação Serra do Sapo do Grupo Serra da Serpentina, e não com a Formação Canjica, que representa a unidade superior do Grupo Serra de São José (Figura 2.2), pois a BIF Canjica é muito menos espessa e ocorre em área menor que a BIF Serra do Sapo, como descrito por Rolim et al. (2016). Os xistos presentes na base da BIF são então relacionados com a formação Meloso. Os dados de ETR do itabirito indicam deposição em ambiente tipo plataforma (tipo Lago Superior), tal como observado nas BIFs do Supergrupo Minas (Mendes et al., 2016; Spier et al., 2007), Grupo Serra da Serpentina (Rolim et al., 2016; Silveira Braga et al., 2015) e no Complexo Guanhães (Barrote et al., 2017).

Evolução estrutural: Horto-Baratinha e Cuité apresentam arcabouço estrutural distinto, no entanto ambos são produtos da fase colisional da orogênese Brasiliiana, que soergueu e justapôs gnaisses arqueanos e supracrustais de fácies anfibolito e idade orosiriana-estateriana, que agora compõem o denominado Bloco Guanhães. Em ambos os depósitos ocorreu o desenvolvimento de zonas de cisalhamento paralelas aos contatos litológicos, provocando a transposição de todas as estruturas sedimentares, e formação da estrutura xistosa. Cuité está localizado em um domínio de maior deformação que Horto-Baratinha, em um ambiente transpressivo que gerou, durante a orogênese Brasiliiana, zonas de cisalhamento oblíquas, foliação boudinada, e falhas de empurrão com vergência para SE, semelhante ao encontrado na região de Morro Escuro (Carvalho et al., 2014). A evolução estrutural em Horto-Baratinha ocorreu em ao menos três fases de deformação, com transposição das estruturas sedimentares e formação da foliação, seguida por duas fases de dobramento flexural com eixos N-S e E-W, o que gerou o padrão de interferência de dobras tipo domo e bacia de escala decamétrica, comprovado pelo modelamento litológico implícito. Durante a fase pós-colisional (560-

490 Ma) corpos pegmatíticos intrudiram a sequência causando alterações hidrotermais no itabirito e nas rochas encaixantes.

Gênese dos corpos de alto teor e sua relação com as intrusões pegmatíticas: O protominério é composto essencialmente por quartzo e hematita lamelar. Três fácies de minério de alto teor foram identificadas, minério hematítico granular com idioblastos de magnetita, que é a fácie dominante em ambos os depósitos, e lentes secundárias de minério hematítico lamelar-granular e minério magnetítico. A variação composicional entre itabirito e minério nas análises de rocha total indica, além de uma forte lixiviação de SiO_2 , o enriquecimento de Fe_2O_3 e alguns elementos traços tais como TiO_2 , As, Sb, W, Ni, Zr, and V. Dados de microquímica nas diversas gerações de óxidos de ferro presentes no itabirito, minério e nas intrusões pegmatíticas indicam baixa concentração de elementos traços na hematita lamelar do itabirito e composição química semelhante entre magnetitas e hematitas granulares do minério e dos pegmatitos, o que corrobora com a hipótese de correlação genética entre essas fases. Além disso, o modelamento geológico implícito 3D demonstra a próxima relação espacial entre intrusões pegmatíticas e corpos de minério de alto teor em Horto-Baratinha.

Conclui-se, que a geração dos óxidos de ferro e o processo de mineralização em Horto-Baratinha e Cuité ocorreram em três fases:

- (1) Fases sin- e tardi-colisional (580-560 Ma): Recristalitação metamórfica e transposição de estruturas sedimentares. Lixiviação parcial de Si ao longo das zonas de cisalhamento. Geração de hematita lamelar.
- (2) Fases tardi- e pós colisionais / colapso gravitacional do orógeno (560~530 Ma): Fusão parcial do granito Borrachudos e geração do magma pegmatítico. Alta razão fluido/rocha. Fluidos redutores de alta temperatura foram responsáveis pela cristalização da magnetita e lixiviação de Si.
- (3) Fase final do colapso gravitacional do orógeno (~530-490 Ma): Pulsos finais das intrusões pegmatíticas e soerguimento final do Bloco Guanhães. Mistura entre os fluidos de alta e baixa temperatura, gerando alta razão fluido/rocha. Progressiva oxidação da magnetita para martita e hematita granular.

Titânio e manganês se comportaram como elementos móveis durante as fases de alta razão fluido/rocha, gerando Mn-magnetita, Ti-hematita e inclusões de ilmenita.

Registro do hidrotermalismo Brasiliano em zircões do Bloco Guanhães e na Serra do Espinhaco

Meridional: Os fluidos hidrotermais gerados durante a orogênese Brasiliiana afetaram principalmente as sequências metassedimentares portadoras de formação ferrífera localizadas próximo a Província

pegmatítica Oriental Brasileira, e provocaram uma alteração menos pervasiva em itabiritos da SdEM, principalmente ao longo de zonas de cisalhamento que facilitaram a percolação dos fluidos. O processo de hidrotermalismo está registrado em zircões detriticos e ígneos (oriundos de gnaisses do Complexo Guanhães e de granitos da Suíte Borrachudos) presentes no Bloco Guanhães e na SdEM, associados às sequências portadoras de itabirito. Os zircões afetados apresentam zonas com espessura de <5 μ m a 50 μ m ricas em urânio e com baixa razão Th/U, localizadas principalmente nas bordas dos cristais. A idade dessas zonas corrobora com as idades de cristalização dos pegmatitos, entre 490 Ma e 560 Ma. Em comparação com os núcleos, as bordas recristalizadas dos zircões detriticos e ígneos apresentam: menor teor de ZrO₂, SiO₂ e Th; maior teor de U, Pb, Hf, Mg, Ca, Fe, Yb e P; diminuição dos valores de ϵ Hf(t); valores maiores de $\delta^{18}\text{O}$. Portanto, os fluidos promoveram recristalização de porções do zircão, em estado sub-sólido, alterando significativamente sua composição química e isotópica. Os pegmatitos e fluidos hidrotermais associados foram provavelmente deslocados de seu local de formação por bombeamento tectônico no final da fase colisional da orogênese.

9. REFERÊNCIAS BIBLIOGRÁFICAS

- Alkmim, F.F., Marshak, S., Pedrosa Soares, A.C., Peres, G.G., Cruz, S.C.P., Whittington, A. 2006. Kinematic evolution of the Araçuaí-West Congo orogen in Brazil and Africa: Nutcracker tectonics during the Neoproterozoic assembly of Gondwana. *Precambrian Res.*, **149**: 43–64. <https://doi.org/10.1016/j.precamres.2006.06.007>
- Alkmim, F.F., Pedrosa Soares, A.C., Noce, C.M., Cruz, S.C.P. 2007. Sobre a Evolução Tectônica do Orógeno Araçuaí-Congo Ocidental. *Geonomos*, **15**:25–43.
- Almeida-Abreu, P.A., Renger, F.E. 2002. Serra do espinhaço meridional: um orógeno de colisão do mesoproterozóico. *Rev. Bras. Geociências*, **32**: 1–14.
- Almeida, F.F.M. 1977. O Cráton do São Francisco. *Rev. Bras. Geociências*, **7**:349–364.
- ARANZ Geo Limited, 2016. LEAPFROG GEO 4.0 HELP. ARANZ Geo Ltd. URL <http://help.leapfrog3d.com/Geo/4.0/en-GB/Content/intro.htm> (acesso em 10.10.17).
- Ayers, J.C., Peters, T.J. 2018. Zircon / fluid trace element partition coefficients measured by recrystallization of Mud Tank zircon at 1.5 GPa and 800 – 1000 ° C. *Geochim. Cosmochim. Acta*, **223**:60–74. <https://doi.org/10.1016/j.gca.2017.11.025>
- Ayers, J.C., Zhang, L., Luo, Y., Peters, T.J. 2012. Zircon solubility in alkaline aqueous fluids at upper crustal conditions. *Geochim. Cosmochim. Acta*, **96**:18–28. <https://doi.org/10.1016/j.gca.2012.08.027>
- Babinski, M., Chemale, F., Van Schmus, W.R. 1995. The Pb/Pb age of the Minas Supergroup carbonate rocks, Quadrilátero Ferrífero, Brazil. *Precambrian Res.*, **72**:235–245. [https://doi.org/10.1016/0301-9268\(94\)00091-5](https://doi.org/10.1016/0301-9268(94)00091-5)
- Barrote, V.R, 2016. *A sequência portadora de formações ferríferas de Guanhães, Minas Gerais, Brasil*. Dissertação de Mestrado, Instituto de Geociências, Universidade Federal de Minas Gerais, Belo Horizonte, 103 p.
- Barrote, V.R., Rosiere, C.A., Rolim, V.K., Santos, J.O.S., McNaughton, N.J. 2017. The proterozoic guanhães banded iron formations, southeastern border of the São Francisco Craton, Brazil: Evidence of detrital contamination. *Geol. USP - Ser. Cient.*, **17**:303–324. <https://doi.org/10.11606/issn.2316-9095.v17-352>

Basson, I.J., Thomas, S.A.J., Stoch, B., Anthonissen, C.J., McCall, M.J., Britz, J., Macgregor, S., Viljoen, S., Nel, D., Vietze, M., Stander, C., Horn, J., Bezuidenhout, J., Sekoere, T., Gous, C., Boucher, H. 2018. The structural setting of mineralisation at Kolomela Mine, Northern Cape, South Africa, based on fully-constrained, implicit 3D modelling. *Ore Geol. Rev.*, **95**:306–324. <https://doi.org/10.1016/j.oregeorev.2018.02.032>

Bau, M., 1996. Controls on the fractionation of isovalent trace elements in magmatic and aqueous systems: evidence from Y/Ho, Zr/Hf, and lanthanide tetrad effect. *Contrib Miner. Pet.*, **123**:323–333. <https://doi.org/10.1007/s004100050317>

Bau, M., Dulski, P. 1996. Distribution of yttrium and rare-earth elements in the Penge and Kuruman iron-formations, Transvaal Supergroup, South Africa. *Precambrian Res.*, **79**:37–55. [https://doi.org/10.1016/0301-9268\(95\)00087-9](https://doi.org/10.1016/0301-9268(95)00087-9)

Bau, M., Koschinsky, A., Dulski, P., Hein, J.R. 1996. Comparison of the partitioning behaviours of yttrium, rare earth elements, and titanium between hydrogenetic marine ferromanganese crusts and seawater. *Geochim. Cosmochim. Acta*, **60**:1709–1725. [https://doi.org/10.1016/0016-7037\(96\)00063-4](https://doi.org/10.1016/0016-7037(96)00063-4)

Berman, R.G. 1991. Thermobarometry using multi-equilibrium calculations: a new technique, with petrological applications In: Gordon, T.M., Martin, R.F. (eds.). Quantitative Methods in Petrology: An Issue in Honor of Hugh J. Greenwood. *Canadian Mineralogist*, p. 833–855.

Borisenko, L.F., Lebedeva, S.I., Serdobova, L.I. 1969. Titanium magnetite and magnetite of iron ore deposits of different genesis. *Int. Geol. Rev.*, **11**:1408–1418. <https://doi.org/10.1080/00206816909475193>

Bostrom, K. 1973. The origin and fate of ferromanganese active ridge sediments. *Stock. Contrib. Geol.*, **27**:149–243.

Boyle, C., Latscha, A. A. 2013. Implicit Geological Modelling of Iron Ore Deposits In: Iron Ore Conference. The Australasian Institute of Mining and Metallurgy. Melbourne, Perth, p. 57–66.

Brito Neves, B.B., Fuck, R.A., Pimentel, M.M. 2014. The Brasiliano collage in South America: a review. *Brazilian J. Geol.*, **44**:493–518. <https://doi.org/10.5327/Z2317-4889201400030010>

Cabral, A.R., Eugster, O., Brauns, M., Lehmann, B., Rösel, D., Zack, T., Abreu, F.R. de, Pernicka, E., Barth, M. 2013. Direct dating of gold by radiogenic helium: Testing the method on gold from Diamantina, Minas Gerais, Brazil. *Geology*, **41**:163–166. <https://doi.org/10.1130/G33751.1>

Cabral, A.R., Lehmann, B., Tupinambá, M., Wiedenbeck, M., Brauns, M. 2011. Geology, mineral chemistry and tourmaline B isotopes of the Córrego Bom Sucesso area, southern Serra do Espinhaço, Minas Gerais, Brazil: Implications for Au-Pd-Pt exploration in quartzitic terrain. *J. Geochemical Explor.*, **110**:260–277. <https://doi.org/10.1016/j.gexplo.2011.06.007>

Cabral, A.R., Zeh, A. 2015. Celebrating the Centenary of “The Geology of Central Minas Gerais, Brazil”: An insight from the Sítio Largo Amphibolite. *J. Geol.*, **123**:337–354. <https://doi.org/10.1086/682047>

Cabral, A.R., Zeh, A., Galbiatti, H.F., Lehmann, B. 2015. Late Cambrian Au-Pd mineralization and Fe enrichment in the Itabira district, Minas Gerais, Brazil, at 496 Ma: constraints from U-Pb monazite dating of Jacutinga lode. *Econ. Geol.*, **110**:263–272. <https://doi.org/10.2113/econgeo.110.1.263>

Carvalho, R.P. de, Rosière, C.A., Rolim, V.K., Lana, C. de C., Santos, J.O.S. 2014. A sequência orosíriana-estateriana e geometria transpressiva na região de Santa Maria de Itabira, Minas Gerais. *Geol. USP - Ser. Cient.*, **14**:101–120. <https://doi.org/10.5327/Z1519-874X201400020006>

Chaves, M.L. de S.C., Brandão, P.R.G., Buhn, B. 2010. Monazita em veios de quartzo da Serra do Espinhaço Meridional (MG): mineralogia, idades LA-ICP-MS e implicações geológicas. *Rev. Bras. Geociências*, **40**:506–515.

Chemale, F., Dussin, I.A., Alkmim, F.F., Martins, M.S., Queiroga, G., Armstrong, R., Santos, M.N. 2012. Unravelling a Proterozoic basin history through detrital zircon geochronology: The case of the Espinhaço Supergroup, Minas Gerais, Brazil. *Gondwana Res.*, **22**:200–206. <https://doi.org/10.1016/j.gr.2011.08.016>

Chen, Y.X., Gao, P., Zheng, Y.-F., 2015. The anatetic effect on the zircon Hf isotope composition of migmatites and associated granites. *Lithos*, **238**:174–184. <https://doi.org/10.1016/j.lithos.2015.09.026>

Claesson, S., Bibikova, E. V., Shumlyanskyy, L., Whitehouse, M.J., Billström, K. 2016. Can oxygen isotopes in magmatic zircon be modified by metamorphism? A case study from the Eoarchean

Claiborne, L.L., Miller, C.F., Walker, B. a., Wooden, J.L., Mazdab, F.K., Bea, F. 2006. Tracking magmatic processes through Zr/Hf ratios in rocks and Hf and Ti zoning in zircons: An example from the Spirit Mountain batholith, Nevada. *Mineral. Mag.*, **70**: 517–543.
<https://doi.org/10.1180/0026461067050348>

Cowan, E.J., Beatson, R.K., Fright, W.R., McLennan, T.J., Mitchell, T.J. 2002. Rapid geological modelling. In: Applied Structural Geology for Mineral Exploration and Mining, International Symposium. Kalgoorlie, p. 23–25.

Cowan, E.J., Beatson, R.K., Ross, H.J., Fright, W.R., McLennan, T.J., Evans, T.R., Carr, J.C., Lane, R.G., Bright, D. V., Gillman, A.J., Oshust, P.A., Titley, M. 2003. Practical Implicit Geological Modelling. In: 5th International Mining Geology Conference, The Australasian Institute of Mining and Metallurgy. Bendigo, p. 89–99.

Dare, S.A.S., Barnes, S.J., Beaudoin, G., Méric, J., Boutroy, E., Potvin-Doucet, C. 2014. Trace elements in magnetite as petrogenetic indicators. *Miner. Depos.*, **49**:785–796.
<https://doi.org/10.1007/s00126-014-0529-0>

Davies, J.H.F.L., Stern, R.A., Heaman, L.M., Rojas, X., Walton, E.L. 2015. Resolving oxygen isotopic disturbance in zircon: A case study from the low $\delta^{18}\text{O}$ Scourie dikes, NW Scotland. *Am. Mineral.*, **100**:1952–1966. <https://doi.org/10.2138/am-2015-5221>

Dickin, A.P. 2005. *Radiogenic isotope geology*. Cambridge University Press, New York, 492 p.

Dill, H.G. 2015. Pegmatites and aplites: Their genetic and applied ore geology. *Ore Geol. Rev.*, **69**:417–561. <https://doi.org/10.1016/j.oregeorev.2015.02.022>

Dossin, I.A., Dossin, T.M., Charvet, J., Cocherie, A., Rossi, P. 1993. Single-zircon dating by step-wise Pb-evaporation of Middle Proterozoic Magmatism in the Espinhaço Range, Southeastern São Francisco Craton (Minas Gerais, Brazil). In: Anais do 2º Simp. do Cráton Do São Francisco. Sociedade Brasileira de Geologia. Salvador, p. 39–42.

Dossin, I.A., Uhlein, A., Dossin, T.M. 1984. Geologia da faixa móvel Espinhaço em sua porção meridional - MG. In: Anais do 33º Congresso Brasileiro de Geologia. Sociedade Brasileira de Geologia. Rio de Janeiro, p. 3118–3132.

Dupuis, C., Beaudoin, G. 2011. Discriminant diagrams for iron oxide trace element fingerprinting of mineral deposit types. *Miner. Depos.*, **46**:319–335. <https://doi.org/10.1007/s00126-011-0334-y>

Dussin, I.A., Dussin, T.M. 1995. Supergrupo Espinhaço: modelo de evolução geodinâmica. *Geonomos*, **3**:19–26.

Dussin, T.M., Duarte, P., Dussin, I.A. 2000. Registro da tectônica Brasiliiana na região de Guanhães (SE, Brasil): Deformação e metamorfismo das rochas de idade pós-Transamazônicas. *Geonomos*, **8**:55–59.

Evans, K.A., McCuaig, T.C., Leach, D., Angerer, T., Hagemann, S.G. 2013. Banded iron formation to iron ore: A record of the evolution of Earth environments? *Geology*, **41**:99–102. <https://doi.org/10.1130/G33244.1>

Fazio, V.S. 2013. *Interpolação Espacial: uma comparação analítica entre redes RBF e krigagem*. Dissertação de Mestrado, Programa de Pós-Graduação em Computação, Universidade Federal de Santa Catarina, Florianópolis, 109 p.

Fernandes, M.L.S. 2001. *O Granito Borrachudos entre Guanhães e Dores de Guanhães (Plutônito Morro do Urubu): Gênese e Evolução*. Tese de Doutorado, Departamento de Geologia, Universidade Federal do Rio do Janeiro, Rio de Janeiro, 172 p.

Fernandes, M.L.S., Marciano, V.R.P.R.O., Oliveira, R.C., Correia Neves, J.M., Diláscio, M. V. 1994. Granitos Borrachudos: um exemplo de granitogênese anorogênica na porção central do Estado de Minas Gerais. *Geonomos*, **2**:23–29.

Ferreira, R. de M.G. 2017. *Origem e idades químicas U-Th-Pb dos distritos pegmatíticos de Itambé (BA) e Santa Maria de Itabira (MG) reveladas pela monazita*. Dissertação de Mestrado, Instituto de Geociências, Universidade Federal de Minas Gerais, 48 p.

Figueiredo e Silva, R.C., Hagemann, S., Lobato, L.M., Rosière, C.A., Banks, D.A., Davidson, G.J., Vennemann, T., Hergt, J. 2013. Hydrothermal fluid processes and evolution of the giant serra norte jaspilite-hosted iron ore deposits, Carajás mineral Province, Brazil. *Econ. Geol.*, **108**:739–779. <https://doi.org/10.2113/econgeo.108.4.739>

Figueiredo e Silva, R.C., Lobato, L.M., Rosière, C.A., Hagemann, S., Zucchetti, M., Baars, F.J., Morais, R., Andrade, I. 2008. A hydrothermal origin for the jaspilite- hosted, giant Serra Norte iron

ore deposits in the Carajás Mineral Province, Pará state, Brazil. *Soc. Econ. Geol. SEG Rev.*, **15**:255–290.

Fisher, C.M., Vervoort, J.D., DuFrane, S.A. 2014. Accurate Hf isotope determinations of complex zircons using the “laser ablation split stream” method. *Geochemistry, Geophys. Geosystems*, **15**:121–139. <https://doi.org/10.1002/2013GC004962>

Flinn, D. 1962. On folding during three-dimensional progressive deformation. *Geol. Soc. London Quart. Jour.*, **118**:385–433.

Gagnevin, D., Daly, J.S., Kronz, A. 2010. Zircon texture and chemical composition as a guide to magmatic processes and mixing in a granitic environment and coeval volcanic system. *Contrib. to Mineral. Petrol.*, **159**:579–596. <https://doi.org/10.1007/s00410-009-0443-0>

Ge, R., Zhua, W., Wu, H., He, J., Zheng, B. 2013. Zircon U–Pb ages and Lu–Hf isotopes of Paleoproterozoic metasedimentary rocks in the Korla Complex, NW China: Implications for metamorphic zircon formation and geological evolution of the Tarim Craton. *Precambrian Res.*, **231**:1–18. <https://doi.org/https://doi.org/10.1016/j.precamres.2013.03.003>

Geisler, T., Schaltegger, U., Tomaschek, F. 2007. Re-equilibration of Zircon in Aqueous Fluids and Melts. *Elements*, **3**:43–50. <https://doi.org/10.2113/gselements.3.1.43>

Ghosh, S.K., Mandal, N., Sengupta, S., Deb, S.K., Khan, D. 1993. Superposed buckling in multilayers. *J. Struct. Geol.*, **15**:95–111. [https://doi.org/10.1016/0191-8141\(93\)90081-K](https://doi.org/10.1016/0191-8141(93)90081-K)

Gomes, S.D., Berger, S., Figueiredo e Silva, R.C., Hagemann, S.G., Rosière, C.A., Banks, D.A., Lobato, L.M. 2018. Oxide chemistry and Fluid inclusion constraints on the formation of itabirite-hosted iron ore deposits and associated pegmatites at the eastern border of the Southern Espinhaço Range, Brazil. *Ore Geol. Rev.*, **95**:821–848. <https://doi.org/10.1016/j.oregeorev.2018.03.025>

Gonçalves G.O., Lana C., Buick I.S., Alkmim, F.F., Scholz, R., Queiroga, G. 2019. Twenty million years of post-orogenic fluid production and hydrothermal mineralization across the external Araçuaí orogen and adjacent São Francisco craton, SE Brazil. *Lithos*, **342**:557–572. <https://doi.org/10.1016/j.lithos.2019.04.022>

Grohmann, C.H., Campanha, G.A.C. 2010. OpenStereo: open source, cross-platform software for structural geology analysis. In: AGU 2010 Fall Meeting, San Francisco.

Grossi-Sad, J.H. 1997. Geologia da Folha Guanhães. In: Grossi-Sad, J.H., Lobato, L.M., Pedrosa-Soares, A.C., Soares-Filho, B.S. (eds.). *Projeto Espinhaço em Cd-Rom (Textos, Mapas E Anexos)*, Belo Horizonte, COMIG, p. 2317–2435.

Grossi-Sad, J.H., Chiodi Filho, C., Santos, J.F., Magalhães, J.M.M., Carelos, P.M. 1990a. Geoquímica e origem da formação ferrífera do Grupo Guanhães, Distrito de Guanhães, MG, Brasil. In: Anais do 36º Congresso Brasileiro de Geologia, Sociedade Brasileira de Geologia. Natal, p. 1241–1253.

Grossi-Sad, J.H., Chiodi Filho, C., Santos, J.F., Magalhães, J.M.M., Carelos, P.M., 1990b. Duas Suítes Graníticas da Borda Sudeste do Cráton Sanfranciscano, em Minas Gerais: Petroquímica e Potencial Metalogenético. In: Anais do 36º Congresso Brasileiro de Geologia, Sociedade Brasileira de Geologia. Natal, p. 1836–1848.

Grossi-Sad, J.H., Mourão, M.A.A., Guimarães, M.L. V., Knauer, L.G. 1997. Geologia da Folha Conceição do Mato Dentro. In: Grossi-Sad, J.H., Lobato, L.M., Pedrosa-Soares, A.C., Soares-Filho, B.S. (eds.), *Projeto Espinhaço em Cd-Rom (Textos, Mapas E Anexos)*. Belo Horizonte, COMIG, p. 2533–2693.

Guadagnin, F., Chemale, F. 2015. Detrital zircon record of the Paleoproterozoic to Mesoproterozoic o cratonic basins in the São Francisco Craton. *J. South Am. Earth Sci.*, **60**:104–116. <https://doi.org/10.1016/j.jsames.2015.02.007>

Guillong, M.M., Maier, D.L., Allan, M.M., Heinrich, C.A., Yardley, B.W.D. 2008. Appendix A6: SILLS: a MATLAB based program for the reduction of laser ablation ICPMS data f homogeneous materials and inclusions. In: Sylvester, P. (ed.). Laser Ablation ICPMS in Earth Sciences: Current Practices and Outstanding Issues. *Mineralog. Assoc. Canada*, p. 328–333.

Hagemann, S.G., Angerer, T., Duuring, P., Rosière, C.A., Figueiredo, R.C., Lobato, L., Hensler, A.S., Walde, D.H.G. 2016. BIF-hosted iron mineral system: A review. *Ore Geol. Rev.*, **76**:317–359. <https://doi.org/10.1016/j.oregeorev.2015.11.004>

Hanchar, J.M., Finch, R.J., Hoskin, P.W.O., Watson, E.B., Cherniak, D.J., Mariano, A.N. 2001. Rare earth elements in synthetic zircon: Part 1. Synthesis, and rare earth element and phosphorus doping. *Am. Mineral.*, **85**:667–680. <https://doi.org/10.2138/am-2001-5-607>

Hartmann, L.A., Endo, I., Saita, M.T.F., Santos, J.O.S., Frantz, J.C., Carneiro, M.A., McNaughton, N.J., Barley, M.E. 2006. Provenance and age delimitation of Quadrilátero Ferrífero sandstones based on zircon U-Pb isotopes. *J. South Am. Earth Sci.*, **20**:273–285. <https://doi.org/10.1016/j.jsames.2005.07.015>

Heilbron, M., Valeriano, C.M., Tassinari, C.C.G., Almeida, J., Tupinambá Siga Jr., M.O., Trouw, R., 2008. Correlation of Neoproterozoic terranes between the Ribeira Belt, SE Brazil and its African counterpart: comparative tectonic evolution and open questions. In: Pankhurst, R.J., Trouw, R.A.J., Neves, B.B., De Wit, M.J. (eds.). West Gondwana: Pre-Cenozoic Correlations Across the South Atlantic Region. *Geological Society*, London, p. 211–237.

Heimann, A., Spry, P.G., Teale, G.S., Conor, C.H.H., Leyh, W.R. 2009. Geochemistry of Garnet-Rich Rocks in the Southern Curnamona Province, Australia, and Their Genetic Relationship to Broken Hill-Type Pb-Zn-Ag Mineralization. *Econ. Geol.*, **104**:687–712.

Hensler, A.S., Hagemann, S.G., Brown, P.E., Rosière, C.A. 2014. Using oxygen isotope chemistry to track hydrothermal processes and fluid sources in itabirite-hosted iron ore deposits in the Quadrilátero Ferrífero, Minas Gerais, Brazil. *Miner. Depos.*, **49**:293–311. <https://doi.org/10.1007/s00126-013-0486-z>

Hensler, A.S., Hagemann, S.G., Rosière, C.A., Angerer, T., Gilbert, S. 2015. Hydrothermal and metamorphic fluid-rock interaction associated with hypogene “hard” iron ore mineralisation in the Quadrilátero Ferrífero, Brazil: Implications from in-situ laser ablation ICP-MS iron oxide chemistry. *Ore Geol. Rev.*, **69**:325–351. <https://doi.org/10.1016/j.oregeorev.2015.02.023>

Hillier, M., Dekemp, E.A., Schetselaar, E. 2013. 3D form line construction by structural field interpolation (SFI) of geologic strike and dip observations. *J. Struct. Geol.*, **51**:167–179. <https://doi.org/10.1016/j.jsg.2013.01.012>

Holland, H.D., Gottfried, D. 1955. The effect of nuclear radiation on the structure of zircon. *Acta Crystallogr.*, **8**:291–300. <https://doi.org/10.1107/S0365110X55000947>

Holland, T.J.B., Powell, R. 1990. An internally-consistent thermodynamic dataset with uncertainties and correlations: the system Na₂O-CaO-MgO-MnO-FeO-Al₂O₃-SiO₂-TiO₂-C-H₂-O₂. *J. Metamorph. Geol.*, **8**:89–124.

Hoskin, P.W.O. 2005. Trace-element composition of hydrothermal zircon and the alteration of Hadean zircon from the Jack Hills, Australia. *Geochim. Cosmochim. Acta*, **69**:637–648. <https://doi.org/10.1016/j.gca.2004.07.006>

Hoskin, P.W.O., Schaltegger, U. 2003. The Composition of Zircon and Igneous and Metamorphic Petrogenesis. In: Han-Char, J.M., Hoskin, P.W.O. (eds.). Rev. Mineral. Geochem. *Mineralogical Society of America*, Washington, p. 27–62.

Hoskin, P.W.O., Black, L.P. 2000. Metamorphic zircon formation by solid-state recrystallization of protolith igneous zircon. *J. Metamorph. Geol.*, **18**:423–439.

Hoskin, P.W.O., Schaltegger, U. 2003. The Composition of Zircon and Igneous and Metamorphic Petrogenesis. In: Han-Char, J.M., Hoskin, P.W.O. (eds.), *Rev. Mineral. Geochem. Mineralogical Society of America*, Washington, p. 27–62.

Jessell, M., 2001. Three-dimensional geological modelling of potential-field data. *Comput. Geosci.* **27**, 455–465. [https://doi.org/10.1016/S0098-3004\(00\)00142-4](https://doi.org/10.1016/S0098-3004(00)00142-4)

Jochum, K.P., Willbold, M., Raczek, I., Stoll, B., Herwig, K. 2005. Chemical Characterisation of the USGS Reference Glasses GSA-1G, GSC-1G, GSD-1G, GSE-1G, BCR-2G, BHVO-2G and BIR-1G Using EPMA, ID-TIMS, ID-ICP-MS and LA-ICP-MS. *Geostand. Geoanalytical Res.*, **29**:285–302. <https://doi.org/10.1111/j.1751-908X.2005.tb00901.x>

Kinny, P.D., Maas, R. 2003. Lu-Hf and Sm-Nd isotope systems in zircon. In: Han-Char, J.M., Hoskin, P.W.O. (eds.), *Rev. Mineral. Geochem. Mineralogical Society of America*, Washington, p. 327–341. <https://doi.org/10.2113/0530327>

Kirkland, C.L., Smithies, R.H., Taylor, R.J.M., Evans, N., McDonald, B. 2015. Lithos Zircon Th/U ratios in magmatic environs. *Lithos*, **212–215**:397–414. <https://doi.org/10.1016/j.lithos.2014.11.021>

Kita, N.T., Ushikubo, T., Fu, B., Valley, J.W. 2009. High precision SIMS oxygen isotope analysis and the effect of sample topography. *Chem. Geol.*, **264**:43–57. <https://doi.org/10.1016/j.chemgeo.2009.02.012>

Klein, C. 2005. Some Precambrian banded iron-formations (BIFs) from around the world: Their age, geologic setting, mineralogy, metamorphism, geochemistry, and origin. *Am. Mineral.*, **90**:1473–1499. <https://doi.org/10.2138/am.2005.1871>

Klein, C., Ladeira, E.A. 2004. Geochemistry and mineralogy of neoproterozoic banded iron-formations and some selected, siliceous manganese formations from Urucum district, Mato Grosso do Sul, Brazil. *Econ. Geol.*, **99**:1233–1244. <https://doi.org/10.2113/gsecongeo.99.6.1233>

Knauer, L.G. 1990. *Evolução geológica do Precambriano da porção centro-leste da Serra do Espinhaço Meridional e metalogênese associada*. Dissertação de Mestrado, Instituto de Geociências, Universidade Estadual de Campinas, Campinas, 298 p.

Knight, R.H., Lane, R.G., Ross, H.J., Abraham, A.P.G., Cowan, E.J. 2007. Implicit Ore Delineation. In: Milkereit, B. (ed.). Proceedings of Exploration 07: Fifth Decennial International Conference on Mineral Exploration. *Decennial Mineral Exploration Conferences*. Toronto, p. 1165–1169.

Knipe, R.J. 1989. Deformation mechanisms - recognition from natural tectonites. *J. Struct. Geol.*, **11**: 127–146. [https://doi.org/10.1016/0191-8141\(89\)90039-4](https://doi.org/10.1016/0191-8141(89)90039-4)

Kruhl, J.H. 1996. Prism- and basal- plane parallel subgrain boundaries in quartz: a microstructural geothermobarometer. *J. Metamorph. Geol.*, **14**:581–589.

Lajaunie, C., Courrioux, G., Manuel, L. 1997. Foliation Fields and 3D Cartography in Geology : Principles of a Method Based on Potential Interpolation. *Math. Geol.*, **29**:571–584. <https://doi.org/10.1007/BF02775087>

Liégeois, J.P., Abdelsalam, M.G., Ennih, N., Ouabadi, A. 2013. Metacraton: Nature, genesis and behavior. *Gondwana Res.*, **23**:220–237. <https://doi.org/10.1016/j.gr.2012.02.016>

Lobato, L., Ribeiro-Rodrigues, L., Vieira, F. 2001. Brazil's premier gold province. Part II: geology and genesis of gold deposits in the Archean Rio das Velhas greenstone belt, Quadrilátero Ferrífero. *Miner. Depos.*, **36**:249–277. <https://doi.org/10.1007/s001260100180>

Ludwig, K.R. 2003. *ISOPLOT 3.00 - Geochronological Toolkit for Excel*. Berkely Geochronol. Center, Spec. Publ. 4, p. 67.

Ludwig, K.R. 2001. *SQUID 1.02: an Users Manual*. Berkeley Geochronol. Centre, Spec. Publ. No. 2., p. 19.

Machado, N., Schrank, A., Abreu, F.R., Knauer, L.G., Almeida-Abreu, P.A. 1989. Resultados preliminares da geocronologia U/Pb na Serra do Espinhaço Meridional. *Boletim da Sociedade Brasileira de Geologia*, **10**:171-173

Machado, N., Schrank, A., Noce, C.M., Gauthier, G. 1996. Ages of detrital zircon from Archean-Paleoproterozoic sequences: Implications for Greenstone Belt setting and evolution of a Transamazonian foreland basin in Quadrilátero Ferrífero, southeast Brazil. *Earth Planet. Sci. Lett.*, **141**:259–276. [https://doi.org/10.1016/0012-821X\(96\)00054-4](https://doi.org/10.1016/0012-821X(96)00054-4)

Magalhães, J.R., Pedrosa Soares, A.C., Dussin, I., Müntener, O., Pinheiro, M.A.P., Silva, L.C. da, Knauer, L.G., Bouvier, A.S., Baumgartner, L. 2018. First Lu-Hf, $\delta^{18}\text{O}$ and trace elements in zircon signatures from the Statherian Espinhaço anorogenic province (Eastern Brazil): geotectonic implications of a silicic large igneous province. *Brazilian J. Geol.*, **48**:735–759. <https://doi.org/10.1590/2317-4889201820180046>

Marciano, V.R.P. da R.O. 1995. *O distrito pegmatítico de Santa Maria de Itabira, MG : mineralogia, geoquímica e zoneografia*. Tese de Doutorado, Universidade de São Paulo, São Paulo, 216 p. <https://doi.org/10.11606/T.44.1995.tde-18112015-111931>

Martins-Neto, M.A. 2000. Tectonics and sedimentation in a paleo/mesoproterozoic rift-sag basin (Espinhaço basin, southeastern Brazil). *Precambrian Res.*, **103**:147–173. [https://doi.org/10.1016/S0301-9268\(00\)00080-2](https://doi.org/10.1016/S0301-9268(00)00080-2)

Martins, B. de S., Lobato, L.M., Rosière, C.A., Hagemann, S.G., Santos, J.O.S., Villanova, F.L. dos S.P., Figueiredo e Silva, R.C., Lemos, L.H. de Á. 2016. The Archean BIF-hosted Lamego gold deposit, Rio das Velhas greenstone belt, Quadrilátero Ferrífero: Evidence for Cambrian structural modification of an Archean orogenic gold deposit. *Ore Geol. Rev.*, **72**:963–988. <https://doi.org/10.1016/j.oregeorev.2015.08.025>

McLennan, S.M. 1989. Rare earth elements in sedimentary rocks: influence of provenance and sedimentary processes. In: Lipin, B.R., McKay, G.A. (eds.), *Reviews in Mineralogy*, p. 169–200.

McLennan, S.M., Taylor, S.R. 1991. Sedimentary Rocks and Crustal Evolution: Tectonic Setting and Secular Trends. *J. Geol.*, **99**:1–21. <https://doi.org/10.1086/629470>

Melo, M.G., Lana, C., Stevens, G., Pedrosa Soares, A.C., Gerdes, A., Alkmin, L.A., Nalini, H.A., Alkmim, F.F. 2017. Assessing the isotopic evolution of S-type granites of the Carlos Chagas Batholith, SE Brazil: Clues from U–Pb, Hf isotopes, Ti geothermometry and trace element composition of zircon. *Lithos*, **284–285**:730–750. <https://doi.org/10.1016/j.lithos.2017.05.025>

Mendes, M. de C.O., Lobato, L.M., Suckau, V., Lana, C. 2014. In situ LA-ICPMS U-Pb dating of detrital zircons from the Cercadinho Formation, Minas Supergroup. *Geol. USP. Série Científica*, **13**:55–68. <https://doi.org/10.5327/Z1519-874X201400010004>

Mendes, M., Lobato, L.M., Kunzmann, M., Halverson, G.P., Rosière, C.A. 2016. Iron isotope and REE+Y composition of the Cauê banded iron formation and related iron ores of the Quadrilátero Ferrífero, Brazil. *Miner. Depos.*, **52**(2): 159–180 <https://doi.org/10.1007/s00126-016-0649-9>

Mojzsis, S.J., Harrison, T.M., Pidgeon, R.T. 2001. Oxygen-isotope evidence from ancient zircons for liquid water at the Earth's surface 4,300 Myr ago. *Nature*, **409**:178–181. <https://doi.org/10.1038/35051557>

Müller, G., Schuster, A.K., Hoefs, J. 1986. The metamorphic grade of banded iron formations: oxygen isotope and petrological constraints. *Fortsch. Miner.*, **64**:163–185.

Mücke, A., Cabral, A.R. 2005. Redox and nonredox reactions of magnetite and hematite in rocks. *Chemie der Erde Geochemistry*, **65**:271–278. <https://doi.org/10.1016/j.chemer.2005.01.002>

Nadol, P., Angerer, T., Mauk, J.L., French, D., Walshe, J. 2014. The chemistry of hydrothermal magnetite : A review. *Ore Geol. Rev.*, **61**:1–32. <https://doi.org/10.1016/j.oregeorev.2013.12.013>

Nasdala, L., Hofmeister, W., Norberg, N., Martinson, J.M., Corfu, F., Dörr, W., Kamo, S.L., Kennedy, A.K., Kronz, A., Reiners, P.W., Frei, D., Kosler, J., Wan, Y., Götze, J., Häger, T., Kröner, A., Valley, J.W. 2008. Zircon M257 - a Homogeneous Natural Reference Material for the Ion Microprobe U-Pb Analysis of Zircon. *Geostand. Geoanalytical Res.*, **32**:247–265. <https://doi.org/10.1111/j.1751-908X.2008.00914.x>

Nasdala, L., Kronz, A., Hanchar, J.M., Tichomirowa, M., Davis, D.W., Hofmeister, W. 2006. Effects of natural radiation damage on back-scattered electron images of single crystals of minerals. *Am. Mineral.*, **91**:1739–1746. <https://doi.org/10.2138/am.2006.2241>

Nielsen, R.L., Forsythe, L.M., Gallahan, W.E., Fisk, M.R. 1994. Major- and trace-element magnetite-melt equilibria. *Chem. Geol.*, **117**:167–191. [https://doi.org/10.1016/0009-2541\(94\)90127-9](https://doi.org/10.1016/0009-2541(94)90127-9)

Noce, C.M., Pedrosa Soares, A.C., da Silva, L.C., Armstrong, R., Piuzana, D. 2007a. Evolution of polycyclic basement complexes in the Araçuaí Orogen, based on U–Pb SHRIMP data: Implications for Brazil–Africa links in Paleoproterozoic time. *Precambrian Res.*, **159**:60–78. <https://doi.org/10.1016/j.precamres.2007.06.001>

Noce, C.M., Pedrosa Soares, A.C., Silva, L.C. da, Alkmim, F.F. de. 2007b. O embasamento arqueano e paleoproterozóico do Orógeno Araçuaí. *Geonomos*, **15**:17–23.

Noce, C.M., Zucchetti, M., Baltazar, O.F., Armstrong, R., Dantas, E., Renger, F.E., Lobato, L.M. 2005. Age of felsic volcanism and the role of ancient continental crust in the evolution of the Neoarchean Rio das Velhas Greenstone belt (Quadrilátero Ferrífero, Brazil): U-Pb zircon dating of volcaniclastic graywackes. *Precambrian Res.*, **141**:67–82.
<https://doi.org/10.1016/j.precamres.2005.08.002>

Oliveira, A.A.K., Leite, C.A. da S. 2000. *Projeto Leste: Folha Ipatinga - SE.23-Z-D-II, escala 1:100.000*. Belo Horizonte, SEME/COMIG/CPRM, 58 p.

Oliveira, A.L.R. De, Javier, F., Alberto, C., Wölle, M., Ortelli, M., Kouzmanov, K. 2017. Nature and evolution of fluids associated with specularite-bearing Fe and Au-PGE (Jacutinga) mineralization during the Brasiliano orogeny in the eastern São Francisco Craton, Minas Gerais, Brazil. *Ore Geol. Rev.*, **86**:130–153. <https://doi.org/10.1016/j.oregeorev.2017.02.017>

Oriolo, S., Hueck, M., Oyhantçabal, P., Goscombe, B., Wemmer, K., Siegesmund, S. 2018. Shear Zones in Brasiliano-Pan-African Belts and Their Role in the Amalgamation and Break-Up of Southwest Gondwana. In: Siegesmund, S., Basel, M.A.S., Oyhantcabal, P., Oriolo, S. (eds.). *Geology of Southwest Gondwana*, Springer, p. 593–613. <https://doi.org/10.1007/978-3-319-68920-3>

Oriolo, S., Oyhantçabal, P., Wemmer, K., Siegesmund, S. 2017. Contemporaneous assembly of Western Gondwana and final Rodinia break-up: Implications for the supercontinent cycle. *Geosci. Front.*, **8**:1431–1445. <https://doi.org/10.1016/j.gsf.2017.01.009>

Pedrosa Soares, A.C., Dardenne, M.A., Hasui, Y., Castro, F.D.C., Carvalho, M.V.A. 1994. *Mapa e Nota Explicativa dos Mapas Geológico, Metalogenético e de Ocorrências Minerais do Estado de Minas Gerais, Escala 1:1.000.000*. Belo Horizonte, SEME/COMIG, 231 p.

Pedrosa Soares, A.C., De Campos, C.P., Noce, C., Silva, L.C., Novo, T., Roncato, J., Medeiros, S., Castañeda, C., Queiroga, G., Dantas, E., Dussin, I., Alkmim, F. 2011. Late Neoproterozoic-Cambrian granitic magmatism in the Araçuaí orogen (Brazil), the Eastern Brazilian Pegmatite Province and related mineral resources. *Geol. Soc. London, Spec. Publ.*, **350**:25–51.
<https://doi.org/10.1144/SP350.3>

Pedrosa Soares, A.C., Noce, C.M., Alkmim, F.F. de, Silva, L.C., Babinski, M., Cordani, U., Catañeda, C. 2007. Orógeno Araçuaí: síntese do conhecimento 30 anos após Almeida 1997. *Geonomos*, 15:1–16.

Pedrosa Soares, A.C., Noce, C.M., Wiedemann, C.M., Pinto, C.P. 2001. The Araçuaí-West-Congo Orogen in Brazil: an overview of a confined orogen formed during Gondwanaland assembly. *Precambrian Res.*, **110**:307–323. [https://doi.org/10.1016/S0301-9268\(01\)00174-7](https://doi.org/10.1016/S0301-9268(01)00174-7)

Peres, G.G., Alkmim, F.F., Jordt-Evangelista, H. 2004. The southern Araçuaí belt and the Dom Silvério Group: geologic architecture and tectonic significance. *An. Acad. Bras. Cienc.*, **76**:771–790.

Pflug, R. 1968. Observações sobre a estratigrafia da Série Minas na Região de Diamantina, Minas Gerais, Notas Prel. 142. Rio de Janeiro, 20 p.

Pidgeon, R.T., O’Neil, J.R., Silver, L.T. 1966. Uranium and Lead Isotopic Stability in a Metamict Zircon under Experimental Hydrothermal Conditions. *Science*, **154**:1538–1540. <https://doi.org/10.1126/science.154.3756.1538>

Pinto, C.P., Silva, M.A. da. 2014. *Mapa geológico do estado de Minas Gerais, escala 1:1.000.000*. Belo Horizonte, CPRM/CODEMIG.

Planavsky, N., Bekker, A., Rouxel, O.J., Kamber, B., Hofmann, A., Knudsen, A., Lyons, T.W. 2010. Rare Earth Element and yttrium compositions of Archean and Paleoproterozoic Fe formations revisited: New perspectives on the significance and mechanisms of deposition. *Geochim. Cosmochim. Acta*, **74**:6387–6405. <https://doi.org/10.1016/j.gca.2010.07.021>

Polat, A., Frei, R. 2005. The origin of early Archean banded iron formations and of continental crust, Isua, southern West Greenland. *Precambrian Res.*, **138**:151–175. <https://doi.org/10.1016/j.precamres.2005.04.003>

Preinfalk, C., Kostitsyn, Y., Morteani, G. 2002. The pegmatites of the Nova Era-Itabira-Ferros pegmatite district and the emerald mineralisation of Capoeirana and Belmont (Minas Gerais, Brazil): Geochemistry and Rb-Sr dating. *J. South Am. Earth Sci.*, **14**:867–887. [https://doi.org/10.1016/S0895-9811\(01\)00082-7](https://doi.org/10.1016/S0895-9811(01)00082-7)

Purtov, V.K., Kotelnikova, A.L. 1993. Solubility of titanium in chloride and fluoride hydrothermal solutions. *Int. Geol. Rev.*, **35**:279–287. <https://doi.org/10.1080/00206819309465529>

Ramsay, J.G. 1967. *Folding and Fracturing of Rocks*. McGraw-Hill, New York, 568 p.

Renger, F.E., Noce, C.M., Romano, A.W., Machado, N. 1994. Evolução sedimentar do Supergrupo Minas: 500 Ma. de registro geológico no Quadrilátero Ferrífero, Minas Gerais. *Geonomos*, **2**:1–11. <https://doi.org/10.1590/S0370-44672008000100011>

Rolim, V.K., 2016. As formações ferríferas da região de Conceição do Mato Dentro - MG: posicionamento estratigráfico, evolução tectônica, geocronologia características e gênese dos minérios. Tese de Doutorado, Instituto de Geociências, Universidade Federal de Minas Gerais, 215 p.

Rolim, V.K., Rosière, C.A., Santos, J.O.S., McNaughton, N.J. 2016. The Orosirian-Statherian banded iron formation-bearing sequences of the southern border of the Espinhaço Range, Southeast Brazil. *J. South Am. Earth Sci.*, **65**:43–66. <https://doi.org/10.1016/j.jsames.2015.11.003>

Rollinson, H.R. 1993. *Using Geochemical Data - evaluation, presentation, interpretation*. Longman Scientific & Technical, 352 p.

Rolo, R.M., Radtke, R., Costa, J.F.C.L. 2017. Signed distance function implicit geologic modeling. *REM - Int. Eng. J.*, **70**:221–229. <https://doi.org/10.1590/0370-44672016700146>

Ronchi, L.H., Giuliani, G., Beny, C., Fogaça, A.C.C. 1992. Caracterização físico-química dos fluidos associados aos veios de quartzo auríferos de Costa Sena, MG. *Rev. Bras. Geociências*, **22**:129–138.

Rosière, C.A., Chemale, F.J. 2000. Itabiritos e minérios de ferro de alto teor do Quadrilátero Ferrífero - uma visão geral e discussão. *Geonomos*, **8**:27–43.

Rosière, C.A., Garcia, O.L., Siemes, H., Schaeben, H. 2013. Domainal fabrics of hematite in schistose, shear zone-hosted high-grade Fe ores: The product of the interplay between deformation and mineralization. *J. Struct. Geol.*, **55**:150–166. <https://doi.org/10.1016/j.jsg.2013.07.017>

Rosière, C.A., Heimann, A., Oyhantçabal, P., Santos, J.O.S. 2018. The Iron Formations of the South American Platform. In: Siegesmund, S., Basei, M.A.S., Oyhantçaba, P., Oriolo, S. (eds.), *Geology of Southwest Gondwana*. Springer, p. 493–521. <https://doi.org/10.1007/978-3-319-68920-3>

Rosière, C.A., Rios, F.J. 2004. The origin of hematite in high-grade iron ores based on infrared microscopy and fluid inclusion studies: The example of the Conceição Mine, Quadrilátero Ferrífero, Brazil. *Econ. Geol.*, **99**:611–624. <https://doi.org/10.2113/gsecongeo.99.3.611>

Rosière, C.A., Siemes, H., Quade, H., Brokmeier, H.G., Jansen, E.M. 2001. Microstructures, textures and deformation mechanisms in hematite. *J. Struct. Geol.*, **23**:1429–1440.
[https://doi.org/10.1016/S0191-8141\(01\)00009-8](https://doi.org/10.1016/S0191-8141(01)00009-8)

Rosière, C.A., Spier, C.A., Rios, F.J., Suckau, V.E. 2008. The itabirites of the Quadrilátero Ferrífero and related high-grade iron ore deposits: an overview. *Rev. Econ. Geol.*, **15**:223–254.

Rosière, C., Bekker, A., Rolim, V.K., Santos, J.O.S. 2017. Post-GOE iron formations of the São Francisco craton: filling the gap in iron formation records. In: GSA Annual Meeting. Geological Society of America. Seattle, p. 3-7. <https://doi.org/10.1130/abs/2017AM-300614>

Rubatto, D. 2017. Zircon : The Metamorphic Mineral. *Rev. Mineral. Geochemistry*, **83**: 10–35.
<https://doi.org/http://dx.doi.org/10.2138/rmg.2017.83.10>

Santos, J.O.S., Chernicoff, C.J., Zappettini, E.O., Mcnaughton, N.J., Hartmann, L.A. 2019. Large geographic and temporal extensions of the Río de la Plata Craton, South America, and its metacratonic eastern margin. *Int. Geol. Rev.*, **61**:56–85.
<https://doi.org/10.1080/00206814.2017.1405747>

Santos, M.N., Chemale, F., Dussin, I.A., Martins, M., Assis, T.A.R., Jelinek, A.R., Guadagnin, F., Armstrong, R. 2013. Sedimentological and paleoenvironmental constraints of the Statherian and Stenian Espinhaço rift system, Brazil. *Sediment. Geol.*, **290**:47–59.
<https://doi.org/10.1016/j.sedgeo.2013.03.002>

Schaltegger, U., Fanning, C.M., Günther, D., Maurin, J.C., Schulmann, K., Gebauer, D. 1999. Growth, annealing and recrystallization of zircon and preservation of monazite in high-grade metamorphism: conventional and in-situ U-Pb isotope, cathodoluminescence and microchemical evidence. *Contrib. to Mineral. Petrol.*, **134**:186–201. <https://doi.org/10.1007/s004100050>

Schmitt, R. da S., Trouw, R.A.J., Van Schmus, W.R., Pimentel, M.M. 2004. Late amalgamation in the central part of West Gondwana: new geochronological data and the characterization of a Cambrian collisional orogeny in the Ribeira Belt (SE Brazil). *Precambrian Res.*, **133**:29–61.
<https://doi.org/10.1016/j.precamres.2004.03.010>

Schöll, W.U., Fogaça, A.C.C. 1979. Estratigrafia da Serra do Espinhaço na região de Diamantina. In: Simpósio de Geologia de Minas Gerais. Diamantina, p. 55-73.

Silva, L.C., Armstrong, R., Noce, C.M., Carneiro, M.A., Pimentel, M.M., Pedrosa Soares, A.C., Leite, C.A., Vieira, V.S., Silva, M.A., Paes, V.J.C., Cardoso Filho, J.M. 2002. Reavaliação da evolução geológica em terrenos pré-cambrianos brasileiros com base em novos dados U-Pb SHRIMP, parte II: Orógeno Araçuaí, Cinturão Mineiro e Cráton São Francisco Meridional. *Rev. Bras. Geociências*, **32**:513–528.

Silva, L.C. da, McNaughtonb, N.J., Armstrong, R., Hartmann, L.A., Fletcher, I.R. 2005. The neoproterozoic Mantiqueira Province and its African connections: a zircon-based U – Pb geochronologic subdivision for the Brasiliano / Pan-African systems of orogens. *Precambrian Res.*, **136**:203–240. <https://doi.org/10.1016/j.precamres.2004.10.004>

Silva, L.C. da, Pedrosa Soares, A.C., Armstrong, R., Noce, C.M. 2011. Determinando a duração do período colisional do Orógeno Araçuaí com base em geocronologia U-Pb de alta resolução em zircão: uma contribuição para a história da amalgamação do Gondwana Ocidental. *Geonomos*, **19**:180–197.

Silva, S.L. da, 2000. *Projeto leste: Folha Coronel Fabriciano - SE.23-Z-D-V, escala 1:100.000*. Belo Horizonte, SEME/COMIG/CPRM, 71 p.

Silveira, V.D. 2016. Geologia e geocronologia de zircões detriticos da região de Serro, Serra do Espinhaço Meridional, Minas Gerais, Brasil. Dissertação de Mestrado, Instituto de Geociências, Universidade Federal de Minas Gerais, Belo Horizonte, 45 p.

Silveira Braga, F.C., Rosière, C.A., Queiroga, G.N., Rolim, V.K., Santos, J.O.S., McNaughton, N.J. 2015. The Statherian itabirite-bearing sequence from the Morro Escuro Ridge, Santa Maria de Itabira, Minas Gerais, Brazil. *J. South Am. Earth Sci.*, **58**: 33–53. <https://doi.org/10.1016/j.jsames.2014.12.004>

Silveira Braga, F.C., Rosière, C.A., Santos, J.O.S., Hagemann, S.G., McNaughton, N.J., Salles, P.V., 2019a. The Horto-Baratinha itabirite-hosted iron ore: a basal fragment of the Espinhaço Basin in the eastern São Francisco Craton. *J. South Am. Earth Sci.*, **90**:12–33. <https://doi.org/10.1016/j.jsames.2018.11.013>

Silveira Braga, F.C., Rosière, C.A., Santos, J.O.S., Hagemann, S.G., Salles, P.V. 2019b. Depicting the 3D geometry of ore bodies using implicit lithological modeling: An example from the Horto-Baratinha iron deposit, Guanhães block, MG. *REM - Int. Eng. J.* in press.

Silveira Braga, F.C., Rosière, C.A., Santos, J.O.S., Hagemann, S.G., Salles, P.V. 2018. Análise estrutural de região polideformada baseado em autovetores e modelamento implícito: estudo de caso do depósito de ferro de Horto-Baratinha, leste do Cráton do São Francisco, Brasil. In: Palermo, N., Araújo Jr., H.I. e, Machado, F.B., Corval, A., Valente, S. de C., Dal'bó, P.F. (eds.), *Anais do 49º Congresso Brasileiro de Geologia*. Sociedade Brasileira de Geologia, Rio de Janeiro, p. 1410.

Sláma, J., Košler, J., Pedersen, R.B. 2007. Behaviour of zircon in high-grade metamorphic rocks: evidence from Hf isotopes, trace elements and textural studies. *Contrib. to Mineral. Petrol.*, **154**:335–356.

Spier, C.A., Oliveira, S.B. de, Sial, A.N., Rios, F.J. 2007. Geochemistry and genesis of the banded iron formations of the Cauê Formation, Quadrilátero Ferrífero, Minas Gerais, Brazil. *Precambrian Res.*, **152**:170–206. <https://doi.org/10.1016/j.precamres.2006.10.003>

Stern, R.A. 2001. A New Isotopic and Trace-element Standard for the Ion Microprobe: Preliminary Thermal Ionization Mass Spectrometry (TIMS) U-Pb and Electron-microprobe Data, Radiogenic Age and Isotopic Studies: Report 14. *Geological Survey of Canada*, 11p.

Stewart, M., Lacey, J. de, Hodkiewicz, P.F., Lane, R. 2014. Grade Estimation from Radial Basis Functions – How Does it Compare with Conventional Geostatistical Estimation ? In: 9th International Minning Geology Conference. Adelaide, p. 129–139.

Stipp, M., Stünitz, H., Heilbronner, R., Schmid, S.M. 2002. The eastern Tonale fault zone: a “natural laboratory” for crystal plastic deformation of quartz over a temperature range from 250 to 700 °C. *J. Struct. Geol.*, **24**: 1861–1884.

Taylor, D., Dalstra, H.J., Harding, A.E., Broadbent, G.C., Barley, M.E. 2001. Genesis of high-grade hematite orebodies of the hamersley province, Western Australia-a discussion. *Econ. Geol.*, **96**:837–873. <https://doi.org/10.2113/gsecongeo.97.1.173>

Teixeira, W., Ávila, C.A., Dussin, I.A., Neto, A.V.C., Bongiolo, E.M., Santos, J.O., Barbosa, N.S. 2015. A juvenile accretion episode (2.35 – 2.32 Ga) in the Mineiro belt and its role to the Minas accretionary orogeny : Zircon U – Pb – Hf and geochemical evidences. *Precambrian Res.*, **256**:148–169. <https://doi.org/10.1016/j.precamres.2014.11.009>

Teixeira, J.B.G., Silva, M. da G. da, Misi, A., Cruz, S.C.P., Sá, J.H. da S. 2010. Geotectonic setting and metallogeny of the northern São Francisco craton,. *J. South Am. Earth Sci.*, **30**:71–83.
<https://doi.org/10.1016/j.jsames.2010.02.001>

Teodoro, M.A.M., 2018. *Análises in situ por ablação a laser ICP-MS em óxidos de ferro e estudos mineralógicos, petrográficos e geoquímicos em itabiritos e veios do depósito Serra do Sapo, MG.* Dissertação de Mestrado, Instituto de Geociências, Universidade Federal de Minas Gerais, 100 p.

Thorne, W., Hagemann, S., Vennemann, T., Oliver, N. 2009. Oxygen Isotope compositions of iron Oxides from high-grade BIF-hosted iron ore deposits of the central Hamersley province, Western Australia: Constraints on the evolution of hydrothermal fluids. *Econ. Geol.*, **104**:1019–1035.
<https://doi.org/10.2113/gsecongeo.104.7.1019>

Valley, J.W. 2003. Oxygen Isotopes in Zircon. In: Han-Char, J.M., Hoskin, P.W.O. (eds.), *Rev. Mineral. Geochem. Mineralogical Society of America*, Washington, p. 343–385.
<https://doi.org/10.2113/0530343>

Valley, J.W., Lackey, J.S., Cavosie, A.J., Clechenko, C.C., Spicuzza, M.J., Basei, M.A.S., Bindeman, I.N., Ferreira, V.P., Sial, A.N., King, E.M., Peck, W.H., Sinha, A.K., Wei, C.S. 2005. 4.4 billion years of crustal maturation : oxygen isotope ratios of magmatic zircon. *Contrib Miner. Pet.*, **150**:561–580.
<https://doi.org/10.1007/s00410-005-0025-8>

Van Baalen, M.R. 1993. Titanium mobility in metamorphic systems: a review. *Chem. Geol.*, **110**:233–249. [https://doi.org/10.1016/0009-2541\(93\)90256-I](https://doi.org/10.1016/0009-2541(93)90256-I)

Vavra, G., Gebauer, D., Schmid, R., Compston, W. 1996. Multiple zircon growth and recrystallization during polyphase Late Carboniferous to Triassic metamorphism in granulites of the Ivrea Zone (Southern Alps): an ion microprobe (SHRIMP) study. *Contrib. to Mineral. Petrol.*, **122**:337–358.
<https://doi.org/10.1007/s004100050132>

Viehmann, S., Bau, M., Bühn, B., Dantas, E.L., Andrade, F.R.D., Walde, D.H.G. 2016. Geochemical characterisation of Neoproterozoic marine habitats: Evidence from trace elements and Nd isotopes in the Urucum iron and manganese formations, Brazil. *Precambrian Res.*, **282**:74–96.
<https://doi.org/10.1016/j.precamres.2016.07.006>

Vollgger, S.A., Cruden, A.R., Ailleres, L., Cowan, E.J. 2015. Regional dome evolution and its control on ore-grade distribution: Insights from 3D implicit modelling of the Navachab gold deposit, Namibia. *Ore Geol. Rev.*, **69**:268–284. <https://doi.org/10.1016/j.oregeorev.2015.02.020>

Watson, E.B. 1996. Dissolution, growth and survival of zircons during crustal fusion: kinetic principles, geological models and implications for isotopic inheritance. *Earth Environ. Sci. Trans. R. Soc. Edinburgh*, **87**:43–56. <https://doi.org/10.1017/S0263593300006465>

Woodcock, N.H. 1977. Specification of fabric shapes using an eigenvalue method. *Bull. Geol. Soc. Am.*, **88**:1231–1236. [https://doi.org/10.1130/0016-7606\(1977\)88<1231:SOFSUA>2.0.CO;2](https://doi.org/10.1130/0016-7606(1977)88<1231:SOFSUA>2.0.CO;2)

Woodhead, J.A., Rossman, G.R., Silver, L.T. 1991. The metamictization of zircon: radiation dose-dependent structural characteristics. *Am. Mineral.*, **76**:74–82.

Woodhead, J.D., Hergt, J.M. 2005. A Preliminary Appraisal of Seven Natural Zircon Reference Materials for In Situ Hf Isotope Determination. *Geostand. Geoanalytical Res.*, **29**:183–195. <https://doi.org/10.1111/j.1751-908X.2005.tb00891.x>

Xia, Q.X., Zheng, Y.F., Yuan, H.L., Wu, F.Y. 2009. Contrasting Lu-Hf and U-Th-Pb isotope systematics between metamorphic growth and recrystallization of zircon from eclogite-facies metagranites in the Dabie orogen, China. *Lithos*, **112**:477–496. <https://doi.org/10.1016/j.lithos.2009.04.015>

Xie, L., Zhang, Y., Zhang, H., Sun, J., Wu, F. 2008. In situ simultaneous determination of trace elements, U-Pb and Lu-Hf isotopes in zircon and baddeleyite. *Chinese Sci. Bull.*, **53**:1565–1573. <https://doi.org/10.1007/s11434-008-0086-y>

Yardley, B.W.D. 2004. *Introdução à petrologia metamórfica*. Editora Universidade de Brasília, Brasília, 432 p.

Zhong, S., Feng, C., Seltmann, R., Li, D., Qu, H. 2018. Can magmatic zircon be distinguished from hydrothermal zircon by trace element composition? The effect of mineral inclusions on zircon trace element composition. *Lithos*, **314–315**:646–657. <https://doi.org/10.1016/j.lithos.2018.06.029>

ANEXOS (APPENDICES)

Anexo 1 (Appendix 1) – Geochronological data

- 1A. Gneiss, granite, schist and quartzite from Horto-Baratinha
- 1B. Schist from Cuité
- 1C. Pegmatite from Horto-Baratinha

Anexo 2 (Appendix 2) - Whole-rock geochemical results

Anexo 3 (Appendix 3) - Average detection limits per element of the in situ LA-ICP-MS

Anexo 4 (Appendix 4) - Average and standard deviation of the LA-ICP-MS analysis

Anexo 5 (Appendix 5) - Analytical procedures related to the zircon analysis

- 5A. Sample preparation and imaging
- 5B. Major and trace elements
- 5C. U–Pb geochronology
- 5D. Lu–Hf isotope analysis
- 5E. ^{18}O and ^{16}O isotope analysis
- 5F. References of the analytical procedures

Anexo 6 (Appendix 6) – Analytical results of zircon analysis

- 6A. U-Th-Pb SHRIMP
- 6B. Chemical composition by electronic microprobe
- 6C. Lu-Hf by LA-ICP-MS
- 6D. $\delta^{18}\text{O}$ by SIMS

Anexo 1 (Appendix 1) – Geochronological data

1A. Gneiss, granite, schist and quartzite from Horto-Baratinha

U-Pb-Th SHRIMP data of detrital zircon grains from sample BAR-R54.

Spot	Isotopic ratios												Ages								
	U	Th	^{232}Th	^{206}Pb	$^{206}\text{Pb}^*$	^{208}Pb	error	^{238}U	error	^{207}Pb	error	^{206}Pb	error	^{238}U	error	ρ	$/^{238}\text{U}$	err	$/^{206}\text{Pb}$	err	Disc.
	ppm	ppm	^{238}U	ppm	%	^{232}Th	%	^{206}Pb	%	^{206}Pb	%	^{235}U	%	^{238}U	%	p	1σ	1σ	$/^{206}\text{Pb}$	1σ	%
N17-17G.2-4	51	17	0.34	28	0.04	0.172	2.3	1.6	1.5	0.276	0.7	24.2	1.7	0.64	1.5	0.91	3172	38	3341	11	+6
N17-17G.1-3	175	134	0.79	76	0.05	0.145	1.5	2.0	0.9	0.213	0.4	14.9	1.0	0.51	0.9	0.90	2650	20	2929	7	+12
N17-17G.2-3	258	176	0.70	112	0.02	0.140	1.1	2.0	0.8	0.187	0.4	13.0	0.9	0.51	0.8	0.89	2638	18	2712	7	+3
N17-17G.6-2	35	17	0.50	15	0.00	0.140	2.7	2.0	1.8	0.179	1.1	12.4	2.1	0.50	1.8	0.86	2625	38	2643	18	+1
N17-17G.3-1	131	72	0.57	56	0.03	0.137	1.6	2.0	1.2	0.191	0.6	13.1	1.3	0.50	1.2	0.88	2613	25	2748	11	+6
N17-17G.2-1	50	39	0.80	21	0.00	0.137	2.3	2.0	1.7	0.190	1.0	12.9	2.0	0.50	1.7	0.88	2593	37	2738	16	+6
N17-17G.4-2	149	104	0.72	63	0.00	0.132	1.4	2.0	1.1	0.176	0.6	11.9	1.2	0.49	1.1	0.89	2573	23	2620	9	+2
N17-17G.4-4	182	100	0.57	75	0.06	0.132	1.4	2.1	1.0	0.184	0.7	12.1	1.2	0.48	1.0	0.83	2513	22	2688	11	+8
N17-17G.4-3	242	308	1.32	97	0.00	0.131	1.1	2.1	0.9	0.172	0.5	11.1	1.0	0.47	0.9	0.89	2465	19	2582	8	+5
N17-17G.2-2	83	58	0.72	33	0.20	0.135	1.7	2.2	1.2	0.175	0.8	11.1	1.4	0.46	1.2	0.84	2447	24	2602	13	+7
N17-17G.1-2	241	156	0.67	94	0.07	0.127	1.7	2.2	0.8	0.183	0.4	11.4	0.9	0.45	0.8	0.89	2407	17	2681	7	+12
N17-17G.5-2	130	119	0.94	50	0.02	0.128	2.5	2.2	2.3	0.171	0.6	10.6	2.4	0.45	2.3	0.97	2388	47	2567	10	+8
N17-17G.7-1	172	107	0.64	64	0.04	0.131	1.7	2.3	1.4	0.202	0.5	12.0	1.5	0.43	1.4	0.94	2303	27	2842	9	+22
N17-17G.6-1	300	118	0.41	77	0.05	0.086	1.3	3.4	0.9	0.105	0.7	24.2	1.7	0.64	1.5	0.91	1680	13	1717	13	+2
N17-17G.6-3	153	97	0.65	38	0.24	0.086	1.5	3.5	1.0	0.103	1.1	14.9	1.0	0.51	0.9	0.90	1632	14	1671	20	+3
N17-17G.1-1	1609	7	0.00	120	0.03	0.018	14.4	11.5	1.2	0.059	1.0	4.4	1.1	0.30	0.9	0.73	537	6	570	22	+3
N17-17G.5-3	1823	35	0.02	135	0.03	0.032	5.6	11.6	0.7	0.059	1.1	4.1	1.3	0.29	1.1	0.64	532	4	562	24	+7
N17-17G.4-1	1906	19	0.01	140	0.05	0.037	8.3	11.7	1.2	0.060	1.3	0.7	1.5	0.09	1.2	0.75	528	6	603	29	+17
N17-17G.5-1	1202	6	0.00	88	0.12	0.023	18.0	11.7	1.2	0.058	1.5	0.7	1.3	0.09	0.7	0.55	528	6	521	34	-10
N17-17G.7-2	1723	20	0.01	126	0.10	0.028	9.2	11.8	1.3	0.059	1.4	0.7	1.8	0.09	1.2	0.67	526	6	556	31	+0
N17-17G.3-2	1722	18	0.01	118	0.37	0.084	5.1	12.5	1.2	0.057	1.2	0.7	2.0	0.09	1.2	0.63	496	6	497	26	+0

Notes: Isotopic ratios are in %;

All isotopic ratios are radiogenic component, corrected for common lead;

* ^{206}Pb (%) = percentage of common ^{206}Pb ;

disc. = discordance, as $100 - 100 \{t[^{206}\text{Pb}/^{238}\text{U}]/t[^{207}\text{Pb}/^{206}\text{Pb}]\}$;

Inverse concordia and ^{208}Pb corrected ratios are used for Cambrian zircons, which have very low $^{232}\text{Th}/^{238}\text{U}$ ratios (bold numbers);

Normal concordia and ^{204}Pb ratios are used for Paleoproterozoic zircon.

U-Pb-Th SHRIMP data of detrital zircon grains from sample BAR-R56.

Spot	ppm	ppm	Isotopic ratios												Ages								
			U	Th	^{232}Th	^{206}Pb	$^{206}\text{Pb}^*$	^{208}Pb	error	^{238}U	error	^{207}Pb	error	^{207}Pb	error	^{206}Pb	error	ρ	$/^{238}\text{U}$	1σ	$/^{206}\text{Pb}$	1σ	Disc.
					^{238}U	ppm	%	^{232}Th	%	^{206}Pb	%	^{206}Pb	%	^{235}U	%	^{238}U	%						
N17-25E.7-2	25	29	1.17	0.00	16	0.180	2.9	1.4	2.4	0.302	1.0	30.2	2.6	0.73	2.4	0.93	3516	66	3479	15	-1		
N17-25E.12-1	85	109	1.32	0.04	47	0.170	1.5	1.6	1.2	0.261	0.5	23.2	1.3	0.64	1.2	0.92	3207	30	3252	8	+2		
N17-25E.2-2	75	67	0.91	0.07	39	0.154	3.3	1.7	3.0	0.275	0.5	22.9	3.1	0.61	3.0	0.99	3052	74	3333	8	+11		
N17-25E.8-1	114	64	0.58	0.02	54	0.150	1.7	1.8	1.1	0.205	0.5	15.6	1.2	0.55	1.1	0.89	2833	24	2865	9	+1		
N17-25E.1-1	82	60	0.76	0.05	39	0.153	1.6	1.8	1.2	0.211	0.7	16.0	1.4	0.55	1.2	0.86	2825	27	2913	11	+4		
N17-25E.6-2	122	59	0.50	0.00	56	0.144	1.6	1.9	1.2	0.209	0.6	15.5	1.3	0.54	1.2	0.90	2770	27	2897	9	+5		
N17-25E.1-2	30	9	0.31	0.51	14	0.130	6.2	1.9	1.9	0.198	1.3	14.5	2.3	0.53	1.9	0.84	2749	44	2810	21	+3		
N17-25E.10-3	143	105	0.76	0.09	63	0.138	1.5	2.0	1.0	0.185	0.6	13.0	1.2	0.51	1.0	0.88	2661	22	2695	9	+2		
N17-25E.3-1	100	64	0.67	0.00	43	0.131	1.8	2.0	1.3	0.175	0.6	12.0	1.5	0.50	1.3	0.90	2608	29	2607	11	-0		
N17-25E.10-2	156	65	0.43	0.03	66	0.139	1.4	2.0	0.9	0.188	0.5	12.9	1.1	0.50	0.9	0.89	2592	20	2728	8	+6		
N17-25E.5-2	104	61	0.61	0.02	44	0.136	1.6	2.0	1.1	0.177	0.6	12.0	1.3	0.49	1.1	0.87	2573	24	2627	10	+2		
N17-25E.14-1	139	126	0.94	0.00	57	0.134	1.2	2.1	1.0	0.185	0.5	12.2	1.1	0.48	1.0	0.89	2525	20	2695	8	+8		
N17-25E.4-2	63	61	1.00	0.46	26	0.123	2.0	2.1	1.4	0.183	0.9	12.0	1.6	0.48	1.4	0.83	2519	28	2677	15	+7		
N17-25E.3-2	159	139	0.90	0.03	65	0.131	1.2	2.1	0.9	0.170	1.1	11.2	1.4	0.48	0.9	0.66	2519	20	2556	18	+2		
N17-25E.11-1	144	111	0.80	0.00	58	0.131	1.2	2.1	1.0	0.172	0.5	11.2	1.1	0.47	1.0	0.88	2495	20	2578	9	+4		
N17-25E.4-1	458	230	0.52	0.01	164	0.124	1.8	2.4	1.2	0.174	1.4	10.0	1.8	0.42	1.2	0.65	2252	22	2593	23	+16		
N17-25E.2-3	285	90	0.32	0.00	95	0.111	1.7	2.6	1.4	0.172	0.4	9.2	1.4	0.39	1.4	0.96	2105	25	2578	7	+21		
N17-25E.7-1	242	135	0.58	0.04	62	0.083	1.4	3.3	0.9	0.106	0.7	4.4	1.1	0.30	0.9	0.80	1689	14	1729	13	+3		
N17-25E.5-1	1852	17	0.01	0.21	139	0.001	2219.2	11.4	3.3	0.058	1.2	0.7	3.5	0.09	3.3	0.94	541	17	525	26	-12		
N17-25E.10-1	2304	22	0.01	0.09	167	0.014	35.2	11.8	0.8	0.058	0.5	0.7	0.9	0.08	0.8	0.82	523	4	531	12	-3		
N17-25E.6-3	2286	58	0.03	0.11	166	0.017	22.1	11.8	0.7	0.061	1.0	0.7	1.2	0.08	0.7	0.56	523	4	630	22	+12		
N17-25E.2-1	2689	122	0.05	0.32	192	0.006	38.3	12.0	0.6	0.064	0.6	0.7	0.8	0.08	0.6	0.65	518	3	727	13	+11		

Notes: Isotopic ratios are in %;

All isotopic ratios are radiogenic component, corrected for common lead;

* ^{206}Pb (%) = percentage of common ^{206}Pb ;

disc. = discordance, as $100 - 100 \{t[^{206}\text{Pb}/^{238}\text{U}]/t[^{207}\text{Pb}/^{206}\text{Pb}]\}$;

Inverse concordia and ^{208}Pb corrected ratios are used for Cambrian zircons, which have very low $^{232}\text{Th}/^{238}\text{U}$ ratios (bold numbers);

Normal concordia and ^{204}Pb ratios are used for Paleoproterozoic zircon.

U-Pb-Th SHRIMP data of zircon grains from sample BAR-R49.

Spot	ppm	ppm	Isotopic ratios												Ages									
			U	Th	^{232}Th	^{206}Pb	$^{206}\text{Pb}^*$	^{208}Pb	error	^{238}U	error	^{207}Pb	error	^{207}Pb	error	^{206}Pb	error	ρ	$/^{238}\text{U}$	err	$/^{206}\text{Pb}$	err	$/^{207}\text{Pb}$	err
N17-17B.5-1	739	655	0.91	198	0.02	0.086	1.1	3.2	1.0	0.106	0.4	4.6	1.0	0.31	1.0	0.94	1747	15	1736	7	-1			
N17-17B.3-1	39	22	0.59	10	0.00	0.088	3.1	3.2	2.2	0.105	1.6	4.5	2.7	0.31	2.2	0.82	1744	34	1716	29	-2			
N17-17B.4-2	41	23	0.58	11	0.00	0.087	3.1	3.2	2.2	0.106	1.5	4.5	2.7	0.31	2.2	0.82	1742	33	1724	28	-1			
N17-17B.4-1	400	131	0.34	104	0.01	0.086	1.4	3.3	1.1	0.107	0.5	4.4	1.2	0.30	1.1	0.90	1703	16	1745	9	+3			
N17-17B.3-2	473	153	0.33	122	0.01	0.086	1.4	3.3	1.1	0.106	0.5	4.4	1.2	0.30	1.1	0.92	1688	16	1740	9	+3			
N17-17B.2-1	1066	146	0.14	255	0.01	0.076	1.3	3.6	0.9	0.105	0.3	4.0	1.0	0.28	0.9	0.95	1585	13	1715	6	+9			
N17-17B.4-3	102	54	0.55	22	0.09	0.082	2.2	4.0	1.5	0.103	1.2	3.6	1.9	0.25	1.5	0.80	1451	20	1678	21	+15			
N17-17B.3-3	580	3	0.01	39	0.09	0.005	574.9	12.6	1.3	0.057	1.9	0.6	2.3	0.08	1.3	0.55	492	6	496	42	-3			

Notes: Isotopic ratios are in %;

All isotopic ratios are radiogenic component, corrected for common lead;

* ^{206}Pb (%) = percentage of common ^{206}Pb ;

disc. = discordance, as $100 - 100 \{ [t^{206}\text{Pb}/^{238}\text{U}] / [t^{207}\text{Pb}/^{206}\text{Pb}] \}$;

Inverse concordia and ^{208}Pb corrected ratios are used for Cambrian zircons, which have very low $^{232}\text{Th}/^{238}\text{U}$ ratios (bold numbers);

Normal concordia and ^{204}Pb ratios are used for Paleoproterozoic zircon.

U-Pb-Th SHRIMP data of zircon grains from sample BAR-R63.

Spot	U ppm	Th ppm	Isotopic ratios										Ages								
			^{232}Th	^{206}Pb	$^{206}\text{Pb}^*$	^{208}Pb	error	^{238}U	error	^{207}Pb	error	^{207}Pb	error	^{206}Pb	error	ρ	^{206}Pb $/^{238}\text{U}$	err 1σ	^{207}Pb $/^{206}\text{Pb}$	err 1σ	Disc.
N17-25B.5-1	105	64	0.63	29	0.15	0.089	2.0	3.1	1.3	0.107	1.5	4.7	2.0	0.32	1.3	0.66	1781	20	1745	27	-2
N17-25B.2-3	102	84	0.85	28	0.15	0.088	2.6	3.2	2.2	0.106	1.0	4.6	2.4	0.32	2.2	0.91	1769	34	1731	18	-3
N17-25B.1-2	403	194	0.50	106	0.00	0.089	2.2	3.3	2.1	0.107	0.4	4.5	2.1	0.31	2.1	0.98	1727	31	1742	7	+1
N17-25B.4-1	30	15	0.52	8	1.36	0.072	7.7	3.3	1.9	0.096	3.9	4.0	4.3	0.30	1.9	0.45	1694	29	1542	73	-11
N17-25B.12-2	115	91	0.82	27	0.00	0.057	1.5	3.7	1.0	0.107	0.8	4.0	1.3	0.27	1.0	0.77	1541	14	1748	15	+13
N17-25B.4-2	660	444	0.70	147	0.14	0.072	2.1	3.9	1.9	0.105	0.5	3.7	2.0	0.26	1.9	0.97	1486	25	1712	9	+15
N17-25B.2-2	1333	92	0.07	97	0.48	0.023	9.3	11.8	0.9	0.062	0.7	0.7	1.1	0.08	0.9	0.76	525	5	670	16	+17
N17-25B.2-1	1726	9	0.01	118	0.11	-0.009	128.8	12.6	0.6	0.058	0.7	0.6	0.9	0.08	0.6	0.68	493	3	515	15	-2
N17-25B.1-1	1897	27	0.01	127	0.31	0.026	47.8	12.8	0.6	0.059	1.3	0.6	1.5	0.08	0.6	0.47	484	3	577	29	+17

Notes: Isotopic ratios are in %;

All isotopic ratios are radiogenic component, corrected for common lead;

* ^{206}Pb (%) = percentage of common ^{206}Pb ;

disc. = discordance, as $100 - 100 \{t[^{206}\text{Pb}/^{238}\text{U}]/t[^{207}\text{Pb}/^{206}\text{Pb}]\}$;

Inverse concordia and ^{208}Pb corrected ratios are used for Cambrian zircons, which have very low $^{232}\text{Th}/^{238}\text{U}$ ratios (bold numbers);

Normal concordia and ^{204}Pb ratios are used for Paleoproterozoic zircon.

U-Pb-Th SHRIMP data of zircon grains from sample BAR-R66.

Spot	Isotopic ratios												Ages									
	U	Th	^{232}Th	^{206}Pb	$^{206}\text{Pb}^*$	^{208}Pb	error	^{238}U	error	^{207}Pb	error	^{207}Pb	error	^{206}Pb	error	ρ	$/^{238}\text{U}$	err	$/^{206}\text{Pb}$	err	1σ	Disc.
	ppm	ppm	^{238}U	ppm	%	^{232}Th	%	^{206}Pb	%	^{206}Pb	%	^{235}U	%	^{238}U	%							
N17-17I.8-1	739	272	0.38	326	0.01	0.136	1.2	1.9	1.0	0.187	0.3	13.2	1.0	0.51	1.0	0.97	2669	22	2716	4	+2	
N17-17I.9-1	914	370	0.42	399	0.00	0.136	1.1	2.0	1.0	0.186	0.2	13.0	1.0	0.51	1.0	0.97	2650	21	2708	4	+3	
N17-17I.7-1	887	358	0.42	377	0.00	0.132	1.1	2.0	1.0	0.185	0.2	12.6	1.0	0.50	1.0	0.97	2594	21	2700	4	+5	
N17-17I.1-1	316	149	0.49	130	0.03	0.134	1.5	2.1	1.2	0.183	0.4	12.0	1.3	0.48	1.2	0.94	2514	25	2676	7	+7	
N17-17I.3-1	355	146	0.43	154	0.04	0.133	1.4	2.0	1.2	0.186	0.4	13.0	1.2	0.51	1.2	0.96	2641	25	2708	6	+3	
N17-17I.1-2	1331	160	0.12	418	0.03	0.100	6.2	2.7	1.2	0.151	0.5	7.6	1.3	0.37	1.2	0.92	2010	21	2357	9	+17	
N17-17I.1-3	1871	36	0.02	451	0.04	0.086	8.1	3.6	1.1	0.157	0.5	6.1	1.2	0.28	1.1	0.92	1595	16	2429	8	+39	
N17-17I.5-1	1939	29	0.02	256	0.00	0.073	5.5	6.5	2.7	0.120	3.5	2.5	4.4	0.15	2.7	0.60	919	23	1963	63	+57	
N17-17I.4-1	489	158	0.33	203	0.05	0.135	1.5	2.1	1.2	0.184	0.4	12.3	1.2	0.48	1.2	0.96	2547	24	2687	6	+6	
N17-17I.3-1	461	319	0.71	197	0.01	0.134	0.9	2.0	0.8	0.185	0.3	12.7	0.8	0.50	0.8	0.92	2605	16	2702	5	+4	

Notes: Isotopic ratios are in %;

All isotopic ratios are radiogenic component, corrected for common lead;

* ^{206}Pb (%) = percentage of common ^{206}Pb ;

disc. = discordance, as $100 - 100 \{ [^{206}\text{Pb}/^{238}\text{U}] / [^{207}\text{Pb}/^{206}\text{Pb}] \}$;

Inverse concordia and ^{208}Pb corrected ratios are used for Cambrian zircons, which have very low $^{232}\text{Th}/^{238}\text{U}$ ratios (bold numbers);

Normal concordia and ^{204}Pb ratios are used for Paleoproterozoic zircon.

1B. Schist from Cuité

U-Pb-Th SHRIMP data of detrital zircon grains from sample CUT-R14.

Spot	Isotopic ratios												Ages										
	U	Th	^{232}Th	^{206}Pb	$^{206}\text{Pb}^*$	^{208}Pb	error	^{238}U	error	^{207}Pb	error	^{207}Pb	error	^{206}Pb	error	\square	$/^{238}\text{U}$	^{206}Pb	err	$/^{206}\text{Pb}$	^{207}Pb	err	Disc.
	ppm	ppm	^{238}U	ppm	%	^{232}Th	%	^{206}Pb	%	^{206}Pb	%	^{235}U	%	^{238}U	%		$/^{238}\text{U}$	1σ	$/^{206}\text{Pb}$	1σ	%		
N17-17H.1-3	131	66	0.52	66	0.02	0.156	1.4	1.7	1.0	0.228	0.9	18.4	1.4	0.59	1.0	0.74	2974	25	3040	15	+3		
N17-17H.6-2	171	83	0.50	86	0.06	0.157	1.6	1.7	1.0	0.238	1.2	19.2	1.6	0.59	1.0	0.65	2973	25	3107	19	+5		
N17-25F.1-2	249	136	0.57	67	0.02	0.092	1.5	3.2	1.0	0.106	0.7	4.6	1.3	0.31	1.0	0.80	1754	16	1731	14	-2		
N17-25F.9-1	386	290	0.78	103	0.03	0.090	1.0	3.2	0.7	0.106	0.5	4.5	0.9	0.31	0.7	0.83	1740	11	1726	9	-1		
N17-17H.6-3	66	39	0.61	17	0.00	0.091	2.1	3.2	1.4	0.107	1.2	4.6	1.8	0.31	1.4	0.75	1736	21	1751	22	+1		
N17-17H.3-1	54	32	0.62	14	0.00	0.085	2.9	3.3	1.5	0.105	1.3	4.4	2.0	0.31	1.5	0.75	1720	23	1711	24	-1		
N17-25F.5-1	78	41	0.54	20	0.00	0.090	2.0	3.3	1.3	0.107	1.1	4.5	1.7	0.30	1.3	0.74	1706	19	1751	21	+3		
N17-17H.4-2	172	132	0.79	45	0.06	0.085	1.5	3.3	1.0	0.106	0.9	4.4	1.4	0.30	1.0	0.76	1700	16	1735	16	+2		
N17-17H.4-1	163	101	0.64	42	0.03	0.087	1.6	3.3	1.1	0.107	0.9	4.4	1.4	0.30	1.1	0.76	1696	16	1746	16	+3		
N17-17H.1-2	53	28	0.54	14	0.45	0.090	3.3	3.4	1.5	0.106	1.9	4.3	2.4	0.29	1.5	0.62	1666	22	1739	35	+5		
N17-25F.7-1	189	108	0.59	47	0.13	0.084	1.9	3.4	1.5	0.104	0.8	4.2	1.7	0.29	1.5	0.87	1650	21	1695	15	+3		
N17-25F.8-1	89	51	0.59	22	0.13	0.084	2.3	3.4	1.2	0.105	1.2	4.2	1.7	0.29	1.2	0.71	1649	17	1719	22	+5		
N17-17H.10-1	1614	316	0.20	404	0.01	0.084	1.8	3.4	1.3	0.105	0.5	4.2	1.3	0.29	1.3	0.94	1649	18	1712	8	+4		
N17-17H.9-2	160	100	0.65	40	0.00	0.081	1.6	3.5	1.1	0.105	0.9	4.2	1.4	0.29	1.1	0.78	1636	16	1720	16	+6		
N17-17E.7-3	353	68	0.20	88	0.06	0.082	1.9	3.5	0.8	0.105	0.6	4.2	1.0	0.29	0.8	0.78	1636	12	1715	12	+5		
N17-17H.9-1	262	59	0.23	65	0.06	0.083	2.1	3.5	0.9	0.105	0.8	4.1	1.2	0.29	0.9	0.76	1628	13	1707	14	+5		
N17-17H.5-1	242	127	0.54	60	0.06	0.082	1.5	3.5	0.9	0.105	0.8	4.1	1.2	0.29	0.9	0.77	1625	13	1707	14	+5		
N17-25F.1-1	1371	969	0.73	336	0.00	0.083	0.8	3.5	0.6	0.106	0.3	4.1	0.7	0.29	0.6	0.92	1617	9	1724	5	+7		
N17-25F.3-1	143	48	0.35	35	0.00	0.081	1.7	3.5	1.0	0.105	0.8	4.1	1.3	0.28	1.0	0.76	1614	14	1718	15	+7		
N17-25F.3-2	107	52	0.50	26	0.15	0.083	2.1	3.5	1.1	0.107	1.1	4.2	1.6	0.28	1.1	0.71	1611	16	1756	20	+9		
N17-17H.6-1	1132	17	0.02	80	0.14	-0.001	719.8	12.2	1.5	0.059	1.3	0.7	2.0	0.08	1.5	0.75	510	7	570	28	-3		
N17-17H.1-1	1562	9	0.01	107	0.08	0.003	500.2	12.5	3.5	0.058	1.2	0.6	3.7	0.08	3.5	0.95	497	17	542	26	+4		

Notes: Isotopic ratios are in %;

All isotopic ratios are radiogenic component, corrected for common lead;

* ^{206}Pb (%) = percentage of common ^{206}Pb ;

disc. = discordance, as $100 - 100 \{t[^{206}\text{Pb}/^{238}\text{U}]/t[^{207}\text{Pb}/^{206}\text{Pb}]\}$;

Inverse concordia and ^{208}Pb corrected ratios are used for Cambrian zircons, which have very low $^{232}\text{Th}/^{238}\text{U}$ ratios (bold numbers);

Normal concordia and ^{204}Pb ratios are used for Paleoproterozoic zircon

1C. Pegmatite from Horto-Baratinha

U-Pb-Th SHRIMP data of zircon grains from sample BAR-R36.

Spot	Isotopic ratios												Ages								
	U ppm	Th ppm	^{232}Th ^{238}U	$^{206}\text{Pb}^*$ ppm	%	^{208}Pb ^{232}Th	error	^{238}U ^{206}Pb	error	^{207}Pb ^{206}Pb	error	^{207}Pb ^{235}U	error	^{206}Pb ^{238}U	error	ρ	^{206}Pb $/^{238}\text{U}$	err 1σ	^{207}Pb $/^{206}\text{Pb}$	err 1σ	Disc.
5104.1-1	86	72	0.87	22	0.431	0.0878	1.99	3.2819	1.40	0.10578	1.26	4.4441	1.88	0.3047	1.40	0.741	1715	21	1728	23	+1
5104.1-3	7542	50	0.01	567	0.055	0.0229	24.87	11.4279	1.03	0.05755	0.65	0.6943	1.22	0.0875	1.03	0.847	541	5	513	14	-6
5104.1-4	7588	56	0.01	565	0.042	0.0317	13.62	11.5306	1.43	0.05738	0.60	0.6861	1.55	0.0867	1.43	0.922	536	7	506	13	-6
5104.2-1	672	222	0.34	175	0.040	0.0889	2.07	3.3017	1.85	0.10629	0.34	4.4385	1.88	0.3029	1.85	0.983	1706	28	1737	6	+2
5104.3-1	5775	38	0.01	402	0.054	0.0284	19.93	12.3313	1.64	0.05746	0.62	0.6437	1.77	0.0811	1.64	0.922	503	8	513	15	+2
5104.3-2	6063	40	0.01	427	0.075	0.0235	24.89	12.1879	1.61	0.05719	0.54	0.6462	1.73	0.0820	1.61	0.932	508	8	496	14	-2
5104.3-3	3320	19	0.01	229	0.090	0.0207	38.48	12.4623	1.47	0.05790	0.59	0.6392	1.63	0.0802	1.47	0.903	497	7	522	15	+5
5104.3-4	131	78	0.62	35	0.152	0.0914	2.11	3.1993	1.78	0.10661	0.82	4.5943	1.96	0.3126	1.78	0.909	1753	27	1742	15	-1
5104.3-5	108	55	0.53	27	0.524	0.0835	2.42	3.3964	1.34	0.10613	1.23	4.3083	1.82	0.2944	1.34	0.738	1664	20	1734	22	+5
5104.4-1	5362	33	0.01	376	0.083	0.0231	37.15	12.2382	2.43	0.05731	0.72	0.6449	2.57	0.0817	2.42	0.944	506	12	501	19	-1
5104.4-2	53	28	0.55	13	0.478	0.0856	3.03	3.3912	1.62	0.10737	1.64	4.3655	2.31	0.2949	1.62	0.704	1666	24	1755	30	+6
5104.4-4	5899	38	0.01	412	0.134	0.0078	114.07	12.2868	2.23	0.05675	0.80	0.6369	2.37	0.0814	2.23	0.942	504	11	482	18	-5
5104.4-5	140	89	0.65	38	0.180	0.0912	1.68	3.2009	1.27	0.10742	0.82	4.6271	1.51	0.3124	1.27	0.841	1753	19	1756	15	0
5104.4-6	139	72	0.54	37	0.241	0.0897	2.21	3.2482	1.78	0.10729	0.85	4.5540	1.97	0.3079	1.78	0.902	1730	27	1754	16	+2
5104.7-1	3484	24	0.01	272	0.000	0.0368	3.70	10.9860	1.04	0.05694	0.49	0.7147	1.15	0.0910	1.04	0.906	562	6	489	11	-15

Notes: Isotopic ratios are in %;

All isotopic ratios are radiogenic component, corrected for common lead;

* ^{206}Pb (%) = percentage of common ^{206}Pb ;

disc. = discordance, as $100 - 100 \{ [^{206}\text{Pb}/^{238}\text{U}] / [^{207}\text{Pb}/^{206}\text{Pb}] \}$;

Inverse concordia and ^{208}Pb corrected ratios are used for Cambrian zircons, which have very low $^{232}\text{Th}/^{238}\text{U}$ ratios (bold numbers);

Normal concordia and ^{204}Pb ratios are used for Paleoproterozoic zircon (italic numbers);

$^{207}\text{Pb}/^{206}\text{Pb}$ ages are used for three analyses with Pb/U ratios affected by disturbance in conductivity during analyses (bold and italic numbers).

U-Pb-Th SHRIMP data of zircon grains from sample BAR-R12.

Spot	U ppm	Th ppm	Isotopic ratios												Ages						
			^{232}Th	^{206}Pb	$^{206}\text{Pb}^*$	^{208}Pb	error	^{238}U	error	^{207}Pb	error	^{207}Pb	error	^{206}Pb	err	^{207}Pb	err	^{206}Pb	Disc.		
			^{238}U	ppm	%	^{232}Th	%	^{206}Pb	%	^{206}Pb	%	^{235}U	%	^{238}U	%	ρ	$/^{238}\text{U}$	1σ	$/^{206}\text{Pb}$	1σ	%
N17-25C.1-3	3315	104	0.03	248	0.05	0.022	9.1	11.5	1.1	0.059	0.9	0.7	1.4	0.09	1.1	0.78	539	6	564	19	-1
N17-25C.1-2	3716	154	0.04	281	0.03	0.025	4.3	11.3	0.6	0.058	0.7	0.7	1.0	0.09	0.6	0.64	545	3	548	16	-2
N17-25C.1-1	4523	159	0.04	350	0.01	0.026	3.6	11.1	0.9	0.058	0.7	0.7	1.1	0.09	0.9	0.80	557	5	516	15	-10
N17-25C.2-1	4342	139	0.03	312	0.07	0.021	10.1	11.9	0.6	0.059	0.8	0.7	0.9	0.08	0.6	0.60	518	3	551	17	+1

Notes: Isotopic ratios are in %;

All isotopic ratios are radiogenic component, corrected for common lead;

* ^{206}Pb (%) = percentage of common ^{206}Pb ;

disc. = discordance, as $100 - 100 \{t[^{206}\text{Pb}/^{238}\text{U}]/t[^{207}\text{Pb}/^{206}\text{Pb}]\}$;

Inverse concordia and ^{208}Pb corrected ratios are used for Cambrian zircons, which have very low $^{232}\text{Th}/^{238}\text{U}$ ratios (bold numbers);

Normal concordia and ^{204}Pb ratios are used for Paleoproterozoic zircon.

Anexo 2 (Appendix 2) - Whole-rock geochemical results

Data	Unit	DL	B-R28	B-S48	B-S40	B-S44	B-S46	B-S31	B-S42	B-S47	B-S34	B-S27	B-S28	B-R27	C-R03	C-R04	B-S11	B-R31	B-R26
SiO₂	%	0.01	37.42	44.13	24.34	18.05	26.28	1.16	0.59	1.99	1.08	0.97	1.80	2.34	0.19	0.42	3.22	2.62	1.58
Al₂O₃	%	0.01	0.08	1.37	0.30	0.73	0.42	0.58	0.24	0.80	0.67	0.72	1.00	1.29	0.43	0.09	1.54	1.53	0.71
Fe₂O₃	%	0.04	62.20	46.39	74.54	79.73	71.84	95.45	96.41	94.78	95.98	97.08	96.07	92.42	99.31	98.51	90.91	92.16	88.38
MgO	%	0.01	0.04	4.81	0.11	1.03	0.56	0.85	0.11	1.02	0.84	0.09	0.24	1.94	0.02	0.27	1.71	2.25	2.84
CaO	%	0.01	0.03	1.93	0.24	0.18	0.31	0.84	1.36	0.52	0.56	0.51	0.11	0.61	0.04	0.02	0.69	0.31	3.11
Na₂O	%	0.01	<0.01	0.08	0.03	0.02	0.01	<0.01	0.02	<0.01	<0.01	0.02	<0.01	<0.01	<0.01	<0.01	0.02	<0.01	<0.01
K₂O	%	0.01	<0.01	0.04	0.05	<0.01	0.06	<0.01	0.01	<0.01	<0.01	0.02	0.13	0.02	<0.01	<0.01	0.57	<0.01	0.11
TiO₂	%	0.01	<0.01	0.05	0.09	<0.01	0.02	0.03	0.02	0.04	0.03	0.11	0.16	0.07	0.01	<0.01	0.13	0.08	0.04
P₂O₅	%	0.01	<0.01	0.13	0.13	0.07	0.15	0.35	0.20	0.31	0.30	0.29	<0.01	0.31	<0.01	0.06	0.44	0.15	1.16
MnO	%	0.01	0.02	0.21	0.05	0.05	0.10	0.09	0.13	0.04	0.06	0.03	0.03	0.06	0.02	0.07	0.07	0.14	0.82
Cr₂O₃	%	0.002	0.002	0.004	0.002	0.003	0.003	0.008	0.003	0.056	0.005	<0.002	0.004	0.004	0.003	0.004	0.004	0.005	0.007
Ba	ppm	1	8	191	15	2	3	4	6	2	4	4	4	4	16	4	22	4	15
Ni	ppm	20	<20	<20	<20	<20	<20	<20	<20	<20	<20	<20	<20	40	<20	<20	<20	21	43
Sc	ppm	1	<1	3	2	1	2	2	2	2	2	2	11	2	2	2	7	3	3
LOI	%	-5.1	0.2	0.7	0.1	0.1	0.2	0.6	0.9	0.4	0.4	0.1	0.3	0.9	0.0	0.5	0.6	0.7	1.1
Sum	%	0.01	99.99	99.91	99.98	99.95	99.97	99.95	99.96	99.95	99.95	99.94	99.84	99.94	99.98	99.97	99.86	99.93	99.90
Be	ppm	1	<1	2	<1	<1	1	4	<1	<1	1	2	<1	<1	<1	<1	2	<1	<1
Co	ppm	0.2	0.5	6.6	1.5	5.3	3.5	4.1	2.1	4.7	3.2	0.6	1.5	9.3	0.6	2.1	5.4	9.4	7.2
Cs	ppm	0.1	<0.1	0.3	<0.1	<0.1	0.3	<0.1	<0.1	<0.1	<0.1	1.1	0.8	<0.1	<0.1	<0.1	2.3	<0.1	0.6
Ga	ppm	0.5	<0.5	1.8	2.5	<0.5	1.1	<0.5	<0.5	<0.5	<0.5	8.9	53.7	1.9	<0.5	<0.5	33.4	2.3	<0.5
Hf	ppm	0.1	<0.1	0.6	0.2	<0.1	0.1	0.2	0.2	0.3	0.3	0.9	3.0	0.6	0.1	<0.1	1.8	0.9	0.2
Nb	ppm	0.1	0.2	1.3	16.5	0.4	0.9	0.6	1.9	0.9	0.7	102.1	566.4	1.0	0.5	0.3	288.0	1.5	1.0

continued

Data	Unit	DL	B-R28	B-S48	B-S40	B-S44	B-S46	B-S31	B-S42	B-S47	B-S34	B-S27	B-S28	B-R27	C-R03	C-R04	B-S11	B-R31	B-R26
Rb	ppm	0.1	<0.1	1.2	1.9	<0.1	4.6	<0.1	0.5	<0.1	<0.1	0.6	9.7	0.3	<0.1	<0.1	55.0	<0.1	7.3
Sn	ppm	1	1	5	28	7	2	2	6	<1	1	76	197	2	<1	<1	119	<1	98
Sr	ppm	0.5	0.5	19.1	7.5	3.8	4.9	8.1	8.9	6.6	6.4	1.4	0.6	6.6	3.5	0.8	2.3	3.6	16.3
Ta	ppm	0.1	<0.1	<0.1	1.6	<0.1	<0.1	<0.1	0.2	<0.1	<0.1	6.9	38.2	<0.1	<0.1	<0.1	23.9	0.1	<0.1
Th	ppm	0.2	<0.2	1.5	<0.2	<0.2	<0.2	0.6	<0.2	0.6	0.7	0.4	<0.2	1.0	0.2	<0.2	0.3	1.8	0.5
U	ppm	0.1	0.7	3.2	2.8	1.0	4.9	4.4	4.0	2.1	1.7	2.3	1.7	3.1	2.0	11.6	3.7	1.4	4.2
V	ppm	8	<8	47	<8	22	66	99	71	47	37	45	135	62	30	43	35	8	105
W	ppm	0.5	5.1	1.9	6.6	2.1	6.5	3.5	7.0	6.4	5.1	6.1	7.4	1.9	5.5	3.1	6.1	4.2	5.9
Zr	ppm	0.1	2.4	28.0	8.1	3.5	14.6	11.3	21.8	14.7	12.8	32.1	78.2	34.6	6.7	5.9	37.6	38.0	25.3
Y	ppm	0.1	6.7	8.5	7.1	42.4	7.9	12.7	11.2	13.2	21.7	22.3	7.3	10.2	1.6	5.6	36.0	7.6	21.0
La	ppm	0.1	1.5	2.4	2.2	0.7	2.0	3.3	2.6	2.8	2.7	1.8	1.8	2.2	5.8	2.7	2.5	2.9	4.9
Ce	ppm	0.1	2.4	5.6	3.9	1.3	3.2	3.9	7.5	3.6	3.8	3.2	2.7	4.4	9.9	3.2	5.5	4.3	10.0
Pr	ppm	0.02	0.37	0.81	0.54	0.20	0.51	0.56	0.93	0.60	0.54	0.38	0.35	0.73	1.45	0.39	0.93	0.61	1.56
Nd	ppm	0.3	1.6	3.9	2.7	1.1	2.4	2.8	4.6	3.1	2.6	1.6	1.5	3.8	5.9	1.7	5.1	3.1	8.3
Sm	ppm	0.05	0.46	1.13	0.73	1.32	0.73	0.88	1.37	0.80	0.98	0.70	0.59	1.15	1.04	0.37	2.54	1.00	2.55
Eu	ppm	0.02	0.17	0.34	0.19	0.53	0.18	0.36	0.31	0.35	0.42	0.20	0.09	0.32	0.26	0.14	0.38	0.40	0.71
Gd	ppm	0.05	0.78	1.11	0.82	3.98	0.94	1.41	1.46	1.43	1.96	1.40	0.87	1.26	0.74	0.49	3.97	1.24	2.59
Tb	ppm	0.01	0.12	0.15	0.12	0.72	0.13	0.23	0.21	0.21	0.33	0.33	0.17	0.17	0.08	0.07	0.82	0.19	0.35
Dy	ppm	0.05	0.72	0.95	0.75	4.57	0.81	1.52	1.26	1.40	2.38	2.36	1.13	1.14	0.38	0.47	5.20	1.10	2.23
Ho	ppm	0.02	0.16	0.24	0.19	1.11	0.19	0.35	0.28	0.35	0.61	0.63	0.26	0.27	0.05	0.12	1.11	0.24	0.53
Er	ppm	0.03	0.48	0.77	0.56	3.24	0.66	1.02	0.98	1.03	1.79	1.91	0.74	0.80	0.15	0.44	3.20	0.71	1.74

continued

Data	Unit	DL	B-R28	B-S48	B-S40	B-S44	B-S46	B-S31	B-S42	B-S47	B-S34	B-S27	B-S28	B-R27	C-R03	C-R04	B-S11	B-R31	B-R26
Tm	ppm	0.01	0.07	0.12	0.08	0.44	0.10	0.14	0.14	0.14	0.26	0.28	0.11	0.11	0.02	0.08	0.42	0.10	0.25
Yb	ppm	0.05	0.44	0.79	0.55	2.61	0.74	1.02	0.93	0.96	1.57	2.01	0.68	0.78	0.10	0.49	2.56	0.71	1.74
Lu	ppm	0.01	0.07	0.12	0.10	0.40	0.13	0.17	0.16	0.16	0.27	0.33	0.09	0.14	0.01	0.08	0.37	0.12	0.30
Mo	ppm	0.1	0.8	0.6	0.6	0.7	0.5	0.5	1.0	0.4	0.5	0.7	0.2	0.4	0.8	3.8	0.2	0.5	0.4
Cu	ppm	0.1	2.4	3.5	1.8	2.5	4.0	2.4	4.6	3.0	2.7	5.1	2.1	2.1	2.7	3.2	4.4	2.3	2.3
Pb	ppm	0.1	1.1	2.0	1.8	0.7	1.0	2.2	3.5	1.5	1.5	1.7	0.9	1.6	1.6	3.7	4.4	1.6	4.3
Zn	ppm	1	3	12	8	4	13	21	12	16	14	5	18	25	2	4	74	44	47
Ni	ppm	0.1	1.4	8.4	4.9	2.5	9.1	10.6	16.6	8.4	8.5	3.8	6.3	35.6	0.4	4.4	17.2	19.9	38.8
As	ppm	0.5	0.7	2.8	1.1	1.7	1.6	19.5	18.5	12.7	17.1	14.9	1.6	11.7	1.9	6.3	15.5	9.9	68.4
Cd	ppm	0.1	<0.1	<0.1	<0.1	<0.1	<0.1	<0.1	<0.1	<0.1	<0.1	<0.1	<0.1	<0.1	<0.1	<0.1	<0.1	<0.1	<0.1
Sb	ppm	0.1	1.6	0.6	1.9	1.6	2.5	2.5	4.0	1.4	2.9	3.4	2.1	1.1	4.0	0.2	2.5	1.7	2.3
Bi	ppm	0.1	<0.1	0.2	0.1	<0.1	<0.1	<0.1	0.2	<0.1	<0.1	<0.1	<0.1	0.2	<0.1	0.2	<0.1	<0.1	0.2
Ag	ppm	0.1	<0.1	<0.1	<0.1	<0.1	<0.1	<0.1	<0.1	<0.1	<0.1	<0.1	<0.1	<0.1	<0.1	<0.1	<0.1	<0.1	<0.1
Au	ppb	0.5	<0.5	<0.5	<0.5	<0.5	<0.5	<0.5	<0.5	<0.5	<0.5	0.7	0.9	3.8	<0.5	<0.5	1.2	0.7	<0.5
Hg	ppm	0.01	<0.01	<0.01	<0.01	<0.01	<0.01	<0.01	<0.01	<0.01	<0.01	<0.01	<0.01	<0.01	<0.01	<0.01	<0.01	<0.01	<0.01
Tl	ppm	0.1	<0.1	<0.1	<0.1	<0.1	<0.1	<0.1	<0.1	<0.1	<0.1	<0.1	<0.1	<0.1	<0.1	<0.1	0.4	<0.1	<0.1
Se	ppm	0.5	<0.5	<0.5	<0.5	<0.5	<0.5	<0.5	<0.5	<0.5	<0.5	<0.5	<0.5	<0.5	<0.5	<0.5	<0.5	<0.5	<0.5
Σ ETR	ppm	-	16.04	26.93	20.53	64.62	20.62	30.36	33.93	30.13	41.91	39.43	18.38	27.47	27.48	16.34	70.6	24.32	58.75
Y/Ho	-	-	41.88	35.42	37.37	38.20	41.58	36.29	40.00	37.71	35.57	35.40	28.08	37.78	32.00	46.67	32.43	31.67	39.62
^a La/Yb _(SN)	-	-	0.25	0.22	0.30	0.02	0.20	0.24	0.21	0.22	0.13	0.07	0.20	0.21	4.28	0.41	0.07	0.30	0.21
^b Ce/Ce* _(SN)	-	-	0.74	0.91	0.83	0.80	0.73	0.65	1.09	0.64	0.72	0.89	0.78	0.79	0.79	0.70	0.81	0.75	0.82
^c Eu/Eu* _(SN)	-	-	1.49	1.59	1.28	1.06	1.17	1.64	1.14	1.75	1.51	0.83	0.58	1.42	1.53	1.76	0.54	1.85	1.45
^d Pr/Pr* _(SN)	-	-	1.08	0.99	0.95	0.93	1.04	0.96	0.92	0.99	0.98	0.98	1.01	0.99	1.10	0.98	0.96	0.95	0.95
^e Pr/Yb _(SN)	-	-	0.27	0.33	0.31	0.02	0.22	0.18	0.32	0.20	0.11	0.06	0.16	0.30	4.63	0.25	0.12	0.27	0.29
^f Y/Y* _(SN)	-	-	0.41	1.41	1.49	1.50	1.60	1.39	1.50	1.50	1.43	1.45	1.07	1.46	0.90	1.87	1.20	1.18	1.54

Notes

^{a b c d e f} PAAS normalization values based on McLennan (1989);

^bCe/Ce*_(SN)=Ce_(SN)/0.5La_(SN)+0.5Pr_(SN); ^cEu/Eu*_(SN)=Eu_(SN)/(0.66Sm_(SN)+0.33Tb_(SN)); ^dPr/Pr*_(SN)=Pr_(SN)/0.5Ce_(SN)+0.5Nd_(SN); ^fY/Y*_(SN)=Y_(SN)/0.5Dy_(SN)+0.5Ho_(SN)

Anexo 3 (Appendix 3) - Average detection limits per element of the in situ LA-ICP-MS

Element	Abundance (ppm)	Element	Abundance (ppm)
O	29.530	Ce140	0.001
Li7	0.956	Nd146	0.005
Na23	3.682	Sm147	0.009
Mg24	0.033	Eu153	0.002
Al27	0.307	Gd157	0.005
Si29	123.082	Dy163	0.003
P31	13.788	Er166	0.003
S34	0.193	Yb172	0.005
Ca43	81.450	Lu175	0.001
Sc45	0.089	Hf178	0.004
Ti47	0.386	Ta181	0.001
Ti49	0.576	W182	0.005
V51	0.040	Au197	0.003
Cr53	0.488	Pb206	0.017
Mn55	0.318	Pb207	0.017
Fe57	11.264	Pb208	0.015
Co59	0.008	Bi209	0.004
Ni60	0.021	Th232	0.001
Cu63	0.164	U238	0.001
Cu65	0.223		
Zn66	0.210		
Ga69	0.019		
Ga71	0.008		
As75	0.241		
Sr88	0.002		
Y89	0.002		
Zr90	0.003		
Nb93	0.002		
Mo95	0.011		
Mo98	0.006		
Ag107	0.022		
Sn118	0.101		
Sb121	0.034		
Cs133	0.008		
Ba137	0.010		
La139	0.001		

Note: Laser beam size and pulse frequency were 30 µm and 5 Hz, with laser energy of 5.5 J/cm²

Anexo 4 (Appendix 4) - Average and standard deviation of the LA-ICP-MS analysis

Granular hematite

Lithotype	Iron ore (HBD)		Iron ore (CTE)		Itabirite (HBD)		Pegmatite (HBD)	
n	28		9		16		9	
Elements	Average	SD	Average	SD	Average	SD	Average	SD
O	30.180	0.042	30.139	0.020	30.079	0.004	30.239	0.010
Li7	-	-	-	-	-	-	-	-
Na23	-	-	-	-	9.794	-	-	-
Mg24	47.988	22.754	7.723	4.611	1.460	0.806	57.929	16.069
Al27	2689.780	529.658	2440.320	582.591	610.794	37.493	3103.247	365.413
Si29	267.861	67.873	213.378	45.370	259.254	49.546	204.950	38.036
P31	17.892	2.886	12.294	-	14.892	2.367	17.095	-
S34	0.569	0.132	0.377	0.116	0.567	0.106	0.463	0.096
Ca43	-	-	-	-	-	-	-	-
Sc45	5.667	4.127	0.682	0.081	0.447	0.082	5.128	0.363
Ti47	2374.725	2186.405	226.403	139.354	27.486	23.171	5332.945	336.727
Ti49	2369.640	2184.941	228.867	138.436	26.736	23.185	5293.413	290.635
V51	63.335	15.984	52.168	3.152	19.090	1.000	40.298	1.797
Cr53	22.665	32.996	22.406	9.284	3.968	2.290	5.004	1.582
Mn55	142.604	114.736	29.322	11.584	21.577	5.536	409.516	23.618
Fe57	692153.750	3458.799	695617.376	880.948	698246.786	120.348	688097.866	475.106
Co59	1.424	1.333	0.106	0.059	0.070	0.030	4.020	0.252
Ni60	3.100	2.979	0.325	0.152	0.130	0.085	12.944	0.804
Cu63	-	-	-	-	0.162	-	-	-
Cu65	-	-	-	-	-	-	0.193	-
Zn66	10.271	10.633	0.313	0.080	0.325	0.075	15.463	3.241
Ga69	12.844	11.509	0.893	0.292	0.357	0.039	11.968	1.036
Ga71	14.672	13.139	0.990	0.347	0.410	0.038	13.686	1.419
As75	0.779	0.219	1.331	0.510	1.410	0.419	0.296	-
Sr88	0.014	0.036	0.006	-	0.025	0.044	0.003	0.001
Y89	0.033	0.099	0.008	0.007	0.004	0.002	0.010	0.010
Zr90	34.988	8.175	13.744	3.474	3.299	1.318	20.098	1.611
Nb93	140.519	158.076	0.328	0.096	0.161	0.045	87.329	16.267
Mo95	1.015	0.891	5.254	1.573	3.000	0.306	0.431	0.058
Mo98	0.994	0.854	5.149	1.551	3.027	0.237	0.446	0.045
Ag107	0.030	-	-	-	0.020	-	-	-
Sn118	219.339	240.522	0.305	0.054	1.929	0.457	204.790	34.325
Sb121	7.244	4.412	1.004	0.382	10.345	1.694	2.710	1.044
Cs133	-	-	-	-	-	-	-	-

continued

Lithotype	Iron ore (HBD)		Iron ore (CTE)		Itabirite (HBD)		Pegmatite (HBD)	
n	28		9		16		9	
Elements	Average	SD	Average	SD	Average	SD	Average	SD
Ba137	0.057	0.102	0.158	0.236	0.027	0.028	0.009	-
La139	0.007	0.010	0.002	0.001	0.002	0.001	0.002	0.001
Ce140	0.019	0.029	0.010	0.010	0.002	0.001	0.004	0.005
Nd146	0.020	0.023	0.005	-	0.008	0.005	0.011	0.006
Sm147	0.012	0.012	0.016	-	0.016	0.007	0.021	0.016
Eu153	0.003	0.002	0.004	0.003	0.002	0.001	0.003	0.002
Gd157	0.020	0.018	0.007	-	0.014	0.011	0.019	0.015
Dy163	0.012	0.010	0.008	0.005	0.007	0.004	0.006	0.003
Er166	0.011	0.010	0.009	-	0.006	0.002	0.006	0.003
Yb172	0.043	0.023	0.030	0.017	0.014	0.007	0.023	0.018
Lu175	0.013	0.008	0.010	0.005	0.003	0.003	0.018	0.014
Hf178	1.558	1.028	0.106	0.040	0.041	0.028	1.291	0.115
Ta181	28.778	31.577	0.012	0.007	0.006	0.003	17.207	1.674
W182	2.125	2.215	2.938	1.204	7.792	0.412	0.461	0.090
Au197	0.021	0.007	-	-	0.004	0.001	0.007	0.003
Pb206	0.133	0.130	0.331	0.291	0.350	0.211	0.079	0.083
Pb207	0.061	0.072	0.065	0.077	0.046	0.024	0.092	0.101
Pb208	0.088	0.116	0.236	-	0.027	0.019	0.106	0.126
Bi209	0.009	0.005	0.007	0.003	0.025	0.038	0.019	0.018
Th232	0.010	0.009	-	-	0.002	-	0.013	0.019
U238	0.155	0.214	0.750	0.650	0.874	0.598	0.027	0.057

Lamellar hematite

Lithotype	Iron ore (HBD)		Iron ore (CTE)		Itabirite (HBD)		Pegmatite (HBD)	
n	10		6		29		13	
Elements	Average	SD	Average	SD	Average	SD	Average	SD
O	30.190	0.033	30.134	0.017	30.080	0.004	30.263	0.019
Li7	-	-	-	-	-	-	-	-
Na23	-	-	-	-	3.696	-	-	-
Mg24	56.211	17.531	5.120	1.705	2.076	0.830	75.922	25.890
Al27	2642.776	287.194	2369.373	570.586	640.743	49.788	2820.001	610.050
Si29	266.294	40.165	193.369	56.408	246.762	40.131	196.637	32.986
P31	32.375	-	-	-	13.785	-	15.418	1.580
S34	0.655	0.127	0.379	0.136	0.549	0.068	0.472	0.116
Ca43	-	-	-	-	-	-	-	-
Sc45	7.250	3.550	0.671	0.038	0.503	0.106	6.937	0.699
Ti47	3177.218	1875.988	170.361	125.612	58.093	44.617	7311.452	522.292
Ti49	3179.381	1873.295	168.526	118.912	57.950	44.702	7302.030	501.512
V51	61.117	11.306	54.785	3.339	18.328	1.576	36.931	1.984
Cr53	75.012	48.489	18.950	10.183	2.699	1.817	2.706	2.366
Mn55	195.228	84.703	21.332	2.353	25.330	3.218	517.357	41.478
Fe57	691080.493	2798.060	695832.367	775.827	698182.941	140.136	686029.602	890.671
Co59	1.932	0.978	0.077	0.043	0.053	0.019	5.295	0.370
Ni60	3.941	2.343	0.205	0.089	0.158	0.106	16.014	1.253
Cu63	-	-	-	-	-	-	-	-
Cu65	-	-	-	-	-	-	0.333	0.164
Zn66	15.210	7.935	0.228	-	0.440	0.507	22.347	5.677
Ga69	18.160	10.696	0.827	0.268	0.374	0.043	14.303	0.652
Ga71	20.521	11.985	0.960	0.306	0.415	0.048	16.107	0.843
As75	1.110	1.098	1.623	0.585	1.760	0.370	0.246	0.039
Sr88	0.008	0.007	0.002	-	0.003	0.001	0.005	0.003
Y89	0.120	0.344	0.008	0.005	0.021	0.059	0.006	0.004
Zr90	37.181	4.100	12.353	3.985	4.024	1.575	21.351	1.163
Nb93	185.066	127.154	0.303	0.117	0.198	0.052	90.477	7.346
Mo95	0.820	1.048	5.847	1.245	2.800	0.354	0.358	0.072
Mo98	0.788	1.024	6.053	1.456	2.843	0.284	0.354	0.040
Ag107	0.031	0.015	-	-	-	-	0.014	0.006
Sn118	278.158	192.032	0.337	0.068	1.344	0.392	175.467	39.645
Sb121	5.504	5.084	1.124	0.241	12.164	1.251	1.428	0.203
Cs133	0.017	-	-	-	0.007	-	0.011	-
Ba137	0.082	0.146	0.037	0.013	0.014	0.008	0.014	0.010

continued

Lithotype	Iron ore (HBD)		Iron ore (CTE)		Itabirite (HBD)		Pegmatite (HBD)	
n	10		6		29		13	
Elements	Average	SD	Average	SD	Average	SD	Average	SD
La139	0.028	0.061	0.001	-	0.004	0.004	0.002	0.001
Ce140	0.194	0.270	0.005	0.005	0.009	0.022	0.008	0.012
Nd146	0.033	0.051	0.016	-	0.012	0.012	0.010	0.011
Sm147	0.073	0.029	0.015	-	0.014	0.001	0.012	0.010
Eu153	0.011	0.020	0.002	-	0.003	0.002	0.007	0.002
Gd157	0.012	0.007	0.006	-	0.015	0.012	0.031	0.030
Dy163	0.024	0.029	0.007	0.004	0.007	0.011	0.009	0.003
Er166	0.023	0.045	0.006	0.003	0.009	0.014	0.006	0.003
Yb172	0.063	0.050	0.022	0.013	0.018	0.014	0.030	0.023
Lu175	0.022	0.014	0.007	0.003	0.009	0.007	0.012	0.007
Hf178	1.988	0.700	0.083	0.046	0.056	0.033	1.498	0.122
Ta181	40.028	27.689	0.010	0.006	0.009	0.006	23.027	4.040
W182	2.084	2.589	3.480	1.175	7.862	0.751	0.317	0.144
Au197	0.020	0.005	-	-	0.003	-	0.007	0.003
Pb206	0.734	0.778	0.506	0.290	0.475	0.266	0.119	0.097
Pb207	0.238	0.359	0.051	0.015	0.053	0.058	0.085	0.125
Pb208	0.480	0.178	-	-	0.308	-	0.074	0.101
Bi209	0.042	0.006	-	-	0.005	0.002	0.029	-
Th232	0.005	0.005	0.002	-	0.004	0.004	0.009	0.011
U238	0.305	0.463	1.415	0.868	1.246	0.556	0.027	0.043

(keno)Magnetite

Lithotype	Iron ore (HBD)		Iron ore (CTE)		Itabirite (HBD)		Pegmatite (HBD)	
n	20		6		5		13	
Elements	Average	SD	Average	SD	Average	SD	Average	SD
O	27.630	0.061	27.726	0.005	27.645	0.002	27.711	0.014
Li7	6.613	1.325	8.654	0.303	4.829	0.735	-	-
Na23	-	-	-	-	-	-	-	-
Mg24	3246.936	1652.791	2963.398	115.505	69.995	11.330	15.718	5.316
Al27	111.528	64.711	401.434	13.354	191.176	69.091	1287.212	307.442
Si29	268.897	82.693	258.601	74.054	287.472	28.149	284.627	56.528
P31	28.551	34.557	-	-	-	-	16.969	-
S34	0.702	0.115	0.553	0.135	0.690	0.126	0.395	0.075
Ca43	-	-	-	-	-	-	-	-
Sc45	0.521	0.164	0.380	0.049	0.126	-	1.409	0.353
Ti47	13.852	21.871	6.716	0.729	0.720	0.217	491.166	254.018
Ti49	13.172	21.746	7.121	0.709	1.011	0.124	487.848	252.888
V51	35.406	14.539	67.681	1.927	6.094	0.295	316.734	7.139
Cr53	11.604	5.167	10.293	0.723	2.303	0.201	176.351	45.808
Mn55	12509.511	3965.464	591.192	22.761	1534.197	200.337	568.111	74.965
Fe57	706015.917	1577.987	718410.825	225.396	720234.610	394.243	719481.366	546.903
Co59	137.574	41.024	2.232	0.097	84.305	0.903	33.609	1.447
Ni60	408.880	258.621	6.209	0.502	651.923	7.790	75.872	2.453
Cu63	0.529	-	-	-	-	-	-	-
Cu65	-	-	-	-	-	-	0.343	-
Zn66	918.584	78.871	9.304	4.856	484.974	92.304	41.738	19.615
Ga69	6.751	1.874	0.418	0.030	1.125	0.060	128.009	15.891
Ga71	7.660	2.116	0.478	0.044	1.281	0.048	145.102	19.228
As75	1.222	2.475	0.297	0.090	-	-	-	-
Sr88	0.015	0.021	0.002	-	0.003	0.002	0.005	0.003
Y89	1.072	2.814	0.004	0.005	0.003	0.002	0.007	0.008
Zr90	0.007	0.004	0.008	0.006	0.004	-	0.011	0.002
Nb93	0.003	0.002	0.006	-	0.002	-	0.007	0.003
Mo95	0.165	0.074	1.231	0.088	0.068	0.045	0.166	0.055
Mo98	0.046	0.040	1.185	0.071	0.046	0.016	0.196	0.036
Ag107	0.020	0.003	-	-	0.033	-	0.019	-
Sn118	0.367	0.101	0.607	0.196	0.373	0.044	11.218	4.686
Sb121	0.041	-	-	-	-	-	0.071	-
Cs133	0.010	-	-	-	-	-	-	-
Ba137	0.321	0.783	0.011	-	0.025	0.010	0.015	0.010

continued

Lithotype	Iron ore (HBD)		Iron ore (CTE)		Itabirite (HBD)		Pegmatite (HBD)	
n	20		6		5		13	
La139	0.170	0.503	0.004	0.003	-	-	0.008	0.008
Ce140	0.343	1.018	0.003	0.002	0.003	0.001	0.005	0.005
Nd146	0.567	0.970	-	-	0.012	0.009	0.015	0.018
Sm147	0.157	0.347	-	-	-	-	0.022	0.010
Eu153	0.060	0.140	0.002	-	0.005	0.004	0.005	-
Gd157	0.214	0.452	0.007	-	0.011	-	0.015	0.009
Dy163	0.171	0.488	0.011	0.008	0.007	0.005	0.010	0.004
Er166	0.218	0.473	0.008	-	0.003	-	0.005	0.003
Yb172	0.137	0.393	0.011	-	0.011	-	0.008	0.005
Lu175	0.074	0.118	0.003	0.002	0.001	-	0.002	-
Hf178	0.006	0.003	0.006	0.004	-	-	0.008	-
Ta181	0.002	0.002	0.002	0.002	-	-	0.003	0.001
W182	0.047	0.066	0.011	-	-	-	0.015	0.004
Au197	0.005	-	-	-	0.003	0.001	0.006	-
Pb206	1.352	3.247	0.068	0.039	-	-	0.029	0.014
Pb207	0.411	1.018	0.040	0.013	0.029	0.006	0.028	0.006
Pb208	0.826	1.403	0.036	0.031	-	-	0.017	-
Bi209	0.008	0.005	0.008	0.003	-	-	-	-
Th232	0.002	-	0.004	-	0.001	-	0.003	-
U238	1.409	3.713	0.006	0.004	0.032	-	0.005	0.004

Martite

Mineral	Iron ore (HBD)		Iron ore (CTE)		Itabirite (HBD)	
Lithotype	4		5		4	
Elements	Average	SD	Average	SD	Average	SD
O	30.005	0.053	30.137	0.047	30.121	0.012
Li7	6.940	1.935	2.647	1.952	3.297	0.368
Na23	15.818	11.487	-	-	109.236	35.130
Mg24	1029.834	424.400	1548.769	398.708	45.985	10.340
Al27	268.788	173.908	369.598	31.260	587.998	153.878
Si29	853.283	500.187	460.651	225.217	477.063	78.227
P31	247.049	45.772	601.257	574.329	1079.921	197.289
S34	0.622	0.189	0.510	0.105	0.581	0.062
Ca43	-	-	166.024	-	-	-
Sc45	0.487	0.162	0.489	0.091	0.107	-
Ti47	1.245	0.085	6.679	1.168	0.607	0.198
Ti49	1.649	0.233	6.716	1.504	0.749	-
V51	26.887	1.189	69.183	2.718	7.773	0.954
Cr53	17.878	4.611	10.290	0.602	2.538	0.569
Mn55	10370.132	2468.803	529.458	20.896	1778.412	127.614
Fe57	685562.161	1718.558	694938.034	1622.554	693367.206	618.861
Co59	129.709	4.484	2.218	0.158	86.276	5.045
Ni60	321.629	17.772	6.379	0.584	706.002	36.378
Cu63	1.543	1.074	1.811	2.604	9.327	0.468
Cu65	1.622	0.938	1.932	2.810	9.397	0.791
Zn66	1052.107	103.568	6.879	4.887	379.740	60.171
Ga69	7.804	1.062	0.408	0.049	2.260	0.319
Ga71	8.548	1.512	0.446	0.054	2.606	0.356
As75	11.395	6.797	6.496	5.351	7.539	1.971
Sr88	0.153	0.105	0.098	0.077	0.042	0.004
Y89	18.123	12.829	4.031	6.597	9.982	2.728
Zr90	0.550	0.897	0.100	0.071	-	-
Nb93	0.008	0.003	0.021	-	0.011	0.008
Mo95	0.474	0.211	1.912	1.196	0.481	0.156
Mo98	0.313	0.227	1.937	1.253	0.535	0.132
Ag107	0.051	0.039	-	-	-	-
Sn118	0.356	0.229	0.389	0.063	0.433	0.060
Sb121	0.206	0.110	0.097	0.054	0.126	0.057
Cs133	0.011	0.004	-	-	-	-
Ba137	8.182	2.508	0.691	0.607	4.399	1.829

continued

Mineral	Iron ore (HBD)		Iron ore (CTE)		Itabirite (HBD)	
Lithotype	4		5		4	
Elements	Average	SD	Average	SD	Average	SD
La139	6.456	2.271	3.058	6.474	1.258	0.241
Ce140	12.187	12.440	6.321	13.245	2.171	0.602
Nd146	4.879	3.534	5.776	11.037	1.426	0.546
Sm147	1.998	1.432	1.005	1.851	0.534	0.235
Eu153	0.913	0.658	0.355	0.717	0.216	0.071
Gd157	2.880	2.050	1.230	2.228	0.975	0.237
Dy163	3.368	2.355	0.819	1.292	1.191	0.488
Er166	3.354	0.832	0.352	0.529	1.102	0.412
Yb172	4.724	1.296	0.343	0.410	1.339	0.475
Lu175	0.492	0.353	0.058	0.085	0.173	0.059
Hf178	0.019	-	0.005	0.003	0.003	-
Ta181	0.003	0.001	0.006	0.005	0.003	0.003
W182	0.621	0.357	0.063	0.068	0.250	0.035
Au197	-	-	0.006	0.006	-	-
Pb206	17.714	11.685	10.058	10.380	80.027	25.247
Pb207	5.505	3.611	5.782	5.742	11.382	2.571
Pb208	4.293	2.923	4.870	4.628	5.723	1.039
Bi209	0.052	0.073	0.378	0.290	0.010	-
Th232	0.017	-	0.006	0.006	-	-
U238	19.482	12.872	4.840	6.986	105.754	31.946

Anexo 5 (Appendix 5) - Analytical procedures related to the zircon analysis

5A. Sample preparation and imaging

The samples were processed with conventional crushing, grinding and screening methods at the LOPAG-DEGEO laboratory of Universidade Federal de Ouro Preto (UFOP), Brazil and at the Instituto de Geociências of Universidade Estadual Paulista (UNESP), in Rio Claro, Brazil. After the screening, the heavy fraction concentration of 60-250 mesh was pre-concentrated by panning. After the concentration, samples were sieved and washed to remove clay and silt size. The 60-250 mesh pre-concentrate was purified using heavy liquid (LST, lithium heteropolytungstate or bromoform) to remove all light minerals. Then a Frantz LB1 magnetic separator was used to separate the less magnetic minerals, such as non-metamict zircons. Zircon was handpicked and organized in an epoxy mount, which was polished and carbon-coated for SEM (Scanning Electron Microscope) study using BSE that were taken using a TESCAN VEGA3 at the Centre for Microscopy, Characterisation and Analysis (CMCA) in The University of Western Australia (UWA). Imaging of the zircon with BSE is critical for identifying internal features, such as the core and rims, and to avoid areas with high common lead content (inclusions, fractures, and metamict areas).

5B. Major and trace elements

The chemical composition of zircon was obtained using the SEM JEOL8530F EPMA electronic microprobe, at 25 kV accelerating voltage and 80 nA current, at the CMCA, in UWA, Perth, Australia. Zircon was analyzed with electron microprobe (EMP) for Si, Ca, Ce, Dy, Er, Fe, Gd, Hf, Lu, Mg, Na, Nb, Nd, O, P, Pb, Ta, Th, Ti, U, Y, Yb, Zr. The used standards were the following: Zircon for Si, Zr, Hf; Periclase for Mg; Jadeite for Na; Wollastonite for Ca; Thorium oxide for Th; pure U; Crocoite for Pb; YPO₄ for Y and P; rutile for Ti; magnetite for Fe; CePO₄ for Ce; GdPO₄ for Gd; NdPO₄ for Nd; YbPO₄ for Yb; REE2 for Lu; ErPO₄ for Er; DyPO₄ for Dy; Manganotantalite for Ta and pure Nb.

5C. U-Pb geochronology

Epoxy mounts were coated with gold for SHRIMP (Sensitive High-Resolution Ion Microprobe) analyses conducted in the laboratory of John de Laeter Centre for Isotope Research at Curtin University, Western Australia. Most SHRIMP analytical spots were in the diameter range of 20-30 µm but the analyses of U-rich (hydrothermalized) zones used a spot size of only 10 µm. Six scans were used for each spot analysis of magmatic zircons and five for detrital zircons. The following masses were analyzed for zircon: ¹⁹⁶Zr₂O, ²⁰⁴Pb, background, ²⁰⁶Pb, ²⁰⁷Pb, ²⁰⁸Pb, ²³⁸U, ²⁴⁸ThO, ²⁵⁴UO. The calibration of Pb/U ratios was conducted using the zircon standards M257 (561.3 Ma - Nasdala et al. (2008)) and BR266 (559 Ma, 903 ppm U - Stern, (2001)). Data with common lead correction greater than about 1% were rejected during the first scan. The uncertainties of individual ages are quoted at the 1σ level, whereas the plotted ages are calculated at 2σ levels (about 95% confidence). SHRIMP data were reduced using SQUID software (Ludwig, 2001) and plots were prepared using ISOPLOT/Ex (Ludwig, 2003).

5D. Lu-Hf isotope analysis

Lu-Hf isotopes in zircon were measured in the GeoHistory Facility in the John de Laeter Centre of the Curtin University, Perth, Australia. Analyses were placed over SHRIMP spots on grains with concordant ages. Spatially, U-Pb and Lu-Hf spot analyses were as close together as possible in

order to analyze domains of the zircon grain with the same isotopic characteristics. Instrumentation includes a Resonetics *RESOlution* M-50A excimer laser, coupled to a Nu Plasma II multi-collector inductively coupled plasma mass spectrometer (LA-MC-ICPMS). Following two cleaning pulses and a 55s period of background analysis, samples were spot ablated for 30 s at a 10Hz repetition rate using a 50 or 33 μm beam and laser energy at the sample surface of 2.2 J cm^{-2} . An additional 15s of baseline was collected after ablation. The sample cell was flushed with ultrahigh purity He (320 mL min^{-1}) and N₂ (1.2 mL min^{-1}) and high purity Ar was employed as the plasma carrier gas. All isotopes (^{180}Hf , ^{179}Hf , ^{178}Hf , ^{177}Hf , ^{176}Hf , ^{175}Lu , ^{174}Hf , ^{173}Yb , ^{172}Yb , and ^{171}Yb) were counted on the Faraday collector array. Time resolved data was baseline subtracted and reduced using Iolite (DRS after Woodhead et al., 2004), where ^{176}Yb and ^{176}Lu were removed from the 176 mass signal using $^{176}\text{Yb}/^{173}\text{Yb} = 0.7962$ and $^{176}\text{Lu}/^{175}\text{Lu} = 0.02655$ with an exponential law mass bias correction assuming $^{172}\text{Yb}/^{173}\text{Yb} = 1.35274$ (Chu et al., 2002). The interference corrected $^{176}\text{Hf}/^{177}\text{Hf}$ was normalized to $^{179}\text{Hf}/^{177}\text{Hf} = 0.7325$ (Patchett et al., 1982) for mass bias correction. Zircons from the Mud Tank carbonatite locality were used as primary standard for all standard corrected Hf ratios (Woodhead and Herdt, 2007). The R33 zircons were used as primary standard for standard corrected Lu/Hf ratio (Fisher et al., 2014). All Analytical ratios of $^{176}\text{Yb}/^{177}\text{Hf}$, $^{176}\text{Lu}/^{177}\text{Hf}$, and $^{176}\text{Hf}/^{177}\text{Hf}$ are reported with 2σ error. For all analyzed grains were used the decay constant of $1.867 \times 10^{-11} \text{ year}^{-1}$ for ^{176}Lu (Söderlund et al., 2004). The chondritic ratios of $^{176}\text{Hf}/^{177}\text{Hf}$ (0.282785) and $^{176}\text{Lu}/^{177}\text{Hf}$ (0.0336) of Bouvier et al. (2008), and the present day depleted mantle of $^{176}\text{Lu}/^{177}\text{Hf}$ (0.0388) and the $^{176}\text{Hf}/^{177}\text{Hf}$ (0.28325) of Andersen et al. (2009) were adopted in calculations. We also calculated two distinct crustal model ages T_{DM} , assuming that the parental magma of the zircons was produced from an average continental crustal source with $^{176}\text{Lu}/^{177}\text{Hf} = 0.015$ (Goode and Vervoort, 2006) or $^{176}\text{Lu}/^{177}\text{Hf} = 0.0125$ (Chauvel et al., 2014).

5E. ^{18}O and ^{16}O isotope analysis

Oxygen isotope ratios of zircon grains were measured using a Cameca IMS 1280 multi-collector ion microprobe at the CMCA, UWA. The sample mounts were cleaned with detergent, distilled water and ethanol in an ultrasonic bath and coated with gold (30 nm in thickness) prior to secondary ion mass spectrometry (SIMS) analyses. Analytical conditions were similar to those outlined in detail by Kita et al. (2009). Oxygen analyses were performed using a 3nA Gaussian Cs+ beam with an impact energy of 20 keV and was focused to a 20 mm spot. Secondary ions were sputtered using a 10 μm -raster and were introduced into the double focusing mass spectrometer within a 110 μm entrance slit and focused in the center of a 4000 μm field aperture (x 130 magnification). Secondary ions were energy filtered using a 40 eV band pass with a 5 eV gap toward the high-energy side. ^{16}O and ^{18}O were collected simultaneously in Faraday cup detectors. A normal incidence electron gun was used for charge compensation. Each analysis spot was pre-sputtered for 10 s, and analyses consisted of 20 s x 4 cycles, which gave an average internal precision of better than $\pm 0.2\%$ (2 standard deviations or SD). Instrumental mass fractionation (IMS) was corrected using Temora 2 following the procedure described in Kita et al. (2009). Corrected $^{18}\text{O}/^{16}\text{O}$ ratios are reported in $\delta^{18}\text{O}$ notation, in per mil variations relative to Vienna standard mean ocean water (VSMOW). Uncertainty on each $\delta^{18}\text{O}$ spot has been calculated by propagating the errors on instrumental mass fractionation determination, including the error on the reference value of the standard and standard deviation of the mean oxygen isotope ratio measured on the primary standard during the session, and internal error on each sample data point.

5F. References of the analytical procedures

- Andersen, T., Andersson, U.B., Graham, S., Åberg, G., Simonsen, S.L., 2009. Granitic magmatism by melting of juvenile continental crust: new constraints on the source of Paleoproterozoic granitoids in Fennoscandia from Hf isotopes in zircon. *J. Geol. Soc. London* 166, 233–247.
- Bouvier, A., Vervoort, J.D., Patchett, P.J., 2008. The Lu–Hf and Sm–Nd isotopic composition of CHUR: Constraints from unequilibrated chondrites and implications for the bulk composition of terrestrial planets. *Earth Planet. Sci. Lett.* 273, 48–57. <https://doi.org/10.1016/j.epsl.2008.06.010>
- Chauvel, C., Garçon, M., Bureau, S., Besnault, A., Jahn, B., Ding, Z., 2014. Constraints from loess on the Hf–Nd isotopic composition of the upper continental crust. *Earth Planet. Sci. Lett.* 388, 48–58. <https://doi.org/10.1016/j.epsl.2013.11.045>
- Chu, N.-C., Taylor, R., Chavagnac, V., Nesbitt, R.W., Boella, R., Milton, J., German, C., Bayon, G., Burton, K., 2002. Hf Isotope Ratio Analysis Using Multi-collector Inductively Coupled Plasma Mass Spectrometry: An Evaluation of Isobaric Interference Corrections. *J. Anal. At. Spectrom.* 17, 1567–1574. <https://doi.org/10.1039/b206707b>
- Fisher, C.M., Vervoort, J.D., Dufrane, S.A., 2014. Accurate Hf isotope determinations of complex zircons using the “laser ablation split stream” (LASS) method. *Geochemistry Geophys. Geosystems* 15, 121–139. <https://doi.org/10.1002/2013GC004962>
- Goodge, J.W., Vervoort, J.D., 2006. Origin of Mesoproterozoic A-type granites in Laurentia: Hf isotope evidence. *Earth Planet. Sci. Lett.* 243, 711–731. <https://doi.org/10.1016/j.epsl.2006.01.040>
- Kita, N.T., Ushikubo, T., Fu, B., Valley, J.W., 2009. High precision SIMS oxygen isotope analysis and the effect of sample topography. *Chem. Geol.* 264, 43–57. <https://doi.org/10.1016/j.chemgeo.2009.02.012>
- Ludwig, K.R., 2003. ISOPLOT 3.00 - Geochronological Toolkit for Excel. Berkely Geochronol. Center, p. 67. Spec. Publ. 4.
- Ludwig, K.R., 2001. SQUID 1.02: a Users Manual. Berkeley Geochronol. Centre, Spec. Publ. No. 2.
- Nasdala, L., Hofmeister, W., Norberg, N., Martinson, J.M., Corfu, F., Dörr, W., Kamo, S.L., Kennedy, A.K., Kronz, A., Reiners, P.W., Frei, D., Kosler, J., Wan, Y., Götze, J., Häger, T., Kröner, A., Valley, J.W., 2008. Zircon M257 - a Homogeneous Natural Reference Material for the Ion Microprobe U-Pb Analysis of Zircon. *Geostand. Geoanalytical Res.* 32, 247–265. <https://doi.org/10.1111/j.1751-908X.2008.00914.x>
- Patchett, J.P., Kouvo, O., Hedge, C.E., Tatsumoto, M., 1982. Evolution of continental crust and mantle heterogeneity: Evidence from Hf isotopes. *Contrib. to Mineral. Petrol.* 78, 279–297. <https://doi.org/10.1007/BF00398923>
- Söderlund, U., Patchett, P.J., Vervoort, D., Isachsen, C.E., 2004. The ^{176}Lu decay constant determined by Lu-Hf and U-Pb isotope systematics of Precambrian mafic intrusions. *Earth Planet. Sci. Lett.* 219, 311–324. [https://doi.org/10.1016/S0012-821X\(04\)00012-3](https://doi.org/10.1016/S0012-821X(04)00012-3)
- Stern, R.A., 2001. A New Isotopic and Trace-element Standard for the Ion Microprobe: Preliminary Thermal Ionization Mass Spectrometry (TIMS) U-Pb and Electron-microprobe Data, Radiogenic Age and Isotopic Studies: Report 14. Geological Survey of Canada.

Woodhead, J.D., Hergt, J.M., 2007. A preliminary appraisal of seven natural zircon reference materials for in situ Hf isotope determination. *Geostand. Geoanalytical Res.* 29, 183–195. <https://doi.org/10.1111/j.1751-908X.2005.tb00891.x>

Woodhead, J.D., Hergt, J.M., Shelley, M., Eggins, S., Kemp, R., 2004. Zircon Hf-isotope analysis with an Excimer laser, depth profiling, ablation of complex geometries, and concomitant age estimation. *Chem. Geol.* 209, 121–135. <https://doi.org/10.1016/j.chemgeo.2004.04.026>

Anexo 6 (Appendix 6) – Analytical results of zircon analysis

6A. U-Th-Pb SHRIMP

Sample/Spot ID	spot position	U (ppm)	Th (ppm)	Th/U	Disc. %	Age	\pm
6666 – quartzite, Morro do Pilar							
d.7-2	rim	1405	123	0.090	4.0	534	7
d.8-1	rim	1278	18	0.010	0.8	536	7
d.7-6	rim	1801	411	0.240	2.0	554	7
d.2-2	core	38	27	0.740	-1.6	1666	32
d.2-3	core	37	26	0.730	0.6	1678	31
d.7-6	core	78	90	1.190	0.5	1767	27
d.5-3	core	148	182	1.270	6.5	1799	14
d.1-1	core	270	152	0.580	2.2	2028	10
d.3-1	core	182	115	0.650	-1.2	2075	12
d.1-2	core	334	161	0.500	1.3	2077	8
d.8-9	core	58	29	0.530	-4.0	2101	21
d.9-2	core	256	164	0.660	6.6	2105	11
d.1-3	core	166	106	0.660	-1.0	2107	12
d.8-1	core	60	44	0.750	3.7	2108	40
d.8-10	core	99	42	0.440	-1.2	2117	15
d.9-1	core	49	32	0.670	-4.3	2153	23
d.9-2	core	112	48	0.450	6.5	2153	21
d.8-4	core	162	69	0.440	0.7	2164	12
d.7-7	core	156	58	0.390	0.5	2171	16
d.8-7	core	50	24	0.500	-3.0	2177	26
d.8-8	core	175	79	0.460	0.9	2181	11
d.7-5	core	113	43	0.390	2.2	2183	16
d.8-5	core	92	61	0.690	-1.9	2203	17
d.7-3	core	236	126	0.550	9.3	2204	12
d.5-2	core	124	51	0.430	6.8	2243	12
d.5-4	core	232	100	0.440	13.0	2618	10
d.3-2	core	230	38	0.170	2.1	2621	8
d.5-1	core	142	40	0.290	7.0	2654	12
d.9-4	core	44	128	2.990	3.3	2725	18
d.2-1	core	168	29	0.180	0.7	2734	42
d.7-1	core	132	116	0.910	6.0	2798	10
d.9-5	core	299	155	0.540	6.6	2815	5
d.8-3	core	119	57	0.500	4.2	2817	11
d.8-6	core	200	97	0.500	5.8	2847	8

continued

Sample/Spot ID	spot position	U (ppm)	Th (ppm)	Th/U	Disc. %	Age	±
6670 – metaconglomerate (matrix), Morro Escuro							
E.4-1	rim	1208	6	0.005	-0.8	505	6
E1-1	core	39	26	0.696	1.0	1753	32
E.6-1	core	127	103	0.839	0.1	1761	23
E.6-3	core	157	126	0.832	4.9	1762	24
E.6-4	core	102	70	0.708	-1.2	1777	25
E.3-3	core	244	101	0.428	10.9	2007	11
E.1-1	core	311	98	0.326	5.8	2037	9
E.5-1	core	144	124	0.885	3.0	2040	13
E.7-1	core	125	195	1.613	2.2	2057	56
E.3-2	core	196	178	0.940	2.4	2087	16
E.5-2	core	49	40	0.856	-1.7	2101	32
E.9-1	core	101	41	0.417	1.0	2116	20
E.7-2	core	80	17	0.223	1.3	2142	23
E.9-5	core	242	232	0.990	8.6	2144	10
E.5-3	core	77	52	0.705	-3.9	2144	29
E.4-2	core	114	95	0.864	-0.3	2207	17
E.8-4	core	102	80	0.811	3.1	2256	16
E.8-3	core	70	38	0.565	1.8	2306	23
E.2-1	core	362	158	0.452	10.9	2554	9
E.7-3	core	313	162	0.536	5.2	2619	7
E.2-4	core	294	147	0.517	4.3	2679	7
E.6-2	core	143	61	0.440	2.5	2695	11
E.4-3	core	101	83	0.842	6.5	2809	12
E.3-1	core	278	128	0.477	0.7	2833	6
E.2-2	core	194	145	0.772	11.0	2942	8
E.9-4	core	81	35	0.448	2.3	2962	11
E.9-2	core	70	74	1.091	0.1	3102	11
E.8-1	core	87	71	0.842	2.8	3115	10
E.8-2	core	83	45	0.557	8.8	3299	10
B-R12 – pegmatite, Horto-Baratinha							
C.2-1_sW	rim	4342	139	0.033	1.1	518	3
R12-1-3	rim	3315	104	0.032	-0.6	539	6
CR12-1-2	rim	3716	154	0.043	-2.0	545	3
CR12-1-1	rim	4523	159	0.036	-10.1	557	5

continued

Sample/Spot ID	spot position	U (ppm)	Th (ppm)	Th/U	Disc. %	Age	±
B-R36 – pegmatite, Horto-Baratinha							
337.3-3-1	rim	3320	19	0.006	4.8	498	7
337.3-1-1	rim	5775	38	0.007	2.1	503	8
337.4-4-1	rim	5899	38	0.007	-4.8	505	11
337.4-1-1	rim	5362	33	0.006	-1.1	506	12
337.3-2-1	rim	6063	40	0.007	-2.5	508	8
337.1-1-1	core	86	72	0.867	0.9	1728	23
337.3-5-1	core	108	55	0.527	4.6	1734	22
337.2-1-2	core	672	222	0.341	2.0	1737	6
337.3-4-1	core	131	78	0.617	-0.7	1742	15
337.4-6-3	core	139	72	0.535	1.5	1754	16
337.4-2-1	core	53	28	0.549	5.8	1755	30
337.4-5-1	core	140	89	0.652	0.2	1756	15
B-R49 – granite, Horto-Baratinha							
BR49-3-3	core	580	3	0.005	-3.3	492	6
BR49-4-3	core	102	54	0.547	15.1	1678	21
BR49-2-1	core	1066	146	0.142	8.6	1715	6
BR49-3-1	rim	39	22	0.588	-1.9	1716	29
BR49-4-2	core	41	23	0.584	-1.2	1724	28
BR49-5-1	core	739	655	0.915	-0.8	1736	7
B.3-2_sW	core	473	153	0.333	3.4	1740	9
BR49-4-1	core	400	131	0.338	2.8	1745	9
B-R54 – paraschist, Horto-Baratinha							
GR54-2-2	rim	1722	18	0.011	0.2	496	6
GR54-7-2	rim	1723	20	0.012	0.5	526	6
GR54-4-1	rim	1906	19	0.010	17.3	528	6
GR54-5-1	rim	1202	6	0.005	-10.1	528	6
GR54-5-3	rim	1823	35	0.020	6.8	532	4
GR54-1-1	rim	1609	7	0.004	3.4	537	6
GR54-6-3	core	153	97	0.650	3.0	1671	20
GR54-6-1	core	300	118	0.408	2.4	1717	13
GR54-5-2	core	130	119	0.944	8.3	2567	10
GR54-4-3	core	242	308	1.315	5.5	2582	8
GR54-4-2	core	149	104	0.723	2.2	2620	9
G.1-2_sW	core	241	156	0.670	12.3	2681	7
GR54-4-4	core	182	100	0.569	7.8	2688	11
GR54-2-1	core	50	39	0.801	6.4	2738	16
GR54-3-1	core	131	72	0.569	6.0	2748	11
GR54-7-1	core	172	107	0.645	22.5	2842	9
GR54-1-2	core	175	134	0.792	11.6	2929	7
GR54-2-3	core	51	17	0.335	6.4	3341	11
G.2-2_sW	core	83	58	0.716	7.2	2602	13
G.6-2_sW	core	35	17	0.499	0.8	2643	18
G.2-3_sW	core	258	176	0.704	3.3	2712	7

continued

Sample/Spot ID	spot position	U (ppm)	Th (ppm)	Th/U	Disc. %	Age	±
B-R56 – paraschist, Horto-Baratinha							
ER56-2-1	rim	2689	122	0.047	10.7	518	3
ER56-6-3	rim	2286	58	0.026	12.2	523	4
ER56-5-1	rim	1852	17	0.009	-12.3	541	17
ER56-7-1	core	242	135	0.577	2.7	1729	13
E.3-2_sW	core	159	139	0.904	1.7	2556	18
ER56-11-3	core	144	111	0.798	3.9	2578	9
ER56-4-1	core	458	230	0.519	15.6	2593	23
ER56-3-1	core	100	64	0.666	-0.1	2607	11
E.4-_sW	core	63	61	0.998	7.1	2677	15
ER56-14-1	core	139	126	0.936	7.6	2695	8
ER56-10-3	core	143	105	0.757	1.5	2695	9
ER56-10-2	core	156	65	0.429	6.0	2728	8
E.1-2_sW	core	30	9	0.310	2.7	2810	21
ER56-6-2	core	122	59	0.502	5.4	2897	9
ER56-1-1	core	82	60	0.758	3.7	2913	11
ER56-12-1	core	85	109	1.323	1.7	3252	8
ER56-2-2	core	75	67	0.914	10.6	3333	8
ER56-7-2	core	25	29	1.172	-1.4	3479	15
ER56-8-1	core	114	64	0.580	1.0	2865	9
ER56-5-2	core	104	61	0.610	2.0	2627	10
B-R63 – granite, Horto-Baratinha							
BR63-1-1	rim	1897	27	0.015	17.3	484	3
BR63-2-1	rim	1726	9	0.005	-2.4	493	3
BR63-2-3	rim	1333	92	0.072	17.3	525	5
BR63-4-1	core	30	15	0.516	-11.3	1542	73
BR63-4-2	core	660	444	0.695	14.7	1712	9
BR63-2-2	core	102	84	0.850	-2.5	1731	18
BR63-1-2	core	403	194	0.498	1.0	1742	7
BR63-5-1	core	105	64	0.632	-2.3	1745	27
BR63-12-2	core	115	91	0.816	13.3	1748	15
B-R66 – orthogneiss, Horto-Baratinha surroundings							
IR66-1-2	rim	1331	160	0.124	17.1	2357	9
IR66-1-1	core	316	149	0.488	7.3	2676	7
IR66-4-1	core	489	158	0.333	6.3	2687	6
IR66-7-1	core	887	358	0.417	4.8	2700	4
IR66-9-1	core	914	370	0.418	2.6	2708	4
IR66-3-1	core	355	146	0.425	3.0	2708	6
IR66-8-1	core	739	272	0.381	2.1	2716	4
B-S15 – paraschist, Horto-Baratinha							
CS15-5-1	rim	1344	9	0.007	4.1	522	4
C.6-1_sW	rim	942	1	0.001	-1.4	522	8
CS15-2-1	core	991	5	0.005	-1.8	528	4
CS15-3-1	rim	724	1	0.001	-5.2	535	5

continued

Sample/Spot ID	spot position	U (ppm)	Th (ppm)	Th/U	Disc. %	Age	\pm
C-R14 – paraschist, Cuité							
HR14-1-1	rim	1562	9	0.006	4.4	497	17
HR14-6-1	rim	1132	17	0.016	-2.8	510	7
FR14-7-1	core	189	108	0.590	3.0	1695	15
HR14-9-1	core	262	59	0.234	5.2	1707	14
HR14-5-1	core	242	127	0.543	5.4	1707	14
H.3-1_sW	core	54	32	0.622	-0.6	1711	24
HR14-10-2	core	1614	316	0.202	4.2	1712	8
FR14-3-1	core	143	48	0.347	6.8	1718	15
FR14-8-1	core	89	51	0.585	4.6	1719	22
HR14-9-2	core	160	100	0.647	5.6	1720	16
FR14-1-1	rim	1371	969	0.730	7.0	1724	5
FR14-9-1	core	386	290	0.777	-0.9	1726	9
FR14-1-2	core	249	136	0.565	-1.5	1731	14
HR14-4-2	core	172	132	0.794	2.3	1735	16
HR14-1-2	core	53	28	0.539	4.8	1739	35
HR14-4-1	core	163	101	0.638	3.3	1746	16
FR14-5-1	core	78	41	0.545	2.9	1751	21
FR14-3-2	core	107	52	0.500	9.4	1756	20
H.1-3_sW	core	131	66	0.520	2.7	3040	15
HR14-6-2	core	171	83	0.502	5.4	3107	19
C-R23 – paraschist, Cuité							
AR23-1-1	core	1530	11	0.008	5.1	494	3
AR23-2-1	core	1223	10	0.008	-2.8	510	6
A.8-1_sW	rim	1137	5	0.004	-4.3	513	4
AR23-7-1	core	47	29	0.646	2.3	1744	26
AR23-5-1	core	83	48	0.594	6.0	1753	20

Notes:

Disc. % = discordance, as $100 - 100 \{ t[^{206}\text{Pb}/^{238}\text{U}] / t[^{207}\text{Pb}/^{206}\text{Pb}] \}$;

Inverse concordia and ^{208}Pb corrected ratios are used for Cambrian zircons, which have very low $^{232}\text{Th}/^{238}\text{U}$ ratios (except samples from Morro do Pilar and Morro Escuro)

Normal concordia and ^{204}Pb ratios are used for Paleoproterozoic and Archean zircons

6B. Chemical composition by electronic microprobe

DL average	Sample ID	6670 – metaconglomerate (matrix) from Morro Escuro - rim analysis				
		n	2			
	Elements	Average	SD	Min.	Median	Max.
0.0075	Si (wt. %)	16.6759	0.9202	16.0252	16.6759	17.3266
0.0244	Zr (wt. %)	49.1490	0.3619	48.8931	49.1490	49.4049
0.0111	Hf (wt. %)	1.7763	0.1575	1.6650	1.7763	1.8877
-	O (wt. %)	36.6852	1.2273	35.8174	36.6852	37.5530
-	total	104.5331	2.5433	102.7347	104.5331	106.3315
32.25	Mg (ppm)	550.71	350.30	303.01	550.71	798.41
97.64	Na (ppm)	-	-	-	-	-
16.48	Ca (ppm)	-	-	-	-	-
91.11	Th (ppm)	-	-	-	-	-
90.48	U (ppm)	434.25	-	434.25	434.25	434.25
157.58	Pb (ppm)	-	-	-	-	-
123.46	Y (ppm)	750.72	237.91	582.49	750.72	918.94
22.87	Ti (ppm)	-	-	-	-	-
19.28	Fe (ppm)	-	-	-	-	-
50.06	Ce (ppm)	206.98	-	206.98	206.98	206.98
48.08	Gd (ppm)	68.18	-	68.18	68.18	68.18
50.33	Nd (ppm)	180.05	-	180.05	180.05	180.05
83.38	Yb (ppm)	410.06	-	410.06	410.06	410.06
89.15	Lu (ppm)	-	-	-	-	-
86.78	Er (ppm)	-	-	-	-	-
91.54	Dy (ppm)	-	-	-	-	-
37.85	P (ppm)	416.56	-	416.56	416.56	416.56
90.51	Ta (ppm)	-	-	-	-	-
106.81	Nb (ppm)	306.86	112.88	227.04	306.86	386.67

continued

DL average	Sample ID	6670 – metaconglomerate (matrix) from Morro Escuro - rim analysis				
		n	2			
	Elements	Average	SD	Min.	Median	Max.
0.0075	Si (wt. %)	16.6759	0.9202	16.0252	16.6759	17.3266
0.0244	Zr (wt. %)	49.1490	0.3619	48.8931	49.1490	49.4049
0.0111	Hf (wt. %)	1.7763	0.1575	1.6650	1.7763	1.8877
-	O (wt. %)	36.6852	1.2273	35.8174	36.6852	37.5530
-	total	104.5331	2.5433	102.7347	104.5331	106.3315
32.25	Mg (ppm)	550.71	350.30	303.01	550.71	798.41
97.64	Na (ppm)	-	-	-	-	-
16.48	Ca (ppm)	-	-	-	-	-
91.11	Th (ppm)	-	-	-	-	-
90.48	U (ppm)	434.25	-	434.25	434.25	434.25
157.58	Pb (ppm)	-	-	-	-	-
123.46	Y (ppm)	750.72	237.91	582.49	750.72	918.94
22.87	Ti (ppm)	-	-	-	-	-
19.28	Fe (ppm)	-	-	-	-	-
50.06	Ce (ppm)	206.98	-	206.98	206.98	206.98
48.08	Gd (ppm)	68.18	-	68.18	68.18	68.18
50.33	Nd (ppm)	180.05	-	180.05	180.05	180.05
83.38	Yb (ppm)	410.06	-	410.06	410.06	410.06
89.15	Lu (ppm)	-	-	-	-	-
86.78	Er (ppm)	-	-	-	-	-
91.54	Dy (ppm)	-	-	-	-	-
37.85	P (ppm)	416.56	-	416.56	416.56	416.56
90.51	Ta (ppm)	-	-	-	-	-
106.81	Nb (ppm)	306.86	112.88	227.04	306.86	386.67

continued

DL average	Sample ID	6670 – metaconglomerate (matrix) from Morro Escuro - rim analysis				
		n	2			
	Elements	Average	SD	Min.	Median	Max.
0.0075	Si (wt. %)	16.6759	0.9202	16.0252	16.6759	17.3266
0.0244	Zr (wt. %)	49.1490	0.3619	48.8931	49.1490	49.4049
0.0111	Hf (wt. %)	1.7763	0.1575	1.6650	1.7763	1.8877
-	O (wt. %)	36.6852	1.2273	35.8174	36.6852	37.5530
-	total	104.5331	2.5433	102.7347	104.5331	106.3315
32.25	Mg (ppm)	550.71	350.30	303.01	550.71	798.41
97.64	Na (ppm)	-	-	-	-	-
16.48	Ca (ppm)	-	-	-	-	-
91.11	Th (ppm)	-	-	-	-	-
90.48	U (ppm)	434.25	-	434.25	434.25	434.25
157.58	Pb (ppm)	-	-	-	-	-
123.46	Y (ppm)	750.72	237.91	582.49	750.72	918.94
22.87	Ti (ppm)	-	-	-	-	-
19.28	Fe (ppm)	-	-	-	-	-
50.06	Ce (ppm)	206.98	-	206.98	206.98	206.98
48.08	Gd (ppm)	68.18	-	68.18	68.18	68.18
50.33	Nd (ppm)	180.05	-	180.05	180.05	180.05
83.38	Yb (ppm)	410.06	-	410.06	410.06	410.06
89.15	Lu (ppm)	-	-	-	-	-
86.78	Er (ppm)	-	-	-	-	-
91.54	Dy (ppm)	-	-	-	-	-
37.85	P (ppm)	416.56	-	416.56	416.56	416.56
90.51	Ta (ppm)	-	-	-	-	-
106.81	Nb (ppm)	306.86	112.88	227.04	306.86	386.67

continued

DL average	Sample ID	6670 – metaconglomerate (matrix) from Morro Escuro - rim analysis				
		n	2			
	Elements	Average	SD	Min.	Median	Max.
0.0075	Si (wt. %)	16.6759	0.9202	16.0252	16.6759	17.3266
0.0244	Zr (wt. %)	49.1490	0.3619	48.8931	49.1490	49.4049
0.0111	Hf (wt. %)	1.7763	0.1575	1.6650	1.7763	1.8877
-	O (wt. %)	36.6852	1.2273	35.8174	36.6852	37.5530
-	total	104.5331	2.5433	102.7347	104.5331	106.3315
32.25	Mg (ppm)	550.71	350.30	303.01	550.71	798.41
97.64	Na (ppm)	-	-	-	-	-
16.48	Ca (ppm)	-	-	-	-	-
91.11	Th (ppm)	-	-	-	-	-
90.48	U (ppm)	434.25	-	434.25	434.25	434.25
157.58	Pb (ppm)	-	-	-	-	-
123.46	Y (ppm)	750.72	237.91	582.49	750.72	918.94
22.87	Ti (ppm)	-	-	-	-	-
19.28	Fe (ppm)	-	-	-	-	-
50.06	Ce (ppm)	206.98	-	206.98	206.98	206.98
48.08	Gd (ppm)	68.18	-	68.18	68.18	68.18
50.33	Nd (ppm)	180.05	-	180.05	180.05	180.05
83.38	Yb (ppm)	410.06	-	410.06	410.06	410.06
89.15	Lu (ppm)	-	-	-	-	-
86.78	Er (ppm)	-	-	-	-	-
91.54	Dy (ppm)	-	-	-	-	-
37.85	P (ppm)	416.56	-	416.56	416.56	416.56
90.51	Ta (ppm)	-	-	-	-	-
106.81	Nb (ppm)	306.86	112.88	227.04	306.86	386.67

continued

DL average	Sample ID	6670 – metaconglomerate (matrix) from Morro Escuro - rim analysis				
		n	2			
	Elements	Average	SD	Min.	Median	Max.
0.0075	Si (wt. %)	16.6759	0.9202	16.0252	16.6759	17.3266
0.0244	Zr (wt. %)	49.1490	0.3619	48.8931	49.1490	49.4049
0.0111	Hf (wt. %)	1.7763	0.1575	1.6650	1.7763	1.8877
-	O (wt. %)	36.6852	1.2273	35.8174	36.6852	37.5530
-	total	104.5331	2.5433	102.7347	104.5331	106.3315
32.25	Mg (ppm)	550.71	350.30	303.01	550.71	798.41
97.64	Na (ppm)	-	-	-	-	-
16.48	Ca (ppm)	-	-	-	-	-
91.11	Th (ppm)	-	-	-	-	-
90.48	U (ppm)	434.25	-	434.25	434.25	434.25
157.58	Pb (ppm)	-	-	-	-	-
123.46	Y (ppm)	750.72	237.91	582.49	750.72	918.94
22.87	Ti (ppm)	-	-	-	-	-
19.28	Fe (ppm)	-	-	-	-	-
50.06	Ce (ppm)	206.98	-	206.98	206.98	206.98
48.08	Gd (ppm)	68.18	-	68.18	68.18	68.18
50.33	Nd (ppm)	180.05	-	180.05	180.05	180.05
83.38	Yb (ppm)	410.06	-	410.06	410.06	410.06
89.15	Lu (ppm)	-	-	-	-	-
86.78	Er (ppm)	-	-	-	-	-
91.54	Dy (ppm)	-	-	-	-	-
37.85	P (ppm)	416.56	-	416.56	416.56	416.56
90.51	Ta (ppm)	-	-	-	-	-
106.81	Nb (ppm)	306.86	112.88	227.04	306.86	386.67

continued

DL average	Sample ID	6670 – metaconglomerate (matrix) from Morro Escuro - rim analysis				
		n	2			
	Elements	Average	SD	Min.	Median	Max.
0.0075	Si (wt. %)	16.6759	0.9202	16.0252	16.6759	17.3266
0.0244	Zr (wt. %)	49.1490	0.3619	48.8931	49.1490	49.4049
0.0111	Hf (wt. %)	1.7763	0.1575	1.6650	1.7763	1.8877
-	O (wt. %)	36.6852	1.2273	35.8174	36.6852	37.5530
-	total	104.5331	2.5433	102.7347	104.5331	106.3315
32.25	Mg (ppm)	550.71	350.30	303.01	550.71	798.41
97.64	Na (ppm)	-	-	-	-	-
16.48	Ca (ppm)	-	-	-	-	-
91.11	Th (ppm)	-	-	-	-	-
90.48	U (ppm)	434.25	-	434.25	434.25	434.25
157.58	Pb (ppm)	-	-	-	-	-
123.46	Y (ppm)	750.72	237.91	582.49	750.72	918.94
22.87	Ti (ppm)	-	-	-	-	-
19.28	Fe (ppm)	-	-	-	-	-
50.06	Ce (ppm)	206.98	-	206.98	206.98	206.98
48.08	Gd (ppm)	68.18	-	68.18	68.18	68.18
50.33	Nd (ppm)	180.05	-	180.05	180.05	180.05
83.38	Yb (ppm)	410.06	-	410.06	410.06	410.06
89.15	Lu (ppm)	-	-	-	-	-
86.78	Er (ppm)	-	-	-	-	-
91.54	Dy (ppm)	-	-	-	-	-
37.85	P (ppm)	416.56	-	416.56	416.56	416.56
90.51	Ta (ppm)	-	-	-	-	-
106.81	Nb (ppm)	306.86	112.88	227.04	306.86	386.67

continued

DL average	Sample ID	6670 – metaconglomerate (matrix) from Morro Escuro - rim analysis				
		n	2			
	Elements	Average	SD	Min.	Median	Max.
0.0075	Si (wt. %)	16.6759	0.9202	16.0252	16.6759	17.3266
0.0244	Zr (wt. %)	49.1490	0.3619	48.8931	49.1490	49.4049
0.0111	Hf (wt. %)	1.7763	0.1575	1.6650	1.7763	1.8877
-	O (wt. %)	36.6852	1.2273	35.8174	36.6852	37.5530
-	total	104.5331	2.5433	102.7347	104.5331	106.3315
32.25	Mg (ppm)	550.71	350.30	303.01	550.71	798.41
97.64	Na (ppm)	-	-	-	-	-
16.48	Ca (ppm)	-	-	-	-	-
91.11	Th (ppm)	-	-	-	-	-
90.48	U (ppm)	434.25	-	434.25	434.25	434.25
157.58	Pb (ppm)	-	-	-	-	-
123.46	Y (ppm)	750.72	237.91	582.49	750.72	918.94
22.87	Ti (ppm)	-	-	-	-	-
19.28	Fe (ppm)	-	-	-	-	-
50.06	Ce (ppm)	206.98	-	206.98	206.98	206.98
48.08	Gd (ppm)	68.18	-	68.18	68.18	68.18
50.33	Nd (ppm)	180.05	-	180.05	180.05	180.05
83.38	Yb (ppm)	410.06	-	410.06	410.06	410.06
89.15	Lu (ppm)	-	-	-	-	-
86.78	Er (ppm)	-	-	-	-	-
91.54	Dy (ppm)	-	-	-	-	-
37.85	P (ppm)	416.56	-	416.56	416.56	416.56
90.51	Ta (ppm)	-	-	-	-	-
106.81	Nb (ppm)	306.86	112.88	227.04	306.86	386.67

continued

DL average	Sample ID	6670 – metaconglomerate (matrix) from Morro Escuro - rim analysis				
		n	2			
	Elements	Average	SD	Min.	Median	Max.
0.0075	Si (wt. %)	16.6759	0.9202	16.0252	16.6759	17.3266
0.0244	Zr (wt. %)	49.1490	0.3619	48.8931	49.1490	49.4049
0.0111	Hf (wt. %)	1.7763	0.1575	1.6650	1.7763	1.8877
-	O (wt. %)	36.6852	1.2273	35.8174	36.6852	37.5530
-	total	104.5331	2.5433	102.7347	104.5331	106.3315
32.25	Mg (ppm)	550.71	350.30	303.01	550.71	798.41
97.64	Na (ppm)	-	-	-	-	-
16.48	Ca (ppm)	-	-	-	-	-
91.11	Th (ppm)	-	-	-	-	-
90.48	U (ppm)	434.25	-	434.25	434.25	434.25
157.58	Pb (ppm)	-	-	-	-	-
123.46	Y (ppm)	750.72	237.91	582.49	750.72	918.94
22.87	Ti (ppm)	-	-	-	-	-
19.28	Fe (ppm)	-	-	-	-	-
50.06	Ce (ppm)	206.98	-	206.98	206.98	206.98
48.08	Gd (ppm)	68.18	-	68.18	68.18	68.18
50.33	Nd (ppm)	180.05	-	180.05	180.05	180.05
83.38	Yb (ppm)	410.06	-	410.06	410.06	410.06
89.15	Lu (ppm)	-	-	-	-	-
86.78	Er (ppm)	-	-	-	-	-
91.54	Dy (ppm)	-	-	-	-	-
37.85	P (ppm)	416.56	-	416.56	416.56	416.56
90.51	Ta (ppm)	-	-	-	-	-
106.81	Nb (ppm)	306.86	112.88	227.04	306.86	386.67

continued

DL average	Sample ID	6670 – metaconglomerate (matrix) from Morro Escuro - rim analysis				
		n	2			
	Elements	Average	SD	Min.	Median	Max.
0.0075	Si (wt. %)	16.6759	0.9202	16.0252	16.6759	17.3266
0.0244	Zr (wt. %)	49.1490	0.3619	48.8931	49.1490	49.4049
0.0111	Hf (wt. %)	1.7763	0.1575	1.6650	1.7763	1.8877
-	O (wt. %)	36.6852	1.2273	35.8174	36.6852	37.5530
-	total	104.5331	2.5433	102.7347	104.5331	106.3315
32.25	Mg (ppm)	550.71	350.30	303.01	550.71	798.41
97.64	Na (ppm)	-	-	-	-	-
16.48	Ca (ppm)	-	-	-	-	-
91.11	Th (ppm)	-	-	-	-	-
90.48	U (ppm)	434.25	-	434.25	434.25	434.25
157.58	Pb (ppm)	-	-	-	-	-
123.46	Y (ppm)	750.72	237.91	582.49	750.72	918.94
22.87	Ti (ppm)	-	-	-	-	-
19.28	Fe (ppm)	-	-	-	-	-
50.06	Ce (ppm)	206.98	-	206.98	206.98	206.98
48.08	Gd (ppm)	68.18	-	68.18	68.18	68.18
50.33	Nd (ppm)	180.05	-	180.05	180.05	180.05
83.38	Yb (ppm)	410.06	-	410.06	410.06	410.06
89.15	Lu (ppm)	-	-	-	-	-
86.78	Er (ppm)	-	-	-	-	-
91.54	Dy (ppm)	-	-	-	-	-
37.85	P (ppm)	416.56	-	416.56	416.56	416.56
90.51	Ta (ppm)	-	-	-	-	-
106.81	Nb (ppm)	306.86	112.88	227.04	306.86	386.67

continued

DL average	Sample ID	6670 – metaconglomerate (matrix) from Morro Escuro - rim analysis				
		n	2			
	Elements	Average	SD	Min.	Median	Max.
0.0075	Si (wt. %)	16.6759	0.9202	16.0252	16.6759	17.3266
0.0244	Zr (wt. %)	49.1490	0.3619	48.8931	49.1490	49.4049
0.0111	Hf (wt. %)	1.7763	0.1575	1.6650	1.7763	1.8877
-	O (wt. %)	36.6852	1.2273	35.8174	36.6852	37.5530
-	total	104.5331	2.5433	102.7347	104.5331	106.3315
32.25	Mg (ppm)	550.71	350.30	303.01	550.71	798.41
97.64	Na (ppm)	-	-	-	-	-
16.48	Ca (ppm)	-	-	-	-	-
91.11	Th (ppm)	-	-	-	-	-
90.48	U (ppm)	434.25	-	434.25	434.25	434.25
157.58	Pb (ppm)	-	-	-	-	-
123.46	Y (ppm)	750.72	237.91	582.49	750.72	918.94
22.87	Ti (ppm)	-	-	-	-	-
19.28	Fe (ppm)	-	-	-	-	-
50.06	Ce (ppm)	206.98	-	206.98	206.98	206.98
48.08	Gd (ppm)	68.18	-	68.18	68.18	68.18
50.33	Nd (ppm)	180.05	-	180.05	180.05	180.05
83.38	Yb (ppm)	410.06	-	410.06	410.06	410.06
89.15	Lu (ppm)	-	-	-	-	-
86.78	Er (ppm)	-	-	-	-	-
91.54	Dy (ppm)	-	-	-	-	-
37.85	P (ppm)	416.56	-	416.56	416.56	416.56
90.51	Ta (ppm)	-	-	-	-	-
106.81	Nb (ppm)	306.86	112.88	227.04	306.86	386.67

continued

DL average	Sample ID	6670 – metaconglomerate (matrix) from Morro Escuro - rim analysis				
		n	2			
	Elements	Average	SD	Min.	Median	Max.
0.0075	Si (wt. %)	16.6759	0.9202	16.0252	16.6759	17.3266
0.0244	Zr (wt. %)	49.1490	0.3619	48.8931	49.1490	49.4049
0.0111	Hf (wt. %)	1.7763	0.1575	1.6650	1.7763	1.8877
-	O (wt. %)	36.6852	1.2273	35.8174	36.6852	37.5530
-	total	104.5331	2.5433	102.7347	104.5331	106.3315
32.25	Mg (ppm)	550.71	350.30	303.01	550.71	798.41
97.64	Na (ppm)	-	-	-	-	-
16.48	Ca (ppm)	-	-	-	-	-
91.11	Th (ppm)	-	-	-	-	-
90.48	U (ppm)	434.25	-	434.25	434.25	434.25
157.58	Pb (ppm)	-	-	-	-	-
123.46	Y (ppm)	750.72	237.91	582.49	750.72	918.94
22.87	Ti (ppm)	-	-	-	-	-
19.28	Fe (ppm)	-	-	-	-	-
50.06	Ce (ppm)	206.98	-	206.98	206.98	206.98
48.08	Gd (ppm)	68.18	-	68.18	68.18	68.18
50.33	Nd (ppm)	180.05	-	180.05	180.05	180.05
83.38	Yb (ppm)	410.06	-	410.06	410.06	410.06
89.15	Lu (ppm)	-	-	-	-	-
86.78	Er (ppm)	-	-	-	-	-
91.54	Dy (ppm)	-	-	-	-	-
37.85	P (ppm)	416.56	-	416.56	416.56	416.56
90.51	Ta (ppm)	-	-	-	-	-
106.81	Nb (ppm)	306.86	112.88	227.04	306.86	386.67

continued

DL average	Sample ID	6670 – metaconglomerate (matrix) from Morro Escuro - rim analysis				
		n	2			
	Elements	Average	SD	Min.	Median	Max.
0.0075	Si (wt. %)	16.6759	0.9202	16.0252	16.6759	17.3266
0.0244	Zr (wt. %)	49.1490	0.3619	48.8931	49.1490	49.4049
0.0111	Hf (wt. %)	1.7763	0.1575	1.6650	1.7763	1.8877
-	O (wt. %)	36.6852	1.2273	35.8174	36.6852	37.5530
-	total	104.5331	2.5433	102.7347	104.5331	106.3315
32.25	Mg (ppm)	550.71	350.30	303.01	550.71	798.41
97.64	Na (ppm)	-	-	-	-	-
16.48	Ca (ppm)	-	-	-	-	-
91.11	Th (ppm)	-	-	-	-	-
90.48	U (ppm)	434.25	-	434.25	434.25	434.25
157.58	Pb (ppm)	-	-	-	-	-
123.46	Y (ppm)	750.72	237.91	582.49	750.72	918.94
22.87	Ti (ppm)	-	-	-	-	-
19.28	Fe (ppm)	-	-	-	-	-
50.06	Ce (ppm)	206.98	-	206.98	206.98	206.98
48.08	Gd (ppm)	68.18	-	68.18	68.18	68.18
50.33	Nd (ppm)	180.05	-	180.05	180.05	180.05
83.38	Yb (ppm)	410.06	-	410.06	410.06	410.06
89.15	Lu (ppm)	-	-	-	-	-
86.78	Er (ppm)	-	-	-	-	-
91.54	Dy (ppm)	-	-	-	-	-
37.85	P (ppm)	416.56	-	416.56	416.56	416.56
90.51	Ta (ppm)	-	-	-	-	-
106.81	Nb (ppm)	306.86	112.88	227.04	306.86	386.67

continued

DL average	Sample ID	6670 – metaconglomerate (matrix) from Morro Escuro - rim analysis				
		n	2			
	Elements	Average	SD	Min.	Median	Max.
0.0075	Si (wt. %)	16.6759	0.9202	16.0252	16.6759	17.3266
0.0244	Zr (wt. %)	49.1490	0.3619	48.8931	49.1490	49.4049
0.0111	Hf (wt. %)	1.7763	0.1575	1.6650	1.7763	1.8877
-	O (wt. %)	36.6852	1.2273	35.8174	36.6852	37.5530
-	total	104.5331	2.5433	102.7347	104.5331	106.3315
32.25	Mg (ppm)	550.71	350.30	303.01	550.71	798.41
97.64	Na (ppm)	-	-	-	-	-
16.48	Ca (ppm)	-	-	-	-	-
91.11	Th (ppm)	-	-	-	-	-
90.48	U (ppm)	434.25	-	434.25	434.25	434.25
157.58	Pb (ppm)	-	-	-	-	-
123.46	Y (ppm)	750.72	237.91	582.49	750.72	918.94
22.87	Ti (ppm)	-	-	-	-	-
19.28	Fe (ppm)	-	-	-	-	-
50.06	Ce (ppm)	206.98	-	206.98	206.98	206.98
48.08	Gd (ppm)	68.18	-	68.18	68.18	68.18
50.33	Nd (ppm)	180.05	-	180.05	180.05	180.05
83.38	Yb (ppm)	410.06	-	410.06	410.06	410.06
89.15	Lu (ppm)	-	-	-	-	-
86.78	Er (ppm)	-	-	-	-	-
91.54	Dy (ppm)	-	-	-	-	-
37.85	P (ppm)	416.56	-	416.56	416.56	416.56
90.51	Ta (ppm)	-	-	-	-	-
106.81	Nb (ppm)	306.86	112.88	227.04	306.86	386.67

continued

DL average	Sample ID	6670 – metaconglomerate (matrix) from Morro Escuro - rim analysis				
		n	2			
	Elements	Average	SD	Min.	Median	Max.
0.0075	Si (wt. %)	16.6759	0.9202	16.0252	16.6759	17.3266
0.0244	Zr (wt. %)	49.1490	0.3619	48.8931	49.1490	49.4049
0.0111	Hf (wt. %)	1.7763	0.1575	1.6650	1.7763	1.8877
-	O (wt. %)	36.6852	1.2273	35.8174	36.6852	37.5530
-	total	104.5331	2.5433	102.7347	104.5331	106.3315
32.25	Mg (ppm)	550.71	350.30	303.01	550.71	798.41
97.64	Na (ppm)	-	-	-	-	-
16.48	Ca (ppm)	-	-	-	-	-
91.11	Th (ppm)	-	-	-	-	-
90.48	U (ppm)	434.25	-	434.25	434.25	434.25
157.58	Pb (ppm)	-	-	-	-	-
123.46	Y (ppm)	750.72	237.91	582.49	750.72	918.94
22.87	Ti (ppm)	-	-	-	-	-
19.28	Fe (ppm)	-	-	-	-	-
50.06	Ce (ppm)	206.98	-	206.98	206.98	206.98
48.08	Gd (ppm)	68.18	-	68.18	68.18	68.18
50.33	Nd (ppm)	180.05	-	180.05	180.05	180.05
83.38	Yb (ppm)	410.06	-	410.06	410.06	410.06
89.15	Lu (ppm)	-	-	-	-	-
86.78	Er (ppm)	-	-	-	-	-
91.54	Dy (ppm)	-	-	-	-	-
37.85	P (ppm)	416.56	-	416.56	416.56	416.56
90.51	Ta (ppm)	-	-	-	-	-
106.81	Nb (ppm)	306.86	112.88	227.04	306.86	386.67

continued

DL average	Sample ID	6670 – metaconglomerate (matrix) from Morro Escuro - rim analysis				
		n	2			
	Elements	Average	SD	Min.	Median	Max.
0.0075	Si (wt. %)	16.6759	0.9202	16.0252	16.6759	17.3266
0.0244	Zr (wt. %)	49.1490	0.3619	48.8931	49.1490	49.4049
0.0111	Hf (wt. %)	1.7763	0.1575	1.6650	1.7763	1.8877
-	O (wt. %)	36.6852	1.2273	35.8174	36.6852	37.5530
-	total	104.5331	2.5433	102.7347	104.5331	106.3315
32.25	Mg (ppm)	550.71	350.30	303.01	550.71	798.41
97.64	Na (ppm)	-	-	-	-	-
16.48	Ca (ppm)	-	-	-	-	-
91.11	Th (ppm)	-	-	-	-	-
90.48	U (ppm)	434.25	-	434.25	434.25	434.25
157.58	Pb (ppm)	-	-	-	-	-
123.46	Y (ppm)	750.72	237.91	582.49	750.72	918.94
22.87	Ti (ppm)	-	-	-	-	-
19.28	Fe (ppm)	-	-	-	-	-
50.06	Ce (ppm)	206.98	-	206.98	206.98	206.98
48.08	Gd (ppm)	68.18	-	68.18	68.18	68.18
50.33	Nd (ppm)	180.05	-	180.05	180.05	180.05
83.38	Yb (ppm)	410.06	-	410.06	410.06	410.06
89.15	Lu (ppm)	-	-	-	-	-
86.78	Er (ppm)	-	-	-	-	-
91.54	Dy (ppm)	-	-	-	-	-
37.85	P (ppm)	416.56	-	416.56	416.56	416.56
90.51	Ta (ppm)	-	-	-	-	-
106.81	Nb (ppm)	306.86	112.88	227.04	306.86	386.67

continued

DL average	Sample ID	6670 – metaconglomerate (matrix) from Morro Escuro - rim analysis				
		n	2			
	Elements	Average	SD	Min.	Median	Max.
0.0075	Si (wt. %)	16.6759	0.9202	16.0252	16.6759	17.3266
0.0244	Zr (wt. %)	49.1490	0.3619	48.8931	49.1490	49.4049
0.0111	Hf (wt. %)	1.7763	0.1575	1.6650	1.7763	1.8877
-	O (wt. %)	36.6852	1.2273	35.8174	36.6852	37.5530
-	total	104.5331	2.5433	102.7347	104.5331	106.3315
32.25	Mg (ppm)	550.71	350.30	303.01	550.71	798.41
97.64	Na (ppm)	-	-	-	-	-
16.48	Ca (ppm)	-	-	-	-	-
91.11	Th (ppm)	-	-	-	-	-
90.48	U (ppm)	434.25	-	434.25	434.25	434.25
157.58	Pb (ppm)	-	-	-	-	-
123.46	Y (ppm)	750.72	237.91	582.49	750.72	918.94
22.87	Ti (ppm)	-	-	-	-	-
19.28	Fe (ppm)	-	-	-	-	-
50.06	Ce (ppm)	206.98	-	206.98	206.98	206.98
48.08	Gd (ppm)	68.18	-	68.18	68.18	68.18
50.33	Nd (ppm)	180.05	-	180.05	180.05	180.05
83.38	Yb (ppm)	410.06	-	410.06	410.06	410.06
89.15	Lu (ppm)	-	-	-	-	-
86.78	Er (ppm)	-	-	-	-	-
91.54	Dy (ppm)	-	-	-	-	-
37.85	P (ppm)	416.56	-	416.56	416.56	416.56
90.51	Ta (ppm)	-	-	-	-	-
106.81	Nb (ppm)	306.86	112.88	227.04	306.86	386.67

continued

DL average	Sample ID	6670 – metaconglomerate (matrix) from Morro Escuro - rim analysis				
		n	2			
	Elements	Average	SD	Min.	Median	Max.
0.0075	Si (wt. %)	16.6759	0.9202	16.0252	16.6759	17.3266
0.0244	Zr (wt. %)	49.1490	0.3619	48.8931	49.1490	49.4049
0.0111	Hf (wt. %)	1.7763	0.1575	1.6650	1.7763	1.8877
-	O (wt. %)	36.6852	1.2273	35.8174	36.6852	37.5530
-	total	104.5331	2.5433	102.7347	104.5331	106.3315
32.25	Mg (ppm)	550.71	350.30	303.01	550.71	798.41
97.64	Na (ppm)	-	-	-	-	-
16.48	Ca (ppm)	-	-	-	-	-
91.11	Th (ppm)	-	-	-	-	-
90.48	U (ppm)	434.25	-	434.25	434.25	434.25
157.58	Pb (ppm)	-	-	-	-	-
123.46	Y (ppm)	750.72	237.91	582.49	750.72	918.94
22.87	Ti (ppm)	-	-	-	-	-
19.28	Fe (ppm)	-	-	-	-	-
50.06	Ce (ppm)	206.98	-	206.98	206.98	206.98
48.08	Gd (ppm)	68.18	-	68.18	68.18	68.18
50.33	Nd (ppm)	180.05	-	180.05	180.05	180.05
83.38	Yb (ppm)	410.06	-	410.06	410.06	410.06
89.15	Lu (ppm)	-	-	-	-	-
86.78	Er (ppm)	-	-	-	-	-
91.54	Dy (ppm)	-	-	-	-	-
37.85	P (ppm)	416.56	-	416.56	416.56	416.56
90.51	Ta (ppm)	-	-	-	-	-
106.81	Nb (ppm)	306.86	112.88	227.04	306.86	386.67

6C. Lu-Hf by LA-ICP-MS

Sample/Spot ID	spot location	Age (Ma)	$\pm 2s$	Present day ratios				Initial Ratios			T_{DM} Model Ages (Ga)		
				$^{176}\text{Hf}/^{177}\text{Hf}$	$\pm 2\text{SE}$	$^{176}\text{Lu}/^{177}\text{Hf}$	$\pm 2\text{SE}$	$^{176}\text{Hf}/^{177}\text{Hf} (\text{t})$	eHf(t)	$\pm 2\text{SE}$	T_{DM}	$T_{DM \text{ a}}$	$T_{DM \text{ b}}$
B-R12– pegmatite, Horto-Baratinha													
C.2-1_sW	rim	518	3	0.2819	0.000025	0.00608	0.00016	0.2819	-20.37	0.66	2.10	2.70	2.50
CR12-1-3	rim	539	6	0.2820	0.000026	0.00651	0.00021	0.2819	-18.53	0.79	2.05	2.60	2.41
CR12-1-2	rim	545	3	0.2820	0.000027	0.00696	0.00026	0.2819	-18.19	0.79	2.06	2.59	2.40
.CR12-1-1	rim	557	5	0.2820	0.00002	0.00486	0.00015	0.2819	-17.41	0.70	1.95	2.55	2.36
B-R36– pegmatite, Horto-Baratinha													
337.3-1-1	rim	503	8	0.2817	0.000027	0.001785	0.000015	0.2817	-26.34	0.64	2.14	3.05	2.81
337.4-4-1	rim	505	11	0.2818	0.000021	0.0018371	0.0000033	0.2818	-24.72	0.58	2.08	2.95	2.73
337.3-2-1	rim	508	8	0.2818	0.000026	0.0018032	0.000006	0.2817	-25.34	0.48	2.11	3.00	2.76
337.4-2-1	core	1755	30	0.2814	0.000042	0.001539	0.000059	0.2813	-11.22	0.62	2.59	3.11	2.98
337.2-1-2	core	1737	6	0.2813	0.000024	0.001529	0.000045	0.2813	-13.49	0.45	2.67	3.23	3.09
337.1-1-1	core	1728	23	0.2814	0.000029	0.000997	0.000016	0.2814	-10.76	0.32	2.54	3.06	2.93
337.4-6-3	core	1754	16	0.2815	0.000039	0.001544	0.000088	0.2815	-6.78	0.45	2.42	2.83	2.73
337.3-4-1	core	1742	15	0.2814	0.000026	0.00084	0.000039	0.2813	-12.21	0.67	2.61	3.16	3.02
B-R49– granite, Horto-Baratinha													
BR49-4-3	core	1678	21	0.2813	0.000024	0.0008608	0.0000054	0.2813	-15.51	0.30	2.68	3.31	3.16
B.3-2_sW	core	1740	9	0.2813	0.000019	0.0009482	0.0000038	0.2813	-13.51	0.12	2.66	3.24	3.10
BR49-4-2	core	1724	28	0.2813	0.000019	0.000845	0.000012	0.2813	-13.19	0.40	2.63	3.20	3.06
BR49-3-1	rim	1716	29	0.2813	0.000019	0.001538	0.000048	0.2813	-14.44	0.70	2.69	3.27	3.13
BR49-5-1	core	1736	7	0.2813	0.000024	0.00117	0.0001	0.2813	-13.52	1.21	2.66	3.23	3.09

continued

Sample/Spot ID	spot location	Age (Ma)	$\pm 2s$	Present day ratios				Initial Ratios			T_{DM} Model Ages (Ga)		
				$^{176}\text{Hf}/^{177}\text{Hf}$	$\pm 2\text{SE}$	$^{176}\text{Lu}/^{177}\text{Hf}$	$\pm 2\text{SE}$	$^{176}\text{Hf}/^{177}\text{Hf}$ (t)	eHf(t)	$\pm 2\text{SE}$	T_{DM}	T_{DM} a	T_{DM} b
B-R54 – paraschist, Horto-Baratinha													
GR54-6-1	core	1717	13	0.2809	0.000054	0.000922	0.000015	0.2809	-28.07	0.67	3.18	4.11	3.88
GR54-7-1	core	2842	9	0.2810	0.000091	0.001541	0.000031	0.2809	-3.09	0.07	3.21	3.44	3.39
GR54-5-2	core	2567	10	0.2813	0.000065	0.001397	0.00004	0.2812	1.95	0.06	2.78	2.91	2.88
G.1-2_sW	core	2681	7	0.2810	0.000033	0.001699	0.000044	0.2809	-6.27	0.18	3.19	3.52	3.44
GR54-4-3	core	2582	8	0.2813	0.000022	0.00102	0.000016	0.2813	5.40	0.10	2.66	2.71	2.70
GR54-4-4	core	2688	11	0.2812	0.000024	0.002475	0.000024	0.2811	1.89	0.03	2.89	3.01	2.98
GR54-4-2	core	2620	9	0.2811	0.000021	0.001335	0.000041	0.2810	-2.51	0.09	2.99	3.24	3.18
GR54-3-1	core	2748	11	0.2810	0.000047	0.0006457	0.0000066	0.2810	-1.51	0.02	3.06	3.27	3.22
GR54-1-2	core	2929	7	0.2810	0.000023	0.001255	0.000025	0.2809	1.85	0.04	3.09	3.20	3.17
B-R56 – paraschist, Horto-Baratinha													
.ER56-7-1	core	1729	13	0.2812	0.00003	0.000805	0.000043	0.2812	-16.96	1.03	2.77	3.44	3.28
ER56-4-1	core	2593	23	0.2811	0.000032	0.001626	0.000017	0.2810	-4.62	0.09	3.05	3.35	3.28
ER56-11-3	core	2578	9	0.2811	0.000031	0.000518	0.000013	0.2811	-1.39	0.04	2.91	3.13	3.08
E.3-2_Sw	core	2556	18	0.2810	0.000025	0.001426	0.000041	0.2809	-9.34	0.33	3.20	3.61	3.51
E.4-2_sW	core	2677	15	0.2806	0.000024	0.000794	0.000015	0.2806	-17.42	0.43	3.59	4.20	4.06
ER56-10-2	core	2728	8	0.2808	0.000034	0.0008	0.00015	0.2808	-9.55	1.82	3.34	3.76	3.66
ER56-3-1	core	2607	11	0.2813	0.000026	0.0007439	0.0000025	0.2813	6.74	0.05	2.63	2.64	2.64
ER56-10-3	core	2695	9	0.2809	0.000029	0.000605	0.000037	0.2808	-8.01	0.52	3.25	3.64	3.55
E.1-2_sW	core	2810	21	0.2810	0.000025	0.00046	0.000021	0.2809	-1.31	0.07	3.10	3.31	3.26
ER56-6-2	core	2897	9	0.2809	0.000035	0.000815	0.00002	0.2808	-2.88	0.08	3.24	3.47	3.42
ER56-2-2	core	3333	8	0.2810	0.000025	0.001029	0.000027	0.2810	11.67	0.33	3.07	2.89	2.93
ER56-7-2	core	3479	15	0.2811	0.000027	0.001247	0.000026	0.2810	17.69	0.45	2.97	2.62	2.70

continued

Sample/Spot ID	spot location	Age (Ma)	$\pm 2s$	Present day ratios				Initial Ratios			T_{DM} Model Ages (Ga)		
				$^{176}\text{Hf}/^{177}\text{Hf}$	$\pm 2\text{SE}$	$^{176}\text{Lu}/^{177}\text{Hf}$	$\pm 2\text{SE}$	$^{176}\text{Hf}/^{177}\text{Hf}$ (t)	eHf(t)	$\pm 2\text{SE}$	T_{DM}	T_{DM} a	T_{DM} b
B-R63 – granite, Horto-Baratinha													
BR63-4-1	core	1542	73	0.2814	0.000023	0.000781	0.000034	0.2814	-16.10	1.47	2.58	3.24	3.08
BR63-1-2	core	1742	7	0.2813	0.00002	0.0010568	0.0000087	0.2813	-13.99	0.18	2.68	3.27	3.12
BR63-2-2	core	1731	18	0.2813	0.000027	0.000928	0.00001	0.2813	-13.95	0.30	2.66	3.26	3.11
BR63-5-1	core	1745	27	0.2814	0.000028	0.001121	0.000061	0.2814	-10.59	0.74	2.55	3.06	2.94
B-R66 – orthogneiss, Horto-Baratinha surroundings													
IR66-3-1	core	2708	6	0.2811	0.000036	0.00273	0.00015	0.2810	-3.16	0.18	3.11	3.34	3.28
IR66-4-1	core	2687	6	0.2811	0.000025	0.00161	0.000056	0.2810	-1.61	0.06	3.02	3.23	3.18
IR66-7-1	core	2700	4	0.2811	0.000019	0.001848	0.000018	0.2810	-2.68	0.03	3.07	3.31	3.25
IR66-8-1	core	2716	4	0.2811	0.000027	0.00242	0.00038	0.2809	-3.45	0.55	3.12	3.37	3.31
IR66-9-1	core	2708	4	0.2811	0.000032	0.00346	0.00044	0.2809	-4.05	0.52	3.15	3.40	3.33
B-S15 – paraschist, Horto-Baratinha													
C.6-1_sW	rim	522	8	0.2819	0.00011	0.0002515	0.0000057	0.2819	-19.41	0.73	1.83	2.65	2.45
CS15-5-1	rim	522	4	0.2819	0.000062	0.0000511	0.0000067	0.2819	-20.20	2.81	1.85	2.69	2.49
CS15-3-1	rim	535	5	0.2818	0.000053	0.0000286	0.0000023	0.2818	-21.74	1.94	1.92	2.80	2.59

continued

Sample/Spot ID	spot location	Age (Ma)	$\pm 2s$	Present day ratios				Initial Ratios			T_{DM} Model Ages (Ga)		
				$^{176}\text{Hf}/^{177}\text{Hf}$	$\pm 2\text{SE}$	$^{176}\text{Lu}/^{177}\text{Hf}$	$\pm 2\text{SE}$	$^{176}\text{Hf}/^{177}\text{Hf}$ (t)	eHf(t)	$\pm 2\text{SE}$	T_{DM}	T_{DM} a	T_{DM} b
C-R14– paraschist, Cuité													
FR14-3-2	core	1756	20	0.2813	0.000025	0.001301	0.000011	0.2813	-13.05	0.26	2.66	3.22	3.08
FR14-3-1	core	1718	15	0.2815	0.000028	0.001264	0.000022	0.2814	-9.95	0.26	2.51	3.00	2.88
FR14-8-1	core	1719	22	0.2815	0.000059	0.001084	0.000076	0.2815	-6.80	0.56	2.38	2.80	2.70
HR14-1-2	core	1739	35	0.2813	0.000023	0.0005896	0.0000088	0.2813	-13.51	0.47	2.65	3.23	3.09
HR14-4-1	core	1746	16	0.2813	0.000017	0.001202	0.000041	0.2813	-14.00	0.61	2.69	3.27	3.13
HR14-4-2	core	1735	16	0.2814	0.000024	0.0010234	0.0000028	0.2813	-12.73	0.16	2.62	3.18	3.05
FR14-5-1	core	1751	21	0.2813	0.000023	0.001096	0.000031	0.2813	-14.34	0.58	2.70	3.30	3.15
H.3-1_sW	core	1711	24	0.2813	0.00002	0.000785	0.000016	0.2813	-14.30	0.50	2.66	3.26	3.12
FR14-9-1	core	1726	9	0.2813	0.000025	0.00142	0.00012	0.2813	-14.49	1.30	2.69	3.28	3.14
FR14-1-2	core	1731	14	0.2814	0.000028	0.002513	0.000019	0.2813	-14.45	0.22	2.72	3.29	3.14
HR14-6-2	core	3107	19	0.2807	0.000029	0.000791	0.000026	0.2807	-3.40	0.13	3.44	3.67	3.61
H.1-3_sW	core	3040	15	0.2808	0.000024	0.0016	0.00011	0.2807	-3.04	0.22	3.37	3.59	3.54
C-R23 – schist, Cuité													
AR23-1-1	core	494	3	0.2818	0.000042	0.000094	0.000014	0.2818	-24.69	3.82	2.00	2.94	2.72
AR23-2-1	core	510	6	0.2821	0.000048	0.00002759	8.3E-07	0.2821	-11.50	0.48	1.51	2.15	2.00
A.8-1_sW	rim	513	4	0.2818	0.000094	0.0000517	0.0000029	0.2818	-23.09	1.49	1.95	2.86	2.64
AR23-5-1	core	1753	20	0.2815	0.000031	0.000398	0.000043	0.2815	-5.79	0.69	2.36	2.77	2.67
AR23-7-1	core	1744	26	0.2813	0.000024	0.000697	0.000014	0.2813	-12.92	0.45	2.63	3.20	3.07

Notes:

Values for ($^{176}\text{Hf}/^{177}\text{Hf}$)CHUR (0.282785) and ($^{176}\text{Lu}/^{177}\text{Hf}$)CHUR (0.0336) are from Bouvier et al. (2008).

eHf(t) calculated using a Lu decay constant of $1.867 \cdot 10^{-11} \text{ a}^{-1}$ (Soderlund et al., 2004).

Two-stage model ages (T_{DM} crustal – a, b) were calculated assuming a mean $^{176}\text{Lu}/^{177}\text{Hf}$ value of 0.015 (Goodge and Vervoort, 2006) and of 0.0125 (Chauvel et al., 2014).

Present-day $^{176}\text{Hf}/^{177}\text{Hf}$ ratio of the depleted mantle = 0.28325 (Anderson et al., 2009)

6D. $\delta^{18}\text{O}$ by SIMS

Sample/Spot ID	spot location	δ18O	2s abs
B-R12 – pegmatite, Horto-Baratinha			
CR12-1-3	rim	6.35	0.32
CR12-1-4	rim	7.31	0.41
CR12-1-2	rim	7.24	0.37
CR12-1-1	rim	6.49	0.34
CR12-1-5	rim	6.31	0.36
CR12-1-6	rim	6.37	0.36
B-R56 – paraschist, Horto-Baratinha			
ER56-2-1	rim	7.61	0.34
ER56-2-2	core	5.54	0.37
ER56-3-1	core	5.12	0.46
ER56-4-2	rim	5.10	0.32
ER56-4-1	core	5.98	0.34
ER56-6-1	rim	7.32	0.35
ER56-6-4	core	5.59	0.37
ER56-6-2	core	6.14	0.38
ER56-7-1	core	6.01	0.33
ER56-7-2	core	5.35	0.33
ER56-10-2	core	6.48	0.37
ER56-10-3	core	5.42	0.45
B-R63 – granite, Horto-Baratinha			
BR63-1-2	core	6.38	0.32
BR63-2-2	core	6.63	0.36
BR63-2-3	rim	5.67	0.42
BR63-2-4	core	6.54	0.37
BR63-4-1	core	6.47	0.38
BR63-4-2	core	6.08	0.32
BR63-4-3	core	6.68	0.37
BR63-5-1	core	6.30	0.36
BR63-5-2	rim	6.46	0.40
BR63-12-1	rim	5.96	0.38
BR63-12-3	core	6.18	0.38
BR63-12-4	core	6.13	0.36
BR63-12-6	core	6.43	0.35
C-R14 – paraschist, Cuité			
FR14-1-1	rim	5.08	0.33
FR14-1-2	core	5.89	0.36
FR14-3-1	core	5.66	0.38
FR14-3-2	core	5.80	0.35
FR14-5-1	core	5.73	0.40
FR14-7-1	core	5.63	0.41
FR14-8-1	core	5.70	0.39

Curriculum Lattes

Flávia Cristina Silveira Braga

Possui graduação em Geologia (2009), mestrado (2012) e doutorado (2019) em Geologia Econômica e Aplicada pela Universidade Federal de Minas Gerais (UFMG). É professora efetiva da Faculdade de Engenharia (FaEng - João Monlevade) da Universidade do Estado de Minas Gerais (UEMG). Atua na área de Geociências, com ênfase em Mineralogia e Geologia do Minério de Ferro, Prospecção Mineral, Geologia Estrutural e Geoprocessamento. Atuou na área de pesquisa mineral em empresa privada. Realizou trabalhos na área de geoprocessamento, mapeamento geológico e confecção de relatórios para DNPM (requerimentos de pesquisa e relatórios finais de pesquisa). Tem experiência em gerenciar projetos de pesquisa mineral, tendo realizado a programação de pesquisa (mapeamento de superfície e subsuperfície, malha de sondagem, trabalhos de topografia, monitoramento ambiental), implantação de banco de dados, tratamento de dados QAQC e modelamento geológico 3D.

Histórico Profissional

UEMG – Universidade do Estado de Minas Gerais

2017 - Atual Vínculo: Servidor Público, Enquadramento Funcional: Professor efetivo (nível IV, grau A),

Faculdades Kennedy

2015 - 2017 Vínculo: Professor auxiliar, Enquadramento Funcional: Professor auxiliar, Carga horária: 18

Outras informações Professora das disciplinas de Geologia Econômica, Desenho e Mapa de Mina, Geologia do Brasil, Petrografia e Topografia.

Terrativa Minerais SA

2010 - 2014 Vínculo: Funcionário, Enquadramento Funcional: Geólogo pleno, gerente de projeto, Carga horária: 44, Regime: Dedicação exclusiva.

Outras informações Entre junho de 2012 a setembro de 2014: Gerente de projeto de pesquisa mineral para potássio nos estados de Pernambuco e Bahia. Realizou a programação de pesquisa mapeamento de superfície e subsuperfície, malha de sondagem, trabalhos de topografia, monitoramento ambiental), implantação de banco de dados, tratamento de dados QAQC, modelamento geológico 3D e redação de relatórios para DNPM. Entre Janeiro de 2010 a maio de 2012: Atuou na área de controle de processos DNPM. Elaborou requerimentos de pesquisa, relatórios finais de pesquisa e habilitações. Realizou trabalhos de geoprocessamento (softwares ArcGis, Micromine, Minesight). Avaliou o potencial mineral para exploração de ferro, zinco, ouro e fosfato, em áreas localizadas nos estados de Minas Gerais, Tocantins, Ceará, Piauí, Pernambuco. Participou do projeto de ferro de Morro Escuro, localizado no município de Santa Maria de Itabira, MG, tendo realizado mapeamento geológico e descrição de testemunhos de sondagem.